A Spontaneous Rayleigh-Brillouin scattering experiment for the characterization of atmospheric Lidar backscatter

Ubachs, W.M.G.; van Duijn, E.-J.; Vieitez, M.O.; Van de Water, W.; Dam, N.; Ter Meulen, J.J.; Meijer, A; De Kloe, J.; Stoffelen, A.; Aben, E.A.A.

2010

document version
Publisher's PDF, also known as Version of record

ESA - AO/1-5467/07/NL/HE

A SPONTANEOUS RAYLEIGH-BRILLOUIN SCATTERING EXPERIMENT FOR THE CHARACTERIZATION OF ATMOSPHERIC LIDAR BACKSCATTER

Final Report

Prof. Dr. W. Ubachs, Dr. E.-J. van Duijn, M.O. Vieitez MSc.
Laser Centre Vrije Universiteit Amsterdam, Netherlands

Prof. Dr. W. Van de Water
Eindhoven University of Technology, Netherlands
Institute for Molecules and Materials, Radboud University Nijmegen

Dr. N. Dam, Prof. Dr. J.J. ter Meulen, Dr. A. S. Meijer
Institute for Molecules and Materials, Radboud University Nijmegen

Dr. J. de Kloe, Dr. A. Stoffelen
KNMI, de Bilt, Netherlands

Prof. Dr. E.A.A. Aben
SRON Utrecht, Netherlands
Laser Centre Vrije Universiteit Amsterdam, Netherlands

CONTENTS

List of Acronyms

2HG	Second Harmonic Generation – create frequency 2ω of and original frequency ω
ADM-Aeolus	Atmospheric Dynamics Mission- Earth Explorer
Aladin	Atmospheric LAser Doppler INstrument
AR coated	Anti-Reflection coated
BK7	borosilicate glass Schott
CCD camera	charge-coupled device camera
CRBS	Coherent Rayleigh-Brillouin Scattering
CW	Continuous Wave (laser light, for example)
E2S	End-to-End Simulator (instrument simulator)
ESA	European Space Agency
F	Finesse (of an etalon)
FFT	Filtering Fourier Transform
FP	Fabry-Perot (etalon)
FSR	Free Spectral Range (of an etalon, for example)
FWHM	Full Width at Half-Maximum (of a line shape)
IMM	Institute for Molecules and Materials
KNMI	het Koninklijk Nederlands Meteorologisch Instituut (The Royal Netherlands Meteorological Institute)
laser	Light Amplification by Stimulated Emission of Radiation
L2b	Aeolus Level 2b product (wind profiles)
LCVU	Laser Centre Vrije Universiteit
Lidar	LIght Detection And Ranging or Laser Imaging Detection And Ranging
LIEG	Laser-Induced Electrostrictive Grating
LOS	Line-of-Sight
Nd:YAG laser	Neodymium-Doped Yttrium Aluminium Garnet (Nd:$Y_3Al_5O_{12}$) crystal as laser medium
NWP	Numerical Weather Prediction
PDF	Probability Density Function
PMT	Photo-Multiplier Tube (light detector)
Q-switch	Quality-factor switch (inside a laser cavity)
RB	Rayleigh-Brillouin
RBS	Rayleigh-Brillouin Scattering
rbs	Updated tenti code, provided by Willem van de Water
RF	Radio Frequency
ROC	Radius Of Curvature (of a mirror, for example)
RUN	Radboud University Nijmegen
SRP	Spontaneous Rayleigh-Brillouin
SRBS	Spontaneous Rayleigh-Brillouin Scattering
SRON	(Nederlands Institute for Space Research)
Ti:Sa laser	Titanium-doped Sapphire crystal as a laser medium
TN	Technical Note
USR	Useful Spectral Range
UV	Ultra-Violet
VU	Vrije Universiteit

Notation and symbols

$\mathbf{r}$	position vector of the particles (molecules or atoms)
t	time
$\boldsymbol{v}$	velocity vector of the particles (molecules or atoms)
c	speed of light in vacuum (299792458 m/s)
$\varepsilon(\mathbf{r},t)$	instantaneous dielectric constant
ε_0	mean dielectric constant
μ_0	mean magnetic permeability
n	index of refraction of the medium
$\mathbf{E}$	Electric field vector
$\mathbf{D}$	Dielectric displacement field vector
$\mathbf{E_0}$	incident electric field
$\mathbf{k_i}$	propagation vector of the incident (SRBS) electric field (laser)
$\mathbf{k_{probe}}$	propagation vector of the (incident) probe (CRBS) electric field (laser)
ν_i	frequency of the incident electric field
$\omega_i = 2\pi\nu_i$	angular frequency of the incident electric field (SRBS)
ω_{probe}	angular frequency of the (incident) probe electric field (CRBS)
λ_i	incident electric field wavelength (in vacuum)
$\mathbf{E_{sc}}$	scattered electric field
$\mathbf{k_{sc}}$	propagation vector of the scattered electric field (SRBS)
$\mathbf{k_{signal}}$	propagation vector of the scattered electric field (CRBS)
ω_{sc}	angular frequency of the scattered wave (SRBS)
ω_{signal}	angular frequency of the scattered wave (CRBS)
$\omega = \omega_i - \omega_{sc}$	angular frequency difference between the angular frequency of the incident wave, ω_i, and that of the scattered wave (SRBS), ω_{sc}
$\omega = \omega_{probe} - \omega_{signal}$	angular frequency difference between the angular frequency of the probe wave, ω_{probe}, and that of the scattered wave (CRBS), ω_{signal}
$\mathbf{k} = \mathbf{k_i} - \mathbf{k_{sc}}$	difference between the wave vectors of the incident and the scattered (SRBS) waves (modulus $k = 2k_i\sin(\theta/2)$)
$\mathbf{k} = \mathbf{k_{probe}} - \mathbf{k_{signal}}$	difference between the wave vectors of the incident and the scattered (CRBS) waves (modulus $k = 2k_{probe}\sin(\theta/2)$)
$\sigma(\mathbf{k}, \omega)$	scattering cross section
$S(\mathbf{k}, \omega)$	Space-time Fourier transform of the density correlation function, gives the shape of the Rayleigh-Brillouin peaks.
ϕ	angle between the electric vector of the incident light wave, $\mathbf{E_0}$, and the propagation vector of the scattered wave, $\mathbf{k_{sc}}$
θ	angle between the incident wave vector ($\mathbf{k_i}$) and the scattered wave vector ($\mathbf{k_{sc}}$)
$\Lambda = (\lambda_i/n)/[2\sin(\theta/2)]$	characteristic scattering wavelength
ρ	gas density
ρ_0	average gas density
n_{den}	number density of molecules
T	temperature
k_B	Boltzmann constant
m	mass of the molecule
$v_T = (2k_BT/m)^{1/2}$	thermal speed of the molecules

v_S	(hypersonic) sound velocity
$x = \omega/(kv_S)$	generalized frequency scale
α_{col}	effective collision frequency
c_P	isobaric heat capacity
c_V	heat capacity at constant volume
$\gamma = c_P/c_V$	adiabatic index
κ	thermal conductivity
Γ	acoustic wave damping
η_S	shear viscosity
ζ	bulk viscosity
$L = v_T \eta_S/(n_{den} k_B T)$	mean free path of the gas molecules
$y = (1/2\pi)(\Lambda/L) = 1/(kL)$	kinetic parameter y
$F_k(v)$	King factor: gives the contribution to the unpolarized scattering due the non-sphericity of the molecules
α	molecular polarizability
J	collision operator
$f(\mathbf{r},\mathbf{v},t)$	microscopic phase-space density
$\Phi(v)$	Maxwell distribution
$h(\mathbf{r},\mathbf{v},t)$	deviation (fluctuation) from equilibrium (Maxwell distribution) of the microscopic phase-space density, $f(\mathbf{r},\mathbf{v},t) = \Phi(v)(1 + h(\mathbf{r},\mathbf{v},t))$
$a\nabla_v\phi$	dipole force term
A	Integrated signal on FP spectrometer A (direct channel [counts])
B	Integrated signal on FP spectrometer B (direct channel [counts])
R	Response of the combined dual edge spectrometer detection system
λ	Laser wavelength [m]
$\delta\lambda$	Doppler shift [m]
v_{LOS}	Component of the local windspeed projected on the line-of-sight of the lidar system

1 Motivation for the study and introduction

The present study is intimately linked to future missions of the European Space Agency. The immediate connection is to the ADM-Aeolus mission (see Figure 1-1) aiming to produce a velocity (wind) profile of vertical layers in the Earth atmosphere *on a global scale*. This is pursued by *active* remote sensing, i.e. by measuring the spectral profile of the back-scattered light from an ultraviolet laser on board of the satellite. An ultraviolet wavelength is chosen in the range where (i) powerful lasers are available, (ii) absorption is minimal, and (iii) the scattering cross section is high, allowing for high quality wind measurements for cloud-free conditions. The backscattered light is encoded with information of the velocity profile of the air-masses in various layers through Mie-scattering by aerosol particles and by Rayleigh-Brillouin scattering of the gaseous constituents of the atmosphere. The LIDAR principle is employed to gather information form the various atmospheric layers: signals triggered and induced by the short-duration laser pulses arrive at different times on the detector, thus allowing for the conversion of temporal information in terms of depth into the atmospheric layers.

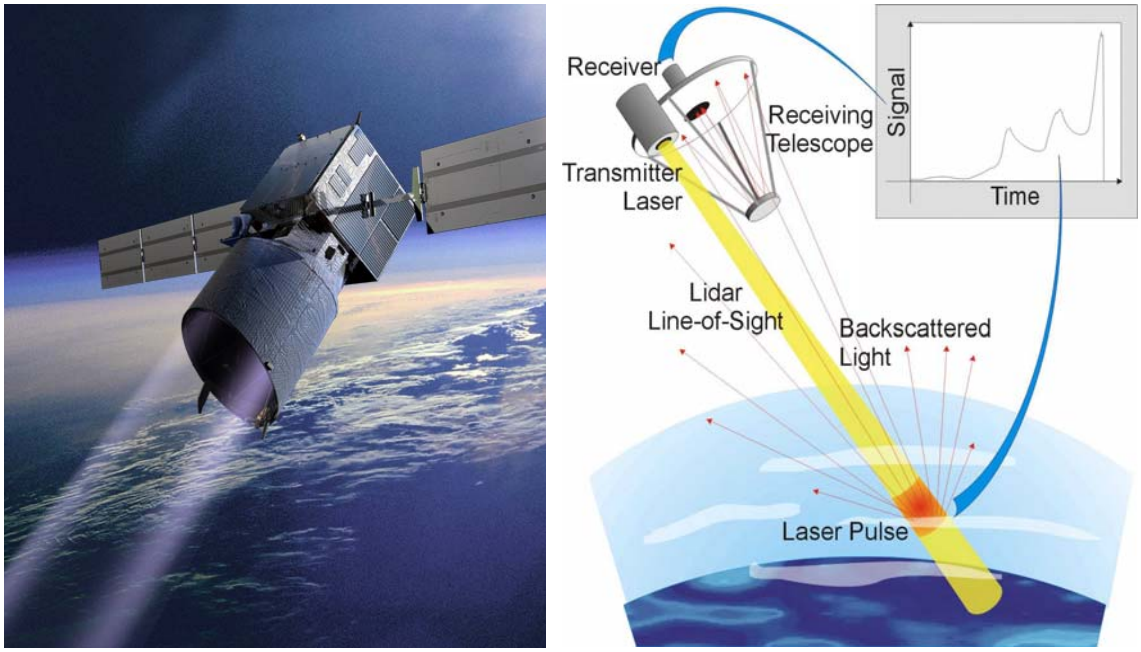

Figure 1-1: A pictorial representation of the ADM-Aeolus satellite mission; on the left the envisioned satellite system, and on the right a physical representation of the wind measurement scheme: a combination of LIDAR and Doppler sensing techniques.

In the recent past it was noted that the fact that expected molecular scattering functions are not just Gaussian profiles may influence the Doppler measurements and impact the wind profile analysis. In fact all the collisional properties of the molecular gas encode the scattering profile: Raman effects of rotational and vibrational origin and all phenomena

related to collisional redistribution of the gas in terms of quantum state populations, velocity changes and orientational redistribution of the molecular axes all affect the scattering profile in a complicated manner. In particular acoustic phenomena known to produce the characteristic Brillouin side-wings on the Doppler profile have a strong effect. This was identified as a major problem in a previous study (the ILIAD report [1]) and it was estimated that neglecting Brillouin effect might result in errors in the radial wind measurement of up to 10% in several cases. These estimates were made on the basis of models known in the literature since the 1970s as the TENTI models, named after a Canadian-based Italian scientist. These TENTI models had only been tested for a few measurement configurations and for a very small subspace of all possible gases, pressures and mixtures. It had not been tested for air under the various atmospheric conditions. Hence the goal of the present project was defined: measuring the spontaneous Rayleigh-Brillouin (RB) scattering profile and comparing them to both versions of the TENTI-models (the so-called TENTI S6 and TENTI S7 varieties) in conditions relevant for upcoming ESA LIDAR missions.

At the same time the project should aim to test the models, and experimentally determine deviations from it, to provide a broad database and understanding of Rayleigh-Brillouin scattering profiles for future atmospheric missions by ESA. In particular the knowledge on improved wind retrieval algorithms may be of relevance for EarthCARE. The objectives of the present study, as defined in the contract, were:

- Quantify the contribution of RB scattering to LIDAR molecular backscatter in a well-defined laboratory experiment.
- Validate the performance of the test equipment by reproducing the measurements of spontaneous RB scattering in N_2 as given by literature.
- Validate the TENTI (S6 and S7) model for atmospheric gas mixtures representing the Earth's atmosphere and assess the necessity of applying refinements to it.
- Make the necessary improvements of the TENTI (S6 and S7) model.
- Make recommendations for the use of the model in the Earth Explorer Core Mission and post-EPS Doppler Wind LIDAR retrieval algorithms.

The task was to set up a laboratory experiment with a suitable laser source to investigate spontaneous Rayleigh-Brillouin molecular backscatter form a target cell, filled with N_2, O_2, dry air, humid air, for ranges of pressures and temperatures relevant for the Earth atmosphere. Experimental differences with the TENTI-descriptions should be quantified.

At the start of the project we have proposed to perform measurements of the molecular scattering profile by investigating *coherent* Rayleigh-Brillouin spectroscopy in addition to the *spontaneous* RB measurements. Specifically for the central goal of understanding the TENTI-models and testing them in an as broad as possible parameter space, a second and independent technique is very valuable.

In the following sections of this report the physical mechanism of Rayleigh-Brillouin scattering will be described, with a review of the scientific literature and the previously obtained results on RB scattering profiles. While there had been a strong activity on spontaneous RB scattering of gases in the 1960s and 1970s, also leading to the formulation of the TENTI-formalism, the subject was left aside since then. The development of coherent RB scattering took place in the last decade. It was shown that the scattering profiles were essentially different (between spontaneous and coherent RB), but they could be related in a similar manner to the TENTI models.

In the framework of the present ESA-funded study a spontaneous RB spectrometer was built at the Laser Centre Vrije Universiteit Amsterdam, while a coherent RB spectrometer was built at the Radboud University Nijmegen. The experimental setups are described in detail in Sections 3 and 4 of this report.

Both approaches were very successful in the sense that they produced very high signal-to-noise scattering profiles for a number of gases and for a variety of pressures. It will be explained that exact back-scattering (at 180 degrees), as will be used in most active remote sensing applications, is difficult if not impossible to operate in the laboratory, while using a scattering cell; this is due to the fact that scattering from the molecular gas is always weaker than the scatter form the material of the entrance window of any cell. For this reason exact back-scatter geometries had never been used in the scientific literature. In both SRB and CRB experiments a compromise was adopted on a scattering angle to test the TENTI profiles. The obtained spectra represent the best experimental data obtained so far to test lines shape models such as TENTI.

The TENTI models were put in an easy to operate FORTRAN-based program that can be run interactively to match the wide variety of data pertaining to both SRB and CRB, at all scattering angles and for all wavelengths. The measurements show that there exist definite discrepancies with the TENTI-6 model, which better represents the experimental findings as was anticipated in the ILIAD study [1]. These discrepancies will be quantified for a number of conditions and the effect on the wind retrieval for the ADM-Aeolus mission will be quantified as well.

This reports end with a conclusion and some recommendations for future research.

2 Introduction to Rayleigh-Brillouin Scattering

We will describe the most important results about spontaneous Rayleigh-Brillouin (RB) scattering. By spontaneous light scattering, we mean light scattering under conditions such that the optical properties of the material system are unmodified by the presence of the incident light beam. The character of the light scattering process is profoundly modified whenever the intensity of the incident light is sufficiently large to modify the properties of the material system.

Light scattering of molecules in the Earth's atmosphere is generally well understood and was described by Rayleigh in his classic paper [2]. Rayleigh' s theory, yielding a cross section for light scattering scaling with $1/\lambda^4$, was based on the basic formalism of electromagnetism. The scattering of an incident light beam of frequency v_o that is propagating through a medium (in our case, the atmosphere) will show, in the most general circumstances, a spectrum that has the form shown in Figure 2-1.

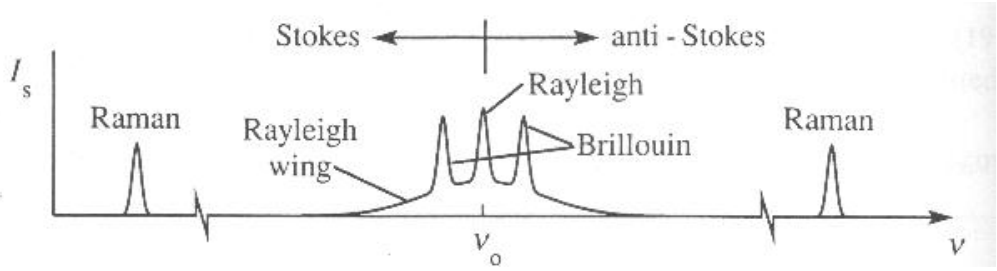

Figure 2-1: Spectrum of the Rayleigh scattered radiation, with incident radiation at frequency v_o.

This spectrum contains the well-known Raman side bands associated with inelastic scattering of molecules with internal vibrational and rotational structure. For the nitrogen molecules, the Raman shifts are 2000 cm^{-1} for the vibrational sidebands, and several cm^{-1} for the rotational sidebands (1 cm^{-1} corresponds to 30 GHz). Stokes components are redshifted, in which case the molecules become excited after scattering, and the Anti-Stokes components are blueshifted. In the latter case the molecules donate energy to the scattered photons. The central part (onwards called Rayleigh-Brillouin feature) is again split in a central scattering peak, known as the Rayleigh peak (called sometimes Gross peak), with side-bands related to acoustic, or kinetic effects in the medium, known as the Brillouin peaks. The central Rayleigh peak is broadened with respect to the incident light due to Doppler shift by the thermal motions of the individual gas molecules in the medium. Molecular re-orientation effects during excitation and caused by collisions may play a role as well; those are particularly well visible in the liquid phase.

The objective of the ADM-Aeolus mission is to measure wind profiles from the Rayleigh-Brillouin backscattered light in a LIDAR configuration, for which the Atmospheric Laser Doppler Instrument (ALADIN) is in preparation. The physical principle of the wind measurements is the Doppler-shift of the backscattered light that is imposed by the motion of the molecules and the solid particles in the atmosphere. The spectroscopic unravelling of the features of Doppler shift, to deduce a wind profile, may become blurred by the phenomenon of broadening and splitting into components of the

Rayleigh-Brillouin line shape. Moreover the exact behaviour of these side bands is not known nor experimentally studied in sufficient detail (examples for molecular nitrogen at various pressures are shown in Figure 2-3: no information seems to be available on the phenomenon in polar gases such as H_2O, nor are experiments performed in gas samples of mixed composition of atmospheric relevance. Roughly speaking the goal of the proposed project is to provide such data, in addition to validation of previous experimental observations, as well as providing a model line shape as a function of pressure, temperature (and hence altitude) and composition of the Earth's atmosphere.

In the following we will develop the relevant equations to understand the origin of the central Rayleigh-Brillouin feature and the parameters that govern its shape.

2.1 The dielectric tensor and the origin of the different scattering terms

The dielectric tensor represents the ability of a (dielectric) medium to respond to an external electric field, such as a laser beam (an electro-magnetic wave). In a general case, it is a second rank tensor. In the case of a molecular gas, it is safe to assume that the medium is isotropic in its average properties.

Light scattering occurs as a consequence of fluctuations in the optical properties of a material medium; a completely homogeneous material can scatter light only in the forward direction [3]. Since light scattering results from fluctuations in the optical properties of a material medium, it is useful to express separately the elements in the dielectric tensor:

$$\varepsilon_{ik} = \varepsilon_0 \delta_{ik} + \Delta\varepsilon_{ik}$$

where ε_0 is the mean dielectric constant (the medium is assumed isotropic) and $\Delta\varepsilon_{ik}$ represents the (temporally and/or spatially varying) fluctuations in the dielectric tensor that leads to light scattering. These fluctuations can be also separated:

$$\Delta\varepsilon_{ik} = \Delta\varepsilon\delta_{ik} + \Delta\varepsilon^{(t)}_{ik}$$

where $\Delta\varepsilon$ is the scalar contribution and $\Delta\varepsilon^{(t)}_{ik}$ is a traceless tensor contribution of the dielectric tensor. The scalar contribution arises from fluctuations in the thermodynamic quantities such as density, temperature, entropy or pressure. Scattering that arises from $\Delta\varepsilon$ is called *scalar light scattering* such as Rayleigh-Brillouin scattering and it has the property of maintaining the polarization of the incident electric field. Because of that, it is sometimes called *polarized Rayleigh scattering*.

Scattering that arises from $\Delta\varepsilon^{(t)}_{ik}$ is called *tensor light scattering*, and the symmetric part of the tensor is responsible for the Rayleigh wing scattering, while the anti-symmetric part of the tensor is responsible for the Raman scattering [3]. It changes the polarization of the incident field and therefore it is sometimes called *depolarized Rayleigh scattering*.

In what follows we will only deal with the scalar light scattering, so we will neglect the tensorial part of the dielectric response.

In general the fluctuations in the dielectric constant can be expressed in terms of density (ρ) and temperature (T) variations in the medium $\Delta\varepsilon = (\partial\varepsilon/\partial\rho)_T\Delta\rho + (\partial\varepsilon/\partial T)_\rho\Delta T$,
but for dilute gases and many liquids the coupling between the dielectric constant and temperature is sufficiently weak that the effects of temperature fluctuations usually can be ignored [4] hence $(\partial\varepsilon/\partial\rho)_T >> (\partial\varepsilon/\partial T)_\rho$.
Then, the main contribution to fluctuations in the dielectric properties comes from fluctuations in the gas density $\rho=\rho(\mathbf{r},t)$:

$\Delta\varepsilon = (\partial\varepsilon/\partial\rho)\Delta\rho = (\partial\varepsilon/\partial\rho)(\rho-\rho_0)$ and ρ_0 is the average gas density.

The dielectric constant can be written as:

$$\varepsilon = \varepsilon_0 + (\partial\varepsilon/\partial\rho)(\rho - \rho_0) = \varepsilon_0 + \varepsilon_1(\rho(\mathbf{r},t)) \quad (2.1)$$

with $\varepsilon_1 << \varepsilon_0$.

2.2 Maxwell equations and the $1/\lambda^4$ scaling of the scattering cross section

Considering the general case in which incident light is scattered by a group of neutral molecules, the Maxwell equations of the system are:

$$\nabla^2\mathbf{E}-\nabla(\nabla.\mathbf{E}) = (1/c^2)[\partial^2(\varepsilon\mathbf{E})/\partial t^2] \quad (2.2)$$

$$\nabla.\mathbf{D} = \nabla.(\varepsilon\mathbf{E}) = 0$$

where $\mathbf{E}$ is the electric field vector in the medium, $\mathbf{D}$ is the dielectric displacement field vector, c is the velocity of light in vacuum and ε is the dielectric constant of the medium. $\mathbf{E}$ is the sum of the incident electric field $\mathbf{E_0}$ and the scattered field $\mathbf{E_{sc}}$.

$$\mathbf{E} = \mathbf{E_o} + \mathbf{E_{sc}} \text{ and } |\mathbf{E_{sc}}| << |\mathbf{E_0}| \quad (2.3)$$

Substituting equations (2.1) and (2.3) into equation (2.2) and setting sums of terms of equal magnitude to zero, we obtain a series of successive equations.
Zero[th] order:

$$\nabla^2\mathbf{E_0} = (\varepsilon_0/c^2)[\partial^2(\mathbf{E_0})/\partial t^2] \text{ (wave equation)} \quad (2.4)$$

First order:

$$\nabla^2\mathbf{E_{sc}} - (\varepsilon_0/c^2)(\partial^2\mathbf{E_{sc}}/\partial t^2) = (1/c^2)(\partial^2\varepsilon_1\mathbf{E_0}/\partial t^2) - (1/\varepsilon_0)\nabla(\nabla.\varepsilon_1\mathbf{E_0}) \quad (2.5)$$

Solutions to equation (2.4) are planar monochromatic waves:

$$\mathbf{E_0} = |\mathbf{E_0}|\exp(i\mathbf{k_i}.\mathbf{r}-i\omega_i t)$$

Where $\mathbf{k_i}$ is the propagation vector of the incident wave and ω_i is its angular frequency, and they fulfil the dispersion relation

$$|\mathbf{k_i}| = (\varepsilon_0)^{1/2}\omega_i/c = n\omega_i/c = 2\pi n/\lambda_i$$

where n is the index of refraction of the medium and λ_i is the laser wavelength (in vacuum).
The solutions to equation (2.5) can be obtained with Fourier analyses (in both space and time) method [4,5]. The **scattering cross section** (σ) can be written as:

$$\sigma(\mathbf{k},\omega) = |\mathbf{E_0}|^2\sin^2\phi\,(\partial\varepsilon/\partial\rho)^2(\omega_i^4/c^4)S(\mathbf{k},\omega) \quad (2.6)$$

where $\mathbf{k} = \mathbf{k_i} - \mathbf{k_{sc}}$ is the difference between the wave vectors of the incident and the scattered waves, ϕ is the angle between the electric vector of the incident light wave, $\mathbf{E_0}$, and the propagation vector of the scattered wave, $\mathbf{k_{sc}}$ and ω is the angular frequency difference between the angular frequency of the incident wave, ω_i, and that of the scattered wave, ω_{sc} ($\omega = \omega_i - \omega_{sc}$). $S(\mathbf{k},\omega)$ is the space and time Fourier transform of the (Van Hove) space-time density correlation function $G(r,t)$. $S(\mathbf{k}, \omega)$ gives the actual shape of the Rayleigh and Brillouin peaks.

From Eq. 2.6 several observations can be made:

- No assumptions on the conditions of the medium have been made yet. Therefore this equation is valid for liquids and all gas conditions.
- There is a ω_i^4 dependence on the angular frequency of the scattered signal ($\omega_i = 2\pi c/\lambda_i$, giving $\sigma \sim 1/\lambda_i^4$). This means that at $\lambda_i = 355$ nm the light scattering process will be more intense than at longer wavelengths: blue light scatters more than red light.
- There is a $\sin^2\phi$ dependence. Therefore, to obtain maximum signal, all the observations must be made at $\phi = 90^\circ$ ($\sin(90^\circ) = 1$) angles with respect to the polarization of the incident light (see Figure 2-2). This is of particular importance if a polarized light source (like a laser) is used.

2.3 Characteristic scattering wavelength

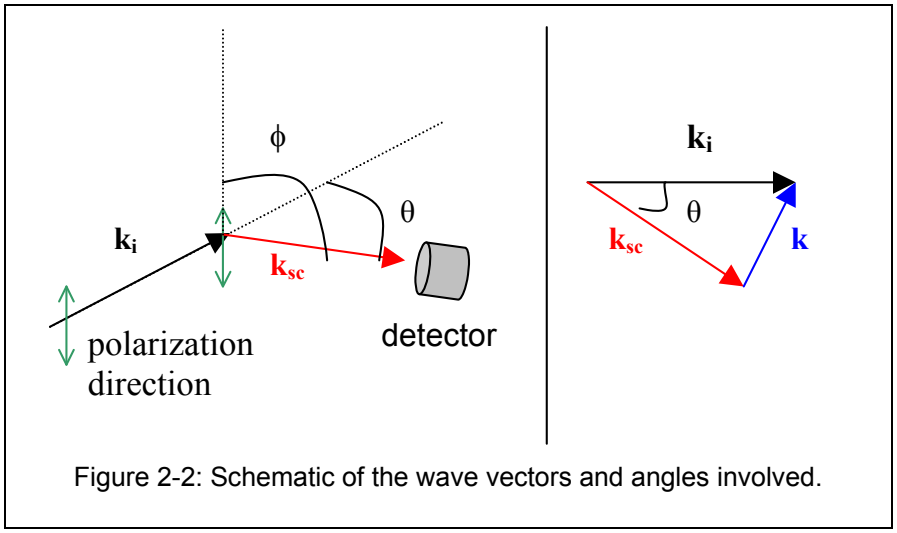

Figure 2-2: Schematic of the wave vectors and angles involved.

To define the characteristic scattering wavelength, observe that $|\mathbf{k_{sc}}| \approx |\mathbf{k_i}|$ and then it can be calculated:

$$|\mathbf{k}| = 2|\mathbf{k_i}|\sin(\theta/2) \qquad (2.7)$$

where θ is the angle between the incident wave vector ($\mathbf{k_i}$) and the scattered wave vector ($\mathbf{k_{sc}}$).
The **characteristic scattering wavelength** is:

$$\Lambda = \frac{2\pi}{k} = \frac{\lambda_i/n}{2\sin(\theta/2)} \qquad (2.8)$$

2.4 Shape of Rayleigh-Brillouin feature and definition of the x and y parameters

The shape of the Rayleigh and Brillouin peaks is determined by the conditions on the density that goes in $S(\mathbf{k}, \omega)$. If the gas is very diluted, it behaves like a system of independent particles moving with straight trajectories, and collisions are not important.

If the gas is very dense, it approaches its fluid behavior, so the dominant equations of motion will be hydrodynamic. The dynamic processes are collision dominated.

To determine whether the gas is “diluted” or “very dense” we use the y parameter, which is proportional to the ratio of characteristic scattering wavelength (Λ) to mean free path (L) of the gas molecules.

$$y = \frac{1}{2\pi}\frac{\Lambda}{L}$$

When the gas is diluted, the probability of collisions between molecules is reduced, and therefore their mean free path increases, so the value of y decreases. This means that y << 1 is the condition for a diluted gas in the so-called *Knudsen regime*. The spectrum of the Rayleigh-Brillouin feature approaches the Doppler line shape of a single Gaussian. When y >> 1, the system is in the *hydrodynamic regime*. The frequency spectrum of the scattered light consists of a central (Rayleigh) Lorentzian-shaped line and two displaced Lorentzian components (Brillouin). In the intermediate region, when y ≈ 1, the system is said to be in the *kinetic regime*. The spectral distribution will not have as much structure as in the hydrodynamic regime, but also will not be as smooth as a Gaussian. As an example, these regimes are shown in Figure 2-3.

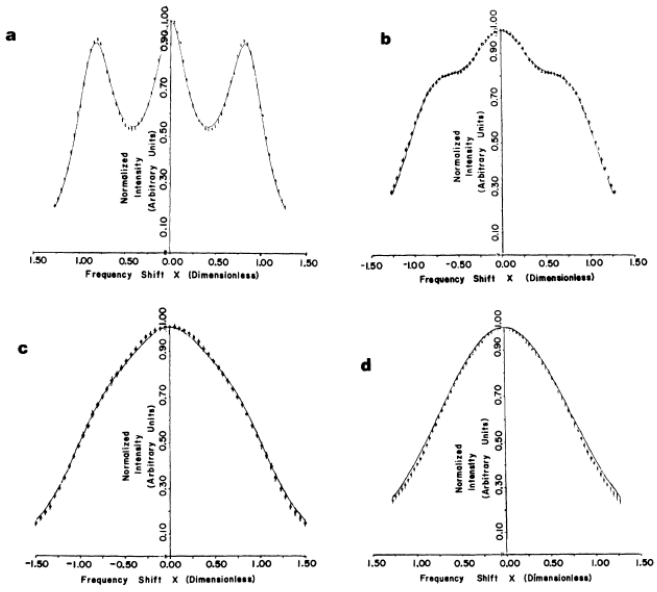

FIG. 2. Spectral profiles: (a) $P=641$ Torr, $y_T=4.39$, $\sigma_{min}=4.39\times10^9$ Hz, $\alpha_{min}=0.29$; (b) $P=154$ Torr, $y_T=1.05$, $\sigma_{min}=1.25\times10^9$ Hz, $\alpha_{min}=0.35$; (c) $P=81$ Torr, $y_T=0.55$, $\sigma_{min}=0.55\times10^9$ Hz, $\alpha_{min}=0.21$; (d) $P=1$ Torr, $y_T=0.007$, $\alpha_{min}\simeq0$, $\sigma_{min}=\simeq0$. Experimental points (closed circles with error bars). Theoretical spectrum is solid curve. $x=\omega/Kv_0$.

Figure 2-3*:* Measured spectral profiles of RBS in N_2 at different pressures (reproduced from Sandoval and Amstrong [6]. (a) p = 641 Torr, y = 4.39, (b) p = 154 Torr, y = 1.05, (c) p=81 Torr, y=0.55, (d) p = 1 Torr, y = 0.007. Points: experimental values. The theoretical spectrum is a solid curve. The dimensionless parameter x is a scaled frequency $x = \omega/(kv_S)$ (with v_S the sound velocity).

The figure demonstrates that different regimes exist, and that gradually go over into each other: at the low pressures in the Knudsen regime, molecules can be treated isolated, while at higher pressures (hydrodynamic), the molecules interact with each other via the sound waves, associated with pressure fluctuations and the Brillouin phenomenon.
It is possible to define a second dimensionless parameter x, representing a *generalized frequency scale*:

$$x = \omega/kv_s$$

with v_s the sound velocity under the chosen conditions.

In the treatment as presented here, any gaseous medium response will be a function of these two dimensionless parameters, which are essentially kinetic. The effects of dynamical interactions between molecules, possibly depending on species-specific intermolecular forces, do not play any role.

2.5 Calculation of the y parameter from temperature and pressure

The mean free path can be calculated:

$$L = v_T/\alpha_{col} \qquad (2.9)$$

where v_T is the thermal speed of the molecules and α_{col} is an effective collision frequency.

$v_T = (2k_BT/m)^{1/2}$ and $\alpha_{col} = P/\eta_S$

where T is the temperature, k_B is the Boltzmann constant, m is the mass of the molecule, P is the pressure and η_S is the shear viscosity.
Then, the y parameter can be written:

$$y = \frac{\lambda_i/n}{4\pi\sin(\theta/2)}\frac{P}{\eta_S\sqrt{2k_BT/m}} \qquad (2.10)$$

or equivalently: $y = \dfrac{n_{den}k_BT}{kv_T\eta_S}$

where n_{den} is the number density of the molecules.

From equation (2.10) several observations can be made:

- y is proportional to the incident wavelength. This means that at longer wavelength (and therefore lower frequency) y will increase and therefore, the shape of the Rayleigh-Brillouin feature will tend to the hydrodynamic shape. This means that the Brillouin peaks will get more resolved (see Figure 2-4). However, as the scattering signal depends as $\omega_i^4 \sim 1/\lambda_i^4$, *the signal intensity will decrease considerably*.
- y is inversely proportional to $\sin(\theta/2)$, and θ is the angle of observation (see Figure 2-2). This means that a gas at the same conditions of pressure, density and temperature, could present a hydrodynamic profile in the forward direction (small θ) and a Gaussian profile in the backward direction ($\theta \approx 180^\circ$) (see Figure 2-5). At $\theta = 0$, there is no Rayleigh scattering, as $|\mathbf{k}| = 2|\mathbf{k_i}|\sin(0) = 0$, and at this point the value of y becomes unphysical.

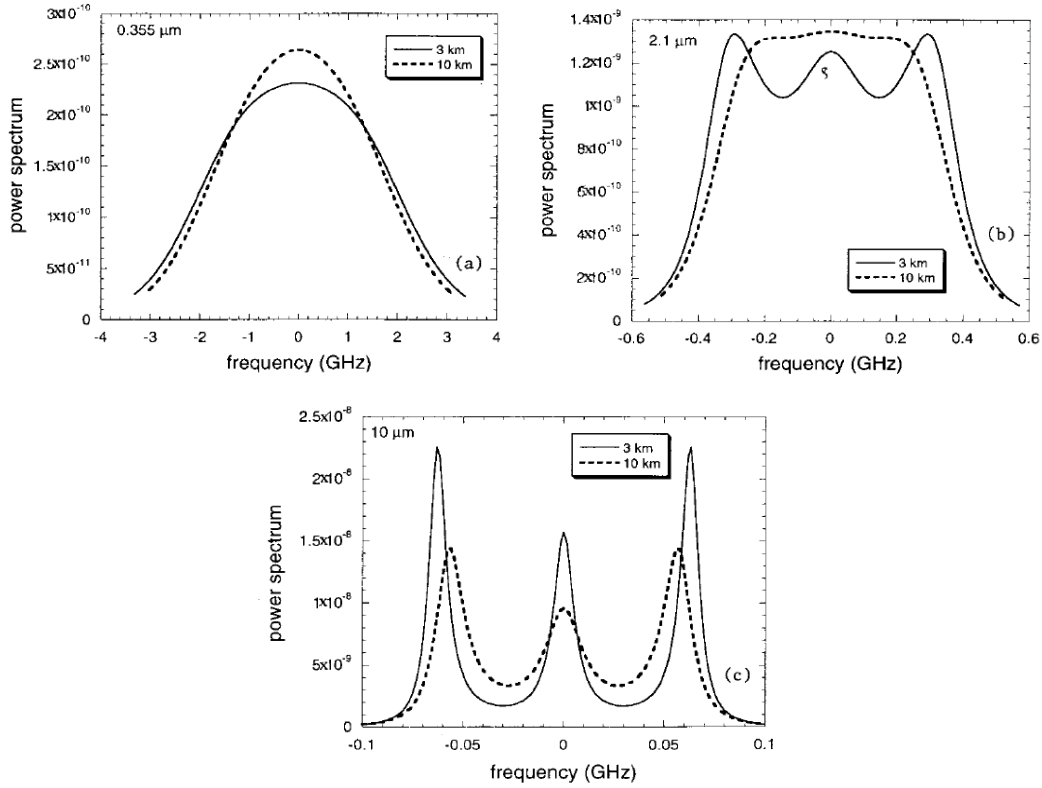

Figure 2-4: Spectra predicted using Tenti's S6 model (reproduced from Rye, [7]) at two altitudes (3km (full line) and 10km (dashed line)) with pressure and temperature obtained using the U.S. Standard Atmosphere model. The atmosphere is considered to consist entirely of N_2. The wavelengths are: (a) 355 nm, (b) 2100 nm and (c) 10000 nm. Note that the y-axis scale is not representative of the measured light intensity: all plots are normalized to give an area under the curve equal to unity.

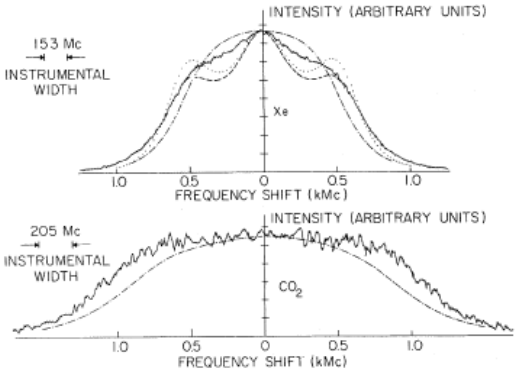

FIG. 2. The spectrum of light scattered from Xe and CO_2 at an angle of 169.4° and pressures near one atmosphere. The curves are experiment (solid), Maxwell molecule theory (dotted), Krook model theory (dashed), and the hydrodynamic approximation (dash-dotted).

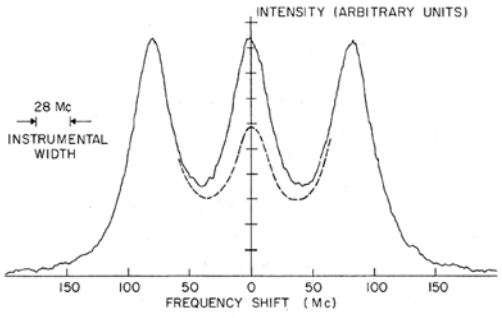

FIG. 1. The spectrum of light scattered from CO_2 at an angle of 10.6° and a pressure of 770 mm of Hg, showing clearly resolved Brillouin components. At the maximum of one of the Brillouin peaks the signal produces about 300 photoelectrons/sec at the photocathode. The dashed curve indicates the subtraction of stray elastically scattered light.

Figure 2-5: Reproduced from Greytak and Benedek, [8]. (1 atmosphere is 760 mmHg).

2.6 Hydrodynamic regime (y>>1)

The overall spectral distribution of the central Rayleigh-Brillouin feature in the hydrodynamic regime consists of three Lorentzians [5,9]:

$$S(k,\omega) \propto \left\{ \left(\frac{\gamma - 1}{\gamma} \right) \frac{k^2 \kappa / \rho_0 c_P}{\omega^2 + \left(\kappa k^2 / \rho_0 c_P \right)^2} + \frac{1}{\gamma} \left[\frac{\Gamma k^2}{\left(\omega + k v_s \right)^2 + \left(\Gamma k^2 \right)^2} + \frac{\Gamma k^2}{\left(\omega - k v_s \right)^2 + \left(\Gamma k^2 \right)^2} \right] \right\} \quad (2.11)$$

where c_P is the isobaric heat capacity, γ is the adiabatic index ($\gamma = c_P/c_V$ and c_V is the heat capacity at constant volume), ρ_0 is the average gas density, κ is the thermal conductivity, Γ is the acoustic wave damping and v_S is the (hypersonic) sound velocity.
The first term is the unshifted Rayleigh central line, and the other two are the Stokes Brillouin scattering and the anti-Stokes Brillouin scattering terms, respectively. The Rayleigh central line has a full width at half maximum (FWHM) of

$$\kappa k^2/\rho_0 c_P = (\kappa/\rho_0 c_P)(2n\sin(\theta/2)\omega_i/c)^2. \quad (2.12)$$

The other two Lorentzians are symmetrical with respect to $\omega = 0$ and have their maximum at the frequency of the phonon or acoustic wave:

$$\omega = \pm k v_s \quad (2.13)$$

with v_S the characteristic velocity of sound in the medium. v_S can be considered the dominant material property governing the distribution of the Rayleigh-Brillouin spectrum. For gases v_S varies from 331 m/s for air, to 1280 m/s for pure molecular hydrogen, the lightest of all gases. The velocity of sound in solid materials is an order of magnitude larger, therewith giving rise to much more distant Brillouin side peaks in the spectrum, i.e. in fused silica. Equation (2.13) can be considered as a dispersion relation, since it depends on the sound (temperature and pressure) properties of the gas, or liquid. The frequency ω represents the Brillouin shift, on the Stokes and Anti-Stokes side. The shift for both Stokes and Anti-Stokes components can be shown to equal:

$$\omega = 2n\sin(\theta/2)\, v_S \omega_i/c \quad (2.14)$$

with θ the scattering angle, defined as $\theta = 0$ in the forward direction (see Figure 2-2).

Hence, in the hydrodynamic regime, the Brillouin peaks shift less in the forward direction and shift more pronouncedly in the backward direction ($\theta = \pi$). Equation (2.14) also indicates the scaling properties of Brillouin side band scattering. The primary dependence is on the frequency of the incident light wave; it is proportional to the frequency ω_i (and the small dispersion effect related to the index of refraction n). It also implicitly gives a relationship between the density of the medium and the Brillouin shift; at higher densities the velocity of sound increases (in molecular hydrogen from 1300 m/s at a few Bar to 1500 m/s at 100 Bar) and therewith the displacement of the Brillouin side peaks from the central Rayleigh peak.

These last equations can be used to define a *dimensionless frequency scaling* (see Section 2.4).

$$x = \omega/k v_s = \omega c/(2n\sin(\theta/2)\, v_S \omega_i)$$

The two Lorentzian expressions for the Brillouin peaks in Eq. (2.11) have a full-width-half-maximum (FWHM) frequency dependence of

$$\Gamma k^2 = \Gamma(2n\sin(\theta/2)\omega_i/c)^2 \quad (2.15)$$

Then, when the frequency increases, the three Lorentzians get broadened with a ω_i^2 dependence, and the two side Brillouin peaks shift further apart from the central (Rayleigh) peak with a ω_i dependence. At small angles θ the Brillouin peaks are less shifted from the central (Rayleigh) peak, but at the same time, they are more resolved.

The area under the unshifted Rayleigh line I_R and under the Brillouin sidebands I_B have a well-known relationship:

$$2I_B/I_R = 1/(\gamma\text{-}1) = c_V/(c_P\text{-}c_V)$$

It is called the Landau- Placzek ratio and its derivation was based on thermodynamic concepts.

It can be proven [5] that the acoustic wave damping has a relation with other thermodynamic quantities:

$$\Gamma = (1/2\rho_0)\{(4/3)\eta_S+\zeta + [(\gamma\text{-}1)/\gamma]\,\kappa/c_V\}$$

where η_S is the shear viscosity and ζ is the bulk viscosity.

2.7 Knudsen regime (y<<1)

In the Knudsen regime, the collisions are no longer important and the Rayleigh-Brillouin feature takes the shape of a single Gaussian, characteristic of Doppler broadening:

$$S(\mathbf{k},\omega)=[(2\pi)^{1/2}/kv_T]\exp(-\omega^2/2k^2v_T^2)$$

where v_T is the thermal speed of the molecules $v_T = (2k_BT/m)^{1/2}$.
The Gaussian is centered around ω=0 and its FWHM is $2[2\ln(2)]^{1/2}kv_T$.

2.8 Kinetic regime (y~1)

In this regime the Boltzmann equation must be solved, as the hydrodynamic equations are no longer valid.

2.9 Depolarization effects on the total Rayleigh-Brillouin cross section

In the above sections, all the tensorial parts of the dielectric response of the medium have been neglected (see section 2.1). This means that the dielectric response of the medium will not change the polarization direction, i.e. the scattered wave will have the *same polarization* as the incident laser beam. This means that if the incident laser beam has circular polarization, the scalar-scattered light (like Rayleigh-Brillouin) will have circular polarization.

If the tensorial dielectric response of the medium is not neglected, a depolarized contribution to the scattering cross section may arise from anisotropy fluctuations. This component of the scattered light is not included in any of the theories in the literature: they all deal with the scalar part of the scattering, which is due to density fluctuations. The depolarized part of the scattering arises from molecular anisotropy (they do not have spherical shape) and anisotropy in the polarizability of the molecule.

While the depolarized scattering may be small, it may not be negligible. It will mostly affect the central peak of the Rayleigh-Brillouin feature, and it can amount to a few % of increase in the total signal. Because the depolarized scattering lacks Brillouin components, its presence may appreciably change the shape of the observed line profile. Unfortunately, we have not been able to find any reported measurement on this subject in the literature.

Using a different approach, an expression for the frequency-dependent cross section for light scattering [10] can be obtained:

$$\sigma(\nu) = \frac{24\pi^3 \nu^4}{n_{den}{}^2} \frac{\left(n_\nu^2 - 1\right)^2}{\left(n_\nu^2 + 2\right)^2} F_{k(\nu)} \qquad (2.16)$$

where σ is the cross section at a frequency ν, n_ν represents the refractive index at a density n_{den}, and $F_{k(\nu)}$ the so-called King correction factor, that depends on depolarization phenomena in scattering. A factor $3/\left(n_\nu^2 + 1\right)$ is related to local electrostatic field effects known as the Clausius-Mossotti or the Lorentz-Lorenz factor. The King correction factor is only important if the scattering sources are non-spherical, so *not* for atoms or spherical molecules. It may be derived from calculable molecular properties (*ab initio* quantum mechanical calculations are performed nowadays) or via depolarization measurements in Raman spectroscopy. The King factor does not depend on the polarization of the incident light, as is clear from symmetry arguments, and it typically it accounts for a several % *increase* of the scattering cross section.

Gas	F_k(18788.4 cm^{-1})	$F_k(\nu)$ expression	References
Ar	1	$F_k(\nu) = 1$	Atoms
N_2	1.035	$F_k(\nu) = 1.034+3.17\text{x}10^{-12}(\nu\ /\text{cm}^{-1})^2$	[10, 11, 12, 13]
O_2	1.103	$F_k(\nu) = 1.096 + 1.385\text{x}10^{-11}(\nu\ /\text{cm}^{-1})^2 + 1.448\text{x}10^{-20}(\nu\ /\text{cm}^{-1})^4$	[10]
CO	1.016	ρ_p (15802.8 cm^{-1}) = 0.0048	[11, 13]
CO_2	1.145	$F_k(\nu) = (1.1364\pm0.0005) + (25.3\pm1.5)\text{x}10^{-12}(\nu\ /\text{cm}^{-1})^2$	[10, 12]
CH_4	1.000	none, taken measurements for CCl_4 (molecule with the same symmetry)	[11]
N_2O	1.225	$F_k(\nu) = \frac{3 + 6\rho_p(\nu)}{3 - 6\rho_p(\nu)}$ and $\rho_p(\nu) = (0.0577\pm0.0007)+(11.8\pm2)\text{x}10^{-6}(\nu/\text{cm}^{-1})^2$	[12]
SF_6	1.000	$\rho_p < 0.2\text{x}10^{-3}$	[11]

Table 2.1: First column: King factors at 18788.4 cm^{-1} (532 nm) for several atmospheric gases. Second column: frequency dependence of the King factor. Third column: References taken from [14].

2.10 The kinetic scaling law

The generalized approach to scaling affirms that the spectrum of $S(\mathbf{k}, \omega)$, which in principle is a function of $\mathbf{k}$, ω, the intermolecular potential and the temperature of the gas, is only a function of two variables, a reduced frequency x and the parameter y. Then, the kinetic scaling law states for atomic gases that experiments may be performed at different angles, density and temperature or with different wavelengths, but the same spectrum will result when plotted as a function of x, provided that y is a constant. Note that the intermolecular forces (dependent on the species) do not play a role in this description.

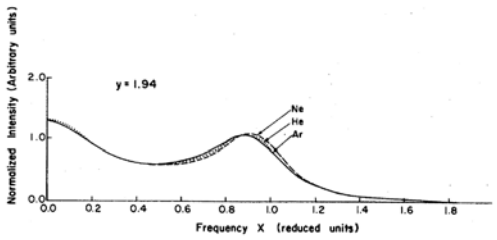

FIG. 4. An intercomparison of the experimental curves of He, Ne, and Ar at y equal to 1.94.

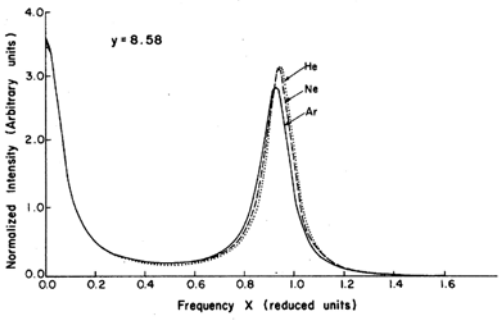

FIG. 6. An intercomparison of the experimental curves of He, Ne, and Ar at y equal to 8.58.

Figure 2-6: Experimental results from Ghaem-Maghami and May [15], where the experimental RB- feature of He, Ne and Ar has been smoothened and normalized to test the scaling properties of the model. A 1% level of uncertainty in the curves is estimated Left: Kinetic regime, y = 1.94. The RB-features agree to the 3% level. Right: Hydrodynamic regime, y = 8.58. The effects of mean field interactions become apparent when entering the hydrodynamic regime.

Ghaem-Maghami and May [15] performed a set of experiments on He, Ne and Ar to test experimentally the scaling of Rayleigh-Brillouin spectra. They found that (when setting the densities and temperatures of the three gases to obtain the same y parameter in al cases) in the kinetic regime the scaling is obeyed to the 3% level. The situation changes when the system goes into the hydrodynamic regime (larger y values), as the mean field effects (different interaction potential) of each molecular species start to appear. This is shown in Figure 2-6.

3 Coherent Rayleigh-Brillouin scattering theory and experimental setup

Laser-illuminated Rayleigh-Brillouin Scattering is used as a diagnostic tool in combustion physics [16] and (supersonic) fluid dynamics [17,18]. The intensity of the RBS provides information on the density, and in some cases, mixture fraction, flow field and flame structure. Assuming an ideal gas mixture, the density measurements can be converted to a temperature, if the pressure is known. The method derives its strength from the complex line shape that incorporates information on all state variables of the scattering medium. The spectral distribution of the RBS provides information on the properties of the complex flow, like shear viscosity, bulk viscosities and collision cross section.

3.1 Background

The nonlinear optical scattering process originates from gas density fluctuations. The density perturbation that gives rise to scattering of the optical fields takes the form of traveling acoustic waves (Brillouin scattering) and stationary isobaric density fluctuations (Rayleigh scattering). In the case of spontaneous Rayleigh-Brillouin scattering sidebands arise due to the natural presence of thermally excited acoustic modes. Alternatively, these acoustic modes can be induced by subjecting the molecules to electric dipole forces in the standing wave field of two crossing laser beams, also called laser-induced electrostrictive gratings (LIEG), illustrated in Figure 3-1. This scheme, called coherent Rayleigh-Brillouin scattering (CRBS), has first been proposed by She et al. [19,20]. Grinstead and Barker [21] experimentally demonstrated CRBS in the collisionless limit, while Pan et al. [22,23] performed measurements in the kinetic regime. Data obtained in rare gases as well as in atmospheric gases at room temperature and various pressures were presented. CRBS has been used for temperature measurements in low density gasses [24] as well as in flames [25]. In the latter case, it was shown that by modeling the flame gas as a mixture of the dominant components (N_2, H, O, CO), the line shape in the collisionless regime is only weakly sensitive to the exact gas composition. Recent developments include the use of traveling gratings (the pump beams consist of different frequencies) to modify the velocity distribution of molecules [26,27] and the theoretical exploitation of the high-intensity regime of CR(B)S [28,29]. Note that the generated gas density perturbation with LIEG is intrinsically different from the spontaneous fluctuations: the perturbations in the former case are introduced externally, and the inducing agent must therefore span all relevant frequencies. Therefore, CRBS spectra will be measured to provide, independently from SRBS, line shapes to verify the Tenti model described in sections 9 and 10.

Coherent RBS can be understood as the scattering of probe photons off the index grating produced by two pump beams. In this respect, CRBS is similar to other four-wave mixing schemes. The coupling to acoustical modes in the scattering medium gives rise to sidebands, similar to the spontaneous case.

3.2 Experimental configuration

A coherent Rayleigh-Brilouin scattering experiment is usually operated as follows:

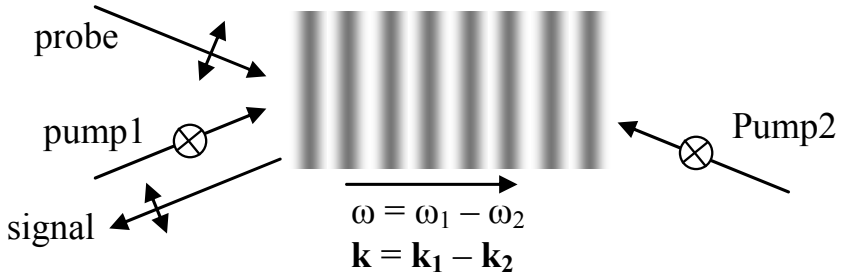

Figure 3-1: Coherent Rayleigh-Brillouin scattering. Light is Bragg-diffracted on the gas density fluctuations created by a laser-induced electrostrictive grating. The optical dipole force pushes the molecules towards the high field intensities of the optical grating.

In Figure 3-1 two pump beams $\mathbf{E_1} = \mathbf{E_{10}}\cos(\mathbf{k_1}.\mathbf{r_1} - \omega_1 t)$ and $\mathbf{E_2} = \mathbf{E_{20}}\cos(\mathbf{k_2}.\mathbf{r_2} - \omega_2 t)$ with the same polarization are focused and crossed at their foci in the gas. $\mathbf{k_1}$ and $\mathbf{k_2}$ are the pump beams' wave vectors, and ω_1 and ω_2 are their frequencies. The inhomogeneous electric dipole force of the laser pushes the molecules towards the high field intensities of the optical grating (potential energy $U = -\frac{1}{2}\alpha|E|^2$, with α as the molecular polarizability) and creates a wave-like density perturbation. In a coherent manner, the acoustic modes are probed by Bragg-diffracting a narrow-band laser on the induced density fluctuations. The scattered signal beam maintains the probe beam polarization and its propagation direction is determined by the phase matching condition

$$\vec{k}_{probe} - \vec{k}_{signal} = \vec{k} = \vec{k}_1 - \vec{k}_2 \qquad (3.1)$$

where $\mathbf{k}$ is the wave vector of the induced density perturbation and is perpendicular to the fringes (see Figure 3-1). The phase matching condition in Eq. (3.1) states that momentum must be conserved during the CRBS process. This holds as well for the energy, and the scattered frequency spectrum is given by:

$$\omega_{probe} - \omega_{signal} = \omega = \omega_1 - \omega_2 \qquad (3.2)$$

Note that the left-hand sides of Eqs. (3.1, 3.2) are inverted with respect to their equivalents in Pan et al. [22]. The frequency of the CRBS signal ω_{signal} is shifted from that of the probe beam ω_{probe} by the frequency of the induced density perturbation ω. The nature of the coherent scattering process ensures that the signal has the properties of a laser beam, that is, coherence, directionality and intensity.

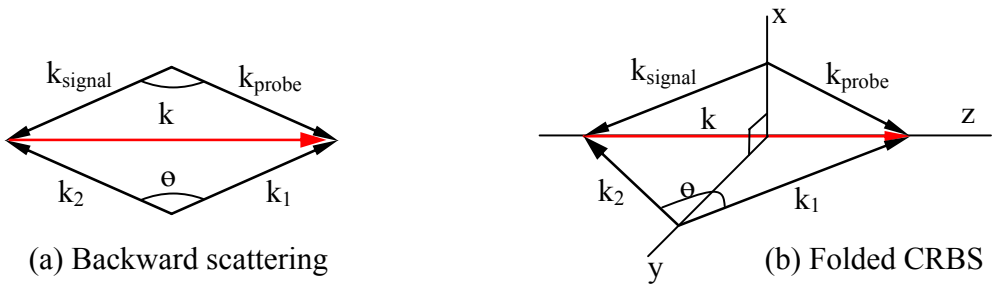

Figure 3-2: Phase matching schemes for coherent Rayleigh-Brillouin scattering. $\mathbf{k_1}$ and $\mathbf{k_2}$ are the pump beams' wave vectors. $\mathbf{k}$ is the wave vector of the induced density perturbation.

The experimental configuration of CRBS follows a generic four-wave mixing experiment and is similar to the Brillouin-enhanced process used for amplified phase conjugation [30]. Figure 3-2(a) depicts the coplanar backward scattering phase matching configuration with crossing pump beams of near 180°. The fringe pattern has a large wave vector $\mathbf{k}$, but a relatively low frequency (~ω), and it provides a strong electric dipole force. Figure 3-2(b) shows a three dimensional backward scattering scheme with two pump beams defining the acoustic wave vector $\mathbf{k}$. The signal beam no longer follows one of the pump beams, which removes the need for perpendicular polarization of the probe beam. This scheme improves the signal-to-noise ratio since the signal beam is separated spatially.

Within the bandwidth of a broadband laser, that provides the two pump beams ω_1 and ω_2, a continuous spectrum of density waves ω is generated in the optical grating (Eq. 3.2). Therefore, a broadband spectrum ω_{signal} emerges from the coherent scattering process with a narrowband (nearly single frequency) probe laser ω_{probe}. The scattered power spectrum $S(\omega_{signal})$ can be resolved by scanning the probe beam ω_{probe} while fixing a Fabry-Perot etalon or by using a resolving Fabry-Perot etalon at a fixed probe frequency.

3.3 A three dimensional (3D) geometrical configuration

Initially it was planned to use a three dimensional (3D) configuration of the lasers beams, as depicted in Figure 3-3.

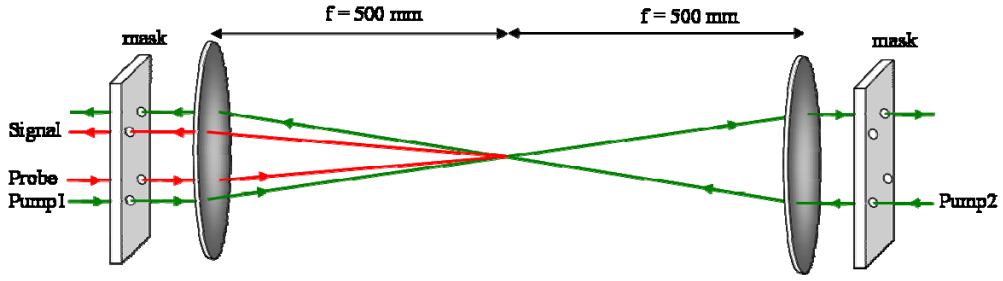

Figure 3-3: The three-dimensional laser beam configuration as originally pursued.

The CRBS spectra obtained in the 3D setup contained an asymmetry and were spectrally narrower than predicted by the theoretical Tenti S6 and S7 model, while the reason for these features was (and still is) unknown. Hence, during construction of a final setup, the configuration was changed from a three-dimensional (3D) setup to a two-dimensional (2D) setup, also to eliminate some degrees of freedom in the four-wave mixing experiment. This has resulted in a more controllable and stable CRBS setup with the highest scattering signal possible, while maintaining a scattering signal free from background radiation. To obtain scattering signal while using a minimum amount of pulse energy to avoid possible non-perturbative physical effects, we have optimized each optical component to improve the signal-to-noise ratio.

3.4 A two dimensional (2D) geometrical configuration

The 2D CRBS setup is schematically drawn in Figure 3-4. It contains an additional thin film polarizer plate and a half-wave plate in comparison with the 3D CRBS setup. The half-wave plate is used to rotate the polarization of the probe beam such that it is orthogonal to that of the pump beams. Simultaneously, this avoids the complexity associated with interference between probe and pump beams generating undesired gas density fluctuations. The thin film polarizer separates the counter-propagating signal beam from the pump beam and redirects the former to the Fizeau spectrometer. For alignment masks are used, as in Figure 3-3, but only the lower two holes in one horizontal plane are used. Thus, apart from the additional polarization optics and the fact that all light beams in the scattering cell are now in a single horizontal plane, there are no differences between the 2D and 3D setups.

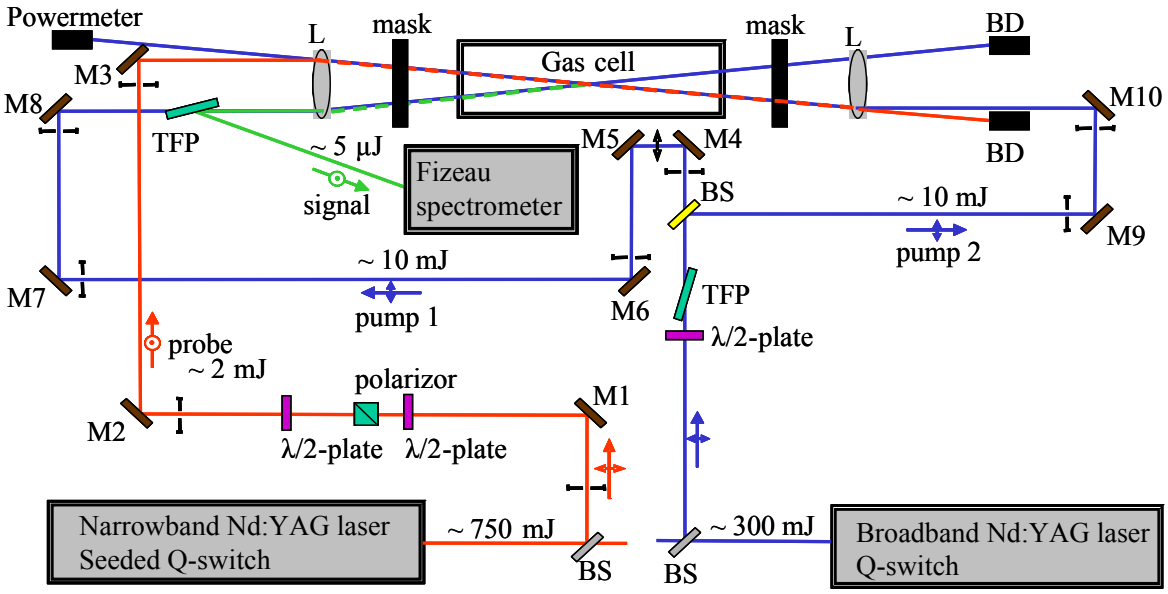

Figure 3-4: Two-dimensional CRBS setup. BS: beam splitter, TFP: thin film polarizer, M: mirror, BD: beam dump. Two pump beams originate from a broad-band Nd:YAG laser, while a probe beam is provided by an injection-seeded frequency-doubled Nd:YAG laser, and are focused by lenses in a gas cell. The scattered signal is spectrally analyzed by a Fizeau spectrometer.

The overlap between probe and pump beams in the 2D four-wave mixing setup is maximized, generating a strong scattering signal beam. Therefore, the pulse energy of the probe and pump beams could be reduced to 2 mJ and 10 mJ, respectively, for measurements in ambient air. The signal beam propagates for about 10 m on the optical table before it was detected by our Fizeau spectrometer in order to separate the signal beam from scattered stray light on optics.

The customized Fizeau spectrometer obtained from Angstrom Ltd. is in principle able to measure the CRBS spectrum on a single shot basis by reading out a photodiode array behind a Fizeau interferometer (see section 3.8). The scattered beam is collected with an optical fiber coupler, focusing the light into a single-mode fiber with a core diameter of 50 μm. The measured signal strength is highly dependent on the alignment of the fiber coupler; a small angular deviation already results in a large displacement of the focus onto the single mode fiber. A misalignment of the fiber coupler can easily result in a reduction of the signal-to-noise (S/N) ratio by a factor two or three. However, as may be expected, the measured shape of the spectrum with the Fizeau spectrometer does not depend on the alignment of the fiber-coupler when using a single mode fiber.

The fiber coupler itself can be misaligned with respect to the signal beam and can be adjusted with the optical mount in which it is mounted. However, during alignment of the CRBS setup, a misalignment with respect to the fiber-coupler can be introduced, because in the 2D CRBS setup, the signal beam path is determined by the beam path of one of the pump beams, see Figure 3-4. That is, changing the alignment of (one of) the pump beams automatically changes the path of the signal beam.

3.5 Beam displacement

As the length of the interaction region of the four-wave mixing process is only several millimeters, optical elements like lenses and optical windows that displace the beams passing through them, can cause a misalignment of the beams and decrease the scattering signal. We briefly discuss the problems and solutions.

3.5.1 Lenses

In standard optical applications, the thin lens approach can be used to calculate the focal length of a lens. However, the accuracy in our CRBS setup to obtain maximum scattering signal demands to consider the thick lenses approach to correct for small deviations in the focal length due to the finite lens thickness. The effective focal length, or simply the focal length *f*, is calculated with respect to the principal planes, and is given by Hecht [31]:

$$\frac{1}{f} = (n_l - 1)\left[\frac{1}{R_1} - \frac{1}{R_2} + \frac{(n_l - 1)d_l}{n_l R_1 R_2}\right] \qquad (3.3)$$

in which R_1, R_2, n_l, d_l are the lens radii of the first and second front surfaces, the index of refraction of the lens material, and the lens thickness, respectively. A rule of thumb for ordinary glass lenses in air is that the principal plane separation H_1H_2 roughly equals one-third of the lens thickness V_1V_2. In our case, the plano-convex lenses of nominally *f* = 500 mm and 3.4 mm thickness have a focal distance displacement of 1.13 mm and give rise to a total separation of the foci of the counter-propagating pump beams in the interaction region of 2.26 mm (twice the displacement of an individual lens).

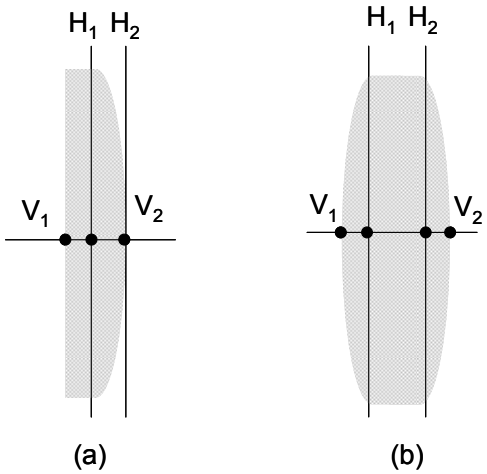

Figure 3-5: Primary H_1 and secondary H_2 principal planes of a plano-convex (a) and a biconvex lens (b). The thickness of the lens dl or V_1V_2 is not negligible, because the actual focal distance f of the lens is measured relative to the principal planes.

Solution

The displacement of the focal distance can be easily corrected for by displacing each lens by 1.13 mm. This results in a scattering beam profile with the same angular beam divergence, shape and pattern as the probe beam, and maximizes the detected signal with the Fizeau spectrometer.

3.5.2 Optical windows

The optical windows of the gas cell, which is placed in the interaction region between the two lenses, also displace the focal points of the lenses, see Figure 3-6. This potentially will decrease the overlap of the pump beams, and therefore also the scattering signal output. The displacement of the focal point can be calculated using:

$$z = \frac{d_l\left(i - \sin^{-1}(i)\frac{1}{n_l}\right)}{i} \qquad \text{for small angles } \tan i \approx i \qquad (3.4)$$

In our case, the windows are 9.53 mm thick and each give rise to a displacement of about 3.18 mm. We assume that within each pump or probe beam, the divergence angle

due to focusing of beam spot is small in comparison to the lateral displacement of the whole beam and can be neglected.

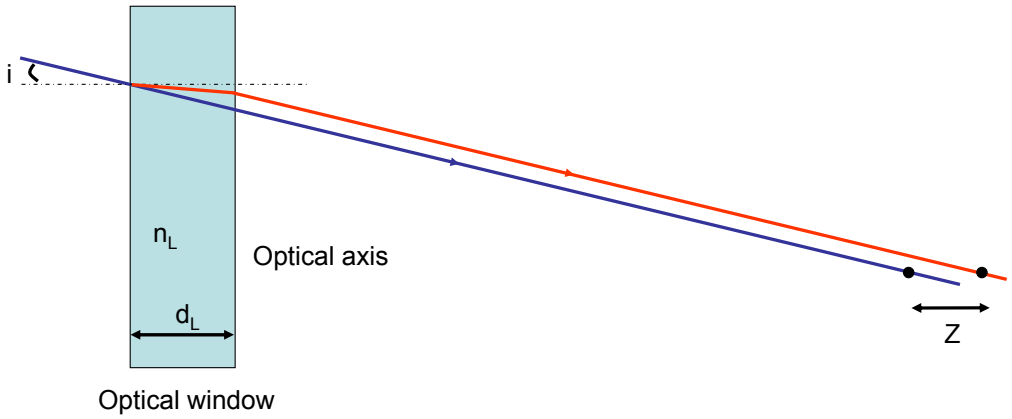

Figure 3-6: Lateral displacement of the beam path due to an optical window. The blue line is the original optical beam path, the red line is the refracted optical beam path due to the window and i is the angle of incidence L: lens.

Solution

This beam displacement can be corrected for by introducing a small angle of the optical windows with respect to the optical axis of the lenses of the same order as the scattering angle, which is 1.4°. In this case, one optical beam path, pump2-probe, is unperturbed by the optical windows as the beams pass perpendicular to the window surface, while the second optical beam path, pump1, is refracted, see Figure 3-7. However, the introduction of a small angle of the windows will not change the lateral displacement significantly and the pump beam path which also determines the scattered beam is displaced by 3.18 mm. Therefore, only a minimal re-alignment of one of the pump beam paths is necessary.

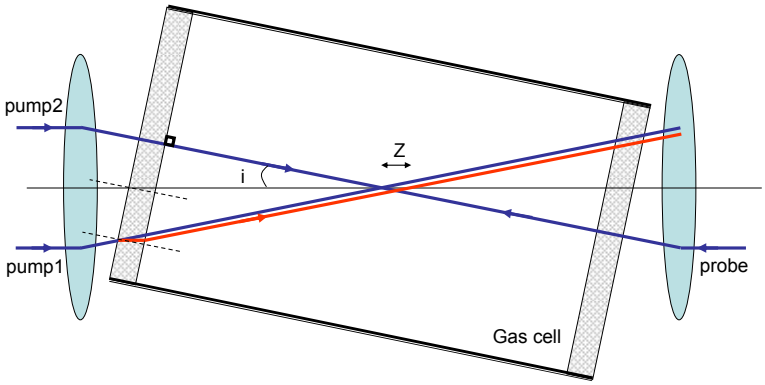

Figure 3-7: Schematic drawing of the gas cell in the interaction region between the two lenses. The blue lines are the original optical paths and the red line is the refracted optical beam path introducing a small displacement of the focus.

3.6 Laser sources

The second harmonic (SH) radiation from an *unseeded* pulsed 10 Hz Nd:YAG laser at 532 nm is employed for the pump beams. The approximated bandwidth and time duration of the pulses is 24 GHz and 10 ns. The pulses from the unseeded Nd:YAG laser are not transform limited (minimum possible pulse duration ΔT for a given spectral bandwidth Δv). The pulse-to-pulse frequency bandwidth is constant. However, the different modes within the bandwidth vary in strength and the frequency distribution is not Gaussian. The output power of the unseeded Nd:YAG laser is approx. 88 mJ per pulse with an output stability of approx. 99%.

The SH radiation from an *injection-seeded* 10 Hz pulsed Nd:YAG laser at 532 nm is used for the probe beam. The approximated bandwidth and time duration of the pulses is 150 MHz and 5 ns. The pulses from the seeded Nd:YAG laser are Fourier-transform limited. The pulse-to-pulse frequency bandwidth is constant and the central frequency is stable. The output power of the seeded Nd:YAG laser is approx. 365 mJ per pulse with an output stability of approx. 99%.

3.7 Gas cell

The gas cell, constructed by the workshop at Radboud University Nijmegen, is shown in Figure 3-8. The cell is tested to hold pressures up to 10 bar and contains connections for gas in- and output, digital pressure meter and vacuum pump. The cell has been placed in the coherent RB setup and after realignment the scattering signal was found.

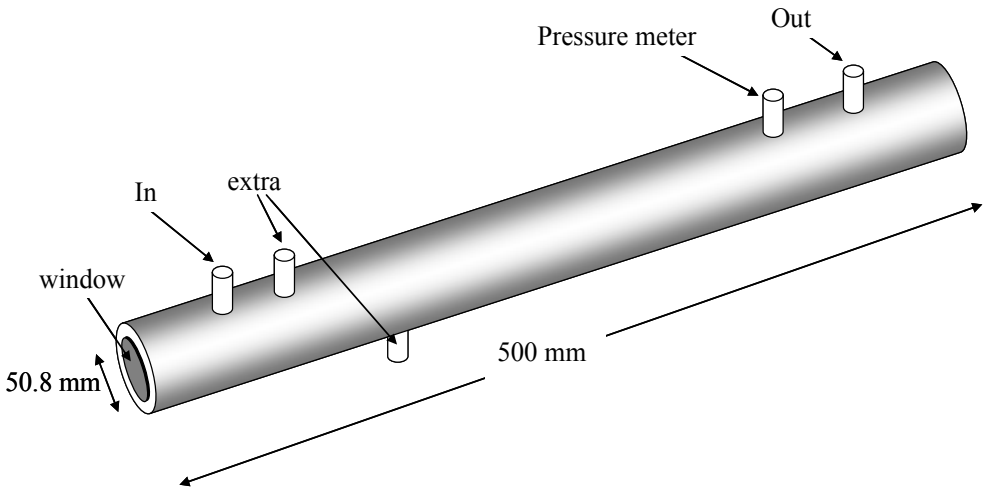

Figure 3-8: Schematic drawing of the CRBS gas cell. A tube of 500 mm long has glass windows (BK7) of 2 inch diameter and 9.53mm thick. The cell is made to operate between 0.1 – 6 atm. We have mounted valves on the cell for controlling and measuring the gas pressure.

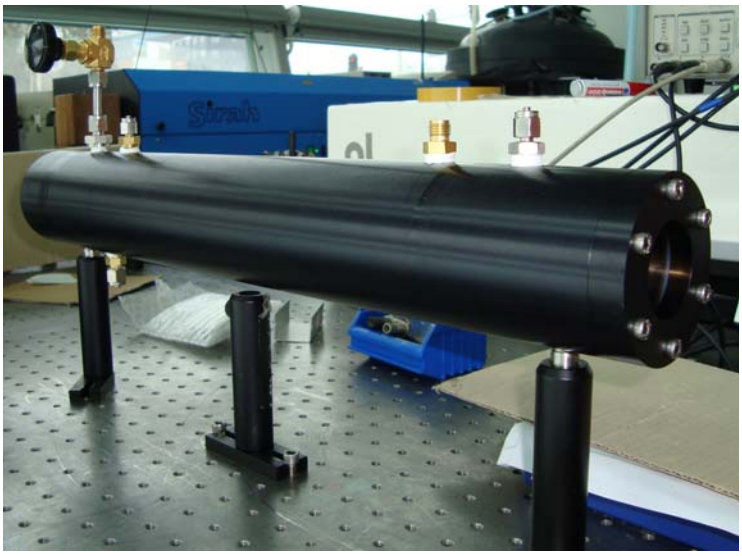

Figure 3-9: Photograph of the constructed high pressure gas cell.

A long cell length is chosen to prevent damaging the glass window. Each laser beam is focused in the interaction region to increase the intensity for the scattering process, but far away from the focal point the intensity is still small. The cell is placed on an adjustable stage for alignment. Figure 3-9 shows a photograph of the gas cell.

3.8 Fizeau Spectrometer

A spectrometer is an optical instrument used to measure the light intensity $I(\nu)$ of specific portion of the electromagnetic spectrum, typically used in spectroscopic analysis to identify materials. The spectrometer, invented by Joseph von Fraunhofer, used simply prisms. The most abundant spectrometers nowadays use a diffraction grating, a movable slit, and some kind of photo detector to resolve the spectra. However, the resolution of ~200 MHz to resolve the CRBS spectrum demands a resolving power $R = \frac{\upsilon}{\Delta\upsilon}$ better than 10^6, which is not feasible with grating spectrometers. Therefore, we have chosen to purchase from Angstrom Co Ltd a Fizeau spectrometer (FS), which has a resolving power of approx. 10^7.

3.8.1 Background on Fizeau spectrometer

A Fizeau spectrometer is based on the same fundamental principles of multi beam interference in a Fabry-Perot etalon and a detailed description is provided in TN1 Part 1 (see section 3.8). The spacing between the mirrors determine the free spectral range (FSR), the reflectivity of the mirrors the Finesse and thus finally also the resolution, and the wedge angle the spectral separation $I(\nu)$. A Fizeau wedge etalon in transmission, as depicted in Figure 3-10, can act as a single shot spectrometer to resolve the spectral components $I(\nu)$. Such a Fizeau spectrometer is also used in the Aeolus satellite for the Mie-channel. The advantage of using a Fizeau interferometer over a FP is that the linear Fizeau fringes are uniformly spaced from order to order, where as the circular FP fringes are not [32]. By using the Fizeau etalon in transmission, it is not possible to determination the central wavelength of the light source. The observed Fizeau

interference fringes behind the wedge are simply recorded with a photodiode array and can be directly related to a relative frequency. Big advantages is that no further digital analysis have to be made to obtain a spectrum and it can operate on a single shot basis.

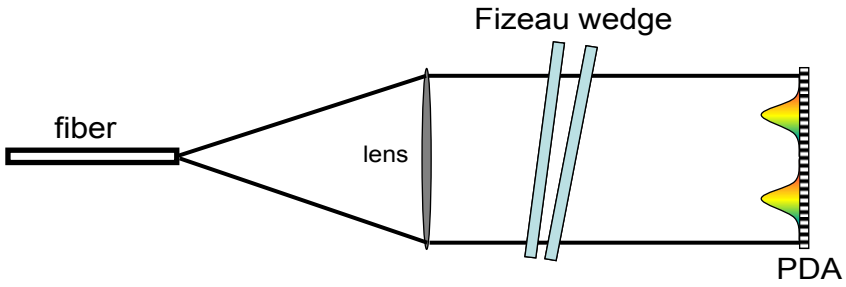

Figure 3-10: Fizeau spectrometer design. Light from a fiber is collimated by a lens and multiple beam interferences between two highly reflective mirrors in the Fizeau wedge causes an interference pattern to arise, which is simply recorded with a photodiode array (PDA).

3.8.2 Fizeau spectrometer design

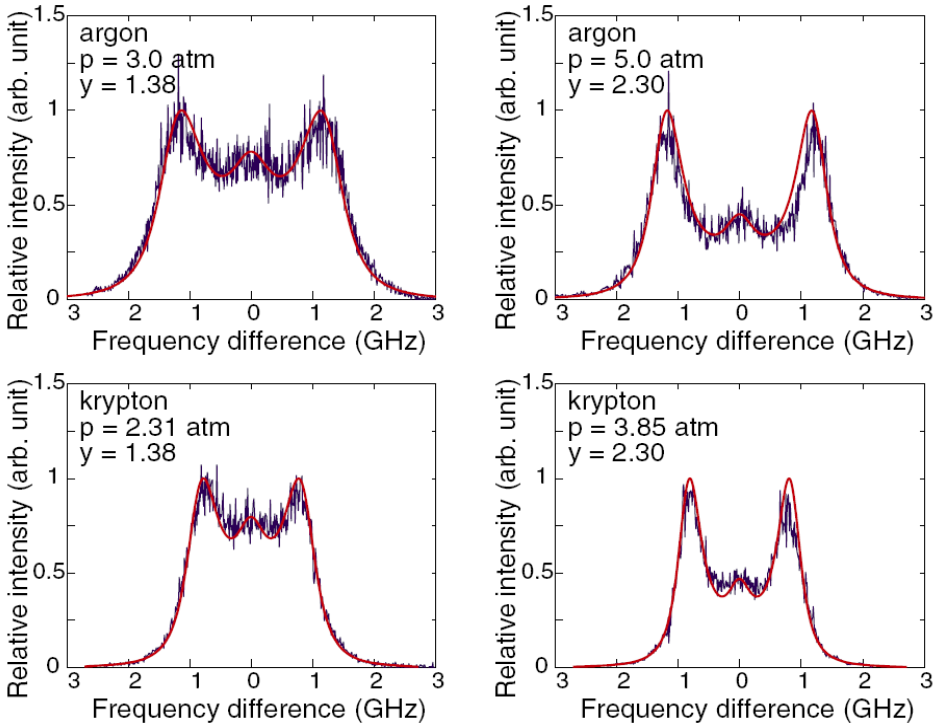

Figure 3-11: Coherent Rayleigh-Brillouin scattering spectra in krypton and argon. The blue curves are the experimental data, the red curves are the simulations [33].

The spectrometer from Angstrom has been designed along our specifications for capturing the coherent RB spectrum. As reference, we have taken the measured spectra from Pan et al. [33], which are shown in Figure 3-11.

The most important parameters are the free spectral range (FSR), resolution and the sensitivity. From the observations and the sound velocities from various gases, we deduce the following design specifications:

- FSR ~ 10 GHz,
- resolution ~ 200 MHz,
- sensitivity ~ 5 µJ per pulse.

3.8.3 Angstrom Co Ltd

The Fizeau spectrometer (FS) has been purchased from Angstrom Co Ltd *(Novosibirsk, Russia, office +7 383 334 8480, mob. +7 913 911 5959)*, which also produces the HighFinesse wavemeter. In collaboration with director and project manager Andrey Photek, we have developed a customized FS for coherent RB measurements. Figure 3-12 show a photograph of the Fizeau spectrometer. The scattered light from the coherent RB process is collected with an input-coupler into a single mode fiber. The

easy software installation and a plug-and-play USB interface make the Fizeau spectrometer easy to operate. The properties of the FS are shown in Table 3.1.

Figure 3-12: Photograph of the Fizeau spectrometer with an optical fiber input and an USB computer interface.

Table 3.1: The FS from Angstrom Co Ltd has the following specifications.

FSR: 10.45GHz	sensitivity: less 1 microJ
finesse: not less 40	wedge angle 19.62 urad
reflectivity: 95%	amount of pixel: 2048
Spectral range: 532 +/- 20 nm	wedge distance: 14.3441mm
resolution: not less 300 MHz	software: evolution of HighFinesse wavelength meter
single shot measurement	software running under Windows USB-2 connection
pixel size: 14*200 um	

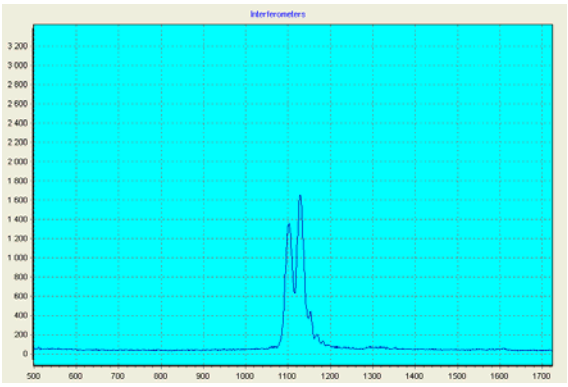

Figure 3-13: Test measurements by Angstrom with the Fizeau spectrometer using a cw YAG laser with a linewidth of about 150 MHz. The two laser lines are spaced 300 MHz.

Figure 3-13 shows test measurements by Angstrom Co Ltd with the FS using a single mode fiber and 0.5 µW laser input intensity. The spectral intensity is plotted as function of the photodiode array point, which can directly be related to a frequency. The picture is

a sum of two data arrays shifted 300 MHz and shows that the two laser lines can be resolved. Note that in the Fizeau wedge multiple beam interference only occurs within the same frequency ν and the resulting spectral profile is the superposition of spectral intensities $I(\nu)$. Figure 3-13 illustrates that the resolution is less than 300 MHz with a finesse of about 60.

3.8.4 Instrument function of the Fizeau spectrometer

A more thorough analysis of the Fizeau wedge fringe profiles in Figure 3-13 shows that the fringes have asymmetric profiles and possesses substructures, which usually lie on one side of the fringes (in this case, on the right hand side), because of the tendency of the higher-order beam to walk in the direction of the wide end of the wedge. The propagation direction of these waves successively differs by twice the wedge angle α, and their amplitudes are likewise reduced as a result of the additional reflections. By considering the coherent superposition of the plane wave, the intensity distribution behind the wedge can be examined. Typically on reflection from a dielectric or metallic mirror, a transverse electric wave experiences a phase shift of approximately π, which will be taken into account in the appropriate reflection coefficient. Let $\mathbf{k} = \mathbf{k}_0 = \mathbf{k}_z$ be the wave vector of the incident plane wave, where $k = 2\pi\lambda$ and λ is the wavelength of the radiation. The transmitted field then is a sum off plane waves, whose wave vectors are $\mathbf{k}_n = (k_{nx}, k_{nz})$ with $k_{nx} = k \sin(2n\alpha)$ and $k_{nz} = k \cos(2n\alpha)$, and whose amplitudes decreases with R^n, where $R = \rho\rho'$ with ρ and ρ' being the associated complex-amplitude reflectivities of the mirrors. Hence, the superposition field at a point $r = (x,z)$ behind the wedge can be written as [34,35]

$$E(x,z) = E_0 \sum_{n=0}^{N} R^n \exp\{ik[\sin(2n\alpha)x + \cos(2n\alpha)z]\} \qquad (3.5)$$

where E_0 is the complex amplitude and the observable intensity is $I=|E(x,z)|^2$.

Figure 3-14(a) shows the calculated transmission function of the Fizeau wedge with properties as tabulated in Table 3.1. An asymmetric profile is observed due to beam walk-off, which is relative small and is expected to have a small effect on the spectral profile. An arbitrary calculated Tenti profile $S(\omega)$ is shown in Figure 3-14(b) and the convolution $S(\omega) \otimes I(\omega)$ with the instrument function. Note that in the Fizeau wedge multiple beam interference only occurs within the same frequency ν and the resulting spectral profile is the superposition of spectral intensities $I(\nu)$.

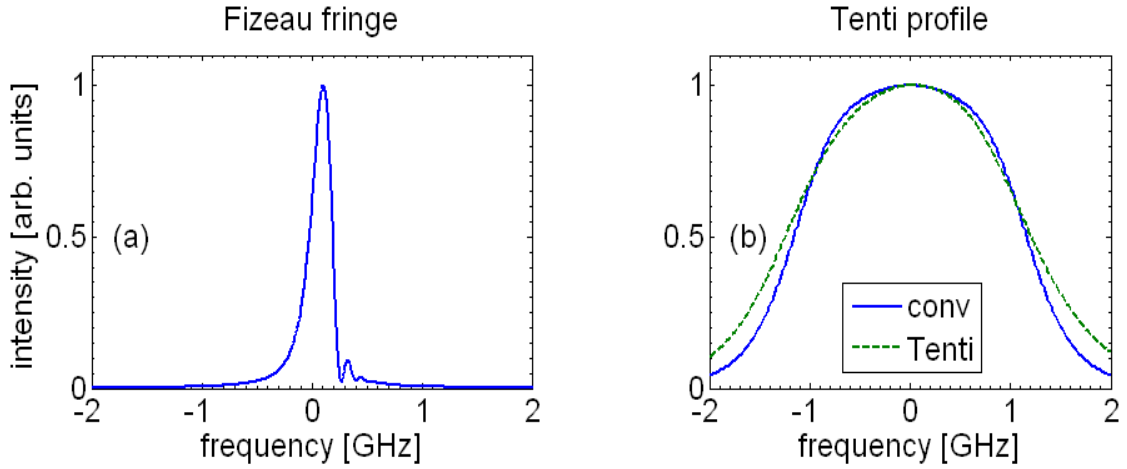

Figure 3-14: (a) Calculated transmission function of the Fizeau wedge (Eq.(3.5)) with properties from Table 3.1. (b) Calculated Tenti profile and the convolution with the calculated transmission function as (a).

3.9 Sensitivity variation over the photodiode array

The Fizeau spectrometer uses a photodiode array (PDA) to measure the intensity of the spectrum behind the Fizeau wedge. Thus the measured spectral intensity with the PDA is determined by the multiple beam interference in Fizeau wedge and the sensitivity and offset of each pixel in the PDA with respect to each other.

The Fizeau spectrometer has a built-in correction for the sensitivity variation of the PDA based on measurements with a white light LED. However, it was determined that the measured spectral intensities still show large artificial amplitude variations, which give rise to large deviations from the predicted Tenti spectra. Our hypothesis was that this artefact was due to the use of a white light source for calibration, whereas the wedge mirrors are highly reflective for only a narrow spectral region around 532 nm. Therefore, we have measured a correction spectrum based on the pump laser beam with a spectral width of 24 GHz. This is larger than the FSR of the Fizeau wedge (10.45 GHz), but it has a central wavelength of 532 nm, which matches the reflectivity of the highly reflective mirrors in the Fizeau wedge. We assume that the broad Gaussian spectral profile of the pump beam gives rise to an effectively flat spectral intensity distribution behind the Fizeau wedge, because the contributions of spectral intensities outside the FSR are folded back.

The observed amplitude variation of the PDA using the pump spectra and a single mode fiber is depicted in Figure 3-15(a), averaging 500 shots. Clearly the variation in amplitude of each pixel is visible as fast oscillations, but the envelope shows a dependence on the spatial intensity distribution of the beam, which has a Gaussian profile.

The contribution of the amplitude variation $(I_{corr}(k,\omega))$ in the measured spectra $I_{CRBS}(k,\omega)$ can be corrected for simply by using the inverse amplitude profile $(I_{corr}(k,\omega))^{-1}$ as measured in Figure 3-15(a) to obtain the CRBS spectra $S(k,\omega) = I_{CRBS}(k,\omega)(I_{corr}(k,\omega))^{-1}$.

Figure 3-15(b) shows a measured CRBS spectrum at 3 bar using nitrogen (N_2) with (green line) and without (blue line) correction. After correction the CRBS spectrum is

smooth and symmetric, and it clearly shows the expected typical features, like Brillouin and Rayleigh peaks.

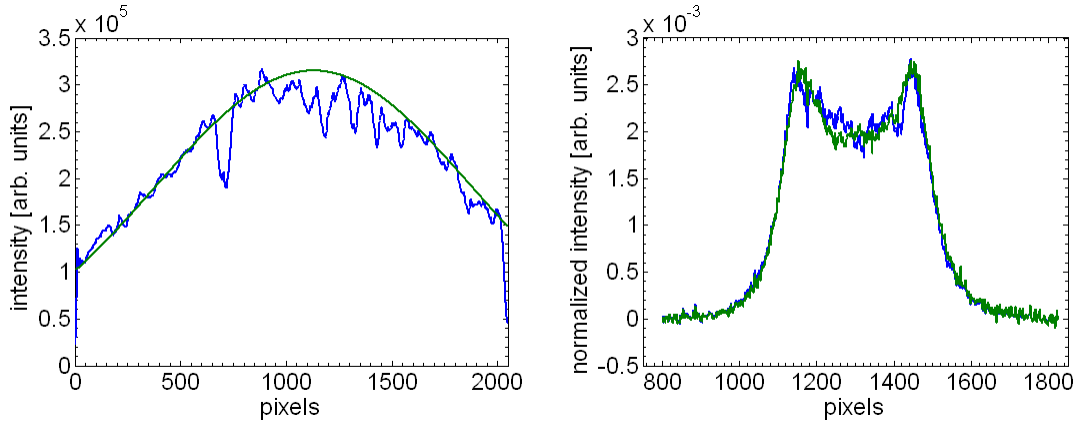

Figure 3-15: (a) Amplitude variation of each pixel in the photodiode array of the Fizeau spectrometer using the broad-band pump laser at 532 nm (blue line) and Gaussian fit to the envelope of the amplitude variation (green line). (b) Measured CRBS spectra with (green line) and without correction (blue line). Each measurement is averaged over 500 shots.

3.10 Spectral narrowing of the CRBS spectrum

The CRBS spectrum narrows when a misalignment is introduced between the pump and probe beams. However, phase matching apparently is still maintained, that is, the Bragg condition is still fulfilled, and the narrowband scattering signal is dependent on the presence of all pump and probe beams. Also, the beam profile and the directionality indicate a phase matching process.

The narrow-band scattering signal can be generated as shown in Figure 3-16 by displacing the pump1 beam, i.e. increasing the scattering angle θ, along which the scattering signal beam propagates in opposite direction towards the Fizeau spectrometer. As pump2 and the probe beam maintain the same direction, like also pump1 and signal, the phase matching conditions remain fulfilled, as shown in Figure 3-17. Measuring the displacement of pump1 (and the signal beam), i.e. the angular change θ, is difficult as these angles are very small and are introduced by adjusting a mirror mount. The physical process involving this spectral narrowing of the CRBS spectrum remains elusive.

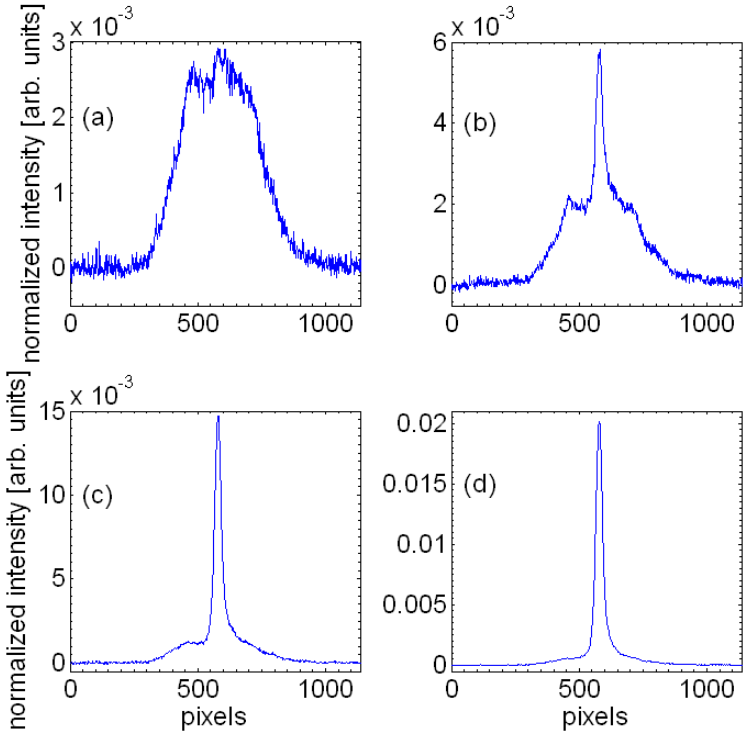

Figure 3-16: Spectral narrowing of the scattering signal for different displacements of pump1 beam and thereby different scattering angles θ with respect to pump2 and probe beams. From figure (a) to (d) the scattering angle is increased by adjusting the mirror mount.

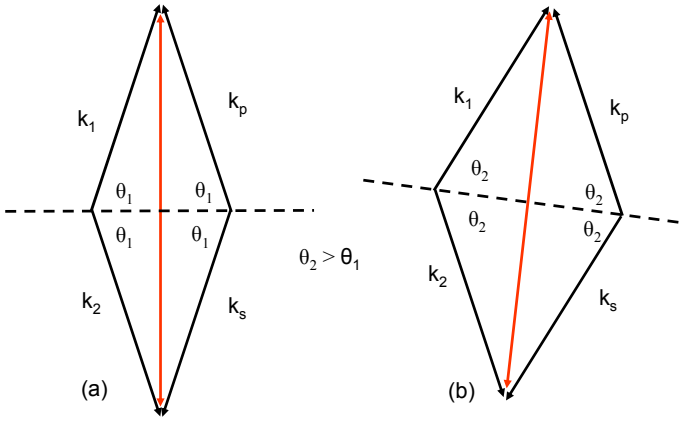

Figure 3-17: Phase matching scheme for (a) CRBS; (b) narrow-band scattering. Pump2 and the probe beam maintain the same direction, but pump1 and therefore also the scattering signal θ change with respect to pump1 and probe beam.

3.11 Pump intensity

One important effect in optical scattering experiment in gases is spectral narrowing. Dicke narrowing is commonly observed in spectral profiles in high-density gases, but in recent experiments with neutral atoms and molecules which are tightly confined in well-

defined potentials created by an externally applied electric field, spectral narrowing effects are also observed.

CRBS is an optically non-resonant four-wave mixing process that scatters a probe beam off the density grating created in the crossing point of two broad-band pump beams via a periodical optical dipole force. Ideally, the induced grating changes the molecular velocity distribution only negligibly. However, when increasing the pump intensities large fractions of the molecular velocity distribution function f(x,v,t) are forced to oscillate within the electric field potential. The velocity distribution of the optical potential is centered around $\Delta v = 0$, if we assume a peaked (say Gaussian) spectral distribution of the pump laser. Thus, groups of molecules within a smaller velocity spread will increasingly dominate the scattering process and the scattered spectrum will narrow as the pump intensity increases.

Recently, Bookey et al. [29] and Shneider et al. [36] have investigated theoretically and experimentally the spectral narrowing in coherent Rayleigh scattering (CRS) processes, but not for CRBS processes. As CRBS is essentially CRS at higher gas pressures, we assume in first order that the same physical process that are involved in spectral narrowing in CRS are applicable for CRBS as well. Shneider et al. show that the pump intensity dependence for CRS in argon at high pump intensities deviates from the expected quadratic one above 10^{14} W/m^2. Bookey et al. measured for several intensities the CRS spectrum and showed also significant spectral narrowing above 10^{14} W/m^2. In Figure 3-18, the relative Rayleigh width is plotted as a function of pump intensity, which shows a spectral narrowing towards higher intensities, with the linewidth showing a roughly exponential decay. A beam with $1/e^2$ intensity radius W is focused by a lens with focal length f onto a diffraction-limited spot with $1/e^2$ radius given by

$$w = \frac{f\lambda}{\pi W} \qquad (3.6)$$

This means in our CRBS setup that the pump beams of 3.5 mm radius are focused onto a diffraction-limited spot size of about $2 \cdot 10^{-8}$ m^2. As all physics occurs within a single pulse, we have to use the instantaneous power, which equals 10^5 W for a 10 ns pulse of 1 mJ. Thus a pulse energy of 20 mJ gives rise to an intensity in the focus of 10^{14} W/m^2, which spectrally narrows the CRS spectrum by about 10%. Therefore, we use pump intensities as low as possible to avoid spectral narrowing, which is equivalent to the non-perturbative regime. Therefore, we are limited to measurement at relatively high pressures, as at low pressures less scattering signal occurs.

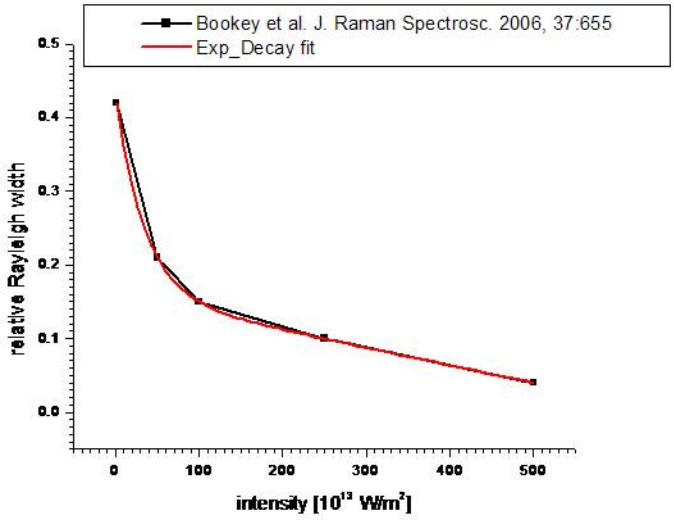

Figure 3-18: Relative Rayleigh scattering linewidth as a function of the pump intensity. Significant spectral narrowing of the CRS spectrum occurs for increasing pump intensity larger than 10^{14} W/m^2.

4 Spontaneous Rayleigh-Brillouin experimental approach

4.1 Rayleigh-Brillouin feature: frequency span

The Rayleigh-Brillouin feature of interest covers a certain frequency span. From Figure 2-4 it is possible to see that for backscatter measurements (θ=180°) at 355 nm on N_2, the Tenti model predicts that it is necessary to cover a region of 6 GHz approximately, if both the Stokes and Anti-Stokes sides are to be measured. Letamendia et al. [37] showed than when using gas mixtures, especially light gases such as H_2 (or H_2O), the spectral features may broaden even further. The frequency span depends also on the angle chosen for measurement; as for small angles the frequency span diminishes (see Figure 2-5). In virtually all cases the full RB-structure fits within 8 GHz.

4.2 Optical filtering versus heterodyne detection of RB scattering

Experimental methods to measure a Rayleigh-Brillouin spectrum can be classified in two basic categories. On the one hand there are optical filtering or direct methods, whereby the scattered light is decomposed in frequency components, dating back to the work of Chiao and Stoicheff [38] and of Greytak and coworkers [39,8] in the 1960s, who were the first to resolve the Brillouin doublet with this technique. The optical decomposition is accomplished by the use of a Fabry-Perot interferometer. One might consider a classical spectrograph for the decomposition but the resolution that is obtained through gratings is generally insufficient for unraveling the Brillouin phenomenon. If a resolution of < 50 MHz is required then classical spectrometers do not provide a solution.

On the other hand optical mixing, optical beating, or frequency modulation techniques may be considered. Here the decisive issue is that a frequency span of some 6.0 – 8.0 GHz should be measured. A heterodyne detection scheme has certain advantages in cases where only the information of low frequencies, i.e. radio-frequencies (RF), carries the scientific information. Eden and Swinney [40] were the first to succeed in detecting Brillouin features where the frequency range was limited to 100 MHz. Simonsohn and Wagner [41, 42] thereupon introduced the use of acousto-optical modulators to frequency shift the excitation beam and then mixed the scattered light with the unshifted laser frequency to obtain a RF-spectrum showing the RB-features. Over the years the dynamic range of the beat methods was further enlarged, first by Shelby, Levenson and Bayer [43] going up to 800 MHz, and then by Matsuoka et al. [44] expanding to 1.7 GHz using fast avalanche-type photodiodes as detectors. These methods may be dubbed “conventional heterodyne” and the frequency response and dynamic range is governed by the response and detection sensitivity of high-speed instruments (detectors and amplifiers) in the RF-microwave domain. In particular the linearity of the response function is an issue that limits the evaluation and the extraction of the underlying physics of the Brillouin features. More recently Tanaka and Sonehara [45] of the University of Tokyo developed the novel twist of the “super-heterodyne” method of detection of light scattering (where they achieve a frequency span of 3 GHz), whereby in fact two independently tuneable single mode lasers are used in a scheme displayed in Figure 4-1.

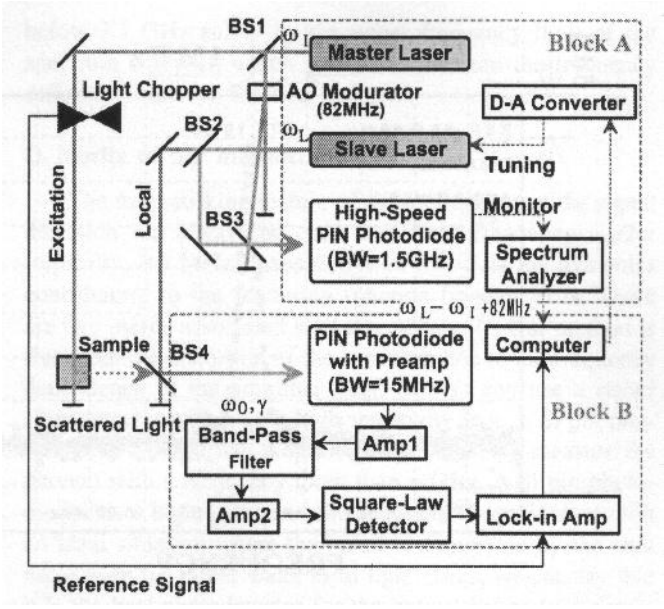

Figure 4-1: Experimental layout of the Superheterodyne detection system by Tanaka and Sonehara [45] for measuring RB-scattering at extremely high resolution.

In the direct detection method the RB-spectrum is recorded with use of a Fabry-Perot analyzer. In the Toronto experiment the Fabry-Perot is scanned by pressure tuning [46], while in the New Mexico experiment [6] a piezo-electric scanning of the FP is introduced. The same was done in the Stony Brook experiments [47,48]. A piezo-electrically scanned Fabry-Perot is a better controllable system and will yield better reproducibility, and hence should be the choice in such a setup.

In comparing the two techniques one can argue that the heterodyne method definitively has the advantage of a better resolution. It is not constrained by the optical transmission characteristics of a transmission optical element such as an etalon, with a limited bandwidth. As a disadvantage one may consider the problem of the dynamic range, which never fully extends to zero frequencies (i.e. the Rayleigh peak), let alone the non-linearities that may occur in the electronic amplification of the signals at the lowest vs. the highest frequencies; hence it will be difficult to experimentally determine the entire RB-profile at once. Also the maximum frequency span may be a limiting factor: the maximum achieved so far [45] is 3 GHz, while 6 GHz seems to be the minimum option to scan the whole RB profile. This is of specific importance for application to the ALADIN project. Further the detection sensitivity of the heterodyne method will be lower than the direct optical method, in view of shifting the signal to RF-frequencies. It is perhaps for this reason that the heterodyne method has not yet been applied to gas-phase studies. For these reasons the Fabry-Perot direct approach seems the best choice to retrieve the information on the RB-scattering spectrum in a gas phase environment.

4.3 Experimental approaches and geometries to measure SRB scattering

Spontaneous Rayleigh-Brillouin scattering experiments were performed by a limited number of research groups in the 1960s and 1970s. Light from a scattering cell is collected at a certain angle and sent through a Fabry-Perot resonator for frequency analysis.

- The scattered light is “made collinear” using a set of lenses and pinholes (see Figure 4-2). This is the most widely used approach.

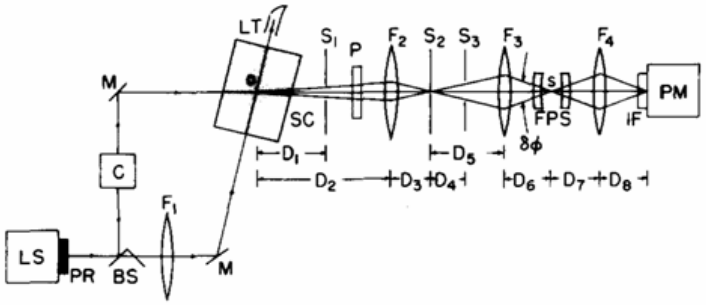

Figure 4-2: Setup used by Lao et al [48] to record RBS. The scattered light is filtered using 3 pinholes (S_1, S_2 and S_3) and a set of 2 lenses (F_2 and F_3). The choice of scattering angle is 60˚.

- The output of the Fabry-Perot cavity is geometrically filtered, again with a set of lenses and pinholes, to remove the extra modes (see Figure 4-3). The choice of the Toronto group was to detect scattered radiation under 90°. ($\theta = \pi/2$, see Figure 2-2).

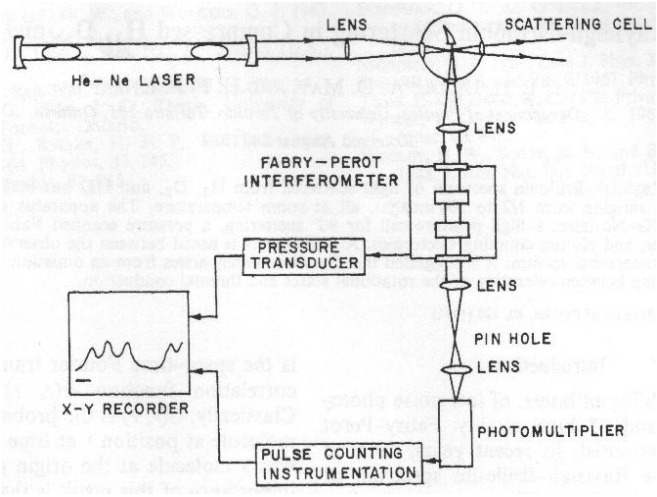

Figure 4-3: Experimental setup of Hara et al. [46]. The scattered light is coupled into the plane Fabry-Perot cavity, and its output is filtered using a set of lenses and a pinhole. The chosen geometry of study is 90˚.

- A mixed approach, where both the input and the output of the Fabry-Perot are optically filtered.

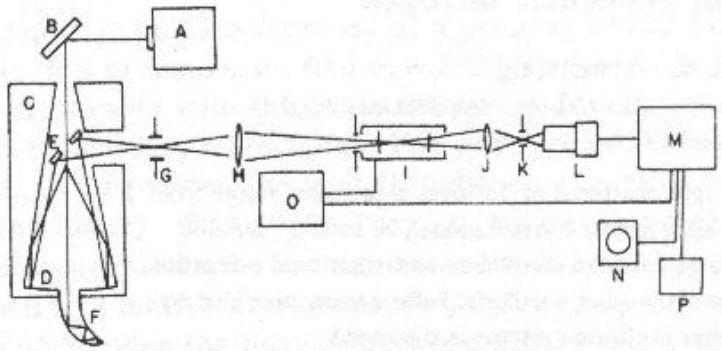

Figure 4-4: Experimental layout of the experiment by Sandoval and Armstrong [6]; scattered light at a forward angle of 15^{o} is collected for signal detection of the Rayleigh-Brillouin spectrum. Note that both the input light to the Fabry-Perot interferometer and output light are filtered with sets of lenses and pinholes.

- The output is not filtered and it is recorded by means that can separate the modes afterwards (see Figure 4-5 and Figure 4-6). In this case, the difficulty lies with the analysis of the obtained data.

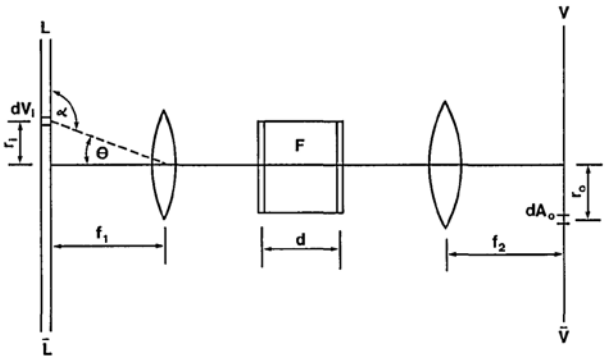

Fig. 1. Fabry–Perot interferometer used in the imaging mode. $L\bar{L}$ is the laser beam, F is the interferometer whose etalon plate spacing is d, and $V\bar{V}$ is the CCD array. The scattering volume dV_i is imaged onto the pixel of area dA_0 located at the coordinate $\bar{r}_0$ on the array.

Figure 4-5: Experimental setup of Lock et al. [17] The recording device was a CCD camera, and the output is shown in Figure 4-6.

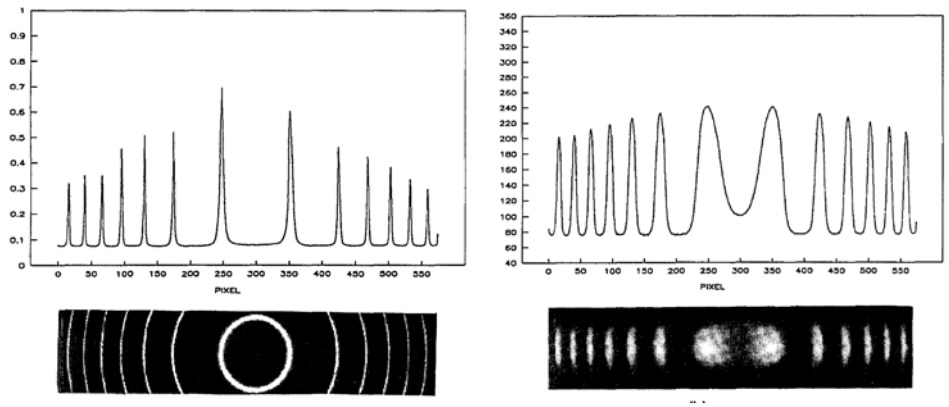

Figure 4-6: Results obtained by Lock et al. Left: the instrumental function of the etalon. Right: the RBS spectrum of N_2 at room temperature.

4.4 Previous experimental results for SRBS

Crucial results on RB-scattering in gas phase media were obtained most notably in the following experiments:

1) Greytak and Benedek [8] used a frequency stabilized HeNe laser (632.8 nm) delivering 0.6 mW to investigate several gases (Ar, Xe, N_2, CO_2, CH_4) at one atmosphere and 25˚C temperature. They obtain spectra in two configurations θ=10.6˚ and θ=169.4˚ using two different Fabry-Perot spectrometers, with 28 MHz and 205 MHz instrumental resolution, respectively.
2) Hara, May and Knaap, [46] investigated the RB-spectrum of the three isotopic variants of molecular hydrogen (H_2, HD and D_2). Parameters are a scattering angle of θ=90°, and an excitation wavelength of 632.8 nm (HeNe laser) with output power of 15 mW. They used a pressure-scanned parallel-plate Fabry-Perot with a Finesse of 50; its FSR varies from 15 GHz, for the H_2 experiments to 10 GHz for the D_2 and HD experiments.
3) Sandoval and Armstrong [6] investigated RB-scattering in N_2 at a range of pressures (1-661 Torr), also with use of a frequency stabilized HeNe laser detecting at a scattering angle of θ=15°. Finesse nor FSR of the piezo-electrically scanned Fabry-Perot are stated but a figure for the instrument width of 40 MHz is specified.
4) Lao, Schoen and Chu [47,48] investigated RB-scattering in a number of gases: CO_2, N_2, C_2F_6 and C_2H_6 and a He-Kr mixture, results of which are shown in Figure 4-7. Gas pressures cover the entire range between 0.1 and 22 atm, and the temperature was kept constant at 29˚ C. Excitation was performed with an Ar-ion laser at 514.5 nm with a power up to 500 mW. The free-spectral range of the Fabry-Perot analyzer was 2 GHz, its Finesse was 65, and the instrument resolution was 31 MHz. Scattering angles were varied, covering 60˚ for most cases and 90˚.
5) Ghaem-Maghami and May [15, 49] investigated the RB spectrum in both the kinetic and hydrodynamic regime of He, Ne and Ar. They performed a test on the "scaling" using the y parameter and the dimensionless frequency $x = \omega/kv_s$ (see Section 2.4).

6) Letamendia and co-workers [37] use gas mixtures of He-Ne and of He-H_2 and He-D_2 in the hydrodynamic regime to test the effect of gas mixtures in the shape of the Rayleigh-Brillouin feature. They use a single-mode Ar-ion laser operating at 514.5 nm with a power of 800 mW, and a confocal (piezoelectrically scanned) Fabry-Perot as a detector. The Fabry-Perot has a Finesse of 50 and a spacing of 5.41 cm. The scattering angles were varied and they covered: 30˚, 45˚, 60˚, 90˚, 120˚, 130˚ and 150˚.

These are the experiments that form a reference database for future comparison.

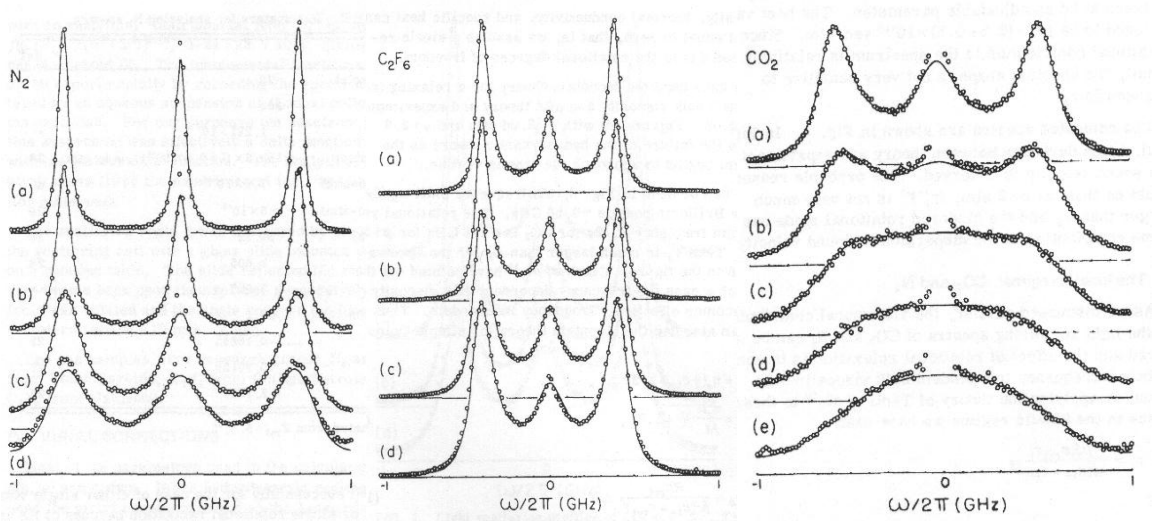

Figure 4-7: Rayleigh-Brillouin scattering of three gases at varying pressures (along vertical scale: must upward spectra toward higher pressures). These data were taken at λ= 514.5 nm [47,48].

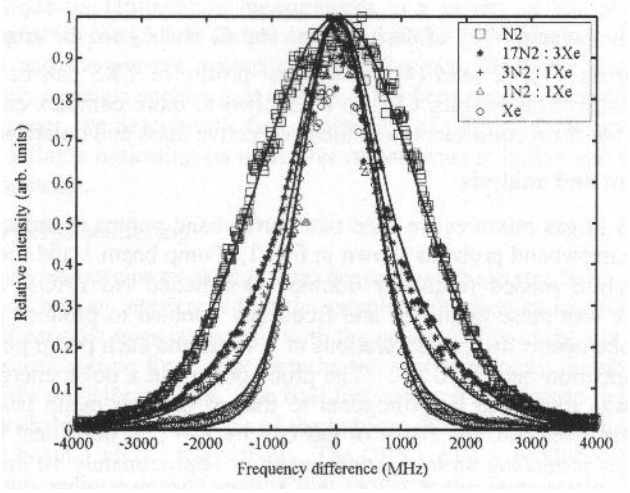

Figure 4-8: Rayleigh-Brillouin scattering spectrum of N_2 diluted with Xenon gas at various relative gas compositions at total pressures of 100 mbar [25].

There exist measurements of heterogeneous *gas mixtures* in the work of Letamendia et al. [37] and Bookey, Bishop and Barker [25]. As an example we refer to Figure 4-8 displaying the narrowing of the Rayleigh feature upon mixing N_2 molecules with heavier Xe atoms. These experiments were performed using coherent Rayleigh scattering.

5 Spontaneous Rayleigh-Brillouin Scattering (SRBS) setup

The main goal of the experiments is to measure the SRBS in various atmospheric gases to test the Tenti model. The Tenti model for SRBS has not been tested since the 1970's and it has never been tested for gas mixtures, such as air. Besides, the testing of the model must be performed in similar conditions as the one that the ADM-Aeolus satellite will experience. This means working with wavelengths in the UV region (355 nm), at atmospheric conditions, i.e. air at pressures in the range 0.1 to 1 bar, and temperatures in the -70° to 70° C interval.

A literature research (see section 4.4) on the experimental setup chosen in the past to measure SRBS showed that most groups had chosen a confocal scanning Fabry-Perot spectrometer. This is also the spectrometer of choice in this work.
The experimental setup is divided then into five sections:

- UV laser light generation (Section 5.2)
- Fabry-Perot etalon spectrometer (Sections 5.3 and 5.4)
- Light collection, imaging and alignment (Section 5.6)
- Data acquisition (Section 5.7)
- Scattering cell (Section 5.9)
- Pressure, temperature, humidity variation (Section 5.10)

A schematic overview of the entire detection system is shown below.

5.1 Schematic of the detection system

Fabry-Perot etalon: its characteristics are explained in Sections 5.3 and 5.8.

Geometrical filtering of the light: the purpose of this stage is to filter undesirable light, and force the scattered light beam to become narrower and collimated and more like a "Gaussian beam". For more details, see Section 5.6.2.

Enhancement cavity: it has the purpose of increasing the light intensity of the laser beam, to create more intense scattered light. For more details, see Section 5.2.3.

Scattering cell: here is where the experiment is performed. It has the possibility of changing the pressure and the temperature of the gas inside. Can go up to 1.5 bar in pressure, and the temperature range is from –70 ° to 70 ° C. The windows of the cell are set at a Brewster's angle, to avoid reflections and power loss inside the enhancement cavity. See Section 5.9.2.

Reference laser alignment and spatial filtering: the reference laser is used to align the Fabry-Perot etalon and to align the geometrical filtering of the light stage. To mimic the scattered light behavior, it is focused in the region where the scattered light is created, so it reaches the collecting lens L_4 as a diverging beam. The laser beam needs to be spatially filtered in an earlier stage because after the doubling frequency cavity, due to the harmonic generation process, the beam comes with elliptical aberrations.

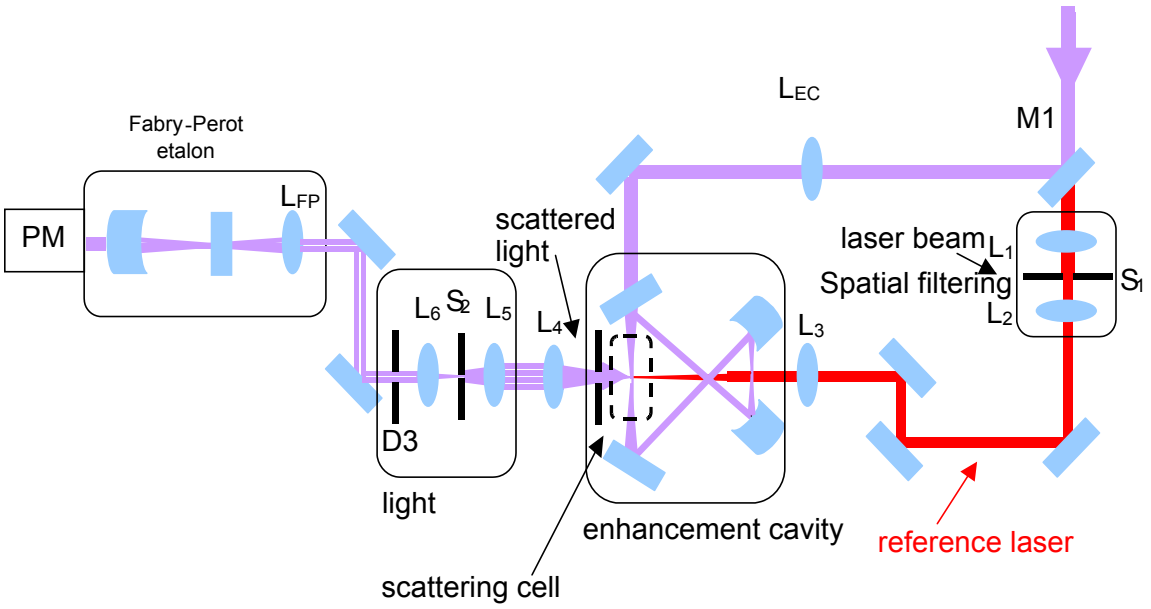

Figure 5-1: **Schematic of the setup** The laser light is divided in two in the first mirror M1, and the part that leaks through the mirror M1 is used as a reference laser (in red, for more clarity). The reference laser is used to align the Fabry-Perot etalon and sets of lenses. Before using the reference beam, it is spatially filtered to make it have a round shape and proper Gaussian beam characteristics, to be able to couple it into the Fabry-Perot etalon. The focal length of both lenses L1 and L2 is 10 cm, and the diameter of the pinhole S1 is 65 μm. The reference beam is later focused by lens L3 and collimated by the collecting lens L4. The focal length of L3 is 20 cm and L4 is 7.5 cm and their focal points coincide in space. The main beam goes to the enhancing cavity (previously passing by the mode matching lens L_{EC} of focal length of 40 cm), with the sole purpose of increasing the laser light intensity. The enhancing cavity focal point coincides in space with the focal point of the lenses L3 and L4. The collecting lens L4 collects the scattered light from this point. The collected light is again spatially filtered, to match the acceptance angle of the Fabry-Perot etalon, in the Geometrical filtering of the light part. The focal length of both L5 and L6 is 5 cm, and the diameter of the pinhole S2 is 50 μm. The collimated output of the "light cleaning" section is further narrowed by diaphragm D3 (diameter 1-1.3 mm) and later is focused using lens L_{FP} (focal length 5 cm) onto the flat mirror of the Fabry-Perot etalon. The light that passes through the etalon is measured using a Photo Multiplier Tube (PMT).

5.2 UV laser light generation

In order to test the Tenti model, the experimental resolution must be on the 100-200 MHz range. This high resolution calls for a laser with a narrow bandwidth. The narrowest pulsed laser available at the Laser Centre is an injection seeded Nd:YAG and it has a bandwidth of 500 MHz at 355 nm. The constraint of keeping the resolution on the 100-200 MHz range imposes that the laser used must have a bandwidth of 10 MHz or less. Such narrow bandwidth lasers are the ones delivering continuous wave (CW). The 690-1100 nm Ti:Sa laser used in the experiment has a bandwidth of 1 MHz at the fundamental wavelength, and this translates to a bandwidth of 2 MHz at the UV wavelength. Therefore the laser bandwidth does not affect the resolution of the experiment at all. However, once the first experiments were performed, the power

delivered by the Ti:Sa system proved to be too low. In order to tackle this problem, two measures were taken:

1. Change the wavelength (slightly) to 365 nm: The Ti:Sa laser power is maximum at 790 nm and works in the range 690 nm to 1100 nm. At 710 nm it delivers 500 mW (fundamental radiation), while at 730 nm it delivers 1500 mW. The process of generation of the UV light (second harmonic generation, SHG) is a non-linear process. This means that it will be power dependent, becoming more efficient when the power of the fundamental laser increases. It is due to this effect that at 710 nm of fundamental radiation (with 500 mW), only 50 mW of UV light is created (10% efficiency), while at 730 nm (1500 mW) the power of the SHG beam is 380 mW (efficiency 25%). The power of the UV at 365 nm is necessary to get an acceptable signal-to-noise in the experiment, and therefore this wavelength will be used for most of the experiment.
2. Create a light enhancing cavity. The idea is to enhance the UV light using an etalon cavity in resonance. The resonant cavity builds up a circulating power that can enhance the power of the laser light 10-20 times. For more details see Section 5.2.3.

The fundamental wavelength could experience a slow drift of frequency during measurement, of a few (5-10) MHz. To avoid this drift, a frequency control system was built (Section 5.2.4).

5.2.1 Laser source (Fundamental wavelength)

The laser source is a Ti:Sa laser pumped by a Millenia laser. The Millenia laser delivers up to 10 W of laser light at 532 nm wavelength, with a stable output power (1% instability in 20 hours). The Ti:Sa laser (Figure 5-2) delivers continuous-wave laser light at 710 nm with an output power of 500 mW at maximum pumping power of the Millenia laser. At 730 nm the output power is 1500 mW. The laser bandwidth is 1MHz and its frequency is stabilized by a frequency control circuit (see Section 5.2.4), therefore the frequency drift is nearly zero.

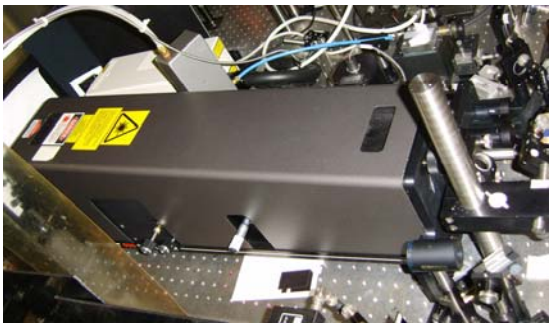

Figure 5-2: Top view of the continuous wave Titanium:sapphire laser (Coherent Inc.).

5.2.2 Frequency doubling (SHG) cavity for creation of UV radiation

The frequency-doubling cavity (Figure 5-3) is fully operational. It doubles the frequency of the laser light from 710 nm to 355 nm, delivering 50 mW of output power, with a bandwidth of 2 MHz. At 365 nm the output power is 380 mW. It is locked to the

frequency of the Ti:Sa laser (via a home-built Hänsch-Couillaud electronic locking scheme), therefore being equally stable.

Figure 5-3: View on the frequency-doubling cavity in operation.

5.2.3 Enhancement cavity

In order to increase the laser light intensity, an enhancing cavity was built. The principle of operation is based on the fact that when light is trapped in a cavity (such as a Fabry-Perot), the cavity sustains that a wave travels many round trips and therefore the power inside the cavity enhances 10-20 times. It works with the same principle as the SHG cavity, but without any SHG crystal.

The enhancement A in power of the percentage light coupled into the cavity is given by:

$$A = \frac{1-R}{\left(1-\sqrt{RV}\right)}$$

where R is the input mirror reflectivity and 1-V is the roundtrip loss, except the input mirror reflectivity. In 1-V, losses due to other mirrors are incorporated. In the case that R=V, A shows a maximum. The enhancing cavity mirror positions are locked to an integer number of round trips and that means that the cavity is in resonance.
In our case we obtain a rather low Finesse (the mirrors used in the cavity were not purchased for this purpose) of 60, and an in-coupling of the laser light of 60%. We estimate the enhancement A of the light to be around 10. This means we will get 3-4 W of UV laser power, when the cavity of properly aligned and locked.

We also experienced several problems of fluorescence on the coating of the mirrors of the enhancing cavity (see Figure 5-4). The origin of this problem is unknown, but the most accepted explanation is contamination of the mirror coatings with PVC plastic, present at the Laser Centre on the floor, cables and surrounding the optical table [50]. The PVC plastic evaporates at ambient temperature and possibly condenses on the mirror surfaces. Due to the high powers sustained inside the enhancing cavity (3-4 W of UV radiation) the fluorescence of these PVC residual traces is noticeable to the naked eye and it generates an enhancement in the dissipative losses per round-trip (1-V). See also section 5.3.2 explaining the phenomena for the etalon.

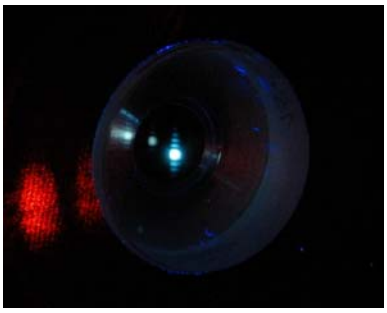

Figure 5-4: One of the highly reflective mirrors in the enhancement cavity showing fluorescence.

As a solution for the problem, the enhancement cavity (Figure 5-5 and Figure 5-6) is submerged into a “micro-climate” of a N_2 gas flow. This has resulted into an improvement of the Finesse of the enhancing cavity etalon, and shows into an increase of 10% more power sustained by the cavity.

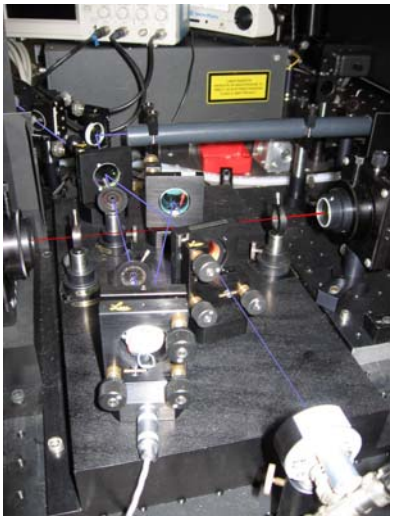

Figure 5-5: Picture of the enhancement cavity. In blue is depicted the path of the main laser beam, in red is depicted the path of the reference laser. The light of the reference laser goes from right to left.

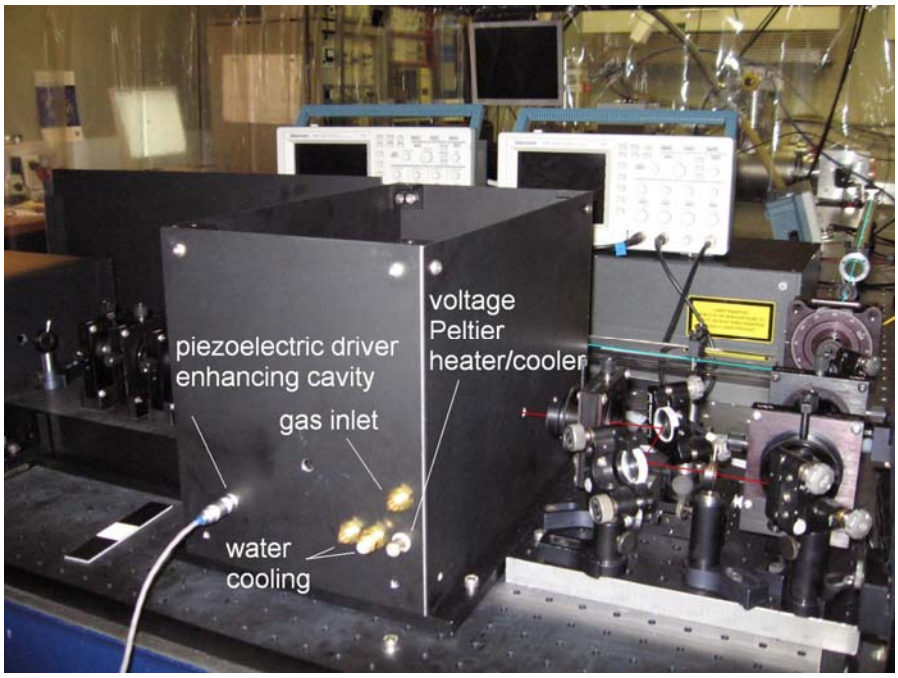

Figure 5-6: The enhancement cavity, together with the cell, is enclosed and flushed with N_2, to prevent external light, dust particles and contamination, and to have an atmosphere free of turbulence.

5.2.4 Frequency control system

Part of the output of the Ti:Sa laser is measured by an ATOS wavemeter, that measures the wavelength and feeds the signal to a computer. This computer communicates with the stabilization computer, that drives a piezoelectric device attached to a mirror inside the cavity of the Ti:Sa laser. In this way a control loop can be implemented, where the frequency of the Ti:Sa can be kept constant (Figure 5-7).

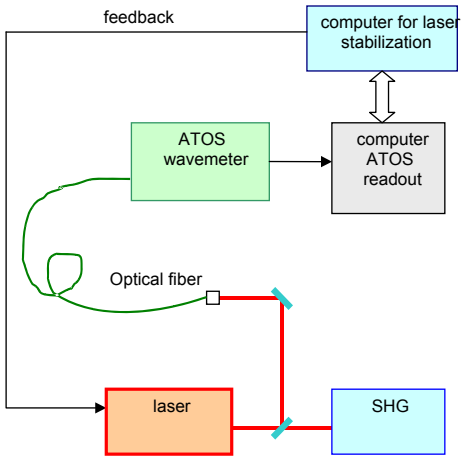

Figure 5-7: Control loop system for controlling the wavelength of the laser.

5.3 Fabry-Perot spectrometer

As mentioned before, the objective of the experimental work is to test the Tenti model at UV wavelength for gases at atmospheric conditions. These conditions impose several constraints on the experimental setup and detection system.

- Working in the UV (355 nm) range: The scattering signal is expected to be more intense in this wavelength region than at higher wavelengths, such as visible or infrared (see section 2.2). However, light scattering in air has never been measured at this wavelength. From a Tenti model calculation [7] the spectrum signal is expected to have a nearly Gaussian shape (a “flattened Gaussian”) with a Full-Width-at Half –Maximum (FWHM) of 3 GHz and a total frequency span of 6 GHz. From this we deduce that the Fabry-Perot must have a Free-Spectral-Range (FSR) that allows for structures that are 6 GHz wide, i.e. a FSR of 7 GHz or more, if only two modes of the etalon are present in the cavity. We purchased concave mirrors to build a confocal cavity of FSR of 15 GHz (one mode only) and this means a cavity that is 10 mm long and with two mirrors of Radius of Curvature (ROC) of 10 mm each. In practice, when the cavity with the two concave mirrors was built, the light incoupling was too low (see section 5.3.2). As a result, the reflectivity of the incopling mirror had to be decreased. As there are no commercially available mirrors with smaller ROC, a confocal etalon composed of a flat and a concave mirror was built instead. This forced us to reduce the length of the cavity to ~5 mm, and therefore the FSR increases to 30 GHz (with one mode). Four modes were measured in the case of the scattered light, and the experimental FSR was 7.5 GHz.
- The Finesse vs. coupled power dilemma: As mentioned before, the experimental resolution must be on the 100-200 MHz range to be able to test the Tenti model. This high resolution cannot be achieved with commercially available spectrometers, so a “home made” Fabry-Perot spectrometer was built. In order to keep the resolution of the spectrometer high, the Finesse of the Fabry-Perot must be high also, on the order of 100. A high Finesse is achieved by increasing the reflectivity of the mirrors used. But increasing the reflectivity of the input mirror of the etalon means the very little light goes into the etalon and then “we are throwing away most of the signal”. Increasing the reflectivity of the output mirror means that very little light comes out of the etalon and therefore is not detected. This is further discussed in Section 5.3.2 and Section 5.3.3.

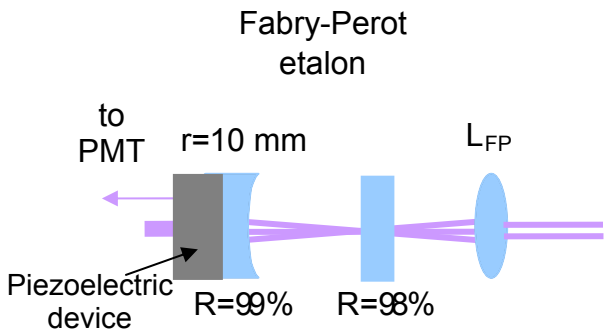

Figure 5-8: Design of the Fabry-Perot etalon.

5.3.1 Fabry-Perot at 355-365 nm

A homemade confocal Fabry-Perot was build with the following characteristics (Figure 5-8):

- The in-coupling mirror is a flat mirror with 98% reflectance (the losses per round trip are almost matched, as the in-coupled power is more than 75% (see Section 5.3.2).
- The out-coupling mirror is a plano-concave mirror with 98.9% reflectance (specification sheet claims 99 ± 0.2 %), and its radius of curvature is 10 mm.
- The finesse achieved is 135 (See Section 5.4.5). The calculated finesse, taking into account the losses is 155 (see Section 5.3.3).
- The Free-Spectral-Range of the etalon is 30.05 ± 0.10 GHz (distance between mirrors of 4.99±0.02 mm). This distance has been optimized and is not going to change for this set of mirrors.
- The in-coupling lens has a focal length of 50 mm.

With this FSR (30 GHz) and the finesse achieved (130); the calculated resolution is 230 GHz.

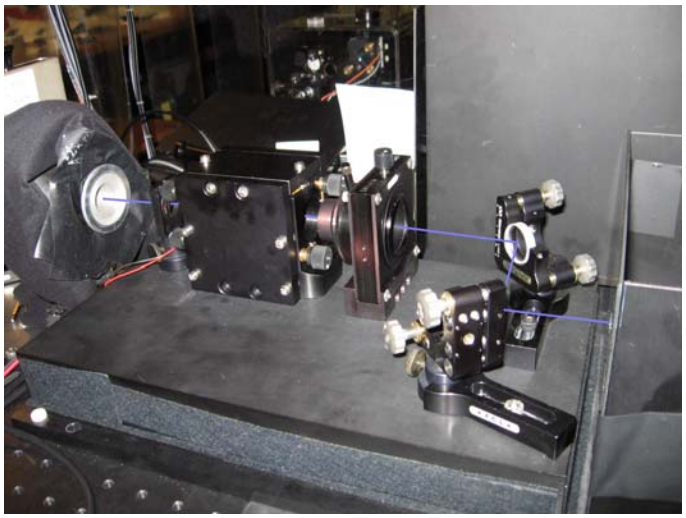

Figure 5-9: Photograph of the etalon. The light is coupled in via two high-reflectance mirrors. In the picture is also visible the in-coupling lens holder and the etalon is inside the black box. Finally, the entrance to the PMT is shown.

5.3.2 Power coupled into a cavity (etalon)

The amount of light coupled into a cavity depends on the impedance matching (reflectivity of the in-coupling mirror) and on the cavity mode matching (choice of in-coupling lens). In the following we assume a perfect Gaussian beam, perfectly mode matched to the cavity. The coupling of the light into the cavity can be calculated as 1-L, and L is the part of the input beam that is reflected at the input mirror when the cavity is on resonance (when the length of the cavity is an integer of the wavelength):

$$L = \left(\frac{\sqrt{R} - \sqrt{V}}{1 - \sqrt{RV}} \right)^2$$

where R is the reflectivity of the in-coupling mirror, and 1-V are the losses per round trip, without taking into account the in-coupling mirror reflectivity. L is minimum when R=V, and this means that at R=V there is maximum light in-coupling. For a perfect etalon, perfectly mode matched and impedance matched, L is equal to zero.
The losses of the light inside a cavity can be classified:

- Transmission losses: the non-total reflectivity of the (out-coupling) mirror supposes a loss of the light inside the cavity (the in-coupling mirror is not taken into account). This means that if a mirror has a reflectivity of 97%, every time the light does a round trip, there will be a loss of 3% on this mirror. When the other losses (more about this below) are negligible, it means that V=97% and therefore the optimal in-coupling of the light happens when the reflectivity of the in-coupling mirror is the same as for the out-coupling mirror.
- Dissipative losses: these losses are related to undesirable phenomena occurring inside the cavity: light scattered by the imperfections on the surface of the mirrors, or fluorescence on the mirror surfaces. If these losses are of the order of the transmitted light (1-R), i.e. a few percent of the light, they are not negligible anymore and they will have an effect on the light coupled into the cavity.

As a numerical example: Rout=99%=0.99 (losses in the cavity due to transmission losses: 0.01). To see the variation of 1-L with R, see the figure below. The figure below shows the optimal in-coupling reflectivity for different amounts of dissipative losses.

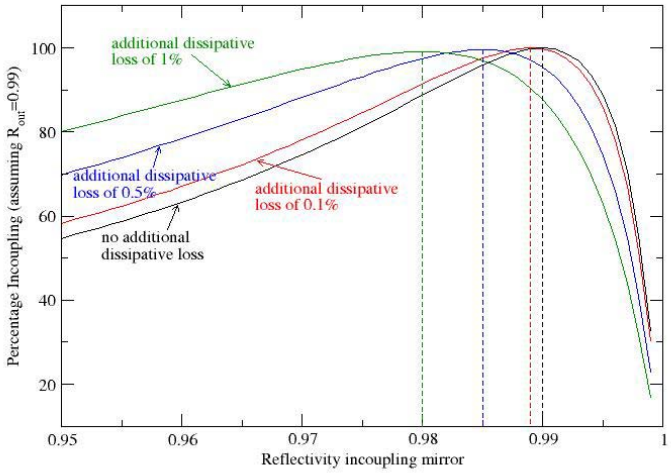

Figure 5-10: Variation of in-coupled light with the reflectivity of the input mirror, for different amounts of dissipative loss. A perfect Gaussian beam is assumed, perfectly mode matched. The reflectivity of the input mirror that gives the maximum in-coupling is shown with a dotted line on each case.

In our experiment, we used several mirrors to see where we got the best impedance matching on the Fabry-Perot:

- R=99.5% in-coupling 5%
- R=99% in-coupling 20%
- R=96% in-coupling 40%
- R=98% in-coupling 70-75%, mirror in use.

Our out-coupling mirror has a reflectivity of 99%. If the dissipative losses were negligible, the best in-coupling mirror would have been the one with 99% reflectivity. The fact that the best in-coupling was obtained with the mirror of 98% reflectivity tells us that the dissipative losses inside the cavity are in the vicinity of 1% of the light.

Apart from these impedance losses that occur even when there is perfect mode matching between the cavity and the laser mode, extra losses occur when the laser mode does not match the mode of the cavity. These losses can be corrected by using the appropriate set of in-coupling lenses. As we obtain a 75% in-coupling into our Fabry-Perot etalon, this means that a 25% of the light is lost and is not transmitted through the etalon. Part of this lost light is dissipated (this is just 1%, we estimate), and a non-perfect impedance matching together with an imperfect mode matching would account for the other 24%. It is almost impossible to be in the 100% in-coupling regime.

5.3.3 Finesse

The Finesse of a cavity with losses can be calculated with:

$$F = \frac{\pi\sqrt{\rho}}{1-\rho}$$

where $\rho=(VR)^{1/2}$ and R is the in-coupling mirror reflectivity and $1\text{-}V$ are the losses per round trip, without taking into account the in-coupling mirror. The losses are caused e.g. by imperfect mirror surfaces, fluorescence, etc. Note that for low dissipative losses ($V \sim R_{out}$) this equation takes the more familiar form: $F = \frac{\pi\sqrt{R_{tot}}}{1-R_{tot}}$, with $R_{tot}=(RRout)^{1/2}$. If a good in-coupling is desired (in a case of weak signal, for example), the effect of the in-coupling mirror reflectivity should be taken into account. The effect on the reflectivity of the in-coupling mirror on the Finesse can be seen on the figure below.

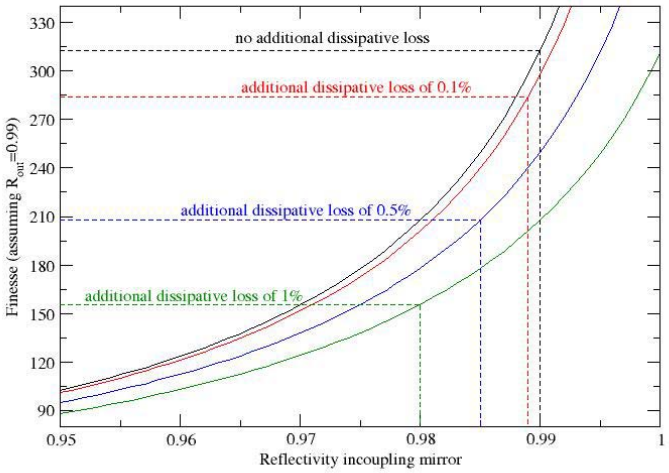

Figure 5-11: Variation of Finesse with the reflectivity of the input mirror for different amounts of dissipative losses. A perfect Gaussian beam is assumed, perfectly mode matched. The reflectivity of the input mirror that gives the maximum power in-coupling on each case is shown with a dotted line for each case.

A compromise between good in-coupling and enough Finesse must be sought on each experiment. On our case, an in-coupling of 75% was achieved (it is nearly impossible to be in the 100% in-coupling regime) with a finesse of 130. The fact that the Finesse did not reach the maximum value (155) means that the light is not perfectly mode matched. The in-coupling of the light was tested with mode matching lenses with focal lengths of 3.5 cm, 5 cm and 7 cm, and 5 cm gave the best results.

5.4 Fabry-Perot spectrometer characterization

The Fabry-Perot etalon has been characterized by a series of measurements. The free spectral range, the instrument function and Finesse of the etalon are shown below, together with a calculation of the opening angle of the etalon.

5.4.1 Cavity Modes in the etalon

The amount of modes inside the cavity depend on the alignment of the light beam and on the mode matching conditions (i.e. how divergent or convergent is the light beam). The reference laser maintains four modes inside the cavity: one main mode (the largest peak), one minor mode (in between the larger peaks) and two smaller ones that can be barely seen when the signal is in logarithmic scale (the one on the left is the most pronounced one, on the right there is almost no peak). These are the same modes that are present in the case of the scattered light. But in the case of the scattered signal, the “small modes” have a much more important contribution.

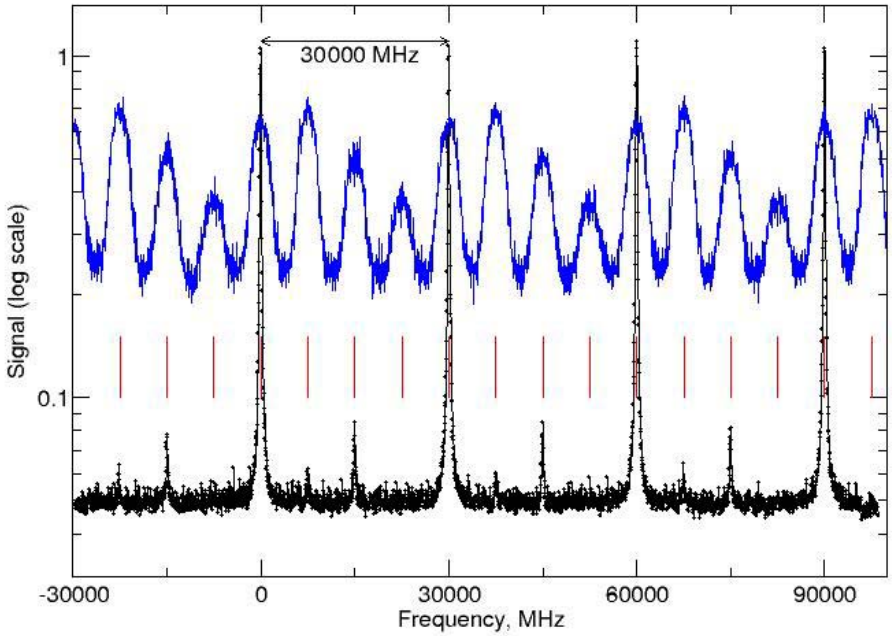

Figure 5-12: Signal in logarithmic scale, to show the mode structure inside the etalon. There are four modes per FSR. In black the signal recorded for the reference laser. The vertical red lines are just indicating the mode peak positions. In blue (the scale and intensity offset are arbitrary, for clarity) the signal from air scattering.

The fact that the cavity sustains 4 modes shortens the FSR. The mode separation is 7.5 GHz, as they are evenly separated. This means that the maximum width of the signal to measure should not be more than 7 GHz. A wider signal will mean that the modes (i.e. the signal spectrum) will overlap and their frequency features will not be discernible. In our system this means we will not be able to measure light gases such as Hydrogen or Helium, as their signal is expected to be wider than the one of air, at atmospheric conditions.

5.4.2 Measurement of the Free Spectral Range

The FSR is measured using the ATOS wavemeter. Keeping the Fabry-Perot etalon at a fixed cavity length, the Ti:Sa laser is scanned, and the difference between two main etalon peaks (aligned with the laser) is measured using the ATOS. The obtained value is 29760 $\pm$ 160 MHz. As there are four modes inside the cavity, the free spectral range is 7440 $\pm$ 40 MHz.

5.4.3 Measurement of the instrument function

The laser bandwidth is 2 MHz, and the Fabry-Perot instrument function is estimated to be 100 times broader. The measured instrument function is a convolution of the laser

bandwidth and the etalon instrumental function. The contribution of the laser is negligible; therefore the instrument function is measured directly by the laser.

The instrument function has an Airy shape, with a width of 230 ± 10 MHz. The width is calculated from an Airy fit of the experimental points.

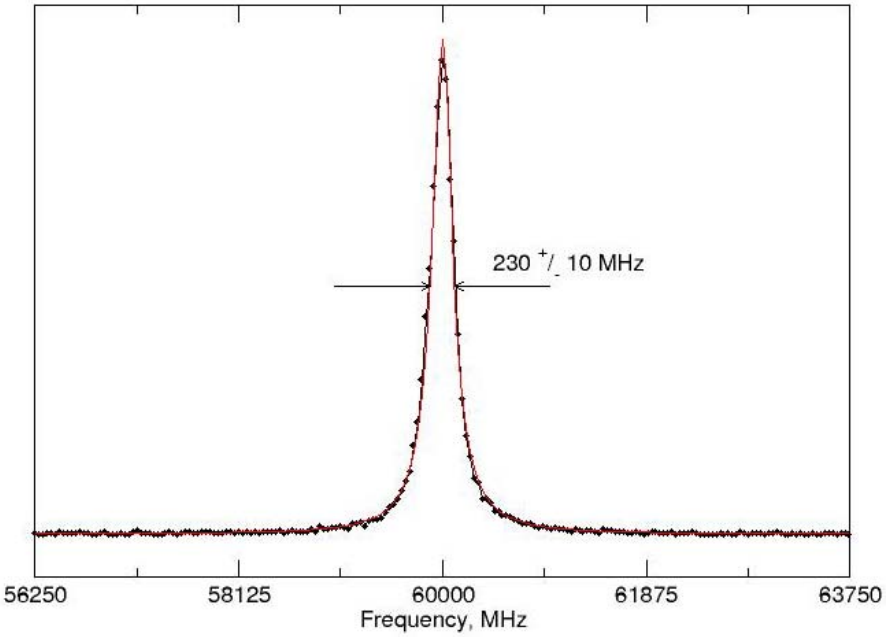

Figure 5-13: Measured instrument function, for the Fabry-Perot detector, PMT and electronics. Black dots: the experimental results (for the laser). Red line: Fit of the results.

5.4.4 The instrument function mathematical expression

The Airy function representing the instrument function can be written as:

$$A = I_0 \cdot \frac{1}{1 + \left(\frac{2 \cdot FSR}{\pi \cdot FWHM}\right)^2 \cdot \sin^2\left(\frac{\pi}{FSR} \cdot f\right)}$$

with I_0 = intensity at maximum, FWHM = full width half maximum = **232 MHz**, and FSR = Free spectral range (distance between modes) = **7440 MHz**, f is the frequency.

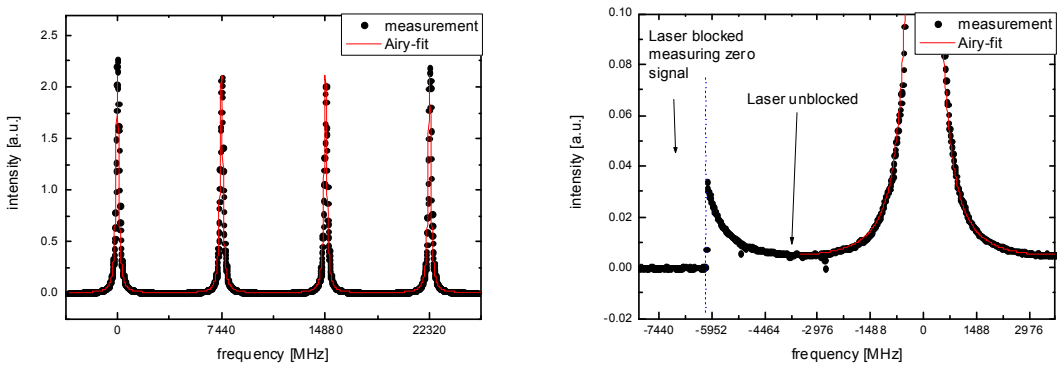

Figure 5-14: Airy fit of the transmitted function of the etalon, with the 4 modes in the etalon of approximately equal height. As it can be seen, the signal does not go to zero between the modes.

5.4.5 Measurement of the Finesse

The Finesse is measured using the laser light as well: the Free-Spectral-Range of the aligned laser (29760 MHz) divided by the Full-Width-Half-Maximum of the Airy-shaped lines.

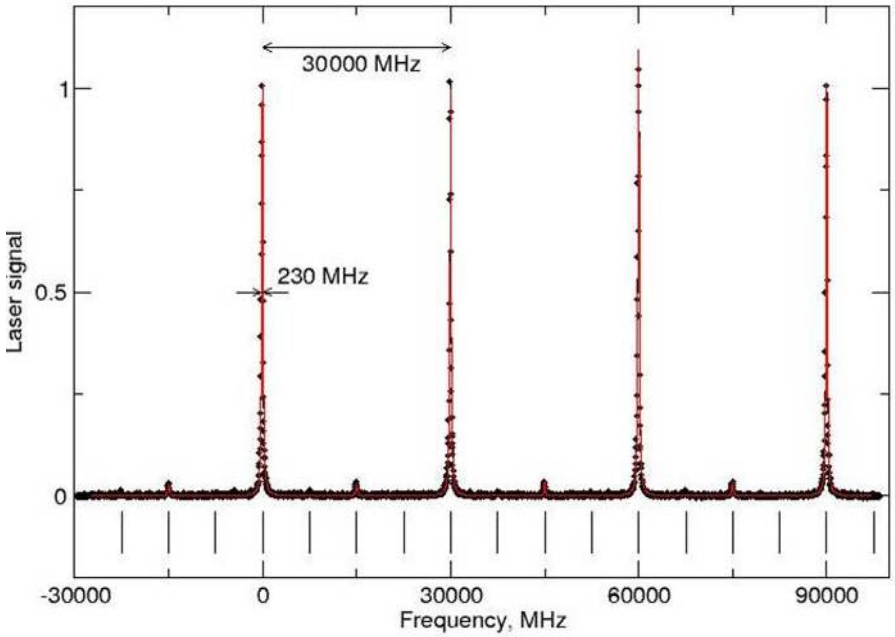

Figure 5-15: Measurement of the laser, showing several FSR of 30 GHz (30000 MHz). The instrumental function resolution is shown for comparison. A small peak in between the two large peaks shows an extra mode inside the cavity. The four cavity modes center positions are indicated with the black vertical lines.

Then, the finesse F is:

$$F = \frac{FSR}{FWHM} = \frac{30000 \pm 100\ MHz}{230 \pm 10\ MHz} = 130.4 \pm 0.4$$

This value coincides with the theoretical value obtained using the reflectivity of the mirrors (see section 5.3.3).

5.5 The effect of the instrument function on the modeled line shape

The proper instrument function improves the prediction of the model greatly. The Airy function described above predicts an offset from zero and takes into account the adjacent modes of the etalon.

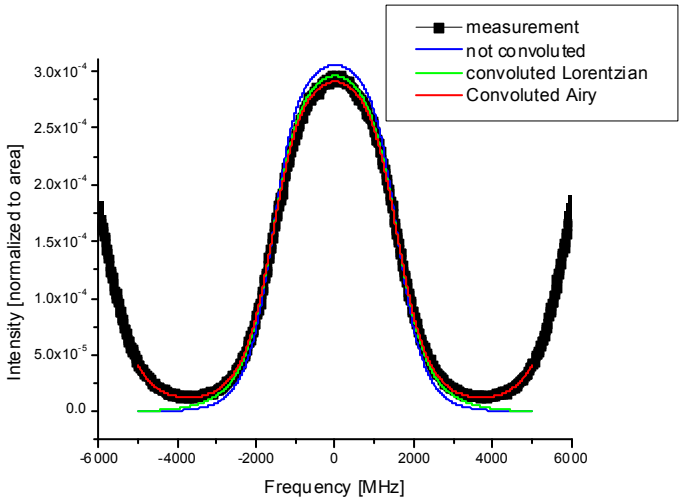

Figure 5-16: Measurement of Nitrogen at 1000 bar (black). The prediction for the model without the convolution of the etalon instrument profile (blue), the prediction of the model using an erroneous Lorentz instrumental function (green), and the proper instrumental function profile, using the Airy function (red) are shown.

5.6 Light collection, imaging and alignment

Apart from creating the UV light (Section 5.2) and measuring the scattered light (Section 5.3), a whole system to filter and align the detection setup has been created.
This system is separated into two main sections:

- Scattered light detection: the main problem to overcome here is that the geometrical shape of the scattered light is not accepted by the Fabry-Perot etalon. A whole system is devised to filter the light and make it acceptable for the Fabry-Perot etalon.
- A reference laser is used, to align the whole detection system of the scattered light.

5.6.1 Geometrical shape of the scattered light

The SRBS light source is a laser beam. Therefore the light is scattered in a cylindrical shape. Below is shown a picture of the light detected by the collecting lens L_4.

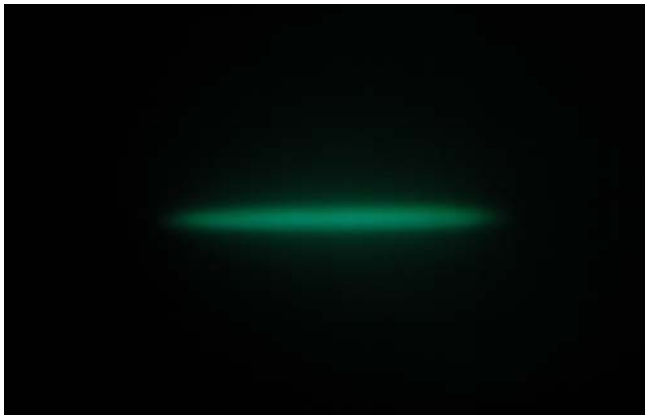

Figure 5-17: The length of the laser light in the image is around 2 mm (conditions of the photograph) and the diameter of the laser beam is ca 200 μm. Note that there are no other sources of light, i.e. no scattered light from the optics or the scattering cell walls.

The geometrical shape of the scattered light (the cylindrical shape) is not accepted by the Fabry-Perot etalon, which requires that the light has a Gaussian beam shape to couple properly into the cavity. The light that is not coupled properly into the etalon creates extra cavity modes, and this would diminish the FSR even further, making the measurement of the SRBS impossible.

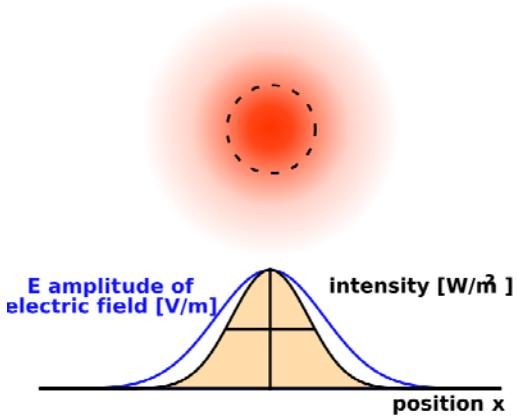

Figure 5-18: Geometrical shape of a Gaussian beam. This is the shape of the light intensity accepted by the Fabry-Perot etalon. Figure is taken from [51].

Therefore the light must be geometrically filtered to be accepted by the Fabry-Perot etalon.

5.6.2 Geometrical filtering of the light

The purpose of this section is to create a collimated beam of light that is accepted by the Fabry-Perot etalon. This part takes the collimated beam from the light collecting lens L4, focuses this beam (using lens L5) into the pinhole S2 (50 μm) and again collimates the light into a narrow beam via lens L6. The total beam diameter, after this filtering process is about 3 mm. This spot area is still too big and this beam is further reduced in diameter via diaphragm D3. The diameter of D3 is 1.3 – 1 mm.
The light coming out of the light-collecting lens L4 is the image of a beam of scattered light. This extended source cannot be coupled into the Fabry-Perot etalon and therefore it generates extra modes inside the Fabry-Perot cavity that make the measurement impossible. Setting a pinhole in front of the light-collecting lens L_4 just diminishes the intensity of the signal, but not its characteristics. Setting up the pinhole S2 solved this issue.

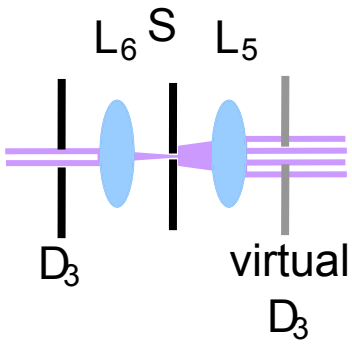

Figure 5-19: Geometrical projection of the scattering volume onto the detection.

The diaphragm D3 plays an important role (see Figure 5-19). It diminishes the size of the spot of the collected scattered light on the Fabry-Perot, and also reduces the collecting angle of the Fabry-Perot (it is less than 1°). Due to the symmetry of the system, the presence of the diaphragm D3 is also equivalent as to have a virtual diaphragm before the focusing lens L5. This effect was experimentally verified by placing a diaphragm D_2 in this position and measuring that the collected light did not diminish in strength when both diaphragms had the same diameter.

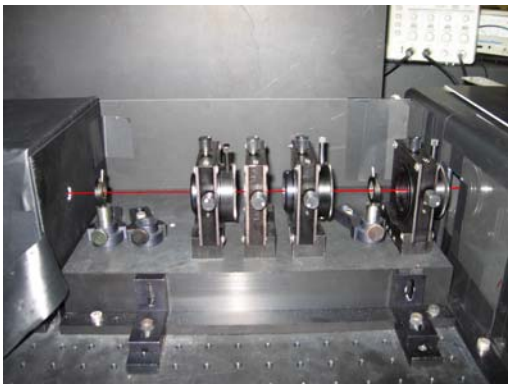

Figure 5-20: Light cleaning stage. The light goes from right to left, and its path is shown in red. The first holder contains the collecting lend L4, followed by a diaphragm (D2) and then by the set L5-S2-L6 of lens, pinhole and lens. The diaphragm D3 is the last components shown. The additional diaphragm D_2 is placed to facilitate alignment, but it does not play any role in the signal collection.

5.6.3 Opening angle of detection

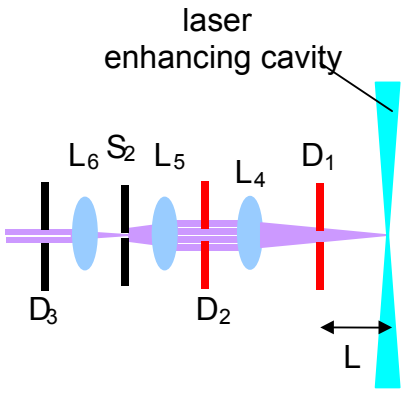

Figure 5-21: Stage for minimizing the opening angle for the RB-scattering.

The opening angle of the detected light is fairly small, 0.7 ± 0.2 °. This was experimentally verified by placing a diaphragm (D1), at a distance L of the laser inside the enhancing cavity. When the diaphragm D3 was 1 mm diameter (conditions of measurement of SRBS), the diameter Φ of the diaphragm D1 that did not diminish the scattered light signal, was 0.8 ± 0.2 mm. The length L is 31 ± 1 mm. Using this dimensions, the angle opening at the detection can be calculated as:

$$\sin(\alpha) = \frac{\phi}{2L} = 0.7 \pm 0.2^{0}$$

The diaphragm D2 is placed to facilitate alignment, but it does not play any role in the signal collection.

5.6.4 Reference laser alignment and cleaning

With a similar intention as with the geometrical filtering stage described before (Section 5.6.2) a laser beam cleaning stage was devised, to allow to better acceptance of the laser beam in the Fabry-Perot. To mimic the scattered light behavior, it is focused in the region where the scattered light is created, so it reaches the collecting lens L_4 as a diverging beam. Therefore after the filtering, the reference laser beam is focused by lens L3 on the focus of the enhancing cavity.

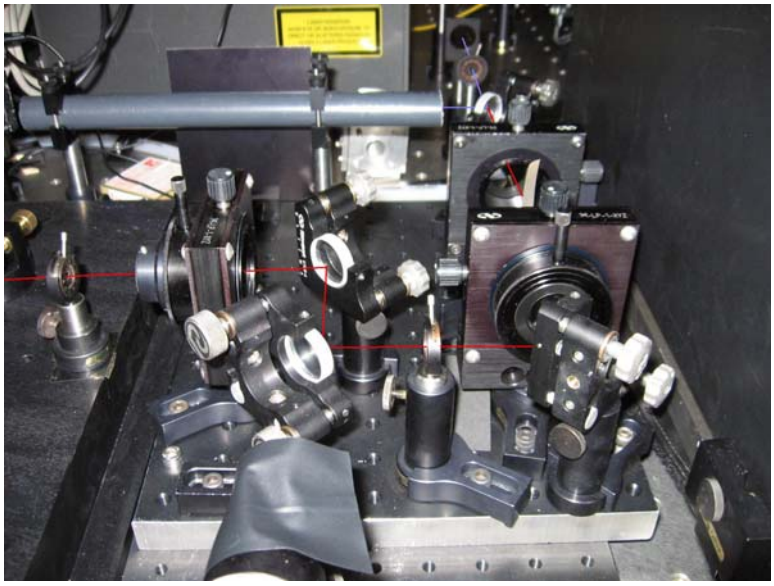

Figure 5-22: Light cleaning stage for the laser beam. The path of the beam is marked in red.

5.7 Data acquisition

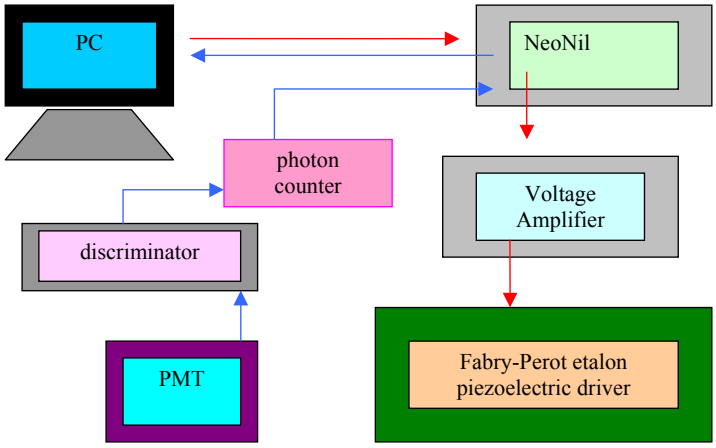

Figure 5-23: Schematic of the data acquisition system. The PC controls the voltage driving the piezoelectric device on the Fabry-Perot etalon, scanning the length of the cavity. For each position, the scattering signal is collected by the PMT. The output of the PMT is discriminated and finally a photon counter signal is read by the computer.

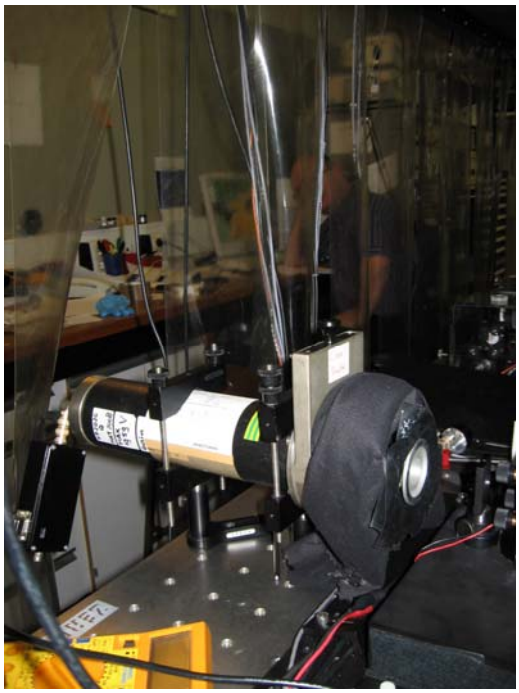

Figure 5-24: Picture of the PMT used in the experiment (Photonis XP2020 Q fast/high gain). In the background it can be seen the equipment used for data acquisition and computer.

5.8 Noise level of the measurements

The Photo-Multiplier-Tube delivers a signal that is proportional to the number of photons detected. This means that it should follow Poisson statistics for the level of noise of the signal. This means:

$$Noise = \sqrt{C}$$

where C is the number of counts detected on the PMT per unit of time (in our case 1s).

5.8.1 Dark counts

All PMT devices have a number of “dark counts”, i.e. a number of counts present even when there are no photons detected. In our case this number was 190 counts. For each measurement the number of dark count was measured and later on subtracted.

5.8.2 Electronic noise problems

The vicinity of other experiments in the lab accounts for the increase in the electronic noise of the measurements. This noise adds as a constant to our measurements (and therefore the noise on the experiment will not behave as pure Poisson noise) and its net effect is to change the dark count level, as well as adding to the background count.

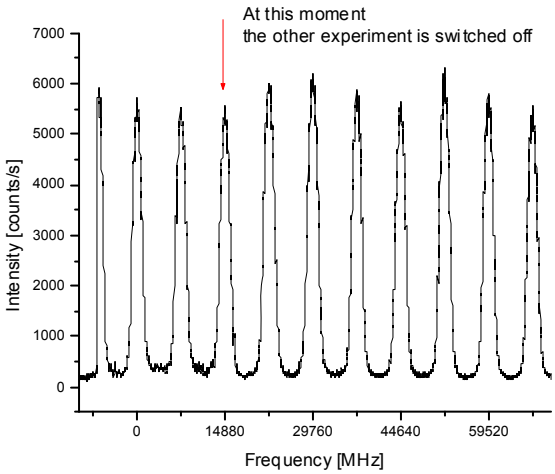

Figure 5-25: Scan of Krypton gas (scan20090609_08) at 1000 mbar. In the middle of the scan the other experiments in the vicinity switched off their machines and the electronic noise level dropped visibly in between the peaks.

The effect of the electronic noise is to add a constant noise value to the overall noise in the intensity. This means that the noise behavior can be modeled to be (Intensity – units of number of counts per unit of time C):

$$Noise = \sqrt{C} + K$$

the behavior is Poisson noise and K is the addition due to the electronic noise. K is found to be of the order of 2-3 counts. How important these 2-3 counts would be depends on the overall intensity of the signal, and this would be different for each measurement. The signal that had the lowest maximum intensity was air at 300 mbar, and it had more than 600 counts. Therefore the electronic noise contributes a maximum 0.5% error on the overall intensity. The contribution of the Poisson noise depends on the amount of counts measured in each case.

5.9 Scattering cell

5.9.1 Choice of the scattering angle

The ADM-Aeolus satellite will measure backscattering, i.e. the angle of detection is 180°. It was intended that this experiment would also measure backscatter. We think this will not be possible for reasons explained below. The Aeolus satellite will work with a pulsed laser and the light observed will come from the atmosphere, not from a scattering cell. This characteristic makes it possible for the Aeolus satellite to measure backscattering. In our measurements we need to measure the light scattered by pure gases and controlled mixtures. This means that our measurements should be performed inside an enclosed space, i.e. a scattering cell. A scattering cell will need input and output windows. Even the best quality windows will always scatter light. The light scattered by the windows will be of the same frequency as the laser. Moreover, the power of the light scattered by optics is much stronger (orders of magnitude stronger) than the light scattered by a gas or air (what we want to measure). It is not possible to filter it by

spectral means (setting a filter) as the frequency of the scattered light by the optics is the frequency we want to measure. The only possible filtering is using geometrical filtering, this means setting pinholes and light dumps. But at 180° it is impossible to block the light scattered by the optics because it is in the line of sight. This is illustrated in the figure below.

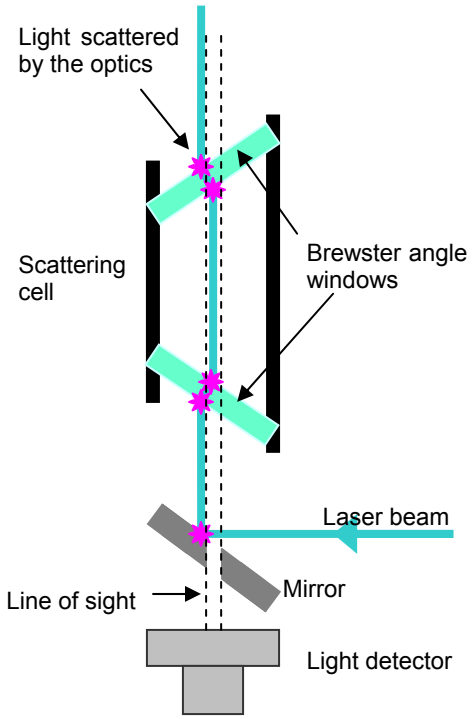

Figure 5-26: Schematic layout of the scattering cell mounted w.r.t. the enhancement cavity.

Discarding the 180° configuration, other angles must be used. To avoid having problems with scattering from the optics, the 90° configuration is the most suitable. For this reason most of the experimental groups have chosen such a configuration (see Section 4.4). It is also the approach in this work. Even in this 90° configuration severe problems were encountered with light scattered by the optical components of the enhancement cavity and from the input and output windows of the cell.

5.9.2 Scattering cell design

A scattering cell for measurements at 90° was designed. The cell has input and output Brewster angle windows for light in the 365-355 nm region, that will minimize reflection losses. The SRB scattered light comes out from an anti-reflection coated window. The cell allows for pressure variation and temperature variation. The temperature is varied using Peltier coolers/heaters (can be used in both operations) and in the case that is needed, the base plate can be cooled or heated by a water flow, for temperature stabilization of the enhancing cavity. The pressure is varied by gas inlets and vacuum pumps. It is built from a solid piece of aluminum that prevents vibration problems and allows for an even heating and cooling of the gas.

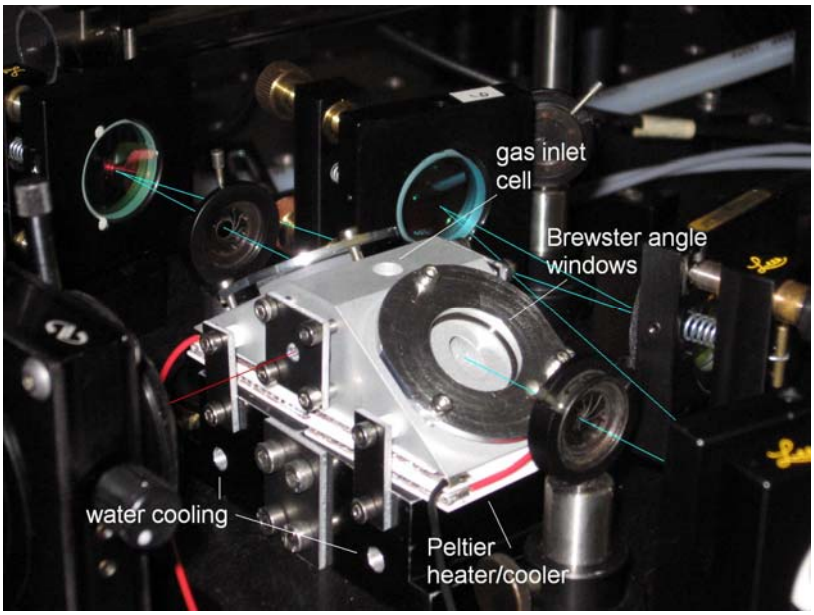

Figure 5-27: The cell mounted inside the enhancement cavity.

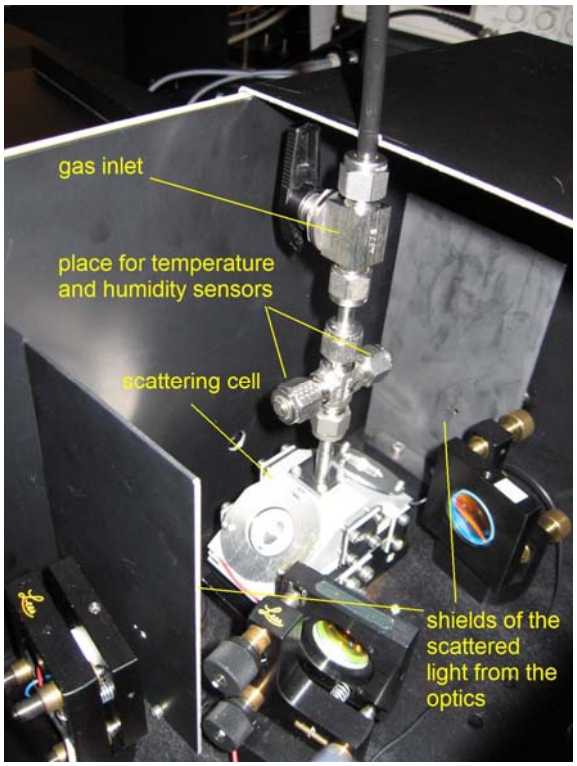

Figure 5-28: The cell mounted inside the enhancing cavity with the gas inlet to the cell.

5.9.3 Scattering angle estimation

The actual measurement of the scattering angle is rather difficult. The cell is designed to give a scattering angle of 90°, but there is always an uncertainty on this value. The uncertainty of the scattering angle has two contributions: the placement of the collecting lens, and the angle of the laser.
The dimensions of the cell are 40 mm wide, by 52 mm where the laser light is passing through. The diameter of the tubes where the laser light passes is 2 mm, on both tubes (see figure below).

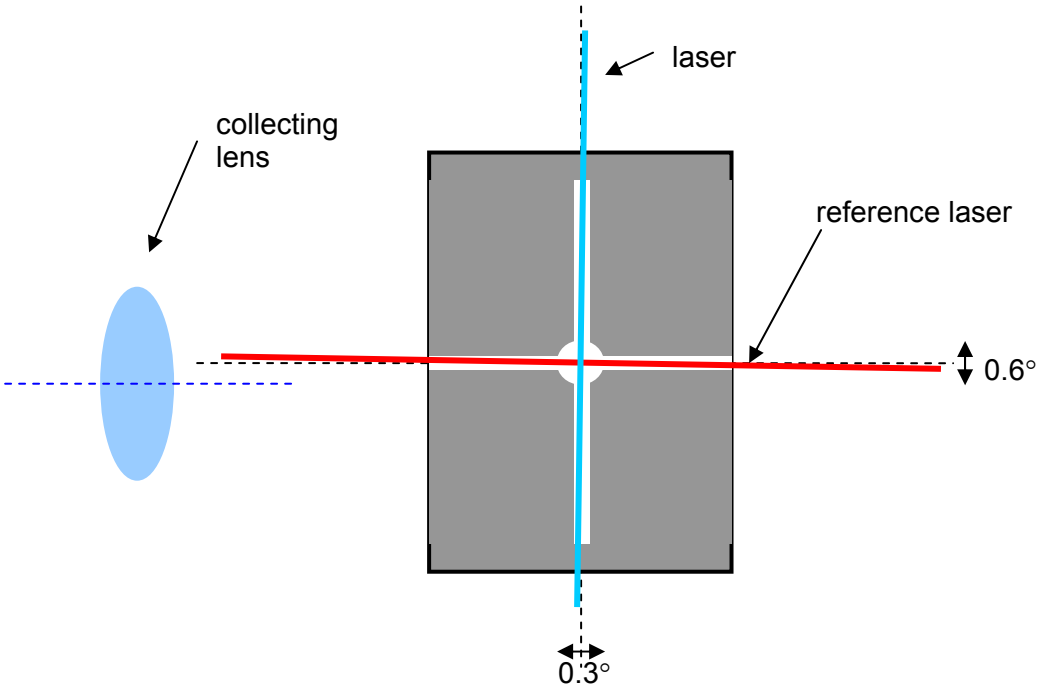

Figure 5-29: Schematic of the scattering cell viewed from the top. The angular deviations stated are the maximum deviations allowed in the system. The collecting lens is purposely drawn misplaced to illustrate the deviation.

The scattering lens was not moved in the horizontal direction during the science measurement campaign. Therefore, if there is a deviation, is of **systematic nature**. The laser beam was realigned day to day and therefore the measurements could present deviations of 0.3°.

5.10 Temperature, pressure and humidity variation

5.10.1 Temperature variation

The base plate of the cell has a stack of Peltier coolers/heaters that reach easily -70° to 70° C. In the gas inlet we will place temperature and humidity sensors that will read the temperature of the gas online.

5.10.2 Pressure variation

The necessary equipment for pressure detection and vacuum pumps is already present and mounted in the setup (Figure 5-30).

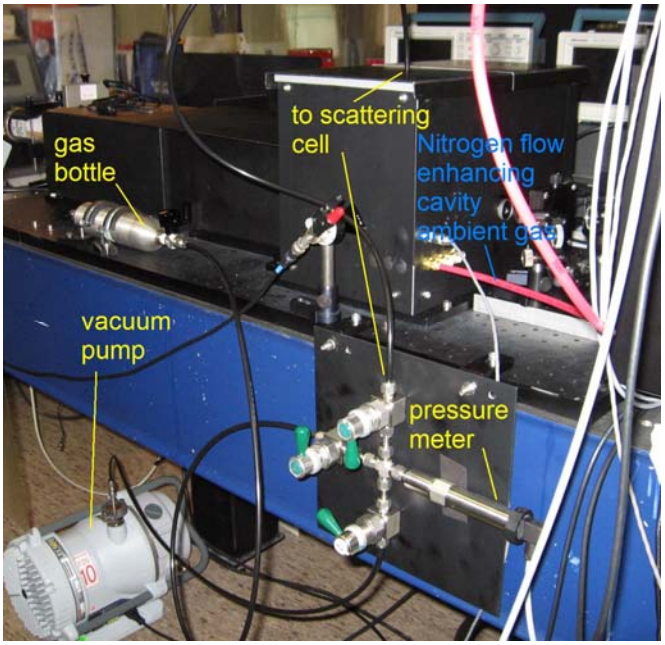

Figure 5-30: Mounted gas system for the SRBS experiments, the baratron shown is the APR 266.

At the moment we have two baratrons (pressure meters) that will cover the regimes to work:

- Compact Capacitance Gauge CMR 271 from Pfeiffer: it is designed to work from 0.1 mbar to 1100 mbar (1mbar is 1hPa), with an accuracy of 0.15% of reading.
- Compact Piezo Gauge APR 266 from Pfeiffer: it is designed to work from 1 mbar to 11000 mbar with an accuracy of 2% full scale. In principle we could work with this head only, as it measures up to the low pressure regime required. The other Baratron head is more accurate, but it does not work for more than 1 bar.

We have also 2 electronic readers for the output of the baratron heads (Single Gauge TPG 261 from Pfeiffer).
The pumps are connected by PVC tubes, to prevent vibrations from the pump to reach the optical table.

5.10.3 Humidity sensors

We have purchased a set of three different humidity sensors to Honeywell (HIH4602-A, HIH4602-C and HIH4000-004), in order to test the dependence of the SRBS shape with water content. These humidity sensors (Figure 5-31) come with a temperature sensor incorporated, and the two HIH 4602 sensors are already calibrated.

Figure 5-31: Humidity sensors from Honeywell. Left: type HIH4602. Right: type HIH4000.

6 Data acquisition and treatment of the results for the SRBS experiments

In this section the procedure of signal acquisition, calibration and averaging is explained. This procedure is the same for all measurements, independent of the gas, pressure or temperature. We will use as an example results from measurements in air, for illustration of procedure.

6.1 How the "raw signal" looks

The measurement is performed by measuring the signal coming from the photon counter after changing the Fabry-Perot cavity length by driving the piezoelectric device attached to the output mirror of the etalon (see Figure 5-23). The driving voltage to the piezoelectric device in the Fabry-Perot is the (amplified) voltage given by the computer.

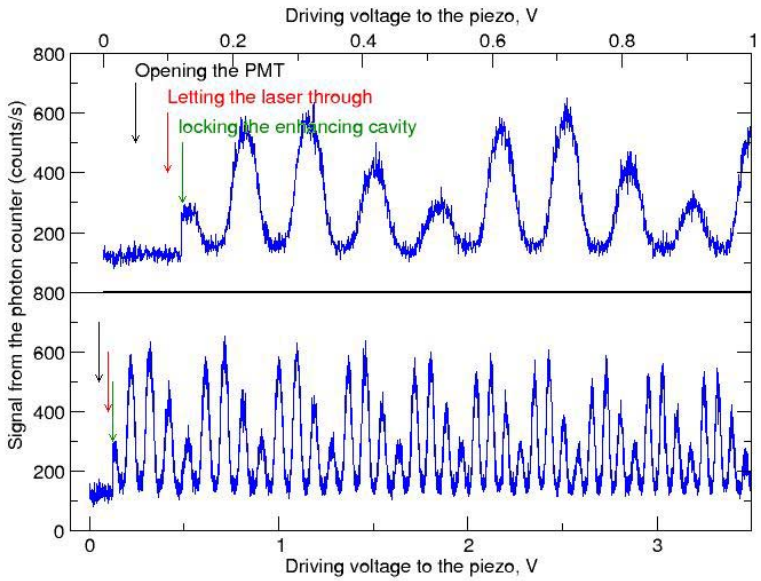

Figure 6-1: How the signal looks when measured. The arrows show when the PMT shutter is open, when the laser signal is allowed into the system and later when the enhancing cavity is locked.

Figure 6-1 shows the signal of the photon counter versus the voltage fed to the amplifier driving the piezoelectric device that changes the Fabry-Perot etalon length. Several things can be noted on this figure:

- There is a dark count on the PMT: this is an unavoidable reality of PMT detectors. There will always be a given number of dark counts, which depend on the detector itself (each detector is slightly different from the others) and the setting of the voltage across the PMT. This dark count does not mean that a photon is detected; it is just "noise" of the device. This is shown by the fact that

there are dark counts even when the PMT shutter is closed and no light is reaching the detector.

- Before opening the shutter of the PMT, it can be assumed that no photons hit the detector. This signal is the signal we set as zero in our measurement. For each measurement taken, the PMT starts with the shutter closed in order to measure the dark counts and to set the zero level.
- As it can be seen, the signal between peaks reaches the zero level, i.e. the different modes do not overlap.
- The nonlinearity of the response of the piezoelectric device is responsible for the apparent varying distance between modes after scanning several FSR.
- Apart from the recording of the photon counter, a signal proportional to the intensity of the laser inside the enhancing cavity is recorded. This allows for corrections of the overall intensity of the scattered light over long scans (not shown in the figures).

6.2 Calibration

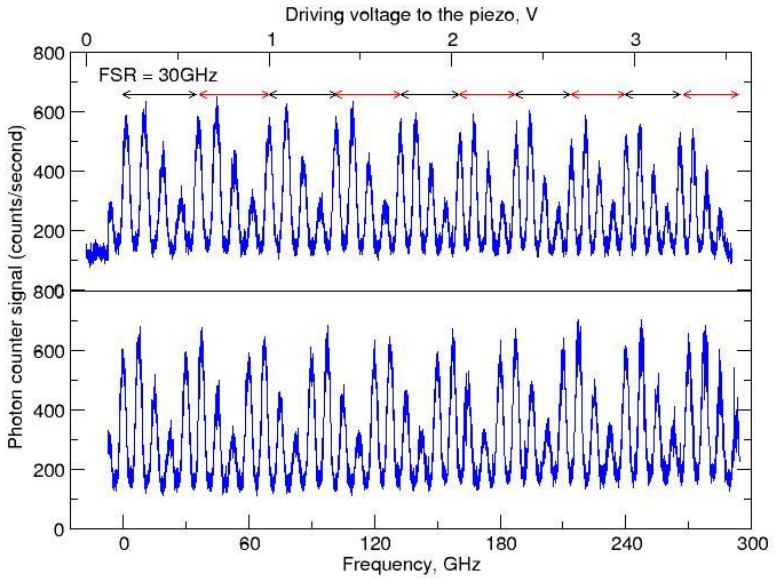

Figure 6-2: Illustration of the calibration procedure. Each repeating pattern is separated exactly 30 GHz. Consecutive peaks are separated 7.5 GHz. Upper part: whole scan versus the voltage sent to the voltage amplifier feeding the piezo. The figure shows that the piezo has a non-linear response with voltage, as each FSR becomes shorter. Lower part: Calibrated signal.

The FSR of the Fabry-Perot has been measured and is known. The FSR pattern repeats every 30 GHz, and each consecutive peak is separated by 7.5 GHz. The scan can be calibrated using this information. The piezoelectric device changing the Fabry-Perot cavity length has a nonlinear voltage response. This is seen in that the distance between the peaks appears to change over the scanned voltage.

6.3 Signal averaging: FSR

The signal of each scan is averaged into the repeating pattern (the FSR). Each peak in the repeating pattern has the same shape, as a fitting proved. The width of each peak is the same, only the intensity is different.

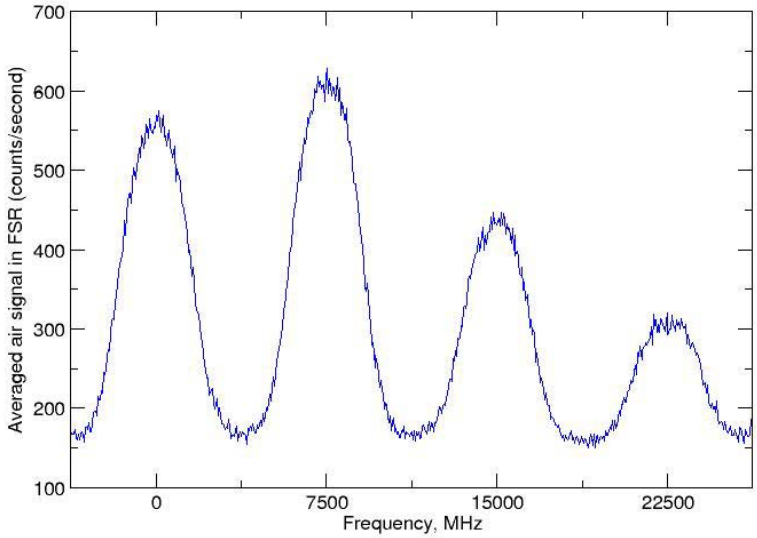

Figure 6-3: Each scan can be averaged into the repeating pattern (FSR).

6.4 Signal averaging: one single peak

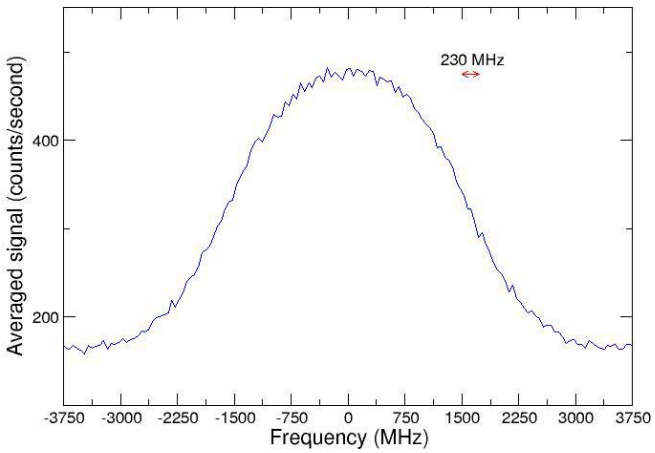

Figure 6-4: Averaged signal obtained from a scan recorded over many fringes. The resolution of the measurement is shown for clarity.

As the signal is the same for all peaks on the averaged FSR, their signals are averaged into a single peak (they are not weighted). To compare different measurements, the signal is normalized to its area, where the frequency is in MHz. The amount of peaks averaged is ca 40, but this number depends on the signal to noise ratio. A set of at least 3 measurements is performed for each gas. Each measurement takes 3 hours, but this depends on the averaging time (that is signal to noise dependent). The alignment of the setup can also take 3-4 hours to be done, and each time the pressure of the gas is modified, the setup must be aligned again.

6.5 Comparison with measurements in open air

From Figure 6-5 it can be seen that the signal obtained for open air and the signal obtained for air in the cell (at atmospheric conditions) are the same. In order to compare both signals, taken at different days and different laser powers, the spectra are normalized to their area. This measurement forms a test on the operation of the cell, not introducing artifacts.

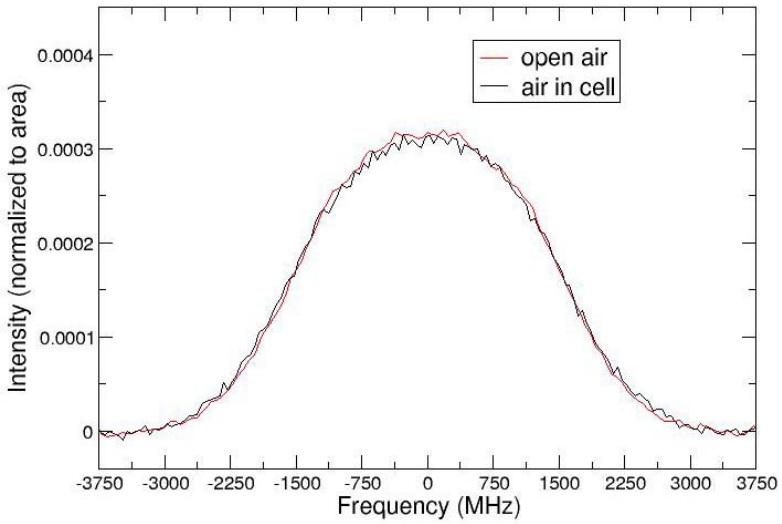

Figure 6-5: Normalized (to the area) spectra of the SRBS in air. Red curve: the scattering from open air, without the scattering cell. Black curve: the scattering from air from inside the scattering cell, at atmospheric conditions. Both curves coincide. The signal to noise of both measurements is comparable, and they took roughly the same amount of time to measure (3 hours).

6.6 Some experimental drawbacks

6.6.1 Necessity for permanent re-alignment of the enhancement cavity

From the design of the scattering cell and enhancing cavity, it follows that when changing the pressure (or gas, or temperature) inside the cell, the enhancing cavity becomes misaligned. This can be understood as follows: the change in pressure will change the refractive index inside the cell. The incoming laser beam (the one that generates the RB scattering we intend to study) will encounter then a different index of refraction inside the cell, and therefore will change its optical path, by changing the angle of propagation. This will result in a misalignment of the enhancing cavity. Therefore, every time the pressure inside the cell changes, a new alignment of the enhancing cavity must be made, and this results that all measurements are performed in slightly different conditions. Once the pressure is changed (and the valve to the cell is closed), the pressure inside the cell does not change, and therefore the alignment does not change either. In some measurements, especially at high pressure, in which more points per curve are necessary and therefore the scanning time increases (one measurement could take 5 hours), the laser system could become slightly misaligned. This did not affect the measured shape, but made the enhancing cavity drop the intensity, and therefore the measured intensity could vary. This is corrected for, by dividing by a signal proportional to the power inside the enhancing cavity.

6.6.2 Mie and Optics and cell walls (OCW) scattering contamination effect

In this section the possibility of OCW signal “contamination” in the spectrum is explored. By Mie signal we mean signal from (microscopic) dust particles that could be present in the gas inlet system, and by OCW scattered light from the optics or the cell walls. In a

sweep generalization, anything that may produce signal at the same wavelength as the laser wavelength, and may appear in the spectrum as “extra counts” at the zero frequency.

As prevention for dust particles, for the latest measurements, a dust filter (filtering particles larger than 5 μm diameter) was placed in the gas inlet of the cell. No difference with other measurements was observed, and therefore the possible contamination with dust particles was discarded.

6.6.3 Measurements with the empty cell

In order to detect a possible OCW scattering contamination from the optics or cell walls, a series of measurements were performed with the cell emptied of any gas. When the cell is empty, no particles are present to scatter the laser light, and therefore no light should be detected. Any possible OCW signal should be measurable this way.

Note: When changing the pressure inside the cell, the index of refraction of the optical path of the laser in the enhancing cavity changes. This means that the laser became misaligned and a new alignment of the laser inside the enhancing cavity had to be performed every time the pressure changed. Therefore, each measurement has slightly different conditions of alignment, power, etc.

6.6.3.1 Measurement 2009.06.15-03

In this experiment a direct measurement of the scattered light is recorded. This means that the light recorded does not go through the Fabry-Perot etalon, but directly to a Photomultiplier tube.

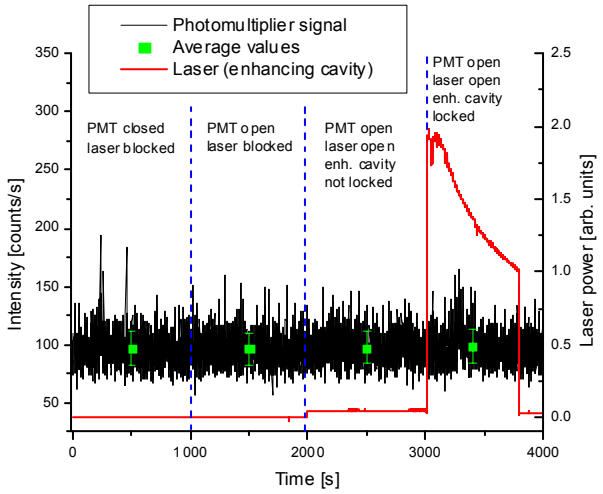

Figure 6-6: Signals recorded when measuring the empty cell (scan2009.06.15-03). The black curve is the signal recorded from the PMT, and the green squares represent the averages of this signal in the intervals denoted with the vertical dashed lines. The red curve is proportional to the intensity of the laser inside the enhancing cavity.

The experiment was performed in 5 stages:

1. The PMT is closed; therefore just the dark counts are recorded. Also the laser is blocked.

2. The PMT is open, but the laser is still blocked. This shows that there are no photons recorded from stray light from the environment of the lab.
3. The PMT is open and the laser light is circulating in the enhancing cavity (the piezo in the enhancing cavity is scanning) but the enhancing cavity is not locked. The signal recorded by the PMT does not increase.
4. The PMT is open and the enhancing cavity is locked. There are several observations to be made: a) the signal recorded by the PMT does not change significantly (the average value increases by 1% and inside the uncertainty region).This indicates that if there is any stray light, it is very weak, and undetectable. b) The power of the laser inside the enhancing cavity decreased continuously and a strong yellow fluorescence was observed on the spot where the laser hit on the walls of the Brewster windows in contact with the vacuum inside the cell.
5. The PMT is open and the laser is passing but the enhancing cavity is unlocked.

The reason for the laser power decreasing inside the enhancing cavity and the fluorescence of the (Fused silica for UV, uncoated) windows is at the moment unknown. It is a reversible process, and seems to occur in the UV region [52]. Contamination with some organic residues could be a cause for this effect, but at the moment this is just speculation.

Other measurements

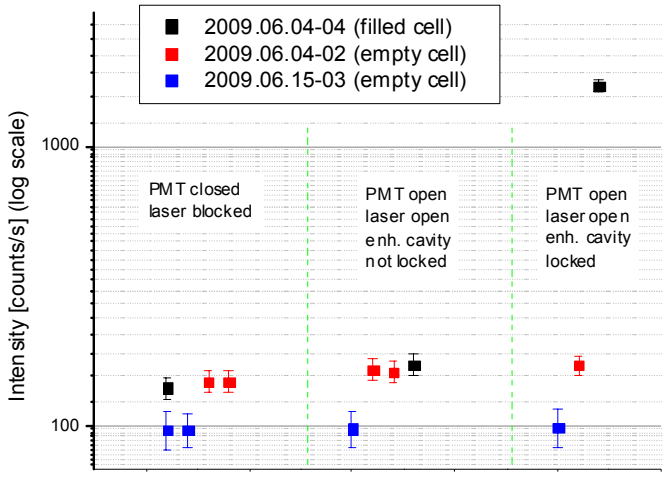

Figure 6-7: Average of the recorded signal on three different occasions. There are 3 different regimes where the signal is averaged: i) when the PMT is closed or the PMT is open and the laser is blocked, ii) when the PMT is open and the laser is circulating in the enhancing cavity, but the enhancing cavity is not locked, iii) when the PMT is open and the enhancing cavity is locked.

As it can be noticed by the measurements performed on different days and conditions, the level of the dark counts changed slightly and even when the PMT is closed the signals of different days do not overlap (see section 5.8.2). It can be noticed that there is always a slight increase on the signal level when the laser is passing and when the laser

is locked. This increase is of the order of 20 counts/s. The slight deviations from the model on the top of the signal (present in all measurements) are of the order of 100 counts/s or more. Nevertheless, these measurements indicate the possibility of having a surplus amount of counts on the top of the peaks, but the amount of counts measured do not account for the quantity of counts deviated from the prediction of the model.

6.6.4 Characterization of the OCW scattering contamination

Measurements (where both the signal of the gas and the light scattered from the optics were recorded) were performed in order to estimate the spectral shape and effect of the possible OCW scattering contamination. Such a measurement is shown in Figure 6-8. In these measurements the effect of the OCW was induced, either removing shielding elements in the enhancing cavity, or by moving the laser beam such as it “touched” the scattering cell walls.

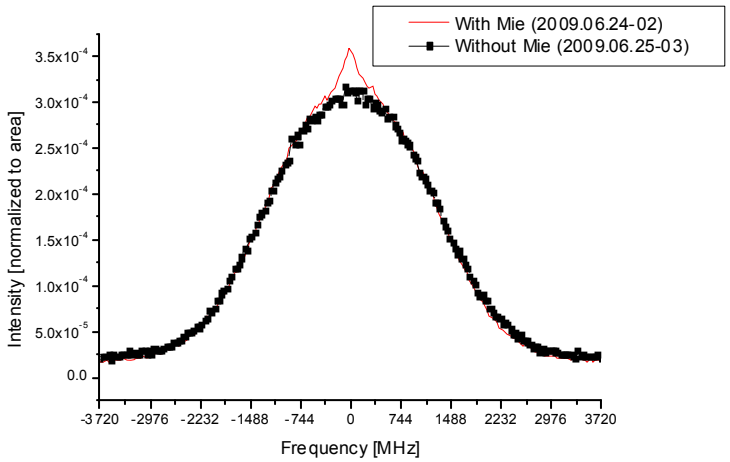

Figure 6-8: To compare different measurements, in which the intensity may vary, the intensity scale is normalized to area equal to one. Measurements performed with O_2 at 500 mbar.

The effect of OCW scattering is to generate extra signal at the zero frequency. The width of the signal is surprisingly large: 1 GHz. This means that in the residual plots, the part to be mistrusted is the central part in a $\pm$ 500MHz area.

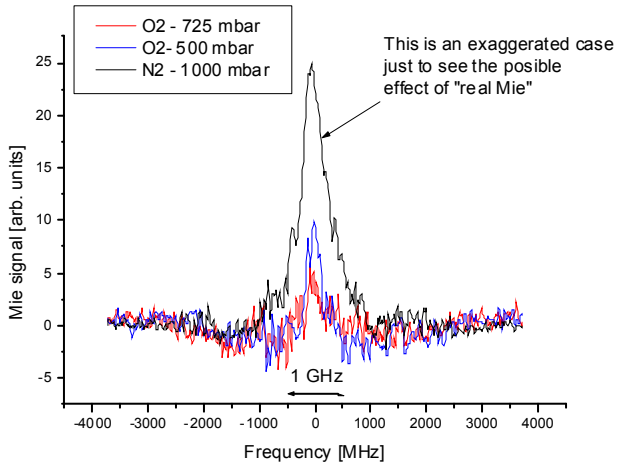

Figure 6-9: Characterization of the generated OCW signal on the experiment. The spectral width of the OCW signal is remarkably large, affecting the central frequencies up to 1GHz. All curves were obtained subtracting the signal without OCW peak to the signal with OCW peak, and renormalizing. The curve in black was obtained when the cell was not shielded from the scattering from the optics in the enhancing cavity. The curves in red and blue are the effect of the laser slightly touching the walls of the inside of the cell.

6.6.5 Asymmetry of the SRB shapes

The first measurements performed at higher pressures revealed that the measured shapes were asymmetric. The asymmetry was undetectable at lower pressures. The solution was to re-align the Fabry-Perot etalon, changing the distance of the mirrors. But if the conditions in the laboratory change drastically (summer/winter temperatures, for example) the etalon must be re-aligned again. And in some cases the asymmetry of the measured SRB shapes is only noticeable after calibration and averaging.

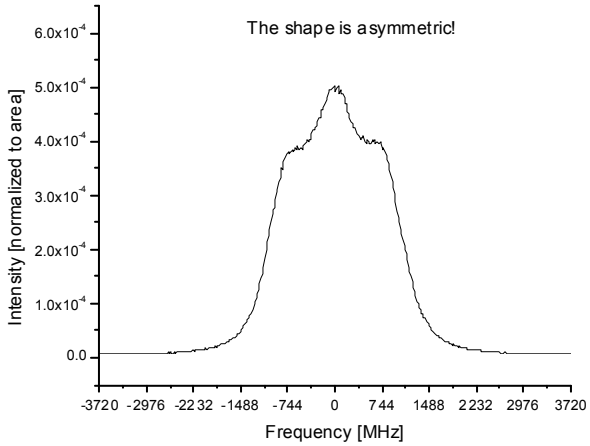

Figure 6-10: Measurement of Krypton at 3000 mbar. The obtained shape is asymmetric; the left shoulder is lower than the right shoulder of the Brillouin peaks.

6.6.6 Background issues

For some measurements, in particular those performed with Oxygen gas, the prediction of the background given by the Tenti model and the background measured differ greatly. This affects the procedures to compare the model with the measurement. The origin of this background mismatch is not well understood, but it might be related to effects of polarization (see section 7.6).

Due to the background mismatch, the new version of the Tenti program (see section 10) has the feature that it compares the model with a measurement, and it matches the level of the background of the model to be equal with the measurement. Afterwards, the model is re-normalized to area 1. As it can be seen in Figure 6-11, once the background of the model is matched to the background of the measurement, the modeled shape coincides very well with the measured one.

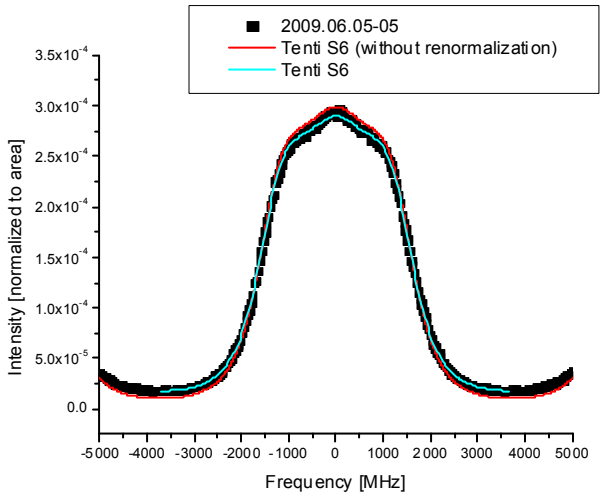

Figure 6-11: Measurement of O_2 at 2000mbar. The model predicts a background level below the measured one; as a consequence, the normalization of the signal makes it appear higher. The curve in red is the model without re-normalization, the curve in blue is the same model, but the curve has been re-normalized to match the background of the measured signal.

6.7 Measurements normalization procedure

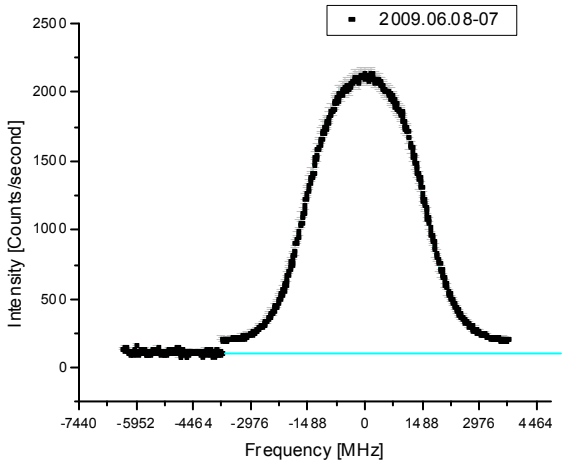

Figure 6-12: All measurements are taken in units of counts (from the Photo-Multiplier Tube) per second. The error bars are shown for the y scale, for the x-scale the error bars are smaller than the points. The main contribution to the noise in the intensity is proportional to the square-root of the counts (see section 5.8.2 for more details on the noise). Therefore it is expected a greater noise on the top of the signal than on the wings, and the contribution of the noise will be different for each measurement (for each intensity). In this case, the maximum contribution of the noise of the intensity is 2.4%, and its average contribution is 1.4%. The frequency maximum uncertainty is 0.08%. The line indicates the place where the zero will be placed.

The normalization is done as follows:

1. The dark count of the PMT is measured at the beginning of the measurement (and sometimes at the end also). The mean of the dark counts are subtracted from the averaged SRBS shape. Therefore, the dark counts set the new “zero”.
2. The area under the curve is integrated in the frequency interval [-3720, 3720] MHz. The curve is normalized to area 1.

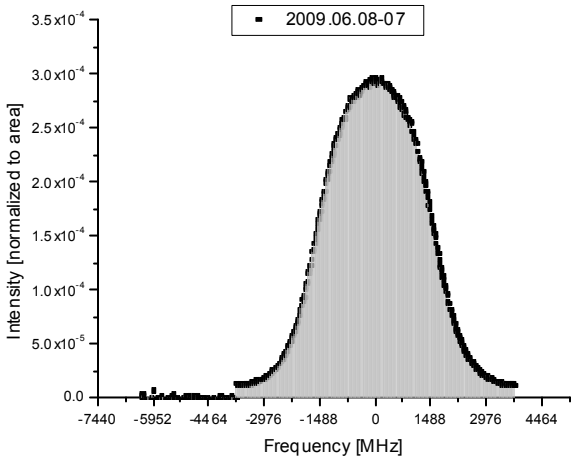

Figure 6-13: Illustration of the normalization procedure.

From the normalization procedure we can deduce:

- The dark count value is important, as it sets the value for the zero and it has an influence on the normalization procedure;
- Any deviation on the dark count will affect how the signal looks and how we compare it to the model.

7 Science measurements SRBS

All the measurements presented below are measured at ambient temperature, unless stated otherwise.

Repeatability: comparison between measurements

In the case that there is more than one measurement, at approximately the same conditions (i.e, ambient temperature, 1 bar) a comparison between the measurements was performed, to have an estimation of the repeatability.
In each case a measurement was chosen (and set in bold in the table) and the difference between measurements was calculated as:

$$\text{Residual Plot} = \frac{y_{\text{measurement}} - y_{\text{chosen}}}{\max(y_{\text{chosen}})}$$

where $y_{measurement}$ are the values of the measurements and y_{chosen} the values of the "chosen" measurement to compare to. All the measurements are taken after normalization and with the background re-set to be equal for all of them.

7.1 Nitrogen (N_2)

7.1.1 N_2- 300 mbar

For the 300 mbar setting, only one measurement was taken, so no repeatability test was done.

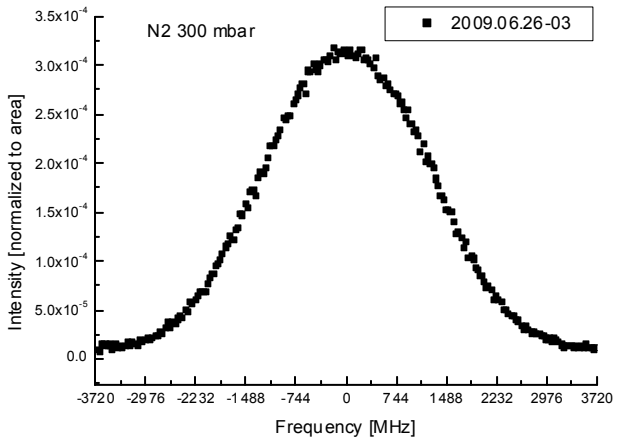

Figure 7-1: To compare different measurements, in which the intensity may vary, the intensity scale is normalized to area equal to one.

Table 7.1: Measurements performed, with their conditions specified. The uncertainty in the temperature is 0.5 K, on the pressure it can amount up to 20 mbar.

Scan (date)	λ (nm)	T (K)	P (mbar)	Points per curve	Number of peaks scanned	Max. intensity (counts/s)	Asymm.	Noise (max)	Noise (aver)
scan20090626_03	366.50	298.6	300	320	13	690	0.8%	4.7%	2.7%

7.1.2 N_2- 500 mbar

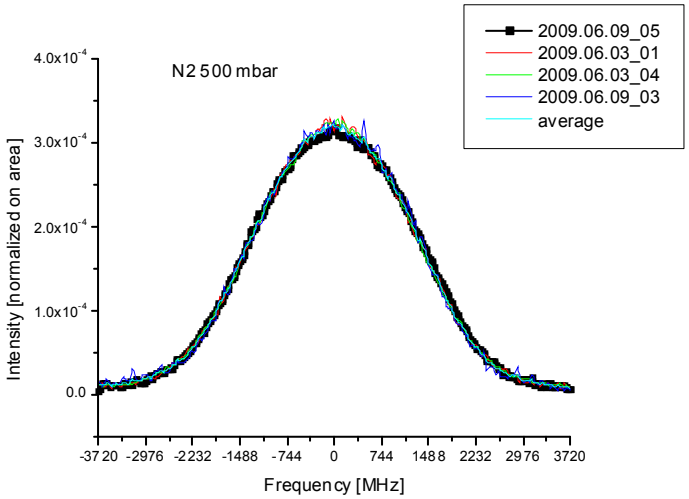

Figure 7-2: To compare different measurements, in which the intensity may vary, the intensity scale is normalized to area equal to one.

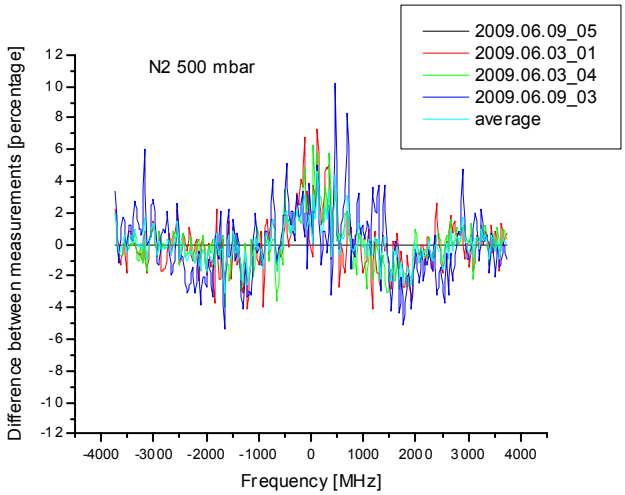

Figure 7-3: Residual plots of the difference between the measurements (and the average), in percentage of the amount of (normalized) signal.

Table 7.2: Measurements performed, with their conditions specified. The uncertainty in the temperature is 0.5 K, on the pressure it can amount up to 20 mbar. The measurement chosen for comparison with the rest of the measurements is marked in bold.

Scan (date)	λ (nm)	T (K)	P (mbar)	Points per curve	Number of peaks scanned	Max. intensity (counts/s)	Asymm.	Noise (max)	Noise (aver)
scan20090603_01	366.42	296.7	507.5	200	8	1046	0.6%	3.5%	1.8%
scan20090603_04	366.52	297.3	510.2	200	18	1010	0.9%	3.6%	1.8%
scan20090609_03	366.50	296.4	545	200	5	1040	1.8%	3.6%	2.0%
scan20090609_05	**366.50**	**296.4**	**545**	**200**	**23**	**915**	**0.5%**	**3.9%**	**2.2%**

7.1.3 N_2- 725 mbar

For the 725 mbar setting, only one measurement was taken, so no repeatability test was done.

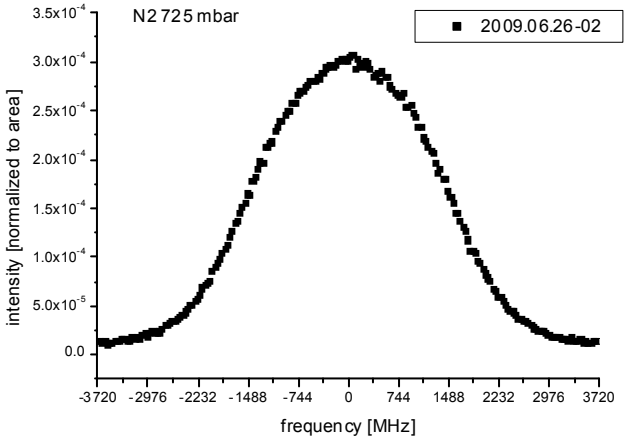

Figure 7-4: To compare different measurements, in which the intensity may vary, the intensity scale is normalized to area equal to one.

Table 7.3: Measurements performed, with their conditions specified. The uncertainty in the temperature is 0.5 K, on the pressure it can amount up to 20 mbar.

Scan (date)	λ (nm)	T (K)	P (mbar)	Points per curve	Number of peaks scanned	Max. intensity (counts/s)	Asymm.	Noise (max)	Noise (aver)
scan20090626_02	366.50	298.6	725	200	13	1410	0.5%	3.0%	1.6%

7.1.4 N_2- 1000 mbar

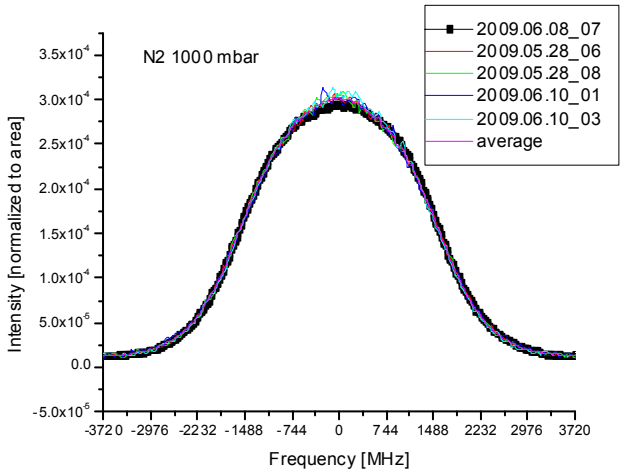

Figure 7-5: To compare different measurements, in which the intensity may vary, the intensity scale is normalized to area equal to one.

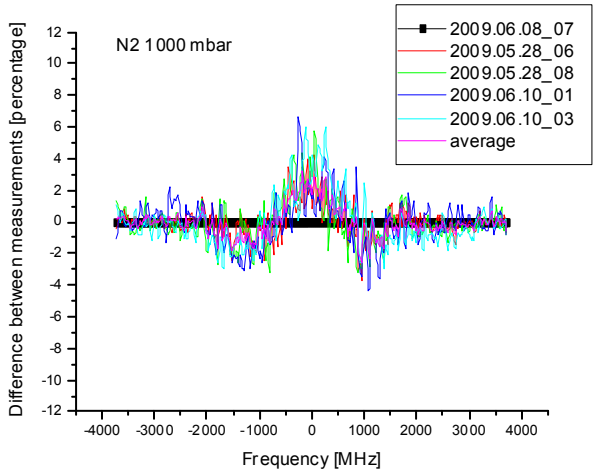

Figure 7-6: Residual plots of the difference between the measurements (and the average), in percentage of the amount of (normalized) signal.

A few of the earlier measurements (scan20090528 and scan20090529) seem to have “a few more counts” on the zero of the frequency axis (coinciding with the frequency of the laser). This difference is still in the deviation of the error-bars, although it seems consistent. See the discussion of this topic in Section 6.6.2. For one measurement (scan20090602_05), this problem is extreme.

Table 7.4: Measurements performed, with their conditions specified. The uncertainty in the temperature is 0.5 K, on the pressure it can amount up to 20 mbar. The measurement chosen for comparison with the rest of the measurements is marked in bold.

Scan (date)	λ (nm)	T (K)	P (mbar)	Points per curve	Number of peaks scanned	Max. intensity (counts/s)	Asymm.	Noise (max)	Noise (aver)
scan20090528_06	366.25	297.4	1089	200	25	1878	0.3%	2.5%	1.4%
scan20090528_08	366.25	297.4	1089	200	6	1871	1.5%	2.5%	1.4%
scan20090608_07	**366.51**	**297.2**	**1080**	**400**	**20**	**2114**	**0.8%**	**2.4%**	**1.4%**
scan20090610_01	366.50	296.0	1050	160	5	1317	0.8%	3.0%	1.6%
scan20090610_03	366.50	296.0	1050	160	16	951	0.6%	3.8%	2.1%
scan20090602_05 OCW contaminated	366.45	298.4	1062.5	200	10	2100	0.2%	2.4%	1.2%

7.1.5 N_2- 1250 mbar

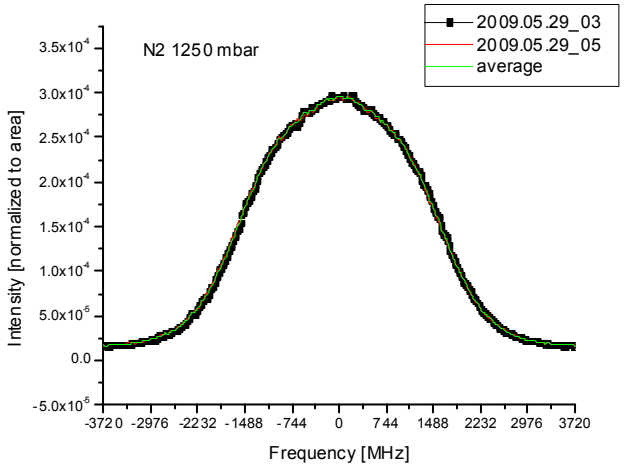

Figure 7-7: To compare different measurements, in which the intensity may vary, the intensity scale is normalized to area equal to one.

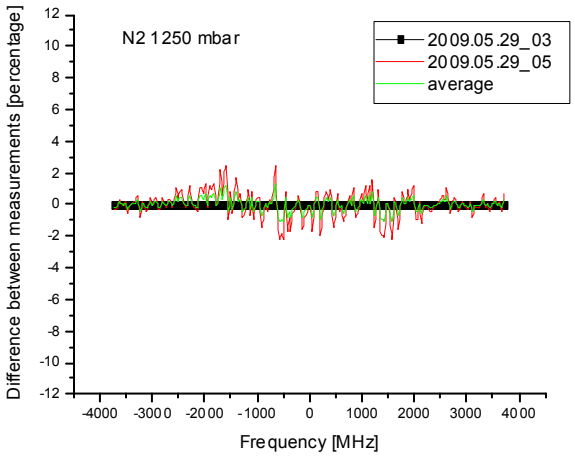

Figure 7-8: Residual plots of the difference between the measurements (and the average), in percentage of the amount of (normalized) signal.

Table 7.5: Measurements performed, with their conditions specified. The uncertainty in the temperature is 0.5 K, on the pressure it can amount up to 20 mbar. The measurement chosen for comparison with the rest of the measurements is marked in bold.

Scan (date)	λ (nm)	T (K)	P (mbar)	Points per curve	Number of peaks scanned	Max. intensity (counts/s)	Asymm.	Noise (max)	Noise (aver)
scan20090529_03	**366.26**	**296.5**	**1250**	**200**	**24**	**1747**	**0.9%**	**2.6%**	**1.4%**
scan20090529_05	366.26	296.5	1250	200	27	1841	0.6%	2.5%	1.4%

7.1.6 N_2- 2000 mbar

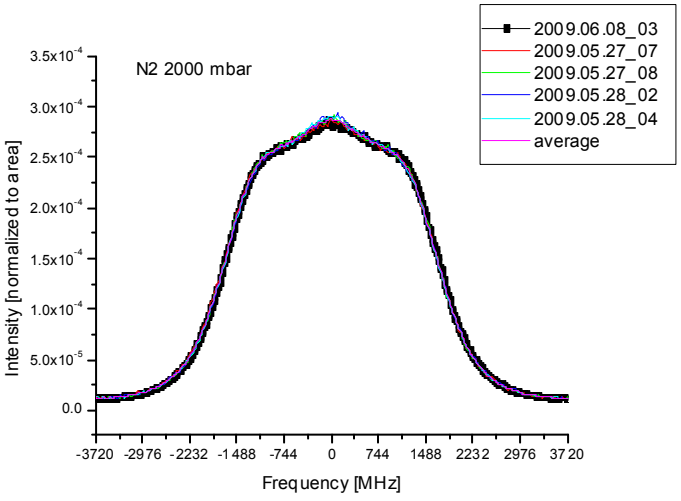

Figure 7-9: To compare different measurements, in which the intensity may vary, the intensity scale is normalized to area equal to one.

Here again seems to be “a few more counts” for the frequencies close to the laser frequency (also on the earlier measurements: scan20090527-scan20090528). See Section 6.6.2 for a discussion on this topic.

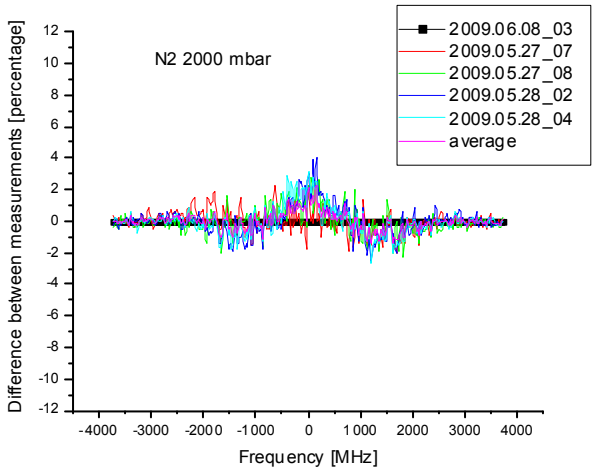

Figure 7-10: Residual plots of the difference between the measurements (and the average), in percentage of the amount of (normalized) signal.

Table 7.6: Measurements performed, with their conditions specified. The uncertainty in the temperature is 0.5 K, on the pressure it can amount up to 20 mbar. The measurement chosen for comparison with the rest of the measurements is marked in bold.

Scan (date)	λ (nm)	T (K)	P (mbar)	Points per curve	Number of peaks scanned	Max. intensity (counts/s)	Asymm.	Noise (max)	Noise (aver)
scan20090527_07	366.25	297.4	2012	400	8	3336	1.1%	1.9%	1.1%
scan20090527_08	366.25	297.4	2012	320	5	3274	0.3%	1.8%	1.0%
scan20090528_02	366.25	297.4	2054	200	10	3143	0.7%	1.9%	1.0%
scan20090528_04	366.25	297.4	2054	200	21	3450	0.2%	1.8%	1.0%
scan20090608_03	**366.51**	**295.5**	**2066**	**400**	**20**	**3411**	**0.4%**	**1.8%**	**1.0%**

7.1.7 N2- 2500 mbar

For the 2500 mbar setting, only one measurement was taken, so no repeatability test was done.

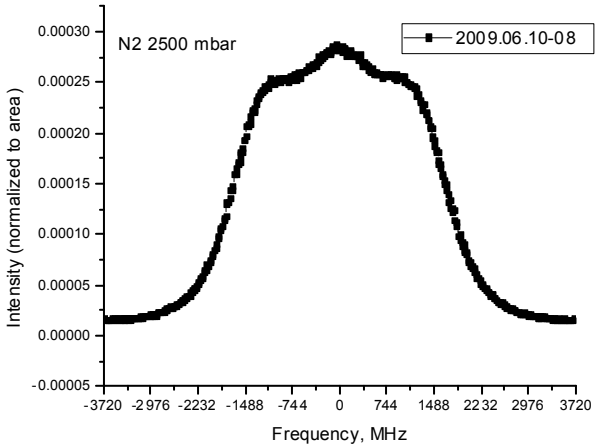

Figure 7-11: To compare different measurements, in which the intensity may vary, the intensity scale is normalized to area equal to one.

Table 7.7: Measurements performed, with their conditions specified. The uncertainty in the temperature is 0.5 K, on the pressure it can amount up to 20 mbar.

Scan (date)	λ (nm)	T (K)	P (mbar)	Points per curve	Number of peaks scanned	Max. intensity (counts/s)	Asymm.	Noise (max)	Noise (aver)
scan20090610_08	366.50	297.7	2538	400	13	3929	2.2%	1.7%	1.0%

7.1.8 N_2- 3000 mbar

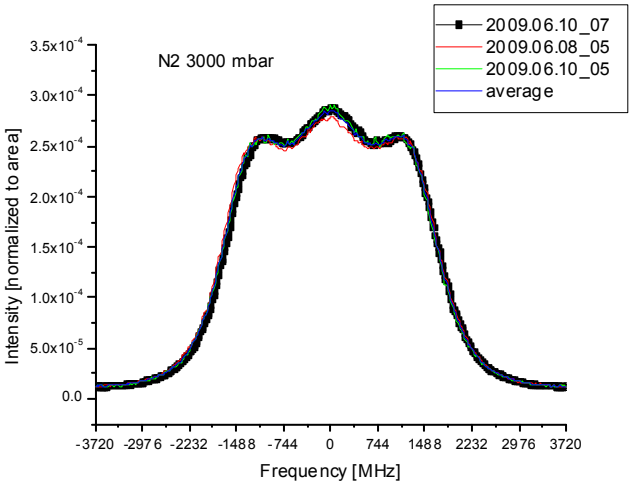

Figure 7-12: To compare different measurements, in which the intensity may vary, the intensity scale is normalized to area equal to one.

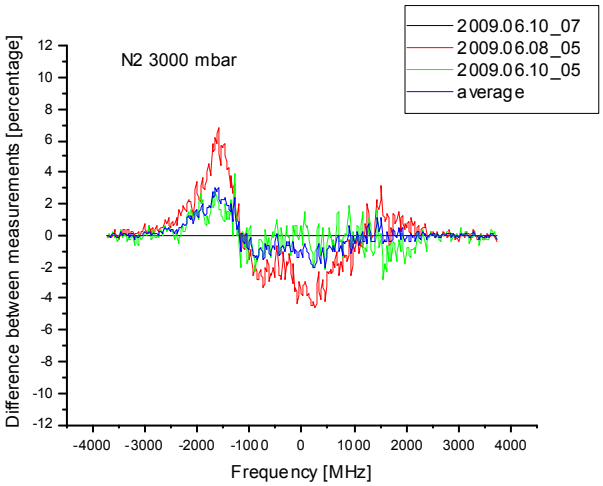

Figure 7-13: Residual plots of the difference between the measurements (and the average), in percentage of the amount of (normalized) signal.

Table 7.8: Measurements performed, with their conditions specified. The uncertainty in the temperature is 0.5 K, on the pressure it can amount up to 20 mbar. The measurement chosen for comparison with the rest of the measurements is marked in bold.

Scan (date)	λ (nm)	T (K)	P (mbar)	Points per curve	Number of peaks scanned	Max. intensity (counts/s)	Asymm.	Noise (max)	Noise (aver)
scan20090608_05	366.51	296.9	3030	200	12	4697	2.8%	1.5%	0.9%
scan20090610_05	366.50	297.1	3030	320	14	2360	1.4%	2.2%	1.1%
scan20090610_07	**366.50**	**297.1**	**3030**	**400**	**14**	**3688**	**1.2%**	**1.7%**	**1.0%**

7.1.9 N_2- 3500 mbar

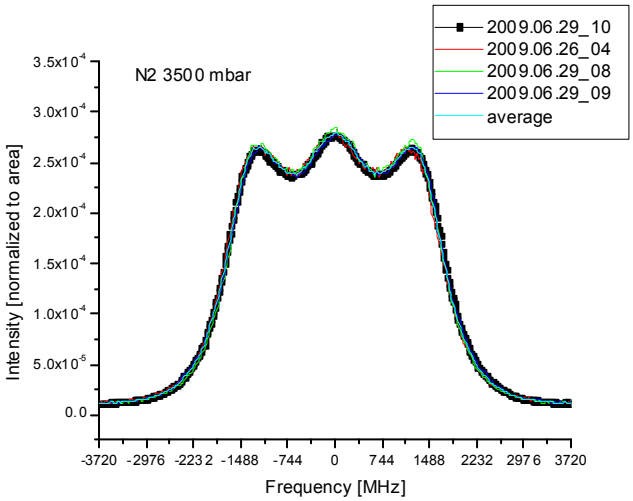

Figure 7-14: To compare different measurements, in which the intensity may vary, the intensity scale is normalized to area equal to one.

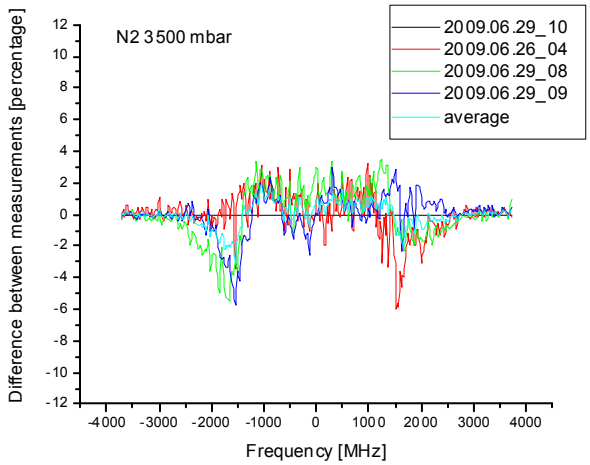

Figure 7-15: Residual plots of the difference between the measurements (and the average), in percentage of the amount of (normalized) signal.

Table 7.9: Measurements performed, with their conditions specified. The uncertainty in the temperature is 0.5 K, on the pressure it can amount up to 20 mbar. The measurement chosen for comparison with the rest of the measurements is marked in bold.

Scan (date)	λ (nm)	T (K)	P (mbar)	Points per curve	Number of peaks scanned	Max. intensity (counts/s)	Asymm.	Noise (max)	Noise (aver)
scan20090626_04	366.50	300.4	3500	200	3	5371	4.3%	1.4%	0.8%
scan20090629_08	366.49	300.4	3500	200	5	5630	0.8%	1.4%	0.7%
scan20090629_09	366.49	300.4	3500	200	8	6428	2.7%	1.3%	0.7%
scan20090629_10	**366.50**	**299.4**	**3500**	**200**	**13**	**6650**	**1.2%**	**1.3%**	**0.7%**

7.2 Oxygen (O_2)

7.2.1 O_2- 300 mbar

For the 300 mbar setting, only one measurement was taken, so no repeatability test was done.

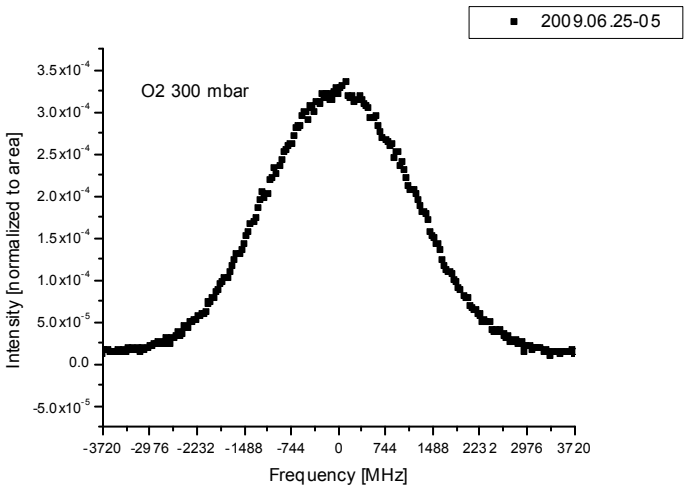

Figure 7-16: To compare different measurements, in which the intensity may vary, the intensity scale is normalized to area equal to one.

Table 7.10: Measurements performed, with their conditions specified. The uncertainty in the temperature is 0.5 K, on the pressure it can amount up to 20 mbar.

Scan (date)	λ (nm)	T (K)	P (mbar)	Points per curve	Number of peaks scanned	Max. intensity (counts/s)	Asymm.	Noise (max)	Noise (aver)
scan20090625_05	366.51	298.0	300	200	18	679	0.6%	4.8%	2.7%

7.2.2 O_2- 500 mbar

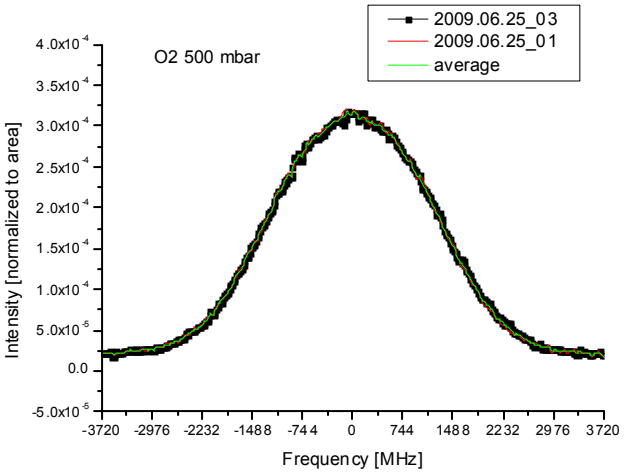

Figure 7-17: To compare different measurements, in which the intensity may vary, the intensity scale is normalized to area equal to one.

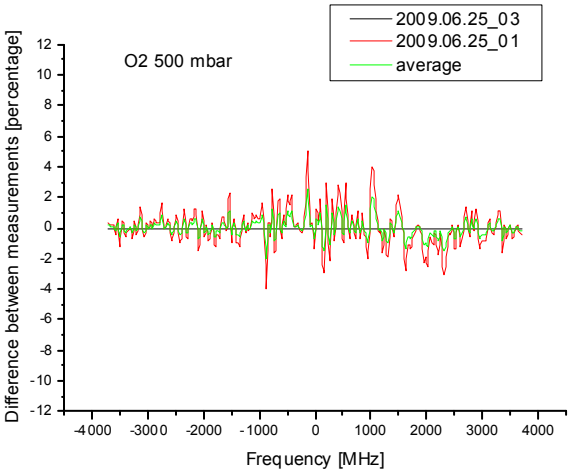

Figure 7-18: Residual plots of the difference between the measurements (and the average), in percentage of the amount of (normalized) signal.

Table 7.11: Measurements performed, with their conditions specified. The uncertainty in the temperature is 0.5 K, on the pressure it can amount up to 20 mbar. The measurement chosen for comparison with the rest of the measurements is marked in bold.

Scan (date)	λ (nm)	T (K)	P (mbar)	Points per curve	Number of peaks scanned	Max. intensity (counts/s)	Asymm.	Noise (max)	Noise (aver)
scan20090625_01	366.50	298.0	500	160	11	1013	0.6%	3.6%	1.9%
scan20090625_03	**366.50**	**298.0**	**500**	**200**	**13**	**1229**	**0.7%**	**3.3%**	**1.9%**
scan20090624_02 OCW contaminated	366.51	297.9	500	200	21	1131	0.3%	3.3%	1.7%

7.2.3 O_2- 725 mbar

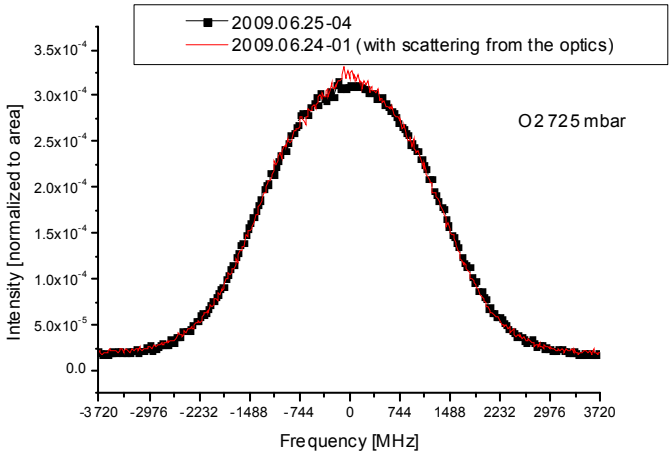

Figure 7-19: To compare different measurements, in which the intensity may vary, the intensity scale is normalized to area equal to one.

The measurement of the 2009.06.24 presents scattering from the optics and cell walls (OCW). See section 6.6.2 for more information of this topic.

Table 7.12: Measurements performed, with their conditions specified. The uncertainty in the temperature is 0.5 K, on the pressure it can amount up to 20 mbar. The measurement chosen for comparison with the rest of the measurements is marked in bold.

Scan (date)	λ (nm)	T (K)	P (mbar)	Points per curve	Number of peaks scanned	Max. intensity (counts/s)	Asymm.	Noise (max)	Noise (aver)
scan20090625_04	**366.51**	**298.0**	**725**	**200**	**13**	**1400**	**0.9%**	**3.0%**	**1.6%**
scan20090624_01 OCW contaminated	366.51	297.9	725	400	10	1554	1.0%	2.8%	1.6%

7.2.4 O_2- 1000 mbar

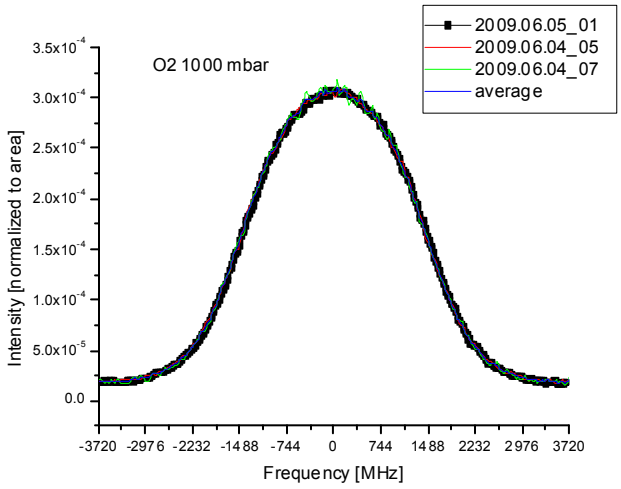

Figure 7-20: To compare different measurements, in which the intensity may vary, the intensity scale is normalized to area equal to one.

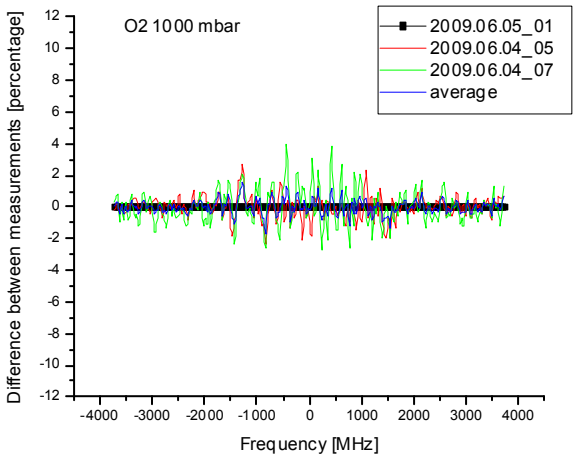

Figure 7-21: Residual plots of the difference between the measurements (and the average), in percentage of the amount of (normalized) signal.

Table 7.13: Measurements performed, with their conditions specified. The uncertainty in the temperature is 0.5 K, on the pressure it can amount up to 20 mbar. The measurement chosen for comparison with the rest of the measurements is marked in bold.

Scan (date)	λ (nm)	T (K)	P (mbar)	Points per curve	Number of peaks scanned	Max. intensity (counts/s)	Asymm.	Noise (max)	Noise (aver)
scan20090604_05	366.52	298.4	1001	160	10	1661	0.6%	2.7%	1.4%
scan20090604_07	366.52	297.4	1001.5	200	2	2684	0.5%	2.7%	1.4%
scan20090605_01	**366.52**	**295.5**	**990.7**	**200**	**23**	**1687**	**0.5%**	**2.7%**	**1.4%**

7.2.5 O_2- 2000 mbar

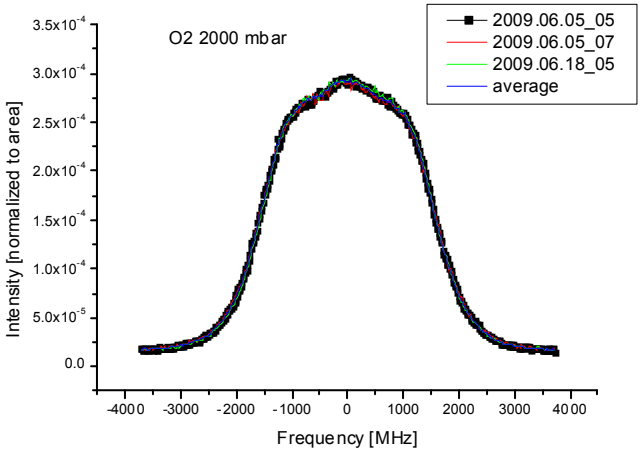

Figure 7-22: To compare different measurements, in which the intensity may vary, the intensity scale is normalized to area equal to one.

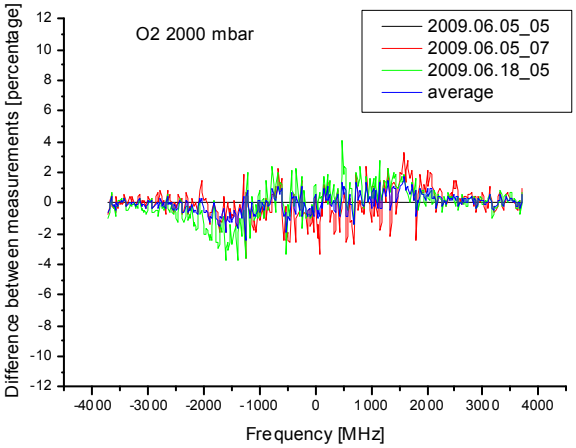

Figure 7-23: Residual plots of the difference between the measurements (and the average), in percentage of the amount of (normalized) signal.

Table 7.14: Measurements performed, with their conditions specified. The uncertainty in the temperature is 0.5 K, on the pressure it can amount up to 20 mbar. The measurement chosen for comparison with the rest of the measurements is marked in bold.

Scan (date)	λ (nm)	T (K)	P (mbar)	Points per curve	Number of peaks scanned	Max. intensity (counts/s)	Asymm.	Noise (max)	Noise (aver)
scan20090605_05	**366.52**	**296.7**	**2035**	**320**	**8**	**2942**	**2.0%**	**2.0%**	**1.1%**
scan20090605_07	366.52	296.7	2035	200	6	2764	0.3%	2.0%	1.1%
scan20090618_05	366.52	297.6	2000	400	14	2010	1.2%	2.4%	1.4%

7.2.6 O_2- 2500 mbar

For the 2500 mbar setting, only one measurement was taken, so no repeatability test was done.

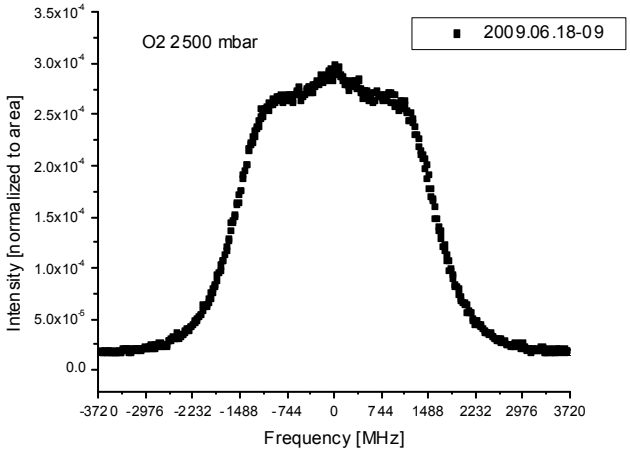

Figure 7-24: To compare different measurements, in which the intensity may vary, the intensity scale is normalized to area equal to one.

Table 7.15: Measurements performed, with their conditions specified. The uncertainty in the temperature is 0.5 K, on the pressure it can amount up to 20 mbar.

Scan (date)	λ (nm)	T (K)	P (mbar)	Points per curve	Number of peaks scanned	Max. intensity (counts/s)	Asymm.	Noise (max)	Noise (aver)
scan20090618_09	366.51	299.1	2495	400	7	1621	1.3%	2.7%	1.6%

7.2.7 O_2- 3000 mbar

For the 3000 mbar setting, only one measurement was taken, so no repeatability test was done.

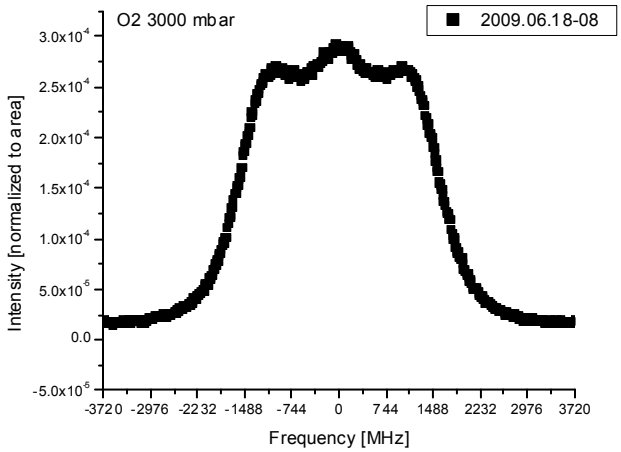

Figure 7-25: To compare different measurements, in which the intensity may vary, the intensity scale is normalized to area equal to one.

Table 7.16: Measurements performed, with their conditions specified. The uncertainty in the temperature is 0.5 K, on the pressure it can amount up to 20 mbar.

Scan (date)	λ (nm)	T (K)	P (mbar)	Points per curve	Number of peaks scanned	Max. intensity (counts/s)	Asymm.	Noise (max)	Noise (aver)
scan20090618_08	366.51	297.6	3003	400	13	1583	0.5%	2.8%	1.7%

7.2.8 O_2- 3500 mbar

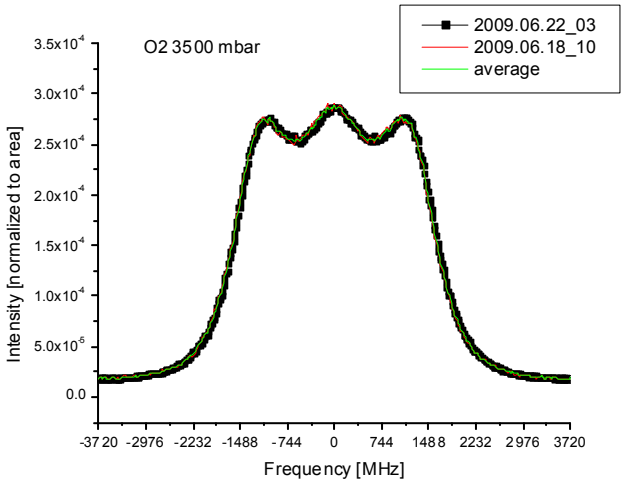

Figure 7-26: To compare different measurements, in which the intensity may vary, the intensity scale is normalized to area equal to one.

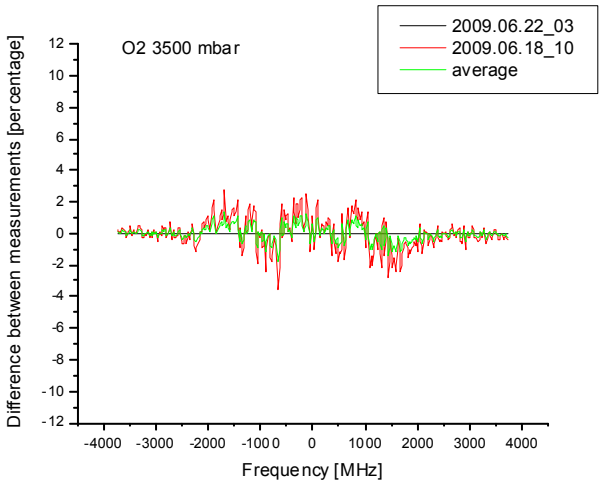

Figure 7-27: Residual plots of the difference between the measurements (and the average), in percentage of the amount of (normalized) signal.

Table 7.17: Measurements performed, with their conditions specified. The uncertainty in the temperature is 0.5 K, on the pressure it can amount up to 20 mbar. The measurement chosen for comparison with the rest of the measurements is marked in bold. The measurements with a polarizer are analyzed in section **7.6**.

Scan (date)	λ (nm)	T (K)	P (mbar)	Points per curve	Number of peaks scanned	Max. intensity (counts/s)	Asymm.	Noise (max)	Noise (aver)
scan20090618_10	366.52	299.1	3495	400	5	1952	0.9%	2.5%	1.4%
scan20090622_03	**366.51**	**297.5**	**3495**	**400**	**8**	**3941**	**0.9%**	**1.7%**	**0.9%**

7.3 (Dry) Air

For the experiment on dry air pre-mixtures of 79% pure N_2 and 21% pure O_2 were used.

7.3.1 Air- 300 mbar

For the 300 mbar setting, only one measurement was taken, so no repeatability test was done.

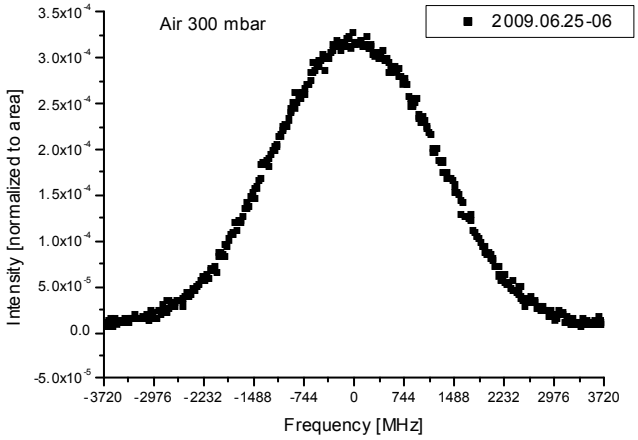

Figure 7-28: To compare different measurements, in which the intensity may vary, the intensity scale is normalized to area equal to one.

Table 7.18: Measurements performed, with their conditions specified. The uncertainty in the temperature is 0.5 K, on the pressure it can amount up to 20 mbar.

Scan (date)	λ (nm)	T (K)	P (mbar)	Points per curve	Number of peaks scanned	Max. intensity (counts/s)	Asymm.	Noise (max)	Noise (aver)
scan20090625_06	366.51	298.0	300	200	16	645	0.3%	5.0%	2.9%

7.3.2 Air- 500 mbar

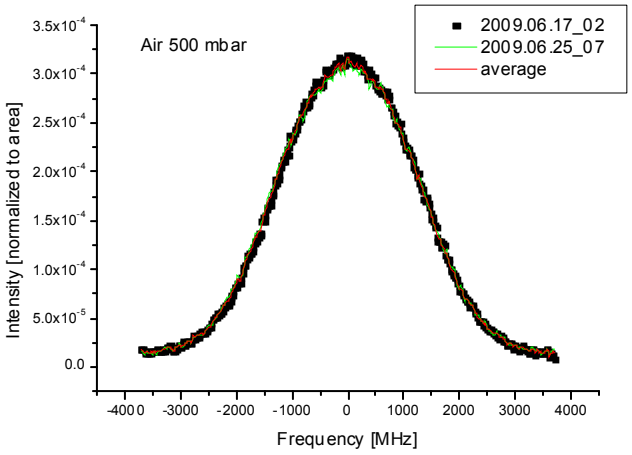

Figure 7-29: To compare different measurements, in which the intensity may vary, the intensity scale is normalized to area equal to one.

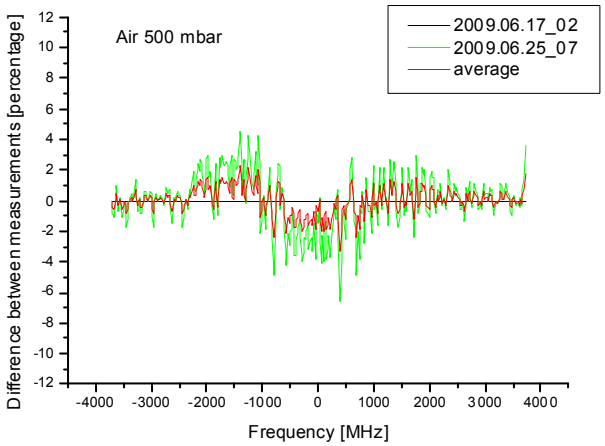

Figure 7-30: Residual plots of the difference between the measurements (and the average), in percentage of the amount of (normalized) signal.

Table 7.19: Measurements performed, with their conditions specified. The uncertainty in the temperature is 0.5 K, on the pressure it can amount up to 20 mbar. The measurement chosen for comparison with the rest of the measurements is marked in bold.

Scan (date)	λ (nm)	T (K)	P (mbar)	Points per curve	Number of peaks scanned	Max. intensity (counts/s)	Asymm.	Noise (max)	Noise (aver)
scan20090617_02	**366.53**	**298.6**	**503**	**400**	**27**	**751**	**0.5%**	**4.6%**	**2.6%**
scan20090625_07	366.51	298.0	504	200	8	962	1.3%	3.8%	2.1%
scan20091001_05 OCW contaminated	366.46	296.7	500	298	17	909	0.6%	3.9%	2.3%

7.3.3 Air- 725 mbar

For the 725 mbar setting, only one measurement was taken, so no repeatability test was done.

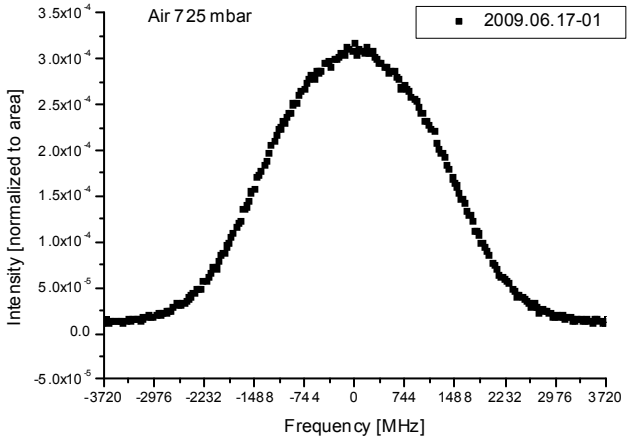

Figure 7-31: To compare different measurements, in which the intensity may vary, the intensity scale is normalized to area equal to one.

Table 7.20: Measurements performed, with their conditions specified. The uncertainty in the temperature is 0.5 K, on the pressure it can amount up to 20 mbar.

Scan (date)	λ (nm)	T (K)	P (mbar)	Points per curve	Number of peaks scanned	Max. intensity (counts/s)	Asymm.	Noise (max)	Noise (aver)
scan20090617_01	366.52	298.6	725	200	19	1007	0.4%	3.7%	2.0%

7.3.4 Air- 1000 mbar

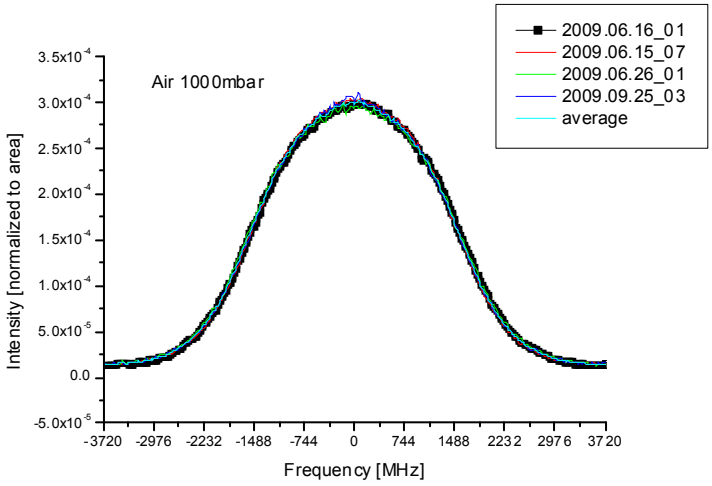

Figure 7-32: To compare different measurements, in which the intensity may vary, the intensity scale is normalized to area equal to one.

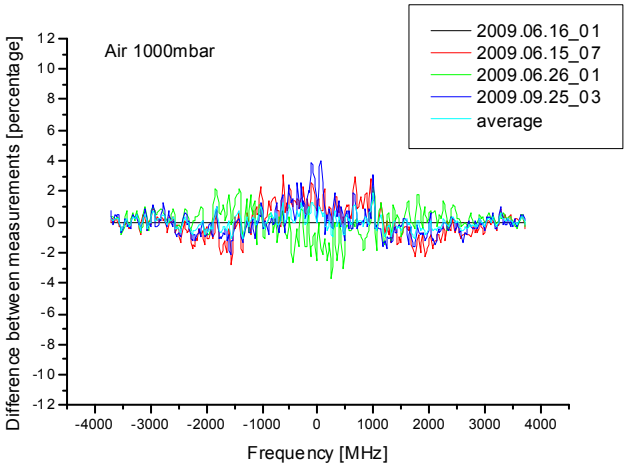

Figure 7-33: Residual plots of the difference between the measurements (and the average), in percentage of the amount of (normalized) signal.

Table 7.21: Measurements performed, with their conditions specified. The uncertainty in the temperature is 0.5 K, on the pressure it can amount up to 20 mbar. The measurement chosen for comparison with the rest of the measurements is marked in bold.

Scan (date)	λ (nm)	T (K)	P (mbar)	Points per curve	Number of peaks scanned	Max. intensity (counts/s)	Asymm.	Noise (max)	Noise (aver)
scan20090615_07	366.53	296.5	1040	400	7	1591	0.2%	2.7%	1.6%
scan20090616_01	**366.53**	**296.0**	**1040**	**160**	**16**	**1403**	**0.4%**	**3.0%**	**1.6%**
scan20090626_01	366.50	298.2	1040	200	17	1655	0.8%	2.3%	1.4%
scan20090925_03	366.46	297.2	1008	297.6	16	1403	0.4%	3.0%	1.6%

7.3.5 Air- 2000 mbar

For the 2000 mbar setting, only one measurement was taken, so no repeatability test was done.

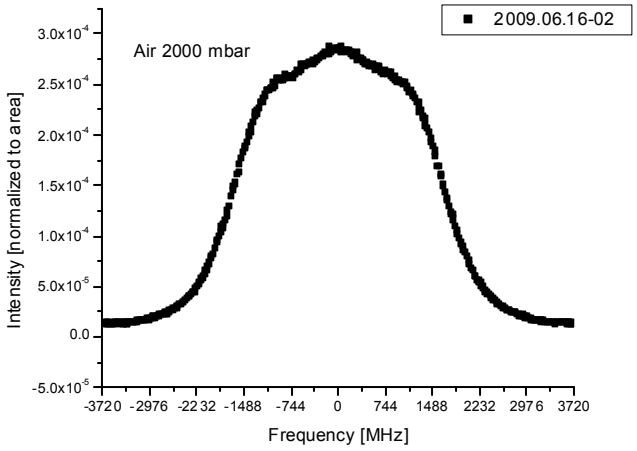

Figure 7-34: To compare different measurements, in which the intensity may vary, the intensity scale is normalized to area equal to one.

Table 7.22: Measurements performed, with their conditions specified. The uncertainty in the temperature is 0.5 K, on the pressure it can amount up to 20 mbar.

Scan (date)	λ (nm)	T (K)	P (mbar)	Points per curve	Number of peaks scanned	Max. intensity (counts/s)	Asymm.	Noise (max)	Noise (aver)
scan20090616_02	366.53	297.3	2015	320	19	2883	0.8%	2.0%	1.1%

7.3.6 Air- 2500 mbar

For the 2500 mbar setting, only one measurement was taken, so no repeatability test was done.

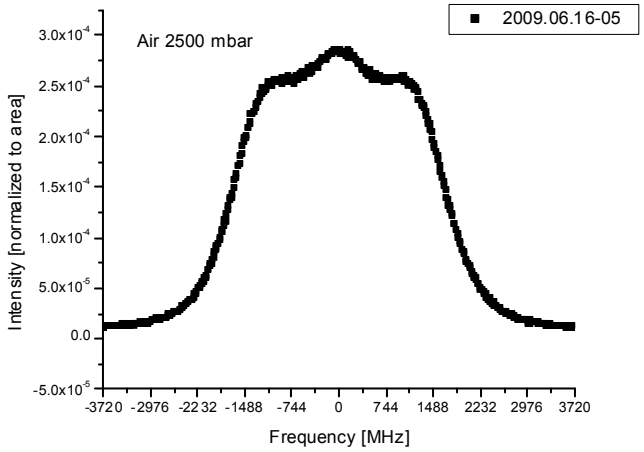

Figure 7-35: To compare different measurements, in which the intensity may vary, the intensity scale is normalized to area equal to one.

Table 7.23: Measurements performed, with their conditions specified. The uncertainty in the temperature is 0.5 K, on the pressure it can amount up to 20 mbar.

Scan (date)	λ (nm)	T (K)	P (mbar)	Points per curve	Number of peaks scanned	Max. intensity (counts/s)	Asymm.	Noise (max)	Noise (aver)
scan20090616_05	366.53	297.3	2524	400	12	2815	1.7%	2.0%	1.2%

7.3.7 Air- 3000 mbar

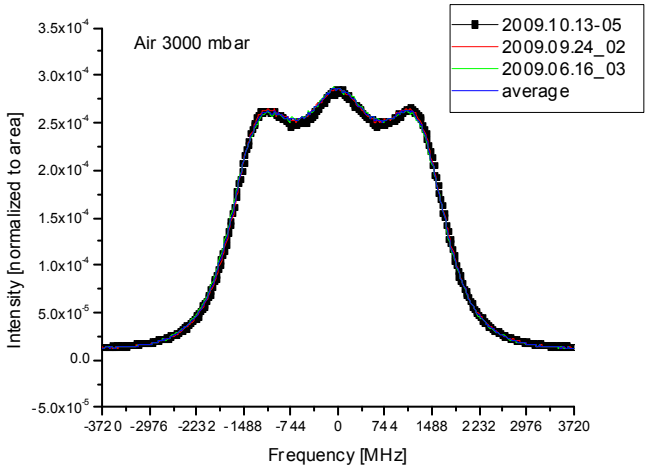

Figure 7-36: To compare different measurements, in which the intensity may vary, the intensity scale is normalized to area equal to one.

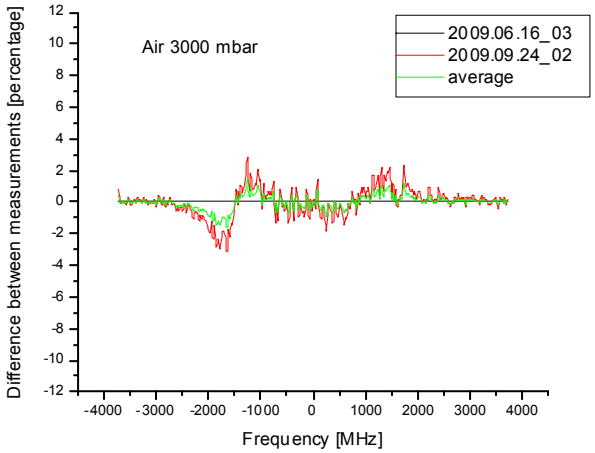

Figure 7-37: Residual plots of the difference between the measurements (and the average), in percentage of the amount of (normalized) signal.

Table 7.24: Measurements performed, with their conditions specified. The uncertainty in the temperature is 0.5 K, on the pressure it can amount up to 20 mbar. The measurement chosen for comparison with the rest of the measurements is marked in bold.

Scan (date)	λ (nm)	T (K)	P (mbar)	Points per curve	Number of peaks scanned	Max. intensity (counts/s)	Asymm.	Noise (max)	Noise (aver)
scan20090616_03	**366.53**	**297.3**	**2999**	**400**	**12**	**3665**	**1.4%**	**1.8%**	**1.0%**
scan20090924_02	366.46	297.2	3006	400	11	4961	0.9%	1.5%	0.8%
scan20091013_03	366.46	296.2	3050	320	5	4735	1.8%	1.5%	0.9%
scan20091013_05	366.46	296.2	3050	320	11	5596	0.2%	1.4%	0.7%

7.4 Temperature measurements

7.4.1 Problems with the temperature measurements

7.4.1.1 Repeatability

The measurements shown so far have been performed at ambient temperature (i.e. temperature inside the laboratory). When a measurement has been repeated after several days or even weeks, the same results have been obtained at a similar pressure, for the same gas, at ambient temperature, even after changing pressures, gases, alignment in between the two measurements. In the case of the temperature variation measurements, every time a measurement has been repeated, the resulting spectrum has changed considerably. Therefore it was concluded that some agent contaminated the scattering cell (vacuum grease, graphite, o-ring material, a previous gas used and impregnated in the cell walls…) in such amounts that it changed the composition of the scattering gas and was noticeable in the SRBS spectrum. Some measures were taken to "combat" the contamination source: the cell was heated and vacuum pumped at the same time (for a prolonged period), and if the source was some sort of impregnation in the cell walls, the repeated heating and pumping should have removed the contamination source. In spite of these efforts, the results showed no enough repeatability.

7.4.1.2 Low temperatures: going below 0° C (273 K)

In the case of the low temperature measurements two problems were encountered. The first one was that in spite of the nitrogen flushing of the enhancing cavity, the space close to the scattering cell had enough water vapor (from ambient air) to create water condensation on the scattering windows. This water vapor condensed and froze on the input windows of the scattering cell and blocked the laser light.

The second problem was that the temperature readout of the temperature sensors was contradictory (not the same). There are two temperature sensors, one mounted on top of the scattering cell (close to the Peltier coolers) and the other one is mounted on the gas inlet of the cell (far from the Peltier coolers). As it was not possible to cool the whole length of the inlet gas pipe, the readout of the temperature sensor furthest from the Peltier coolers was just slightly below ambient temperature (20° C instead of 23° C). This created a problem in the fact that the temperature of the gas is a gradient and therefore

not completely known. And because the pressure is deduced from the temperature value, using the gas law (pV=nkT), the value of the pressure is also unknown.
For the higher temperatures, it was possible to install a heater around the inlet gas pipe to the cell, and therefore as the whole volume was heated to the same temperature, the temperature sensors showed the same temperature readout.

7.4.2 Air 1000 mbar: 321 K (48° C) and 333 K (60° C)

Table 7.25: Measurements performed, with their conditions specified. The uncertainty in the temperature is 1 K. The pressure was calculated using the temperature value with the gas law (pV=nkT).

Scan (date)	λ (nm)	T (K)	P (mbar)	Points per curve	Number of peaks scanned	Max. intensity (counts/s)	Asymm.	Noise (max)	Noise (aver)
scan20090925_04	366.46	321.2	1006	320	16	1893	0.4%	0.9%	0.5%
scan20090928_02	366.46	333.2	1042	200	19	1973	0.9%	0.9%	0.4%

7.4.3 Preliminary comparison with the Tenti models S6 and S7 for air

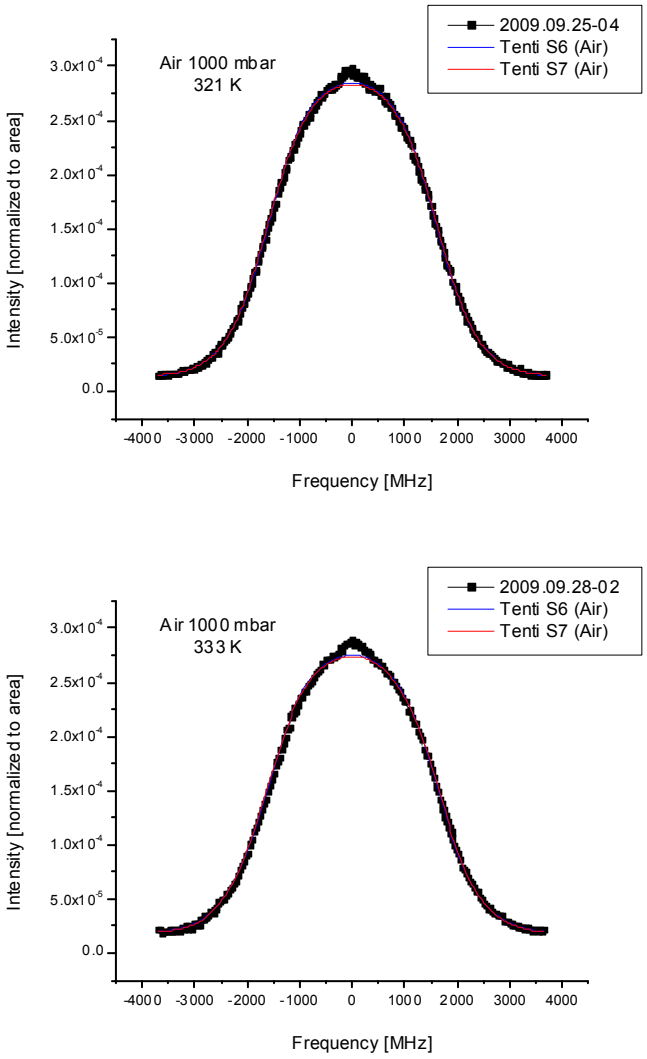

Figure 7-38: Representative measurement (in black full squares), and the calculated shape from the Tenti models: in blue the 6-moment model, in red the 7-moment model.

7.4.4 Residual plots

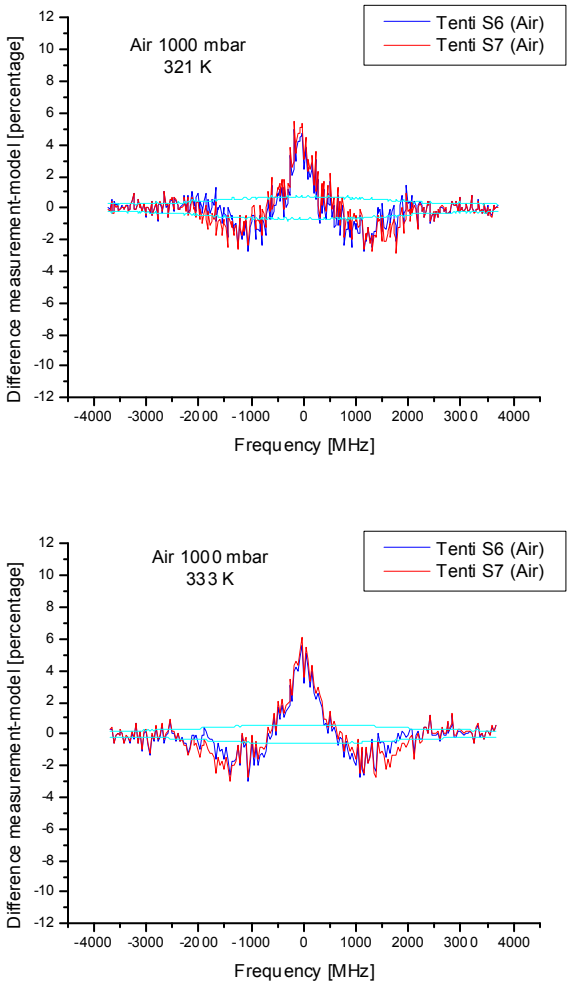

Figure 7-39: Residual plots of the difference between the measurement and the model, in percentage of the amount of (normalized) signal. The uncertainty on the intensity is shown by the two curves in light blue.

In both cases, the residual plots show a deviation of 2% for Tenti S6 on the wings and also 4% deviation at the top. For Tenti S7 the deviations are slightly larger and starting at lower frequencies for the wings.

7.4.5 Air 3000 mbar: 333 K (60° C) and low temperature (~4° C)

Table 7.26: Measurements performed, with their conditions specified. The uncertainty in the temperature is 1 K. The pressure was calculated using the temperature value with the gas law (pV=nkT).

Scan (date)	λ (nm)	T (K)	P (mbar)	Points per curve	Number of peaks scanned	Max. intensity (counts/s)	Asymm.	Noise (max)	Noise (aver)
scan20091013_04	366.46	277.2	2844	320	6	4347	0.7%	0.9%	0.4%
scan20091013_06	366.46	333.2	3431	320	6	4271	0.4%	0.8%	0.4%

Note that on the measurement performed at low temperatures, the temperature sensors showed two distinct readouts: one sensor showed 277K while the other showed 293K. See Section 7.4.1.2 for a more detailed discussion of this topic.

7.4.6 Preliminary comparison with the Tenti models S6 and S7 for air

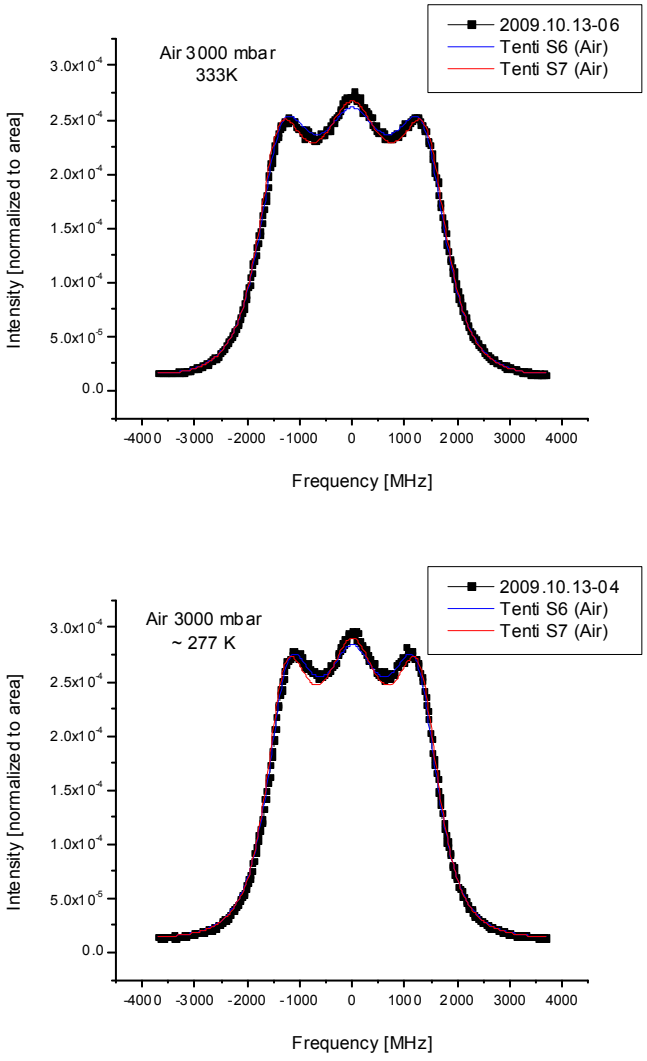

Figure 7-40: Representative measurement (in black full squares), and the calculated shape from the Tenti models: in blue the 6-moment model, in red the 7-moment model.

7.4.7 Residual plots

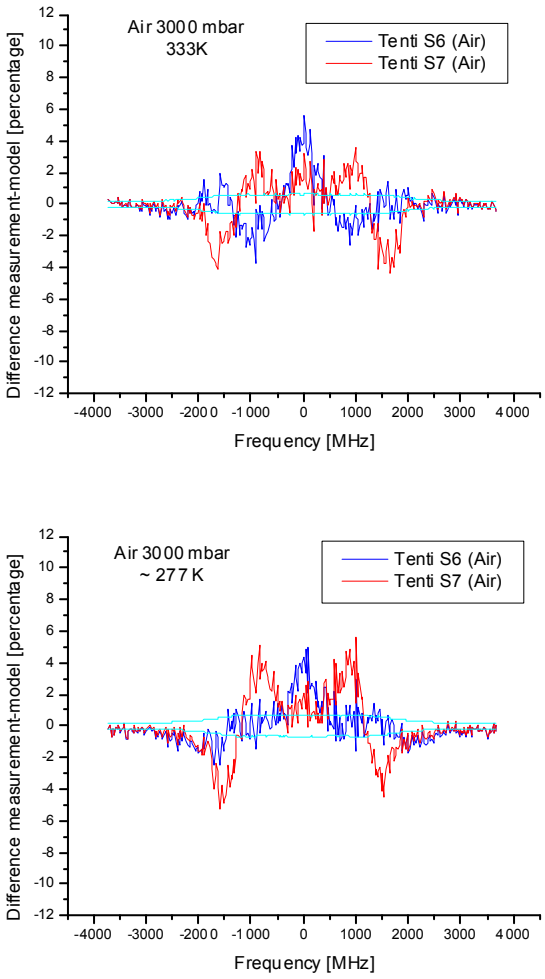

Figure 7-41: Residual plots of the difference between the measurement and the model, in percentage of the amount of (normalized) signal. The uncertainty on the intensity is shown by the two curves in light blue.

The results of the temperature measurements shown are encouraging, as the differences model-measurement are not much larger than for the measurements at ambient temperature. However, the temperature measurements had serious problems with repeatability, and therefore these results are preliminary and must be validated.

7.5 Dry and humid air measurements

Humidity measurements were performed for air at 1040 mbar. The aim was to measure at similar conditions as when humidity may play a role in the ADM-Aeolus retrieval: at sea level. There were three measurements: i) at 0% humidity, ii) when the humidity was

increasing, iii) and when there was a 100% humidity (saturated water vapor) in the cell. The humidity sensor HIH4602A was used to measure the humidity content.

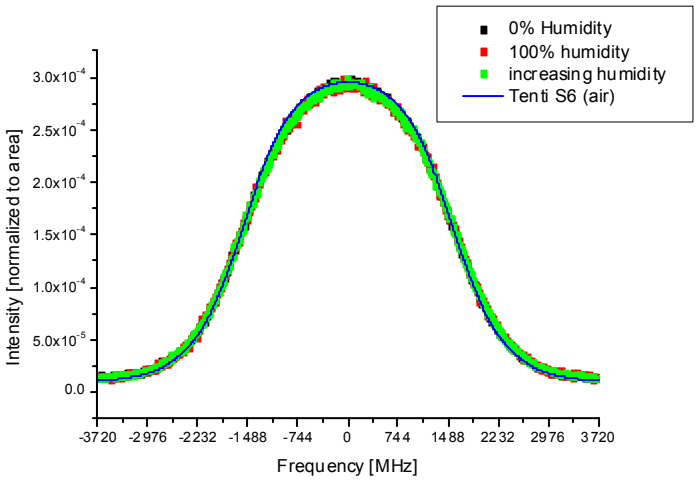

Figure 7-42: Measurements of air at 1000 mbar. The measurements were performed in the same conditions. The dry air measurement is similar to the measurements presented before. A drop of water was added into the cell and the measurement with “increasing humidity” was performed. Later a measurement with 100% humidity alone was done. The Tenti S6 model is plotted for comparison.

Table 7.27: Measurements performed, with their conditions specified. The uncertainty in the temperature is 0.5 K, on the pressure it can amount up to 20 mbar.

Scan (date)	λ (nm)	T (K)	P (mbar)	Points per curve	Number of peaks scanned	Max. intensity (counts/s)	Asymm.	Noise (max)	Noise (aver)
scan20090629_12 0% humidity	366.50	299.4	1040	200	13	1635	0.8%	2.7%	1.6%
scan20090629_13 varying humidity	366.50	301.2	1040	400	15	1976	0.5%	2.5%	1.5%
scan20090629_14 100% humidity	366.50	301.2	1040	400	8	1899	0.5%	2.5%	1.5%

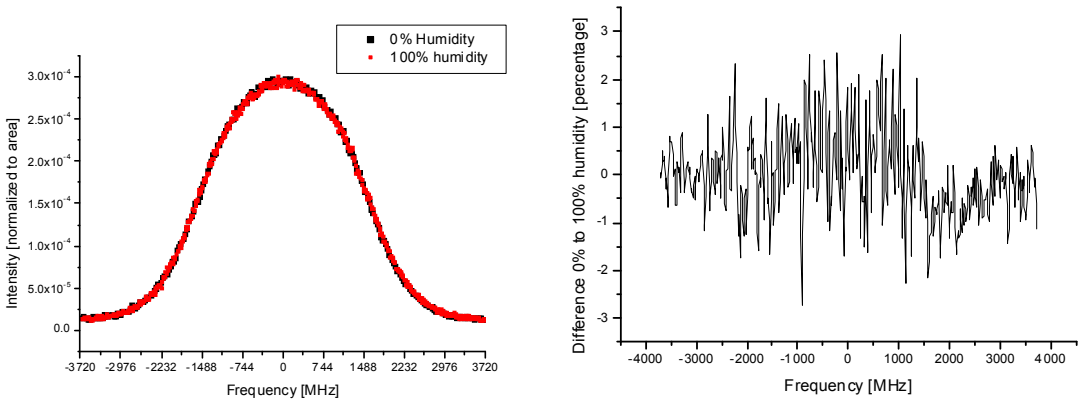

Figure 7-43: Measurements of 0% and 100% humidity alone for better comparison. The plot on the right is the difference between 0% humidity and 100% humidity, divided by the maximum value of the measurement with 0% humidity.

It can be concluded that the humidity effect in these conditions is not detectable. There are no striking differences between measurements with or without water vapor. The residual plot shows a scattering of points around zero.

7.6 Polarization effects

The ADM-Aeolus detector of the Rayleigh channel detects only the part of the light that is polarized [53]. The polarization of the scattered light is the same as the outgoing laser light polarization.

In the setup used to perform these measurements, there is only one optical component that has any influence on the light polarization. This component is the Brewster's angle windows of the scattering cell. These windows ensure that the polarization of the laser light that generates the scattered light is linearly polarized and its orientation is vertical. However, in the detection part of the setup used here, there is no polarization component, so both the polarized and depolarized parts of the scattered light are detected.

The spectrum of the depolarized light component has not been measured directly, but there is a model calculation made by Zheng [54] (See Figure 7-44). In order to assess the effect of the depolarized light on the SRBS shape measured, a measurement with a polarizer (Glann-Taylor, extinction 10^5) placed in the detection system was performed. The amount of scattered light that is depolarized can be estimated from the King factor (see section 2.9). For N_2 and air it is estimated to amount to 3-4%, and it is ca 6% for Oxygen. As O_2 presumably presents a stronger effect of the depolarized light, Oxygen was chosen to perform the polarization experiment. Because only 5% of the signal was expected to be measured at cross angles of the polarizer, the highest pressure achieved 3500 mbar, was used to account for signal loss.

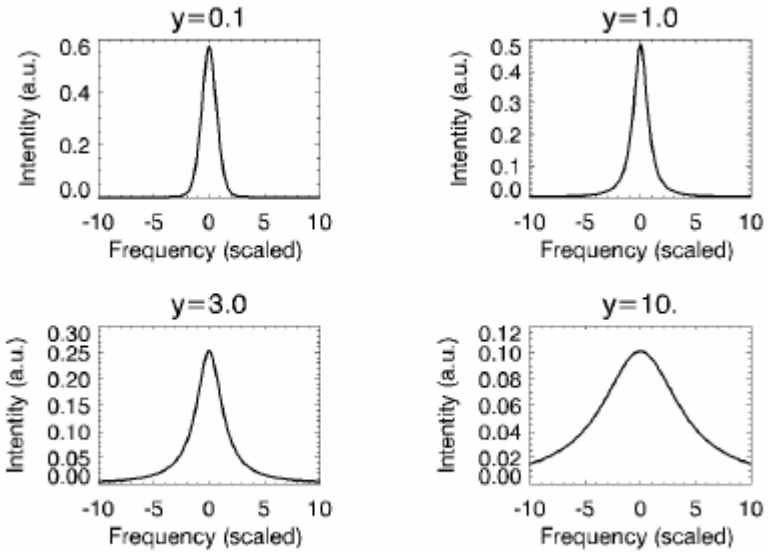

Fig. 5. Calculated depolarized Rayleigh-Brillouin scattering spectra at different y values.

Figure 7-44: Calculated spectra of the depolarized SRB scattering, at different y values. Taken from Zheng [54].

7.6.1 Results and conclusions of the polarization measurements

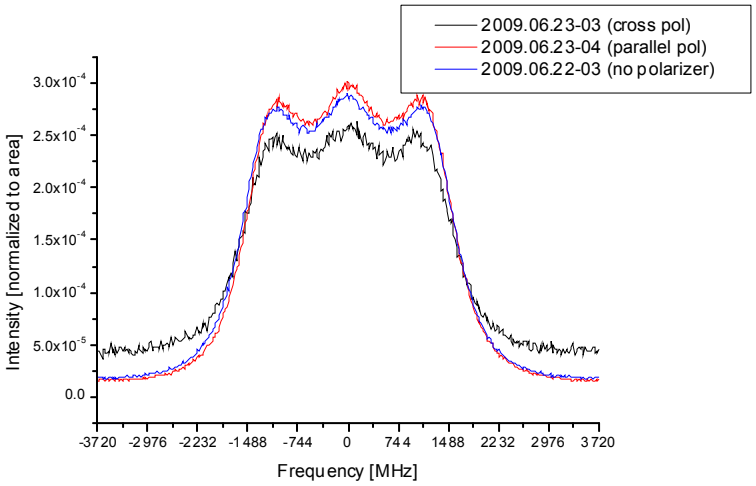

Figure 7-45: Spectra of O_2 gas at 3500 mbar and ambient temperature (the y value is 1.8154). The black curve is with a polarizer at a 90° angle with respect to the laser polarization, the red curve is with the polarizer at a 0° angle with respect to the polarization of the laser, and the blue curve is a measurement without polarizer.

Table 7.28: Measurements performed, with their conditions specified. The uncertainty in the temperature is 0.5 K, on the pressure it can amount up to 20 mbar.

Scan (date)	λ (nm)	T (K)	P (mbar)	Points per curve	Number of peaks scanned	Max. intensity (counts/s)	Asymm.	Noise (max)	Noise (aver)
scan20090622_03 no pol.	366.51	297.5	3495	400	8	3941	0.9%	1.7%	0.9%
scan20090623_03 cross pol.	366.51	297.9	3500	400	4	717	1.1%	4.4%	2.9%
scan20090623_04 parallel pol.	366.51	297.9	3500	400	5	3924	2.0%	1.7%	0.9%

The measurement with the polarizer at a 0° angle with respect to the polarization of the laser is very similar to that without polarizer, only that there are less background counts. When normalizing to area equal to unity makes the measurement to appear “higher” in the plot. The measurement with the polarizer at a 90° angle with respect to the laser polarization still is “contaminated” with the much stronger signal of the polarized scattering, but the remarkable feature of this spectrum is the disproportionally large background signal. The measurement without polarizer has the contribution of the depolarized light, and therefore its background is slightly larger. As a preliminary conclusion, the effect of the depolarized part of the spectrum seems to add a background level on the measured signal, but not change its shape in a detectable way.

7.7 Preliminary comparison with the Tenti model

We have shown that we have measured the line shapes of the RBS returns from different gases (N_2, O_2) and gas mixtures (air) at various pressures. The temperature sensors and humidity sensors were mounted inside the scattering cell and humidity dependence was measured as well. A small set of temperature measurements was obtained for air. Tables containing all the preliminary measurement-model deviations are presented below.

Table 7.29: Measurement and models as presented in previous sections, for measurements performed at different pressures and ambient temperature.

P [bar]	N2	O2	Air
0.3	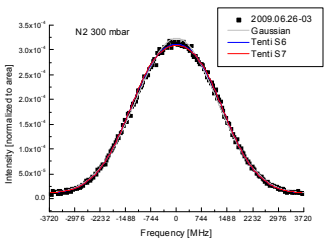	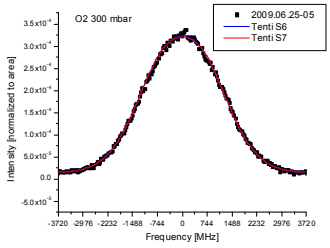	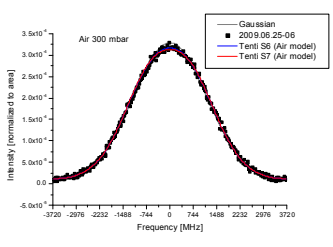

0.5	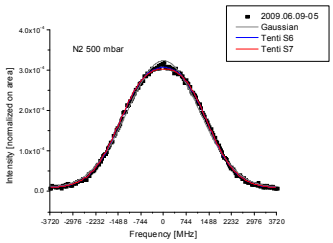 N2 500 mbar 2009.06.09-05 Gaussian Tenti S6 Tenti S7 Intensity (normalized on area) Frequency [MHz]	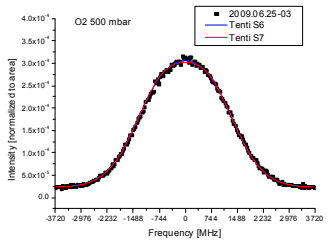 O2 500 mbar 2009.06.25-03 Tenti S6 Tenti S7 Intensity (normalized to area) Frequency [MHz]	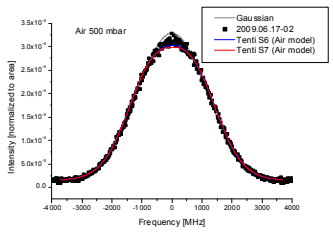 Air 500 mbar Gaussian 2009.06.17-02 Tenti S6 (Air model) Tenti S7 (Air model) Intensity (normalized to area) Frequency [MHz]
0.7	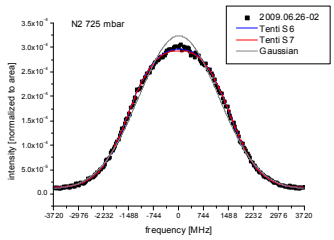 N2 725 mbar 2009.06.26-02 Tenti S6 Tenti S7 Gaussian Intensity (normalized to area) frequency [MHz]	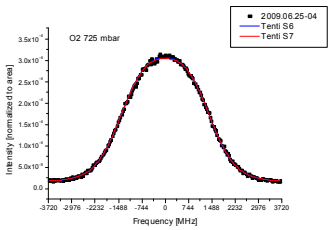 O2 725 mbar 2009.06.25-04 Tenti S6 Tenti S7 Intensity (normalized to area) Frequency [MHz]	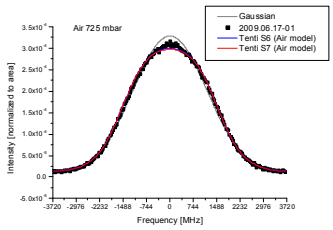 Air 725 mbar Gaussian 2009.06.17-01 Tenti S6 (Air model) Tenti S7 (Air model) Intensity (normalized to area) Frequency [MHz]
1	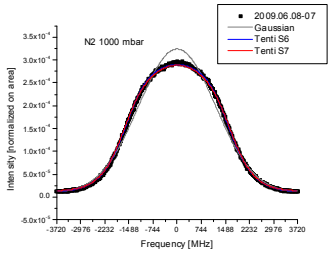 N2 1000 mbar 2009.06.08-07 Gaussian Tenti S6 Tenti S7 Intensity (normalized on area) Frequency [MHz]	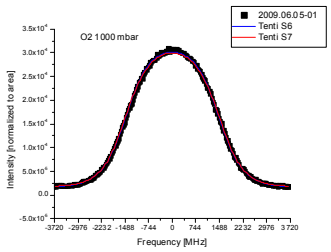 O2 1000 mbar 2009.06.05-01 Tenti S6 Tenti S7 Intensity (normalized to area) Frequency [MHz]	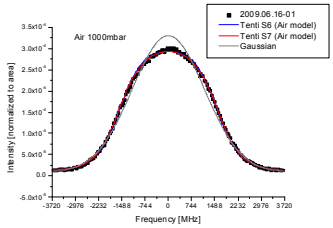 Air 1000mbar 2009.06.16-01 Tenti S6 (Air model) Tenti S7 (Air model) Gaussian Intensity (normalized to area) Frequency [MHz]
2	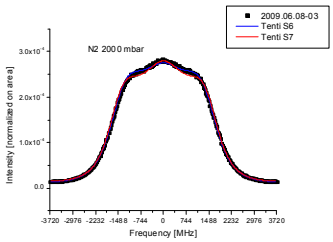 N2 2000 mbar 2009.06.08-03 Tenti S6 Tenti S7 Intensity (normalized on area) Frequency [MHz]	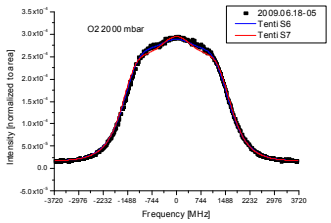 O2 2000 mbar 2009.06.18-05 Tenti S6 Tenti S7 Intensity (normalized to area) Frequency [MHz]	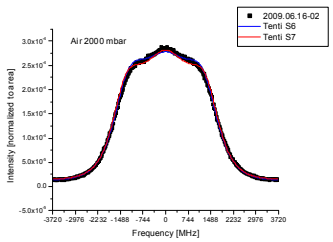 Air 2000 mbar 2009.06.16-02 Tenti S6 Tenti S7 Intensity (normalized to area) Frequency [MHz]
2.5	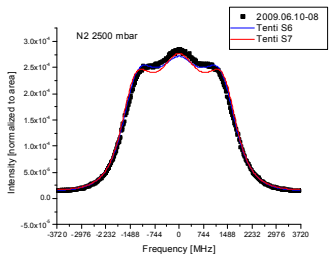 N2 2500 mbar 2009.06.10-08 Tenti S6 Tenti S7 Intensity (normalized to area) Frequency [MHz]	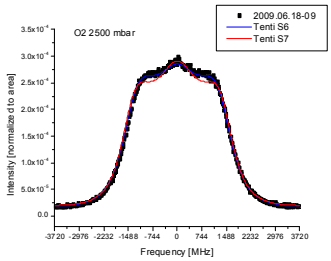 O2 2500 mbar 2009.06.18-09 Tenti S6 Tenti S7 Intensity (normalized to area) Frequency [MHz]	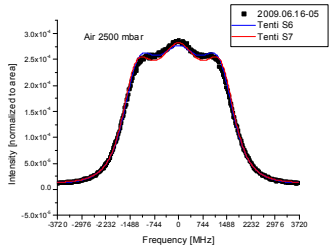 Air 2500 mbar 2009.06.16-05 Tenti S6 Tenti S7 Intensity (normalized to area) Frequency [MHz]
3	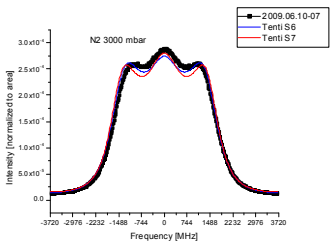 N2 3000 mbar 2009.06.10-07 Tenti S6 Tenti S7 Intensity (normalized to area) Frequency [MHz]	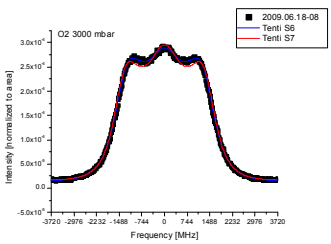 O2 3000 mbar 2009.06.18-08 Tenti S6 Tenti S7 Intensity (normalized to area) Frequency [MHz]	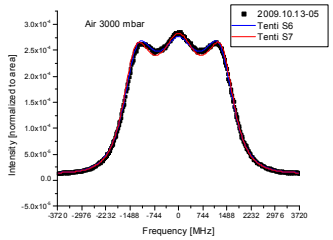 Air 3000 mbar 2009.10.13-05 Tenti S6 Tenti S7 Intensity (normalized to area) Frequency [MHz]

3.5	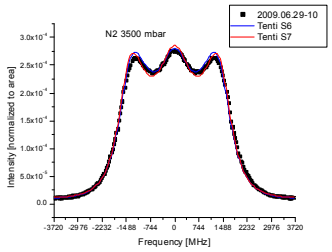	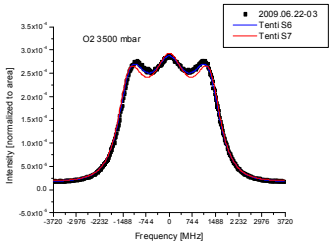	Not measured

Table 7.30: Deviations model-measurement as presented in previous sections, for measurements performed at different pressures and ambient temperature.

P [bar]	N2	O2	Air
0.3	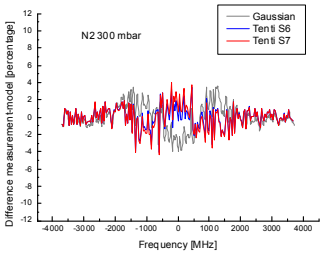	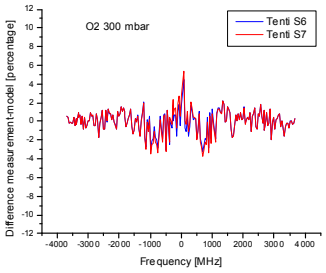	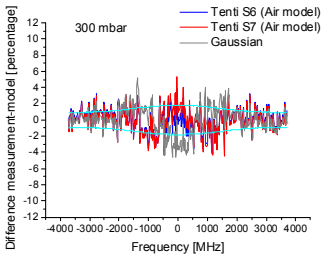
0.5	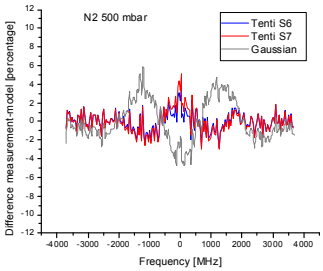	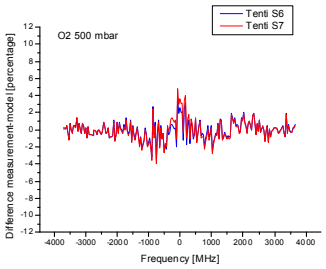	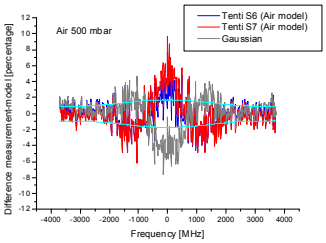
0.7	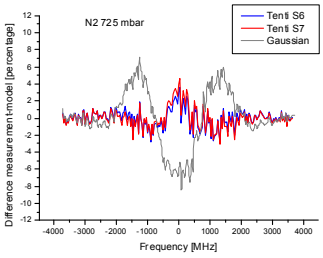	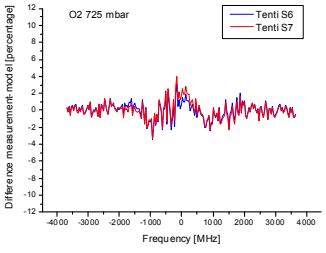	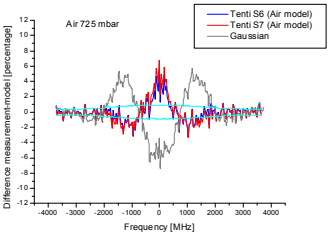

1	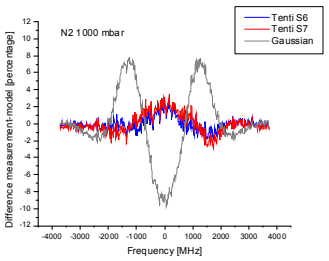	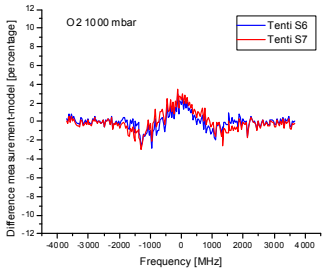	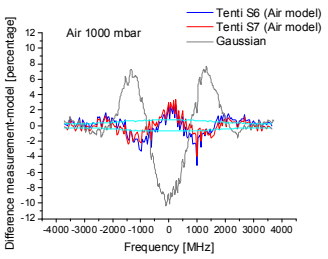
2	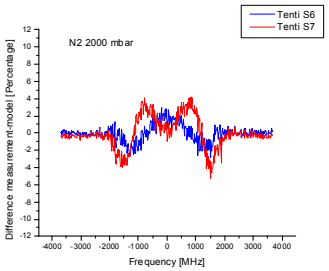	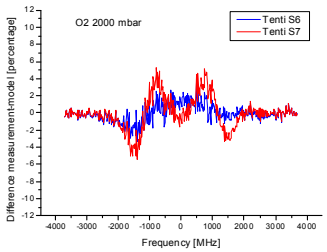	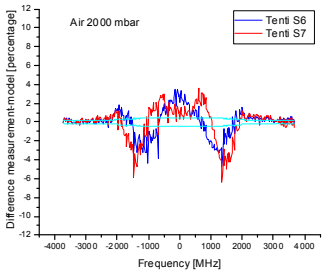
2.5	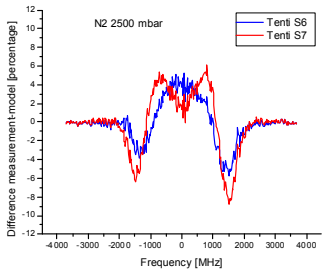	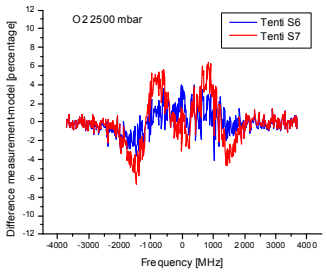	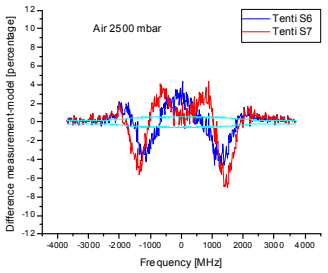
3	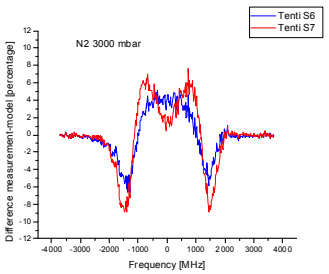	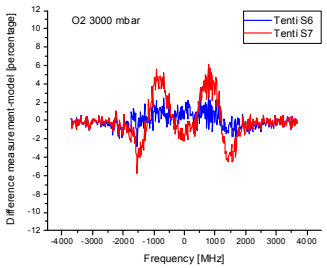	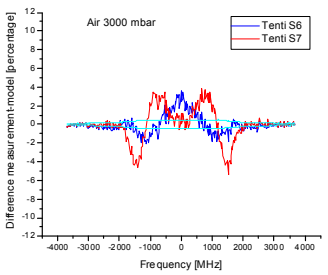
3.5	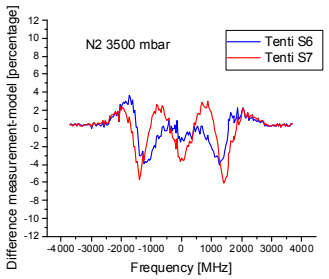	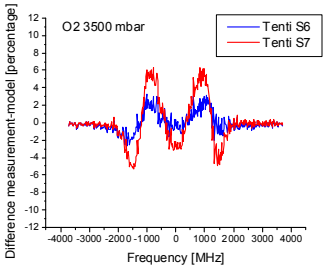	Not measured

As it was observed in Section 6.6.2, a possible contamination with scattering from the cell walls could be present in the measurements. The frequency span of this

contamination is [-500 MHz, 500 MHz], and therefore all measurements should be mistrusted to have “more signal” on that frequency region. Therefore, on the comparison measurement-model, the most important deviations are at the wings.

8 Results on CRBS

8.1 Science measurements of coherent Rayleigh-Brillouin scattering

We present experimental coherent Rayleigh-Brillouin scattering measurements of atmospheric gases like nitrogen (N_2), oxygen (O_2), carbon dioxide (CO_2), argon (Ar) and dry air, and of the reference gas krypton (Kr) at 1000, 2000 and 3000 mbar at 293 K. As discussed in section 3 a coplanar or 2D geometrical layout of the laser beams led to reproducible and stable results, and all data shown here were obtained in this configuration. The comparison of the experimental results with model calculations based on the Tenti S6 and S7 models will be the subject of section 9.8.
As discussed in section 3, the CRBS setup does not allow to measure at lower pressures, as more pump and probe intensity is needed to obtain a scattering signal, which could result in measurements being performed in the non-perturbative regime. Varying the temperature in our experiment is not practical, because of the size of the scattering cell.

For each gas, we measured 10 spectra, which are each averaged over 500 shots, normalized and corrected for the sensitivity variation over the PDA, as discussed in section 3. Each CRBS measurement shows smooth, symmetric spectra with typical features from scattered signal on induced density fluctuations, like Brillouin and Rayleigh peaks. The comparison of measured CRBS with the Tenti 6 and 7 moment models will be the subject of section 9.8. We therefore refrain from comparing our spectra to calculations in this section.

In the following figures, the raw data are shown on the right (typically 10 measurements of 500 shots each, to show the reproducibility) and the retrieved CRBS spectra (averages, extracted from the raw data by the procedure described above) on the left. A short analysis concludes this section.

8.1.1 Nitrogen (N_2)

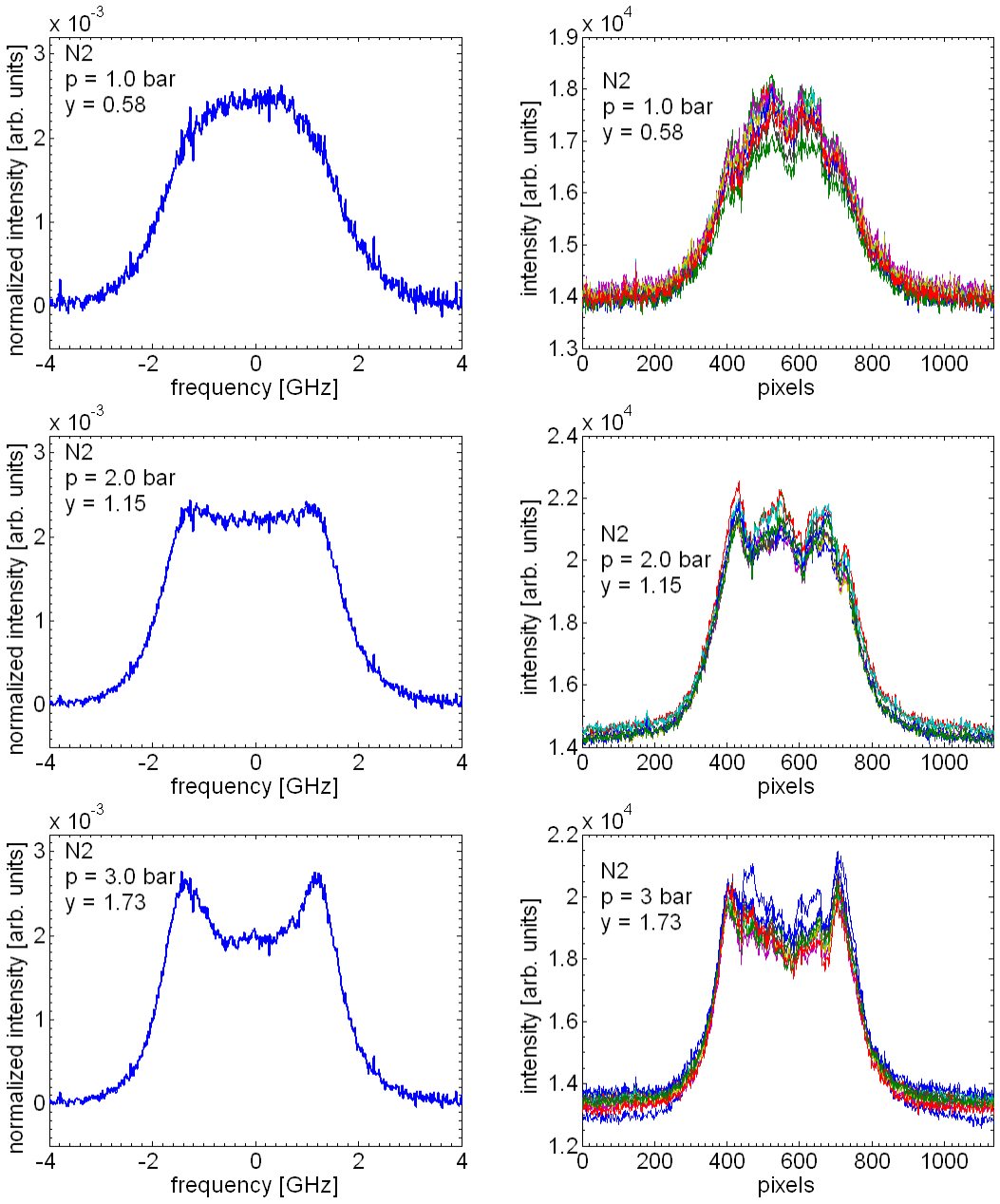

Figure 8-1: Experimental results on Coherent Rayleigh Brillouin scattering at 532 nm for various pressures in N_2. On the right raw data, on the left averaged data.

8.1.2 Oxygen (O2)

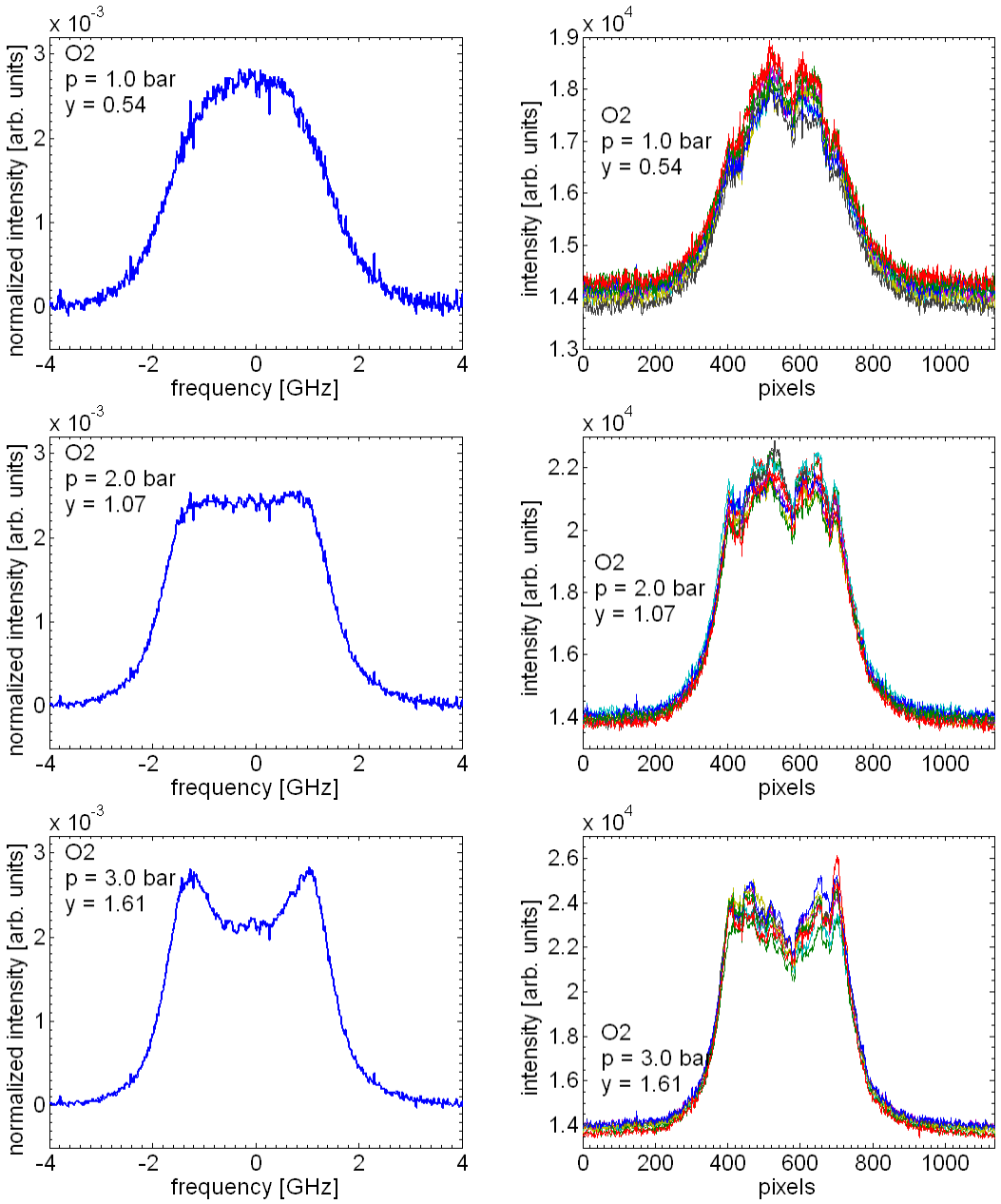

Figure 8-2: Experimental results on Coherent Rayleigh Brillouin scattering at 532 nm for various pressures in O_2. On the right raw data, on the left averaged data.

8.1.3 Carbon dioxide (CO_2)

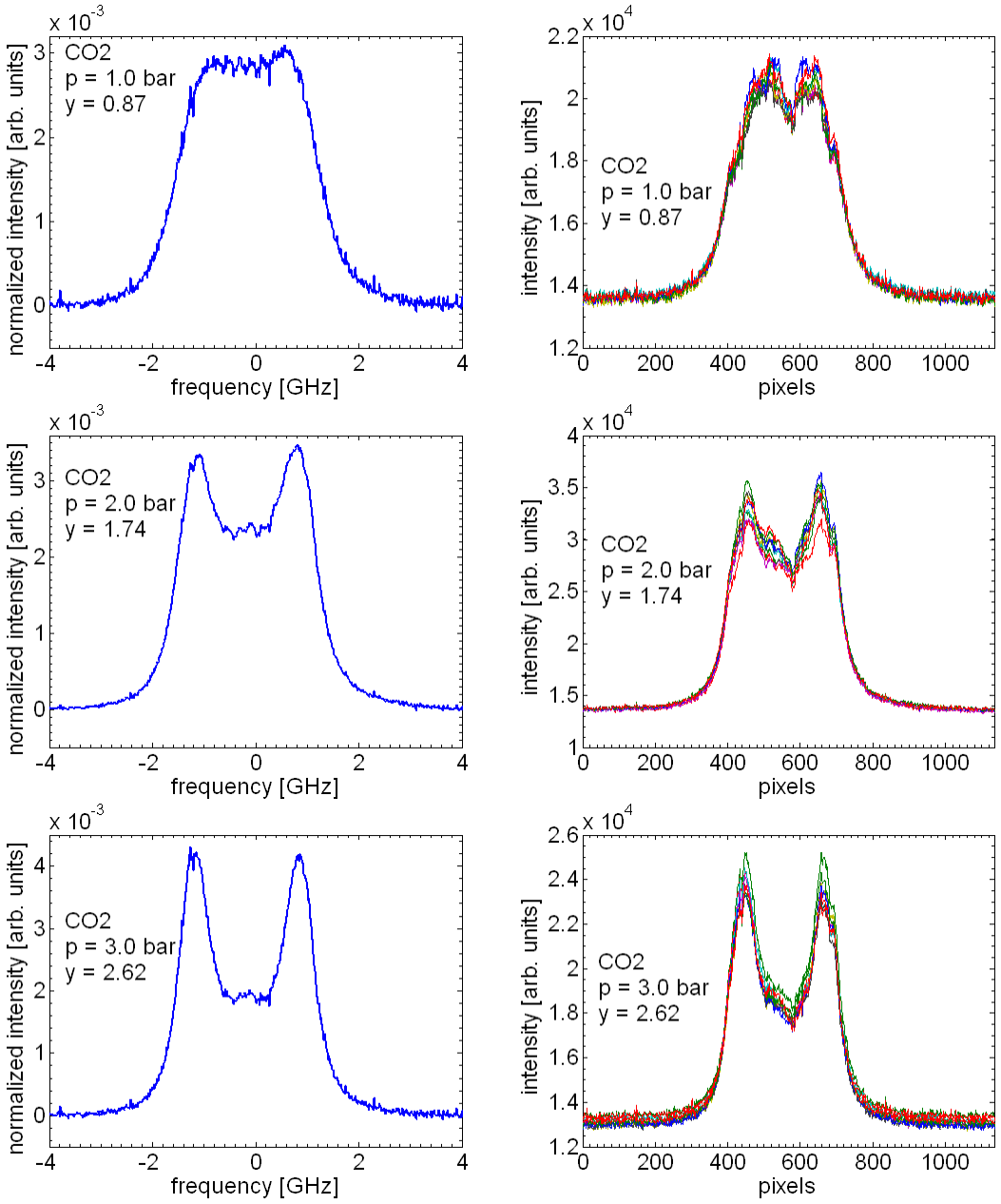

Figure 8-3: Experimental results on Coherent Rayleigh Brillouin scattering at 532 nm for various pressures in CO_2. On the right raw data, on the left averaged data.

8.1.4 Argon (Ar)

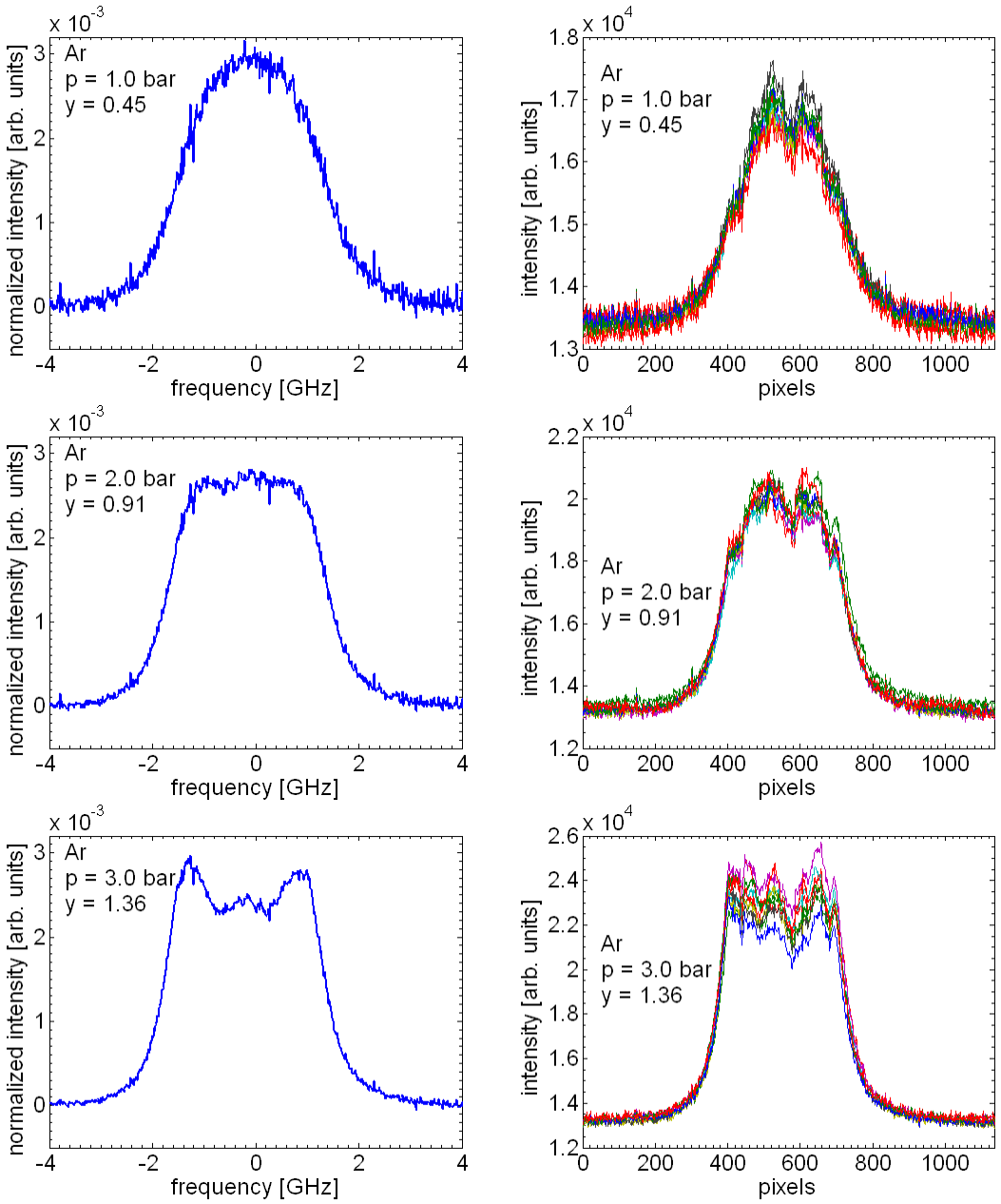

Figure 8-4: Experimental results on Coherent Rayleigh Brillouin scattering at 532 nm for various pressures in Ar. On the right raw data, on the left averaged data.

8.1.5 Air

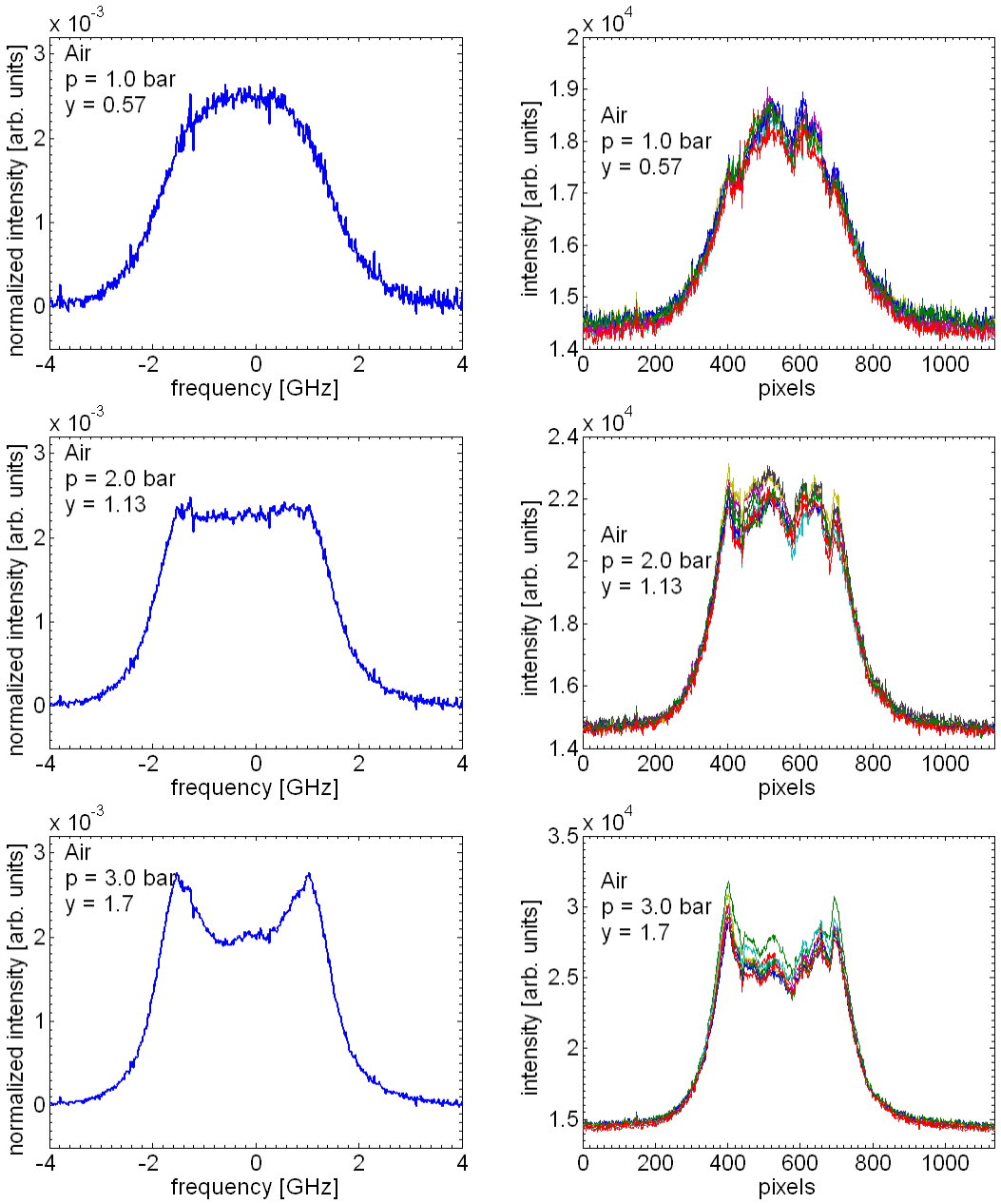

Figure 8-5: Experimental results on Coherent Rayleigh Brillouin scattering at 532 nm for various pressures in Air. On the right raw data, on the left averaged data.

8.1.6 Krypton (Kr)

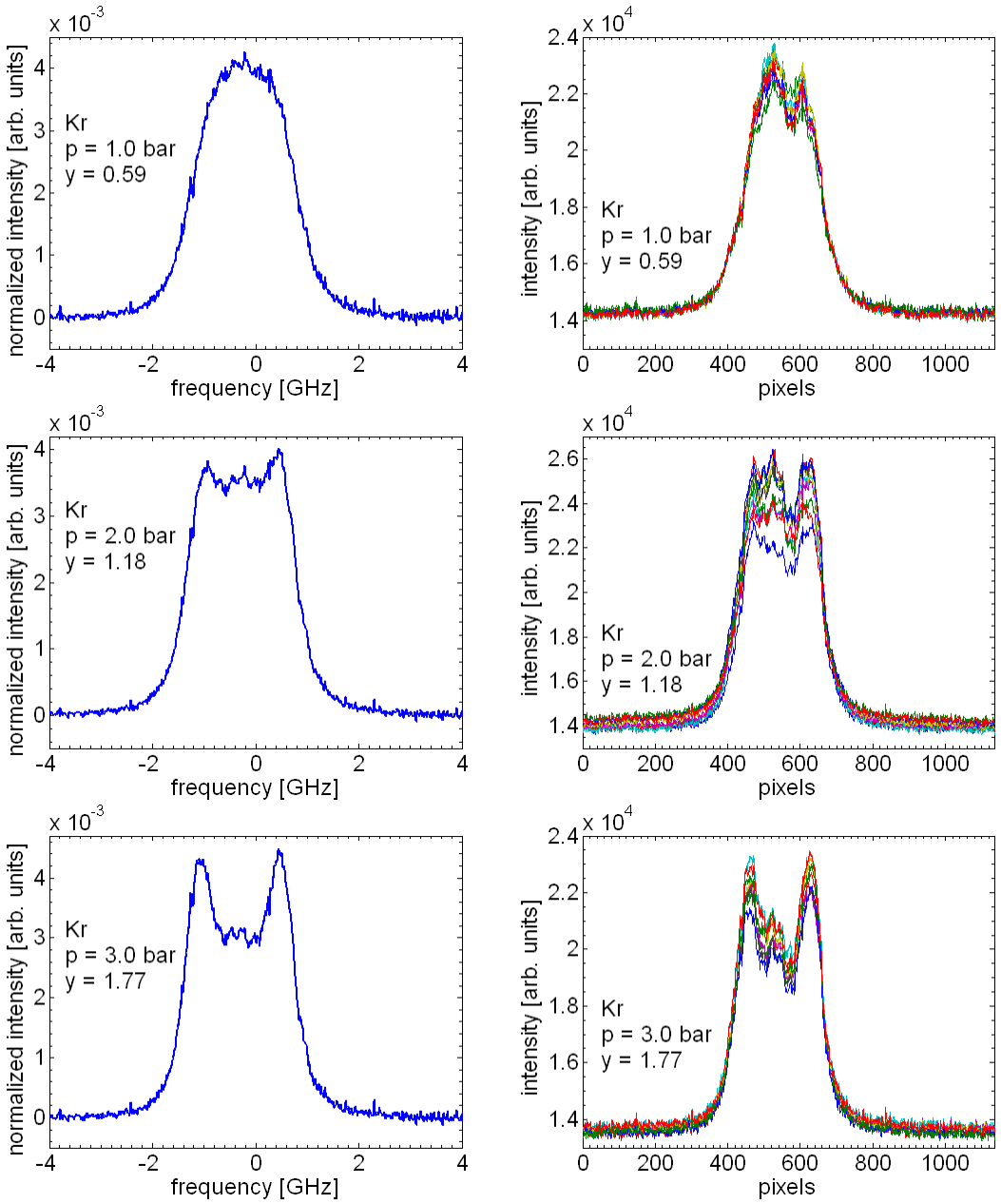

Figure 8-6: Experimental results on Coherent Rayleigh Brillouin scattering at 532 nm for various pressures in Kr. On the right raw data, on the left averaged data.

8.2 Analysis

The comparison of the experimental spectra with the Tenti models will be the subject of section 9.8. Here we restrict ourselves to a few general observations.

- The raw data (panels at the right in the above figures) typically reproduce within 5% (1σ, based on peak height).
- Occasionally, individual raw data traces show relatively large deviations from the average (see e.g. the traces for 2.0 bar Kr). This may be due to a relatively slow drift in the intensity of (one of) the laser beams, or perhaps instabilities in the alignment. In all cases, it is the absolute intensity that is affected, not the lineshape. As long as the absolute signal is not relevant, the deviations can be removed by simple scaling, if desired.
- The measurement noise (essentially the only noise in the wings of the spectra) decreases (in a relative sense) with increasing pressure. This contribution likely arises from the uncooled detector array. In the central region of the spectra, the badly reproducing mode structure of the laser is likely to contribute to the noise in individual spectra as well.
- For all gases, the RB lineshapes are essentially symmetric. (Note that the small frequency offset in some of the graphs is just an artefact of the data processing routine.) Obviously, the remaining measurement noise, and notably the remaining contribution of the laser mode structure, may occasionally fake a slight asymmetry in the lineshapes.
- For all gases, the RB lineshape is clearly not Gaussian, but shows the structure that is at least qualitatively predicted by the Tenti model. The comparison to the Tenti-model will be discussed in the section 9.8.

8.3 Conclusions

The CRBS spectra have been improved considerably by

i) changing the setup from 3D to 2D;
ii) recalibration of the flat-field and offset corrections of the Fizeau spectrometer;
iii) reduction of the pump intensity.

With this improved setup, CRBS spectra have been measured in N_2, O_2, air, CO_2, Ar, and Kr at pressures of 1, 2 and 3 bar.

An explanation has been provided for the retainment of the phase matching conditions upon minor misalignment, but the concomitant spectral narrowing is still elusive, and should be subject of further research.

The reason for the qualitative difference between the spectra obtained in the 2D and 3D setups is not understood.

9 Validation and refinement of the Tenti model

9.1 The Tenti model

Spontaneous Rayleigh-Brillouin scattering in gases originates from thermal density fluctuations. A key parameter is the ratio *y* of the scattering wavelength $2\pi/k$ to the mean free path between collisions:

$$y = \frac{p}{kv_0\eta} = \frac{nk_BT}{kv_0\eta} \tag{9.1}$$

with *k* the scattering wave vector, *n* the number density, *T* the temperature, *p* the pressure, v_0 the thermal velocity,

$$v_0 = \sqrt{\frac{2k_BT}{M}} \tag{9.2}$$

and η the (shear) viscosity. The definition of *y* is based on the simple (dimensional) relation between the mean free path between collisions and the shear viscosity η. Variants of this definition exist, for example [23] uses the mean thermal speed instead of v_0. In the sequel we will stick to Eq. (9.1).

In the kinetic regime $0.3 \le y \le 3$, which is the relevant regime of this project, neither the individual particle approach nor the continuum approach applies, and one has to resort to solving the Boltzmann equation for the density fluctuations. At even smaller *y*, the density is so low that we enter the Knudsen regime and the scattering is solely due to individual thermal molecules; in this case the wavelength dependence of scattered radiation is given by the Rayleigh distribution:

$$I(k,\omega) = \frac{2\sqrt{\pi}}{kv_0}\exp\left[-\left(\frac{\omega}{kv_0}\right)^2\right] \tag{9.3}$$

which is a Gaussian.

Let us now demonstrate the inadequacy of the simple Rayleigh line profile for spontaneous light scattering on air at pressures *p* = 0.3 and 1~bar. As Figure 9-1 illustrates, the error made is very large, and it can be concluded that it is not an option to ignore the Brillouin phenomenon at these pressures. Obviously, whether at *p* = 0.3 bar the individual particle regime is applicable or not depends on the precision of the experiments. Ours is such that at these low pressures, collective effects can be clearly recognized.

For spontaneous Rayleigh-Brillouin scattering the spectral line shape $I(k,\omega)$, where *k* is the scattering wavenumber and ω is the frequency of the scattered light, is proportional to the real part of the integral of the solution of the Boltzmann equation over velocity space $\nu(k,\omega)$, whilst for coherent scattering it is proportional to $|\nu(k,\omega)|^2$. This

distinction rests in a subtle difference in interpretation of the Boltzmann equation, on which we will comment in section 9.5.

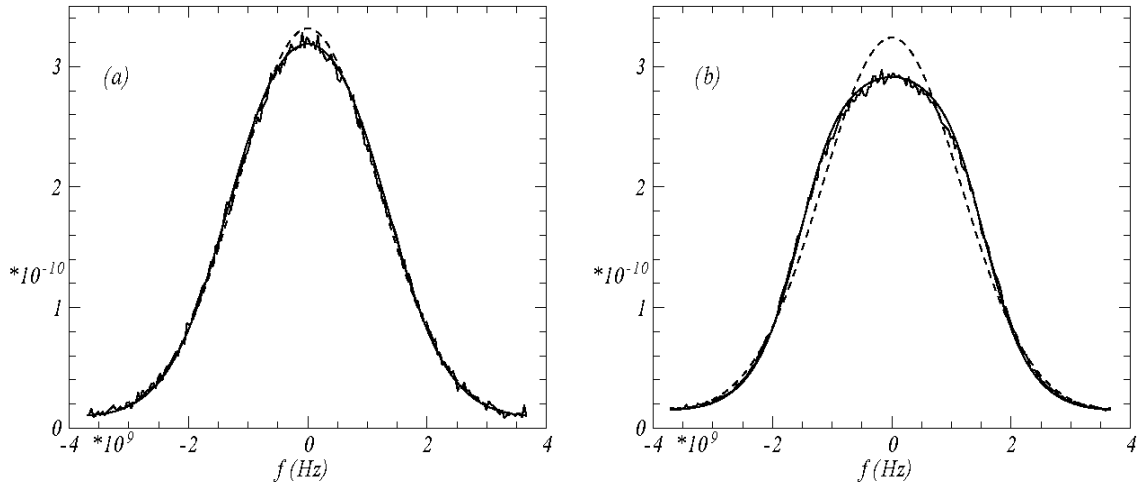

Figure 9-1: Spontaneous Rayleigh-Brillouin scattering on dry air, with the measured line shape compared to the Rayleigh line profile for (a) p = 0.3 bar and (b) p = 1 bar. The experiments, and the way in which they are compared to the model are explained below.

In principle, the solution of the Boltzmann equation is determined by the cross section of elastic and inelastic collisions between molecules, and in principle detailed knowledge about the collision cross sections would be needed. However, the problem is that such knowledge is not available and models must be devised.

9.1.1 The Tenti model: recycling information

An intelligent design of collision models is the core of the description of the line shape of scattered light. This design follows two steps: first the solution of the Boltzmann equation is expanded in an orthonormal system (the Sonine polynomials), which is truncated after a few (6 or 7) members. Then, it is ensured that the approximated collision integral reproduces the known transport coefficients, which appear as parameters in the approximation.

Therefore, these models *recycle information*: from known values of the transport coefficients of the continuum world, that is the macroscopic flow of gases, they reconstruct the collision operator needed in the kinematic approach. Two errors can arise in this procedure:

(i) the truncation of the collision operator is not adequate,
(ii) the transport coefficients are not known precisely.

Two truncations are already known: the Tenti S6 and S7 models. In this report we will also compare the measurements to a hard-sphere model for mixtures. We will argue that new models must be designed that allow for mixtures of molecules with internal degrees of freedom. This is a significant effort, and would make a separate project.

For a single-species gas, the transport coefficients needed are the shear viscosity η, the thermal conductivity, the heat capacity, and the bulk viscosity η_b. Of these

transport coefficients, the bulk viscosity is essentially dependent on the frequency. Its known value has been determined in experiments involving ultrasound. As the frequencies in light scattering are much larger, η_b must be considered as poorly known for light scattering.

Mixtures have additional transport coefficients that describe the relative motion of one species with respect to the other one, and a mixture model should involve these extra parameters.

9.1.2 Boltzmann equation

The Boltzmann equation for the microscopic phase space density *f(r, v, t)*, with *r* the position and *v* the velocity of the particle at time *t*, reads for a monatomic gas:

$$\left(\frac{\partial}{\partial t} + v \cdot \nabla\right) f = J(f, f) \tag{9.4}$$

where *J* is the collision operator, which for realistic models of polyatomic molecules involves both elastic and inelastic collisions to excited states.

Hydrodynamics is described by the linearization *f(r,v,t)* = ϕ(v) (1 + *h(r,v, t)*), where ϕ(v) is the Maxwell distribution. The hydrodynamic variables, such as density, velocity and heat flux are the velocity moments of *f*. It is the deviation *h* from thermal equilibrium that describes macroscopic transport. Accordingly, the linearized Boltzmann equation is:

$$\left(\frac{\partial}{\partial t} + v \cdot \nabla\right) h = J[h] \tag{9.5}$$

9.1.3 Coherent and spontaneous scattering

In the unforced case, Rayleigh-Brillouin scattering is due to the decay of density waves with wavenumber set by the scattering wavenumber *k*. An interesting twist to the problem of Rayleigh-Brillouin scattering was provided quite recently by experiments and theory on coherent Rayleigh-Brillouin scattering [9,55]. It differs from spontaneous Rayleigh-Brillouin scattering in that density fluctuations are now induced by subjecting the molecules to dipole forces in the electric field of a standing light wave. In this case, Eq. (9.5) needs to be augmented by the velocity-changing dipole force term:

$$a \cdot \nabla_v \phi \tag{9.6}$$

with **a** the dipole force, that directly acts on the zero-order Maxwellian ϕ(v):

$$\left(\frac{\partial}{\partial t} + v \cdot \nabla\right) h + a \cdot \nabla_v \phi = J[h] \tag{9.7}$$

Otherwise, the treatment of the collision operator *J* proceeds *in precisely the same manner* as for spontaneous Rayleigh-Brillouin scattering. This was described in a paper by Pan *et al.* [22].

In coherent Rayleigh-Brillouin scattering light is scattered by the induced dipoles, such that the scattered radiation inherits coherence from the standing optical wave field, and is concentrated in a beam that points in the direction which is determined by 4-wave phase matching conditions. This results in a tremendous increase of the detector signal, and a complete Rayleigh-Brillouin spectrum could be registered in a single laser shot. However, the spectral width of the pump field, while coherent, must be larger than the spectral width of the Rayleigh-scattered radiation, which is a challenge when using pulsed lasers. Otherwise, coherent Rayleigh-Brillouin scattering and spontaneous Rayleigh-Brillouin scattering provide *the same test* of line shape models. A few possible modes of coherent Rayleight Brillouin scattering are sketched in Figure 9-2.

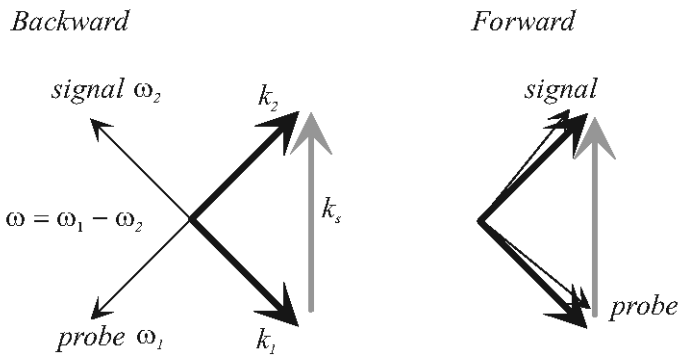

Figure 9-2: Arrangements of coherent Rayleigh-Brillouin scattering. The dipole forces a(k,ω) are set up by the two pump beams with wave vectors k_1 and k_2, and with the length of the scattering wave vector $k = |k_s| = |k_1 - k_2|$. The Rayleigh profile $\omega = \omega_1 - \omega_2$ is picked from the broad spectral line shape of the pump beams. In the forward mode the beams are separated using polarizers.

The kinetic models for the line shape of coherent Rayleigh-Brillouin scattering need exactly the same macroscopic information as those for spontaneous Rayleigh-Brillouin scattering, and are described by the same approximated collision integral. However, the spectra are different, and thus provide a different magnifying glass on the accuracy of these models. The dipole force **a** is determined by the pump beam intensity, and by the polarizability α of the molecules. For a single-species gas, information about α is not needed, as it is a mere scale factor of the spectra. Information about α is only needed for a mixture of gases. However, in this case the same information would be needed for spontaneous Rayleigh-Brillouin scattering, because the scattering intensity is proportional to α.

9.1.3.1 Solving the Boltzmann equation

This was done in two seminal papers on which the now widely spread Tenti S6 S7 models are based [9,55]. These models refer to the linearized collision integral in Eqs. (9.5) and (9.7). For a special intermolecular force $F \sim r^{-5}$ (the Maxwell force), the Sonine polynomials form an eigen system of the linearized collision operator. Through the use of this complete orthonormal system, the linearized Boltzmann equation can be cast into matrix form:

$$AX = B \tag{9.8}$$

and, to give a flavor of the matrix elements in the case of spontaneous Rayleigh-Brillouin scattering. The full equation can be found in [22].

$$\begin{pmatrix} -J_{030}I_{00}^{00} - \frac{1}{n} & . & . & . \\ . & & . & . \\ . & & . & . \\ . & & . & . \end{pmatrix} \begin{pmatrix} \nu(k,\omega) \\ . \\ . \\ . \end{pmatrix} = -\frac{1}{n} \begin{pmatrix} I_{00}^{00} \\ . \\ . \\ . \end{pmatrix} \tag{9.9}$$

The linearized Boltzmann equation describes the relaxation of a density perturbation. For spontaneous Rayleigh-Brillouin scattering the right-hand side of Eq. (9.8) contains the initial condition, such that for a binary mixture there are two separate solutions for two separate initial perturbations. Then, the scattered light intensity is proportional to the real part of $\nu(k,\omega)$ (or the real part of the sum of complex amplitudes for mixtures). For coherent Rayleigh-Brillouin scattering the right-hand side of Eq. (9.8) is proportional to the forcing amplitude **a** of the pump field, and the scattered light intensity is proportional to $|\nu(k,\omega)|^2$. This distinction rests on the fundamental understanding of light scattering, on which we will comment in section 9.9.

The functions $I(k,\omega)$ in Eq. (9.9) can be expressed in terms of the plasma dispersion function, which contains all of the wavenumber-frequency dependence of the line shape. We will comment on practical computation issues of this function in section 9.5.

It was shown in [55] that, from the two truncations, surprisingly the 6-moment model (the Tenti S6 model) provides the superior fit of experimentally measured line shapes, probably because of an effective resummation of the truncated expansion. In fact, the design of models appears quite delicate, especially where it concerns the treatment of inelastic collisions between molecules with reachable internal degrees of motion.

9.2 Mixtures of gases

The standard lines shape models (the Tenti models) are for gases consisting of a single kind of molecule. However, natural air is a mixture of several gases. If the components of a mixture have different mass or different collision cross sections, another relaxation mechanism arises when equilibration of translational energy between the species requires several collision times τ. Although this effect may not be strong in air as its main constituents O_2 and N_2 are comparable molecules, a kinetic theory of the spectral line shape in mixtures is needed.

A naive but perhaps effective approach may be to consider air as a fictitious gas, with effective transport coefficients, determined by molecules with an effective mass, and effective internal degrees of freedom. However, as the light scattering cross section

is proportional to the molecular polarizability α, the scattering signal is predominantly determined by the mixture members with the largest α. While such an approach may work, it is not internally consistent, and an agreement between model and experiment must be deemed fortuitous.

Early on, Brillouin light scattering experiments in mixtures have been done by the group of Letamendia in Bordeaux [37,56]. Their idea has been to do mixtures of noble gases with a very large disparity of masses (Xe/He). Due to the inefficiency of the energy transfer by collisions, thermal equilibrium is reached slowly, and the constituents have effectively two temperatures. This is a very special situation, which will not be encountered in our case, but which is interesting from a fundamental point of view.

A kinetic model for both coherent an spontaneous Rayleigh-Brillouin scattering been published by Marquez [57,58] and provides an improved reproduction of the spectra (over the hydrodynamical model that was originally tried by Letamendia) [37,56].

However, the macroscopic description of mixtures needs many more transport coefficients whose values are not always known precisely. The solution followed in [57,58] is to view the mixture molecules as hard spheres. For hard spheres, all transport coefficients, including the mixture ones, follow from the hard sphere radius. In fact, this radius is the one that gives the best reproduction of the transport coefficients of the single-species gas, which then extends to the inter-species transport coefficients. In the case of coherent Rayleigh-Brillouin scattering this mixture model correctly allows for the different response of the species to the standing electric field of the crossed pump beams.

The disadvantage of course is that no effects of the internal degrees of freedom can be described in this manner. However, it may correctly describe the kinetic relaxation of a mixture whose constituents have different mass. As this model should work perfectly for a simple noble gas, we shall compare it to scattering experiments on Kr.

9.3 Bulk viscosity

Apart from the approximation to the collision integral, which is intrinsic to the Tenti models, another source of error is incomplete knowledge of some transport coefficients. Of those needed, i.e. the shear viscosity η, the heat conductivity λ_c, the heat capacity c_i, and the bulk viscosity η_b, the latter is not known very well but it has a large influence on the line shape.

The origin of the bulk viscosity is the relaxation of the internal degrees of freedom of a poly-atomic molecule in collisions. Usually, the associated relaxation time τ_i is a multiple of the mean time between collisions τ_c. So far, all experimental information about η_b comes from measurements of the absorption of ultrasonic waves, which are difficult [59]. Due to the emergence of the time constant τ_i, the bulk viscosity depends on the frequency of sound. As in light scattering experiments the probed wavenumbers, and, consequently, the sound frequencies are at least 1 to 2 orders of magnitude larger than in acoustic experiments, the currently known values of η_b may not be reliable for light scattering. A similar argument can be made for the heat capacity c_i of the internal modes of motion.

For example, if vibrational levels have energies comparable to k_BT, and therefore can be reached in collisions, they generally come with very long relaxation times τ_i, and thus large values of η_b. However, these vibrational levels may remain frozen in light

scattering experiments because of the high frequencies involved. This was demonstrated by Pan *et al.* in coherent Rayleigh-Brillouin light scattering experiments on CO_2 [33]. They could only explain their experimental results by assuming a much smaller η_b than what was known so far in the literature.

While the bulk viscosity η_b may provide a convenient parameter in which internal molecular degrees of freedom can be lumped, its fundamental basis remains highly controversial [60]. Clearly, the only correct manner to describe gases with internal degrees of freedom would be to treat each internal state as separate species in a multi-component kinetic theory.

There is no bulk viscosity in a stationary flow at zero frequency. Therefore, η_b depends on *f* in an essential way and must be considered as a big unknown in our experiments, which are done at frequencies that are much larger than the acoustical ones on which the literature values of η_b are based. Therefore, we will try systematically to obtain a better reproduction of measured line profiles by varying η_b.

9.4 The plasma dispersion function

Usually, the plasma dispersion function is defined as:

$$w(z) = \frac{1}{\sqrt{\pi}} \int_{-\infty}^{\infty} \frac{e^{-t^2}}{t - z} dt \qquad (9.10)$$

which is also the definition used by Tenti and Boley. The real part of the complex argument *z* is the dimensionless frequency ω/kv_0, while the imaginary part is the *y* parameter Eq. (9.1). Clearly, if *z* is on the real axis (*y* = 0), w(z) becomes the (dimensionless) Rayleigh distribution. Therefore, the plasma dispersion function and its moments are the building blocks of the scattered light spectrum, and it is important to have a dependable way to compute them.

The plasma dispersion function can be expressed in terms of the error function with complex argument. An excellent and fast algorithm for this is provided by the NAG numerical library function s15ddf (the function of the NAG routine):

$$w(z) = i\sqrt{\pi}\, s15ddf(z) \qquad (9.11)$$

If this library is not available, the Fortran program by Tenti provides a plasma dispersion function in the first quadrant, which can be moved to negative reduced frequencies by using the symmetry:

$$w(z) = -w^*(-z^*) \qquad (9.12)$$

Also Pan provides a plasma dispersion function, which takes up a large fraction of his code. However, it has relatively large errors. For small *y*-parameters, the error can be as large as 1 %. The differences between the program by Tenti and Boley and the NAG routine are not larger than 10^{-9}. Both the NAG version of *w(z)* and the version by Tenti

and Boley are implemented in the program rbs (see Appendix (ESA –AO/1-5467/07/NL/HE-TN4, part 2)).

9.5 The Van Hove correlation function

Let us briefly dwell on a fundamental issue related to the interpretation of the Boltzmann equation, which appears to be different for spontaneous and coherent Rayleigh Brillouin scattering. According to van Hove, the scattered light intensity is proportional to the Fourier transform of the microscopic density correlation function.

$$S(k,\omega) = \int e^{i(kr-\omega t)} G(r,t)\, dr dt \qquad (9.13)$$

where *G(r, t)* is the probability to find a particle at a distance *r* at time *t*, if it was at the origin at *t = 0* and *S* is the scattering amplitude. This density correlation function is the solution of the linearized Boltzmann equation. Let us call this solution $n_0\nu(r, t)$, where n_0 is the unperturbed density, then the scattering amplitude is the real part Re of the (complex) solution of the linearized Boltzmann equation:

$$S(k,\omega) = \mathrm{Re}\left[n_0 \nu(k,\omega) \right] \qquad (9.14)$$

So, the scattered light intensity is directly proportional to the solution of the Boltzmann equation.

In coherent Rayleigh-Brillouin scattering, this solution $n_0\nu(k,\omega)$ is proportional to the dipole force **a**(k,ω) due to the pump beams:

$$a(k,\omega) = \alpha \frac{k}{m} E_1(\omega) E_2^* \sin(kx - \omega t) \qquad (9.15)$$

which is assumed broadband, so that $E_{1,2}$ can be replaced by constants. If van Hove's interpretation would also apply to the driven (coherent) case:

$$S(k,\omega) \propto \sqrt{I_1 I_2} \qquad (9.16)$$

However, the usual practice is to view the coherent case as a time-stationary, rather than an initial value problem. Then, the solutions of the linearized Boltzmann equation are viewed as fluctuating density perturbations, and:

$$S(k,\omega) = n_0^2 \nu(k,\omega) \nu^*(k,\omega) \propto I_1 I_2 \qquad (9.17)$$

These two interpretations predict a very different dependence on the intensity of the pump beams, which has not been measured. Therefore, we describe in section 9.9 an experiment to decide between the two hypotheses.

In conclusion, there is no ambiguity as to the interpretation of the spontaneous Rayleigh-Brillouin scattering experiments, but the coherent Rayleigh-Brillouin scattering experiments need a more careful foundation.

9.6 The instrument profile

9.6.1 Etalon used in the spontaneous measurements

The spectral response *S(f)* of the etalon was measured in a separate experiment, and could be parametrized very well by the formula:

$$S(f) = \left[1 + \left(\frac{2 f_{fsr}}{\pi \Delta} \sin\left(\frac{\pi f}{f_{fsr}} \right) \right)^2 \right]^{-1} \qquad (9.18)$$

where f_{fsr} is the free spectral range of the etalon, f_{fsr} = 7.44 x 10 GHz, and Δ = 0.232 GHz is the Airy-width of the transmission peak. All computed model spectra were convolved with *S(f)*, and since the free spectral range is relatively small, it is important to allow for the periodic nature of *S(f)*. In principle, also a convolution over the distribution of wave vectors *k* is needed due to the finite aperture size of the detector. The associated opening angle is estimated 0.7°. This *k* uncertainty affects both *x* (the reduced frequency) and the *y*-parameter; the etalon frequency width Δ only affects *x*. However, a quick calculation teaches that the effect of the *k*-uncertainty on *x* is a factor 20 smaller than the etalon width Δ, and is a factor 6 x10^{-3} in y. So we may neglect the *k* uncertainty due to the finite aperture.

9.6.2 The Fizeau wavemeter used in the coherent experiment

The response of a Fizeau dispersive element is described extensively in the literature [35]. Briefly, its response to a monochromatic plane wave is determined by multiple reflections off the two faces of the wedge. The response can be computed from known parameters, that is the reflectivity of the wedge faces, the central separation *d* of the wedge, the central wavelength λ_c and the wedge angle θ_w. The free spectral range is given by $\lambda\sin(2\alpha)$. Figure 9-3 compares the computed response to the measured one using monochromatic light from the probe laser.

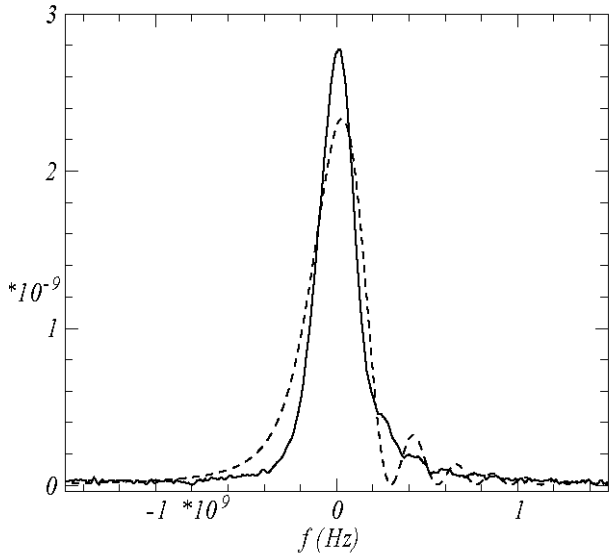

Figure 9-3: The response of the Fizeau interferometer. Full line: measured, dashed line: modeled by computing 128 repeated reflections of a plane monochromatic wave with λ = 532.2456 nm, θ_w = 17.05 x 10^{-6} rad, and *d* = 14.9157 mm. Both response functions were used to compare models to experimental results.

Since the Fizeau spectrometer is a nonlinear dispersive device, the sum over repeated reflections must be done for each wavelength of the input spectrum, which makes the convolution of the model lengthy. However, to reasonable approximation, the response can be written as a convolution with the response on a monochromatic wave, made periodic over the free spectral range. In allowing for the Fizeau instrument function, we followed two approaches: one in which the response was computed numerically from the known Fizeau parameters, and one in which a convolution over a measured response function was used. No significant differences between the results of these two approaches were found.

9.7 Normalizing the experimental data

The light scattering experiments do not provide an absolute intensity. Doing so would require a tremendous effort in precise characterization of the experiment geometry and the quantum efficiency of the light detector, and would still result in a relatively large error of the intensity scale. In order to provide an absolute intensity for the computed model spectrum, information about the molecular dipole polarizability would be needed. Therefore it was decided to separately normalize the experimental and computed spectra such that:

$$\int_{-f_b}^{f_b} I(f)df = 1 \qquad (9.19)$$

9.7.1 Spontaneous Rayleigh-Brillouin scattering experiments

Ideally, the bounds f_b of the integration should be such that $I(\pm f_b) = 0$, however, for the spontaneous Rayleigh-Brillouin scattering experiments the free spectral range of the etalon is not much larger than the width of the measured spectra, which for air molecules is approximately 4 GHz. Therefore we take $f_b = f_{fsr}/2$ in the normalization. Another problem is the signal background I_{e0} in the experiment, which must be subtracted from the raw measured spectrum $I_{er}(f)$ before normalization of $I_e(f) = I_{er}(f) - I_{e0}$. It turns out that I_{e0} is not just the dark current of the used photomultiplier, but also contains a small contribution, I'_{e0} of broadband fluorescence of the cell windows. We discovered that this contribution also depends on the exposure history of the cell windows.

Therefore it was decided to correct the model spectra $I_m(f)$ for this poorly known background contribution, by setting $I_m(f) = aI_e(f) - I'_{e0}$, and determine I'_{e0} and the proportionality constant a in a least squares procedure for the wings of the spectra. If the measured spectra would have the correct background, $a = 1$ and $I'_{e0} = 0$. The wings of the spectra were defined as frequencies such that $I_m(f) \leq \max(I_m)/2$. The shifted model spectrum $I'_m(f) = I_m(f) + I'_{e0}$ was then normalized again such that

$$\int_{-f_b}^{f_b} I_m'(f)\,df = 1 \qquad (9.20)$$

This procedure, which converges quickly, gave a small but perceptible shift of the background; it increased the wing intensity $I_m(f_{fsr}/2)$ by approximately 25%.

In conclusion, when comparing experimental to computed spectra, the vertical scales were determined completely by normalization, whilst a small correction was done on the dark background. However, the noise in these experiments is so small that the background must be considered as a free parameter.

9.7.2 Coherent Rayleigh-Brillouin scattering experiments

The background in the coherent Rayleigh-Brillouin scattering experiments is mainly made of dark current of the CCD array in the Fizeau spectrometer, it is large, and of the order of the signal strength. Therefore, the same procedure was followed as in section 6.7, but now to find the experimental background. Knowledge of this background is required for the correction with the measured Fizeau response function. As the free spectral range of the Fizeau spectrometer is larger than that of the etalon used in section 5, an alternative procedure is to determine the background from the tails of measured spectra. Both procedures were tried, with the main conclusions unaltered. Also, as the absolute frequency scale of the Fizeau spectrometer, is not determined well, both measured and model spectra were centered on $f = 0$.

In conclusion, as the spectra measured in the coherent Rayleigh-Brillouin scattering experiment have a large background, determination of the background is essential, which leads to two free parameters in the comparison between experiment and theory.

9.8 Comparison to experiment

As already explained, the comparison to experiment involves the determination of the background in the experiment, and a normalization of both experiment and model spectra. The coherent spectra were also centered at $f = 0$. Then, the error σ is defined as:

$$\sigma^2 = \frac{1}{N}\sum_{i=1}^{N}\left(I_{e,1} - I_m\left(f_i\right)\right)^2 \qquad (9.21)$$

where $I_{e,i}$ is the spectrum measured at frequency f_i, and $I_m(f)$ is the model spectrum. If an independent measure of the statistical error σ_s could be determined, the ratio $\sigma^2/\sigma_s^2=\chi^2$, which should be 1 for a perfect fit between model and experiment with no adjustable parameters. We emphasize that Eq. (9.21) gives the same weight to all points of the spectrum.

In the sequel we will compare for each gas, side to side, the spontaneous Rayleigh-Brillouin scattering and coherent Rayleigh-Brillouin scattering spectra. These spectra were measured with different wavelengths. For the spontaneous case we used 366 nm, while for the coherent experiments it is 532 nm. However, for Rayleigh-Brillouin scattering it is the scattering wavenumber that matters, which for the two cases is nearly equal; it is k = 2.43 x 10^{-7} m^{-1} and k = 2.43 x 10^{-7} m^{-1} for the spontaneous and coherent case, respectively.

9.8.1 Nitrogen

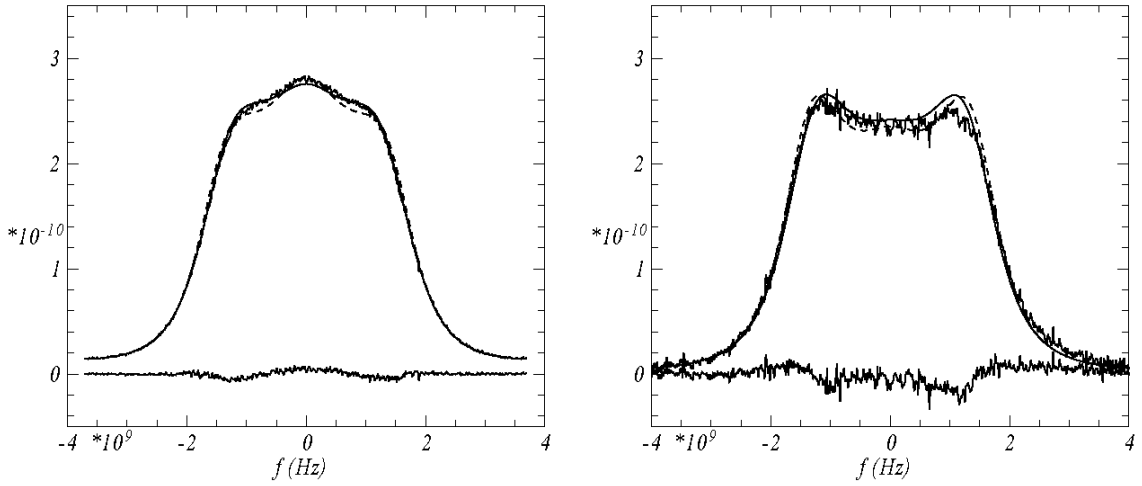

Figure 9-4: Spontaneous Rayleigh-Brillouin scattering and coherent Rayleigh-Brillouin scattering on N_2 at p = 2 bar. (a) Spontaneous Rayleigh-Brillouin scattering at scattering wavevector k = 2.43 x 10^{-7} m^{-1}, (b) coherent scattering at scattering wavevector k = 2.36 x 10^{-7} m^{-1}. Full lines, data, comparison to Tenti S6, residues, dashed lines: comparison to Tenti S7 model. The Tenti S6 model has a significantly smaller residue, as may be concluded from Figure 9-5.d, and Figure 9-6.d.

9.8.1.1 Spontaneous Rayleigh-Brillouin scattering

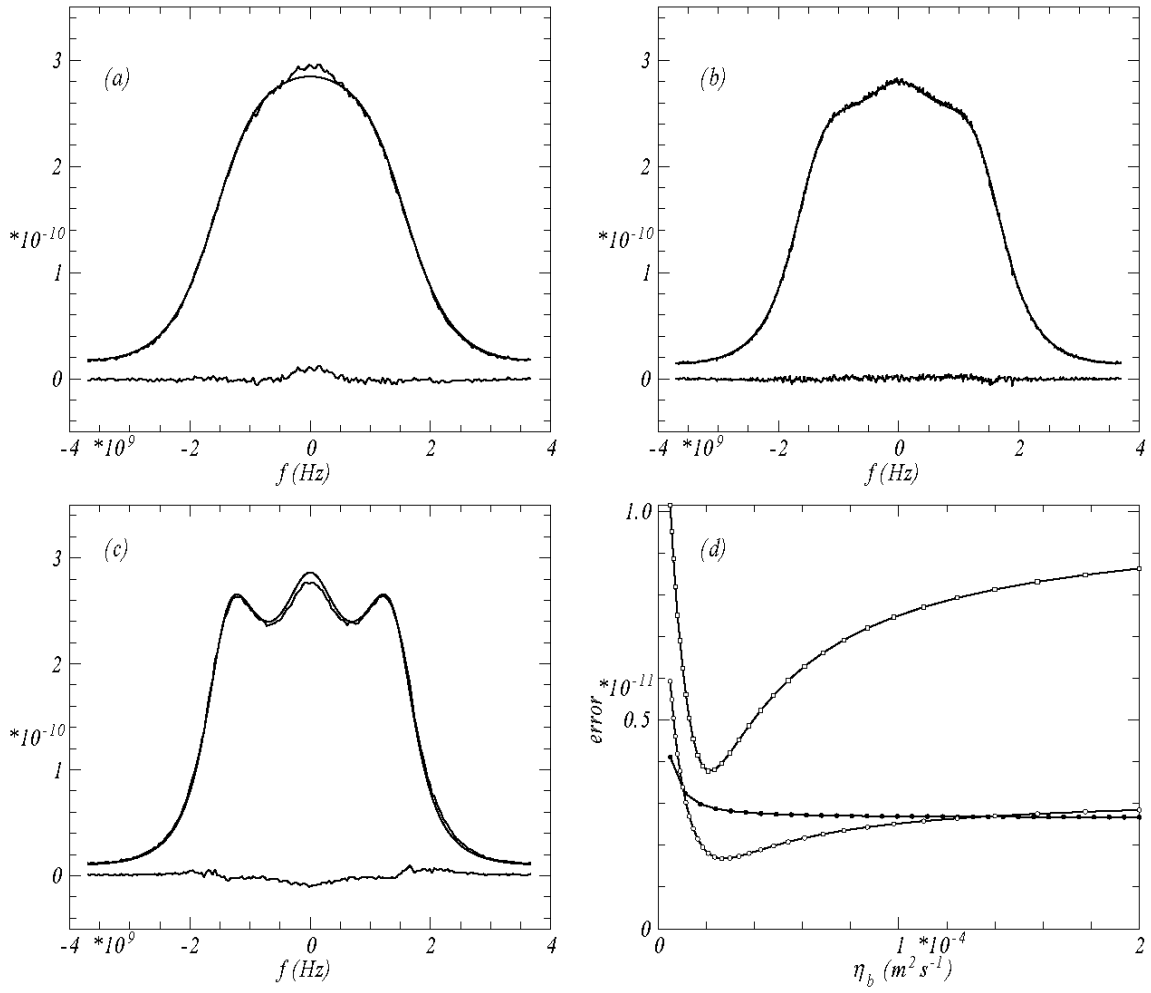

Figure 9-5: N_2 spontaneous Rayleigh-Brillouin scattering. The spectra are computed for the best value of η_b. (a) p = 1 bar, η_b =1.29 x 10^{-5} kg $m^{-1}s^{-1}$ (the literature value), (b) p = 2 bar η_b =2.82 x 10^{-5} kg $m^{-1}s^{-1}$ (c) p = 3.5 bar, η_b =2.22 x 10^{-5} kg $m^{-1}s^{-1}$ (d) Error as a function of η_b, dots, open circles and open squares, p = 1, 2, 3.5 bar, respectively. The best values for η_b used in (b,c) are the positions of the minima.

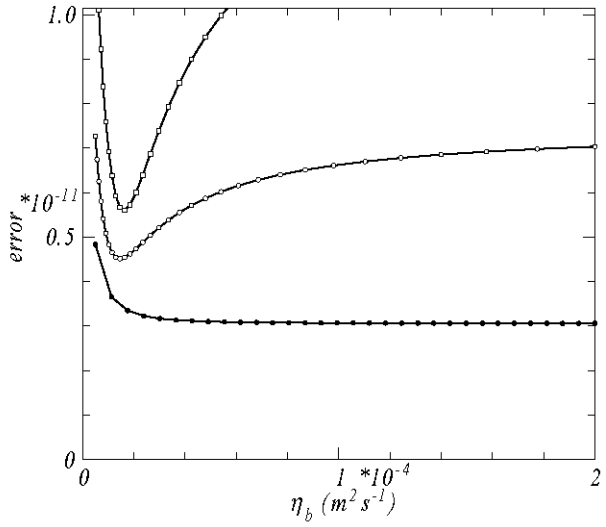

Figure 9-6: N_2 spontaneous Rayleigh-Brillouin scattering. Same as Figure 9-5(d), but now the error is for the Tenti S7 model. For pressures ≥ 2 bar, the S7 model has significantly larger errors.

From the experiments on spontaneous Rayleigh-Brillouin scattering on N_2 shown in Figure 9-5 and Figure 9-6 we conclude that the S6 model has a smaller error than the S7 model, while both models indicate that the bulk viscosity must be chosen ~ 2 x 10^{-5}, which is significantly larger than the literature value η_b = 1.29.

For p = 2 and 3 bar we have computed in the S6 and S7 models the value of η_b which minimizes σ, and because there is no well-defined value for p = 1 bar, we there used the literature value of η_b. The p = 1 spectrum has a small residue at *f* = 0 which must be ascribed to spurious reflections in the cell.

9.8.1.2 Coherent Rayleigh-Brillouin scattering

Figure 9-7 shows that the statistical error for the low-pressure experiments on coherent Rayleigh-Brillouin scattering is much larger than in the spontaneous Rayleigh-Brillouin scattering experiment. Clearly, in agreement with the SRBS experiments, the S6 model indicates that the bulk viscosity must be chosen larger than the literature value, but there no longer is a clear minimum of the error. Because $\sigma(\eta_b)$ does not show a minimum, we have (arbitrarily) computed all models for η_b =2 x 10^{-5} kg $m^{-1}s^{-1}$.

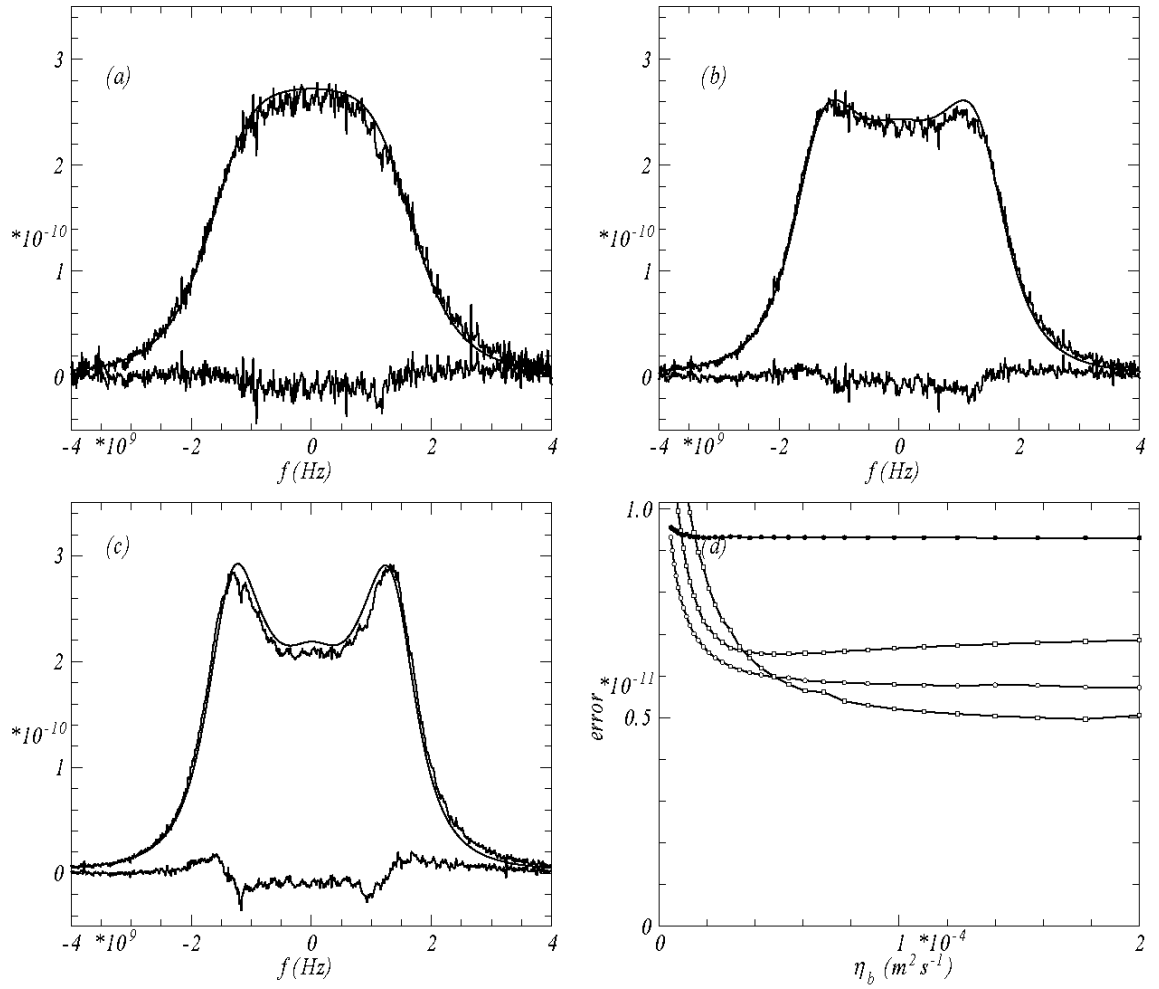

Figure 9-7: N_2 coherent Rayleigh-Brillouin scattering. Determining the best value of η_b for N_2. (a) p = 1 bar, η_b =2 x 10^{-5} kg $m^{-1}s^{-1}$; (b) p = 2 bar, η_b =2 x 10^{-5} kg $m^{-1}s^{-1}$; (c) p = 3 bar, η_b =2 x 10^{-5} kg $m^{-1}s^{-1}$, (d) Error as a function of η_b, dots, open circles and open squares, p = 1, 2, 3 bar, respectively. There are two different experiments for p = 3 bar. The error indicates that η_b has to be chosen larger than the literature value, but there is not a clear minimum. We have therefore chosen η_b =2 x 10^{-5} kg $m^{-1}s^{-1}$ in (a,b,c).

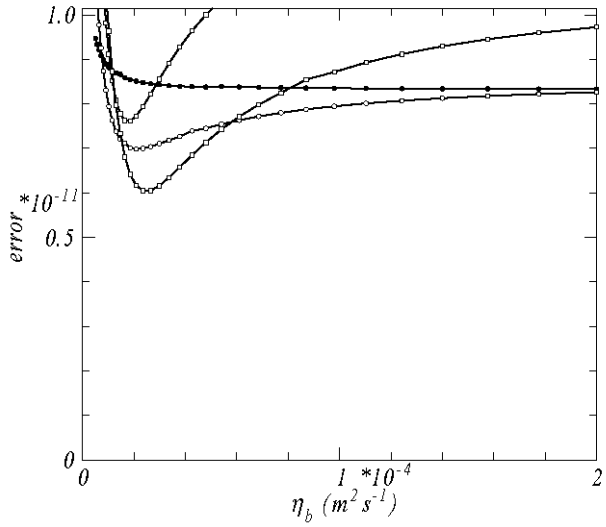

Figure 9-8: N_2 coherent Rayleigh-Brillouin scattering. Same as Figure 9-7(d), but now the error is for the Tenti S7 model. There are two different experiments for p = 3 bar. For pressures ≥ 2 bar, the S7 model has significantly larger errors.

9.8.2 Oxygen

9.8.2.1 Spontaneous Rayleigh-Brillouin scattering

From the spontaneous Rayleigh-Brillouin scattering experiments on O_2 shown in Figure 9-9 and Figure 9-10 we conclude that the S6 model has a smaller error than the S7 model, but, unlike N_2, all models indicate that the literature value of η_b is adequate. Remarkably, the experiment at atmospheric pressure does not really depend on the value of η_b. Probably this is because the spectrum lacks marked sound features whose shape strongly depends on η_b.

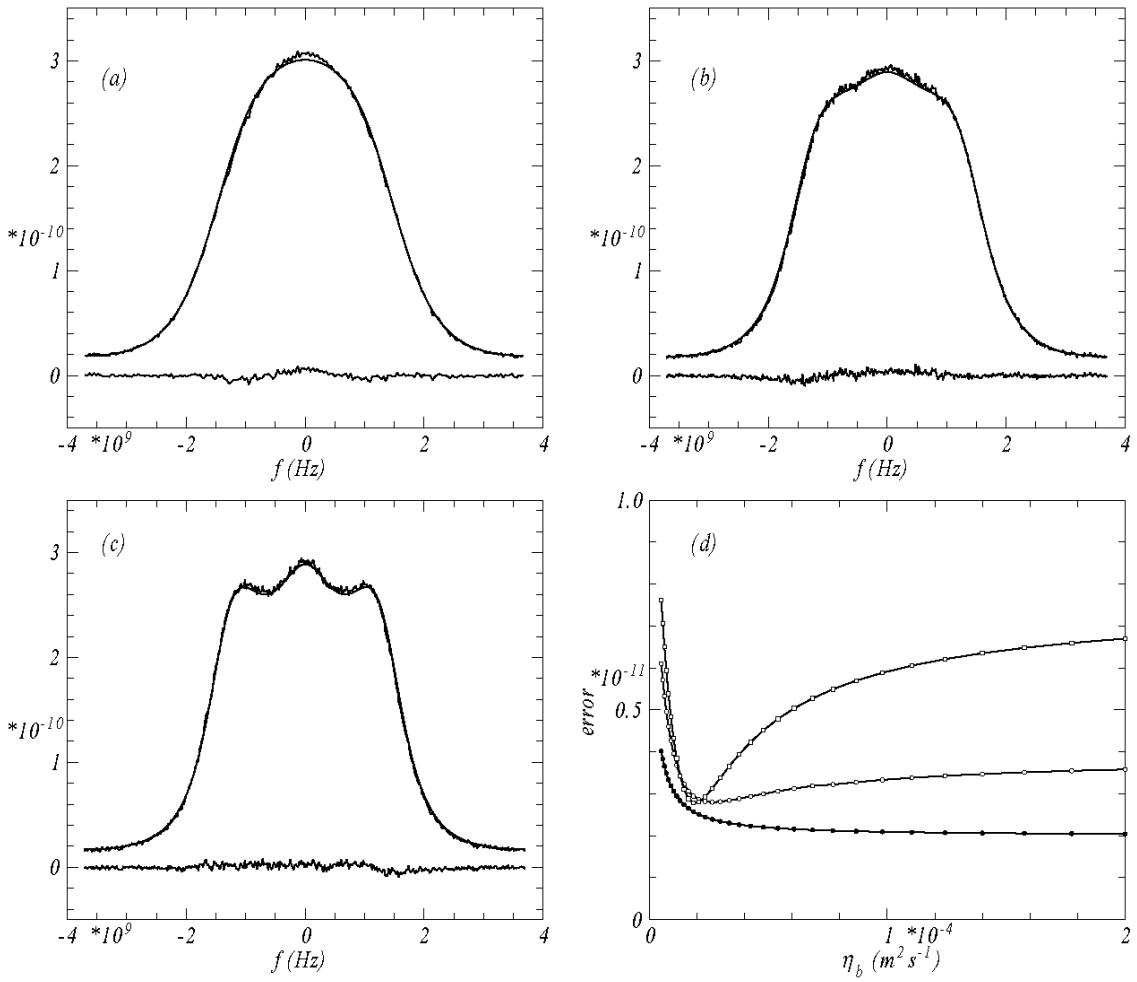

Figure 9-9: O_2 coherent Rayleigh-Brillouin scattering. (a) p = 1 bar, η_b = 2.021 x 10^{-5} kg $m^{-1}s^{-1}$ (the literature value); (b) p = 2 bar, η_b =2.021 x 10^{-5} kg $m^{-1}s^{-1}$; (c) p = 3 bar, η_b =2.021 x 10^{-5} kg $m^{-1}s^{-1}$, (d) Error as a function of η_b, dots, open circles and open squares, p = 1, 2, 3 bar, respectively.

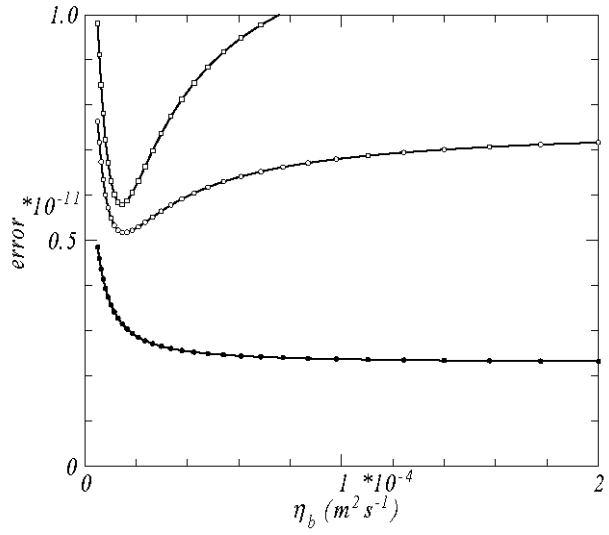

Figure 9-10: O_2 spontaneous Rayleigh-Brillouin scattering. Same as Figure 9-9(d), but now the error is for the Tenti S7 model. For all pressures considered, the S7 model has significantly larger errors.

9.8.2.2 Coherent Rayleigh-Brillouin scattering

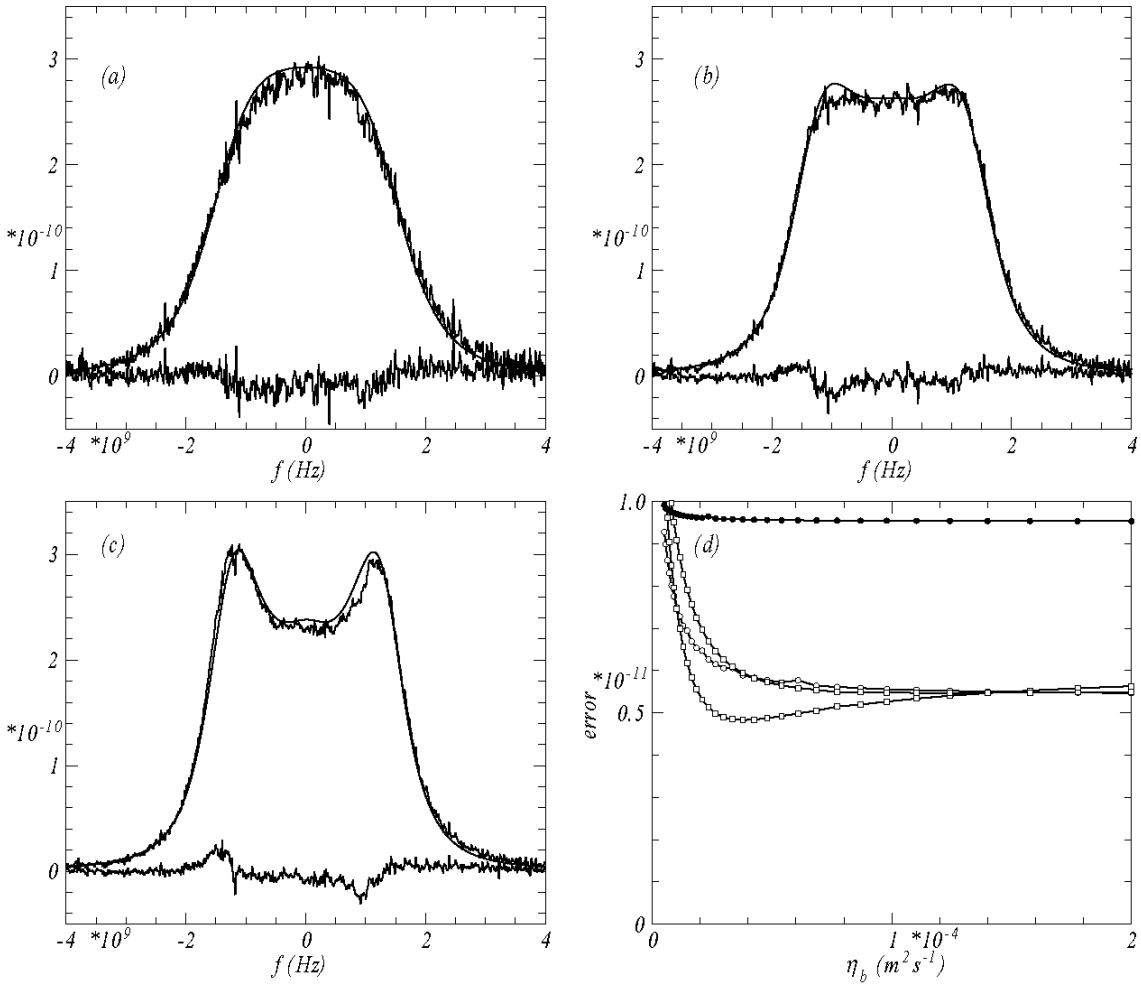

Figure 9-11: O_2 coherent Rayleigh-Brillouin scattering. (a) p = 1 bar}, η_b = 2.021 x 10^{-5} kg $m^{-1}s^{-1}$; (the literature value); (b) p = 2 bar}, η_b = 2.021 x 10^{-5} kg $m^{-1}s^{-1}$; (c) p = 3 bar, η_b = 2.021 x 10^{-5} kg $m^{-1}s^{-1}$. (d) Error as a function of η_b, dots, open circles and open squares, p = 1, 2, 3 bar, respectively. There are two different experiments for p = 3 bar.

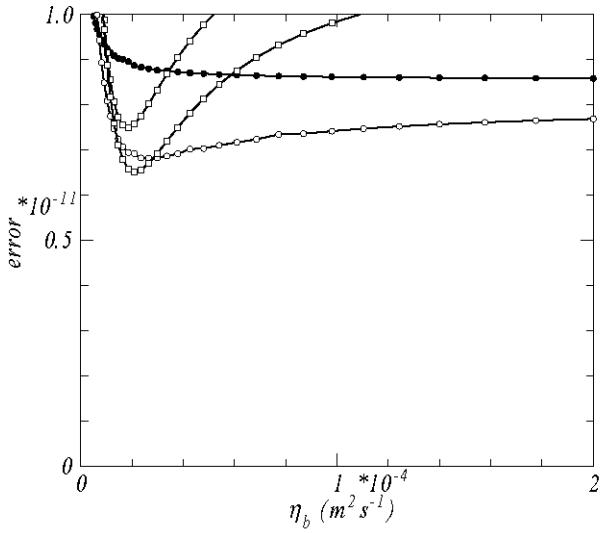

Figure 9-12: O_2 coherent Rayleigh-Brillouin scattering. Same as Figure 9-11(d), but now the error is for the Tenti S7 model. For all pressures considered, the S7 model has significantly larger errors. There are two different experiments for p = 3 bar.

9.8.3 Dry and humid air

9.8.3.1 Spontaneous Rayleigh-Brillouin scattering

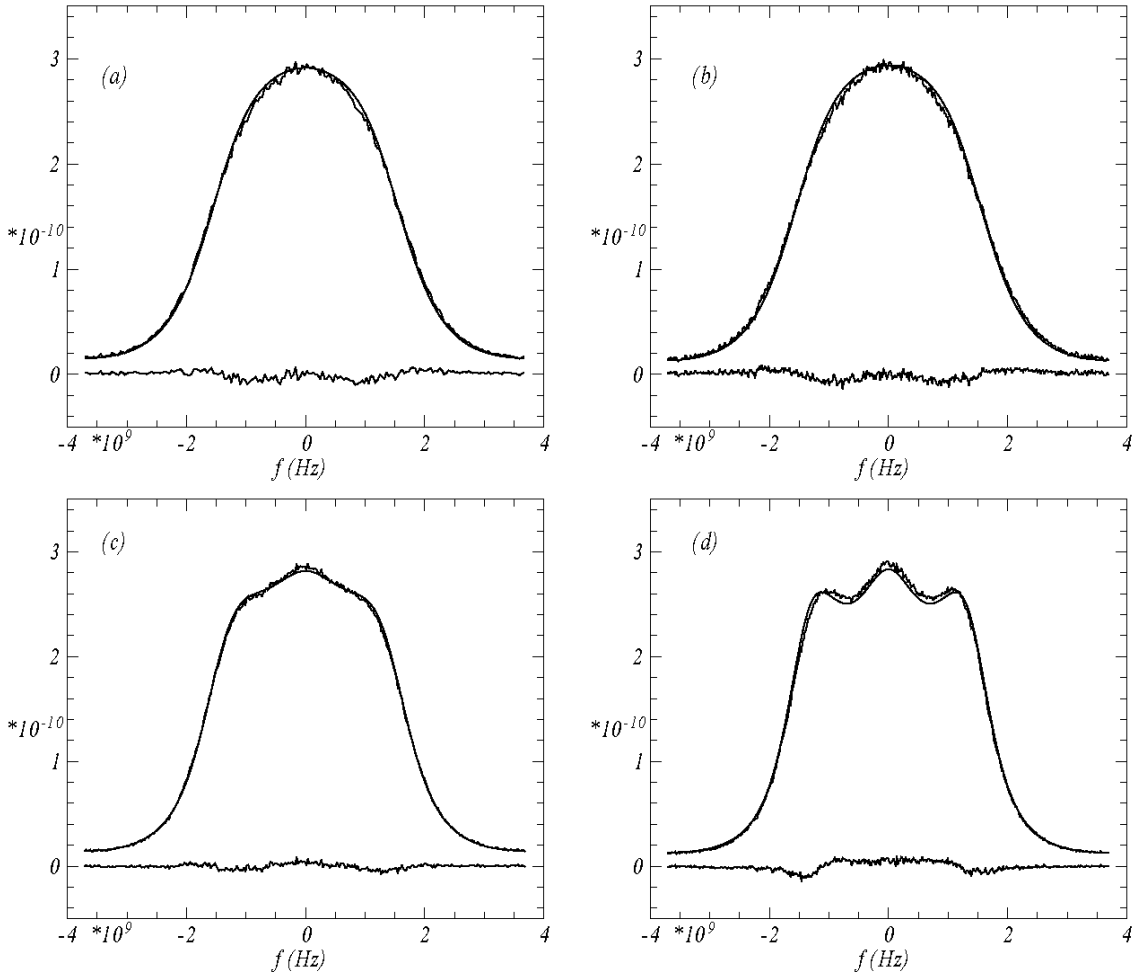

Figure 9-13: Dry and humid air, spontaneous Rayleigh-Brillouin scattering. (a) dry air p = 1 bar, η_b = 1.0881 x 10^{-5} kg $m^{-1}s^{-1}$ (the literature value); (b) air with 100% humidity, p = 1 bar, η_b = 1.088 x 10^{-5} kg $m^{-1}s^{-1}$; (c) dry air, p = 2 bar, η_b = 2 x 10^{-5} kg $m^{-1}s^{-1}$. (d) dry air, p = 3 bar, η_b = 2 x 10^{-5} kg $m^{-1}s^{-1}$.

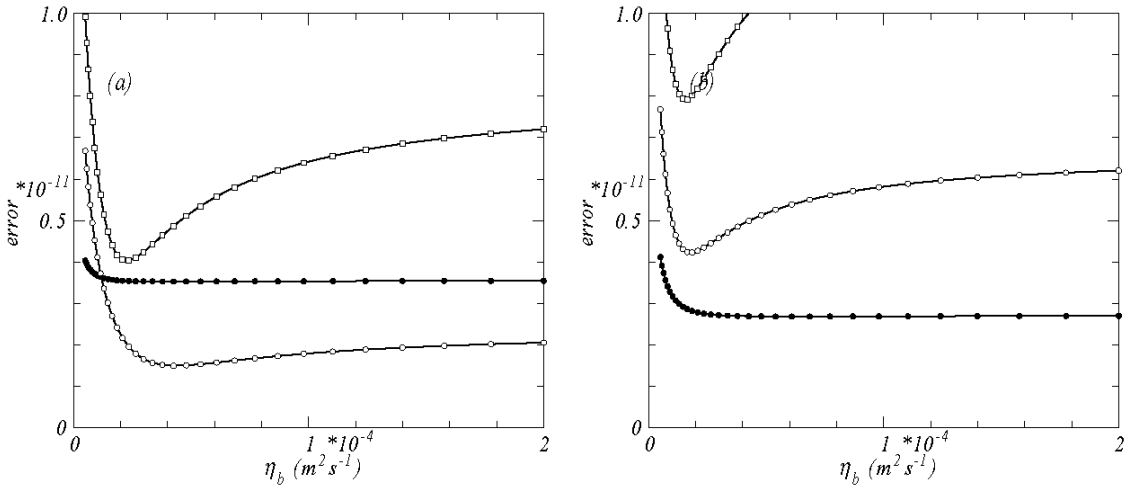

Figure 9-14: Dry air, spontaneous Rayleigh-Brillouin scattering. (a) Error of the S6 model as a function of η_b, dots, open circles and open squares, p = 1, 2, 3 bar, respectively.

From the spontaneous Rayleigh-Brillouin experiments on wet and dry air shown in Figure 9-13 and Figure 9-14 we conclude that the S6 model has a smaller error than the S7 model. Similar to our findings for N_2, all models indicate that a larger value for η_b has to be chosen than the literature value $\eta_b = 1.0881 \times 10^{-5}$ kg m^{-1}s^{-1}. We also conclude that at atmospheric pressure, no difference between wet and dry air can be observed. The best value for η_b for p = 2, 3 bar is the position of the minimum in Figure 9-14(a) for the p = 3 case. The computed p = 1 spectrum does not depend sensitively on η_b, so that we have computed it using the literature value $\eta_b = 1.0881 \times 10^{-5}$ kg m^{-1}s^{-1}.

9.8.3.2 Coherent Rayleigh-Brillouin scattering

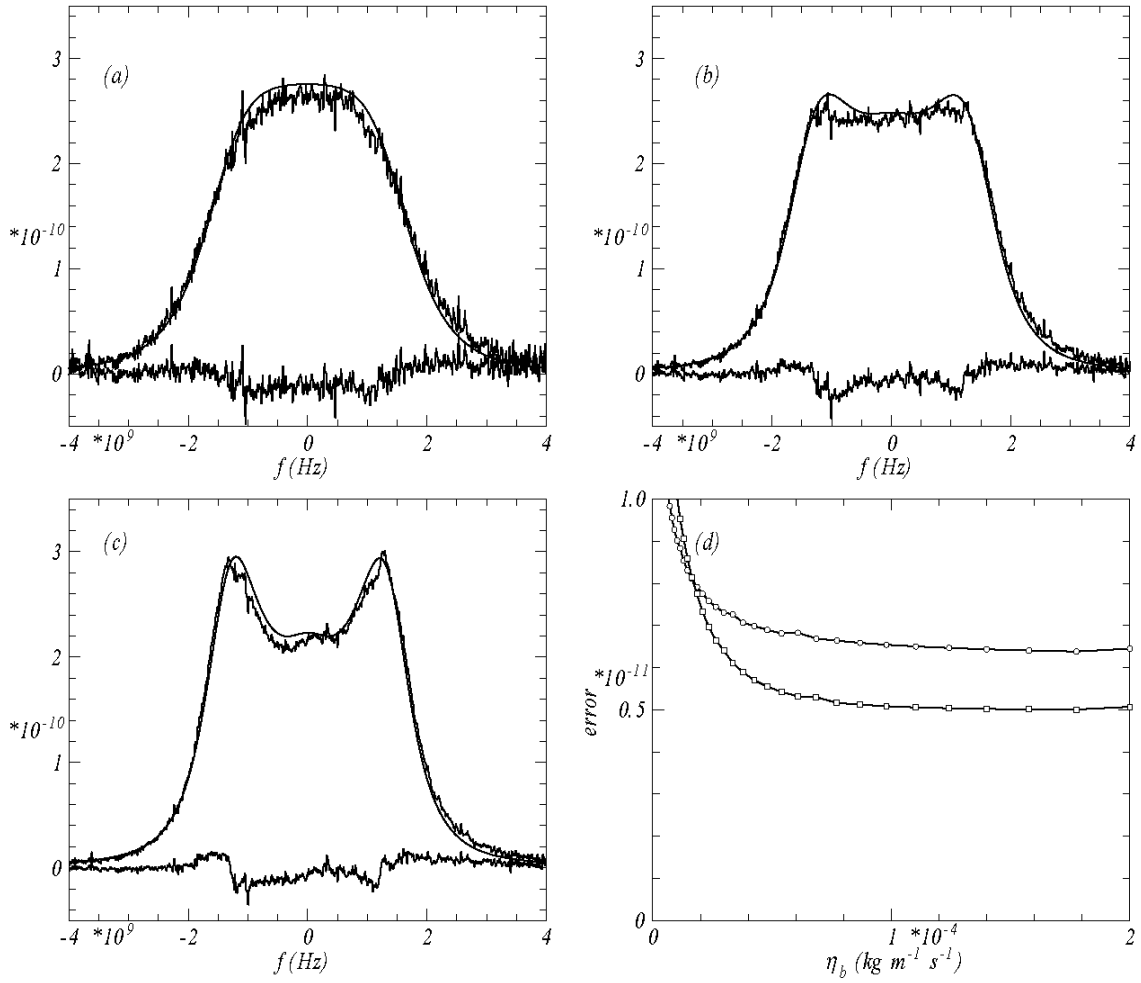

Figure 9-15: Dry Air, coherent Rayleigh-Brillouin scattering. (a) dry air p = 1 bar, η_b = 1.0881 x 10^{-5} kg $m^{-1}s^{-1}$ (the literature value); (b) dry air, p = 2 bar, η_b = 2 x 10^{-5} kg $m^{-1}s^{-1}$. (c) dry air, p = 3 bar, η_b = 2 x 10^{-5} kg $m^{-1}s^{-1}$. (d) Error as a function of η_b, circles and open squares, p = 2, 3 bar, respectively. Due to the large statistical fluctuations, the error for the p = 1 case is larger than 1 x10^{-11}.

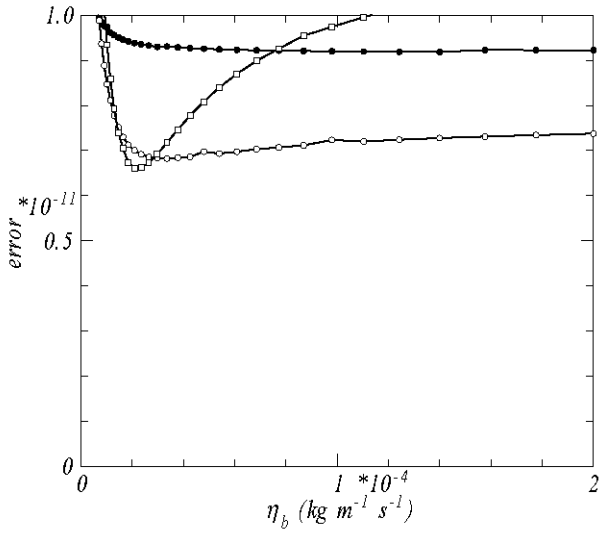

Figure 9-16: Dry Air, coherent Rayleigh-Brillouin scattering. Same as Figure 9-15 but now for the S7 model.

From the coherent Rayleigh-Brillouin scattering experiments on wet and dry air shown in Figure 9-14 and Figure 9-15, we conclude that the S6 model has a smaller error than the S7 model. Similar to our findings for N_2, all models indicate that a larger value for η_b has to be chosen than the literature value $\eta_b = 1.0881 \times 10^{-5}$ kg m^{-1}s^{-1}.

9.8.4 The Marquez mixture model

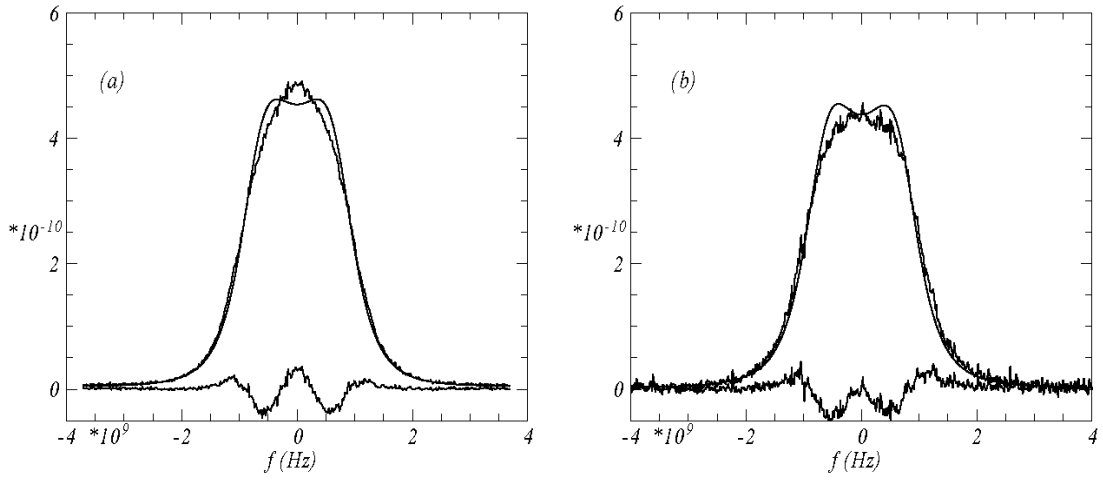

Figure 9-17: Krypton, p = 1 bar, comparison to the Marquez mixture model. (a) spontaneous Rayleigh-Brillouin scattering, (b) coherent Rayleigh-Brillouin scattering.

Successful comparisons of the mixture model by Marquez have been done for spontaneous Rayleigh-Brillouin scattering on mixtures of noble gases at high pressures [58], and for cohrent Rayleigh-Brillouin scattering on Ar with lowest pressure p = 1.5 atm [57]. Therefore no information existed for the accuracy of the mixture model at low pressures. This comparison has now been done in Figure 9-17, with the conclusion that the mixture model does not provide a good fit, not even to a single-component noble gas.

The input to the mixture model is the hard-sphere radius of the Kr atom. Whereas the shear viscosity computed by the model, η = 2.38 x 10^{-5} kg $m^{-1}s^{-1}$ compares favorably to the literature value (2.50), the heat conductivity from the model is a factor 2 smaller than the literature value. This also reflects in the poor representation of the experimental spectra at these relatively low pressures. Although the mixture model works better at high pressures, we will therefore not consider it further for this report.

9.9 Dependence of the Coherent Rayleigh-Brillouin scattering on pump laser intensity

In these experiments we will decide which of the two interpretations discussed in section 9.5 pertains. The problem is that for coherent Rayleigh-Brillouin scattering the pump laser intensity and spectrum fluctuates from shot to shot. Let us assume that we integrate over the spectral distributions. Let I_m^i be the spectrally integrated signal at shot *i*, similarly I_{pmp}^i is the pump, then, if the relation is linear,

$$I_m^i = I_{pmp}^i I_T \tag{9.22}$$

where I_T is the true TENTI-spectrum, we can simply average:

$$I_m^{(1)} = \frac{1}{N}\sum_{i=1}^{N} I_m^i = \left(\frac{1}{N}\sum_{i=1}^{N} I_{pmp}^i\right) I_T \tag{9.23}$$

where the I_p (the expression in brackets in the last term in Eq 9.23) is the reading on the power meter (assumed to be averaged over sufficiently long times).

However, if the dependence is quadratic:

$$I_m^i = \left(I_{pmp}^i\right)^2 I_T \tag{9.24}$$

we must average the square root of the signal:

$$I_m^{(2)} = \frac{1}{N}\sum_{i=1}^{N} \sqrt{I_m^i} = \left(\frac{1}{N}\sum_{i=1}^{N} I_{pmp}^i\right) \sqrt{I_T} \tag{9.25}$$

An experiment was performed in order to decide between the two hypotheses. At each average pump intensity setting, N = 500 spectra were measured and the averages $I_m^{(1)}$ and $I_m^{(2)}$ were plotted as function of I_p in Figure 9-18. The conclusion of this figure is that $I_m^{(2)}$ gives a better linearity which also passes through the origin. Therefore, the signal of coherent Rayleigh-Brillouin scattering depends quadratically on the pump laser intensity.

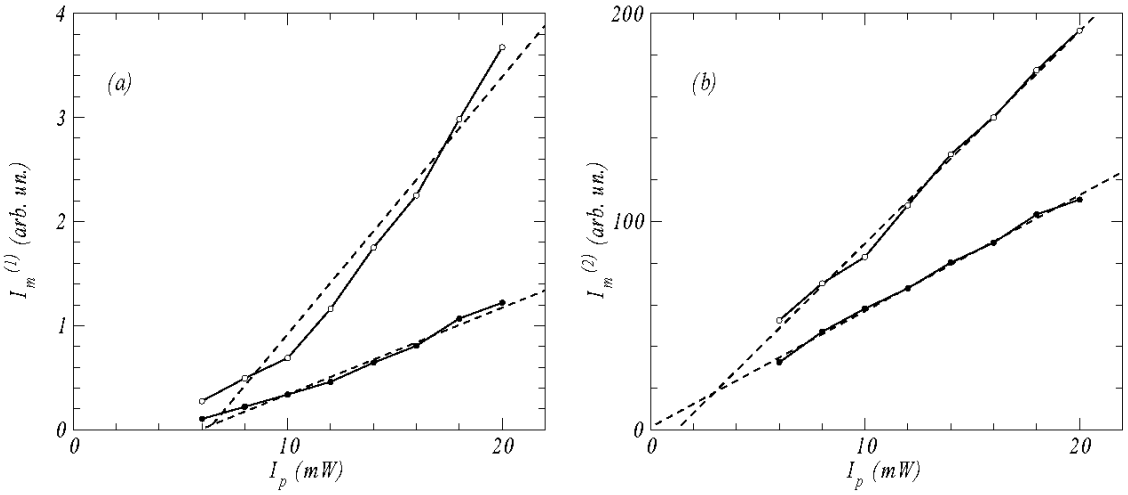

Figure 9-18: Coherent Rayleigh-Brillouin scattering signal versus pump power for N_2. (a) Plotting as linear dependence (Eq. 9.22), (b) Plotting as quadratic dependence (Eq. 9.24). In both figures: dots correspond to p = 2 bar and open circles to p = 3 bar.

9.10 Remark on Zheng's approach

The need to revisit line shape models for use in practical atmospheric light scattering was also felt by Zheng [5,54]. This work follows Tenti's approach, but now allows for rotational degrees of freedom by considering a different approximation to the linearized collision kernel. At the pressures relevant for this proposal, the effects were very small and no comparison was made to experimental results. However, the work's valuable message is that one should do things right first before devising practical line shape models. Indeed, what should be done right first in the present project is to devise collision models for mixtures of molecular species with internal degrees of freedom.

10 A program to compute the Tenti S6 model

In this project it has been concluded that the best model for both spontaneous Rayleigh-Brillouin scattering and coherent Rayleigh-Brillouin scattering is provided by the Tenti S6 model. The mathematics of which is elaborately and nicely didactically described by Pan [22]. In fact, most of our analysis effort went into models that did not work out in the end, and in the interface to the experiments.

The core part of the code, the part that computes the S6 model, has been kindly provided to us by Xingguo Pan and is in the file “pans6.for”. The Fortran code is described and listed in TN4 part 2 of this study. For further reading, please consult this TN. Pan gave the permission to place the source code on the ESA server, but only if no commercial use is intended. The main program is in the file “rbs.for”, it is listed in Appendix, the program that reads the data base is in “gas_data.for”. For further details, please consult TN4 part 2 from this study which contains a detailed descriptions of these files.

An object library {rbs.lib} contains the code with all models, a plasma dispersion function, and all code needed to compare to experiments.

This object library can be bypassed completely, and the entire program can be built from just the source files supplied. This is controlled by the compiler directive {bare}. However, in that case the program will only have the bare functionality that was agreed upon in the contracts: it will compute the S6 spectrum from the input parameters, and from the transport coefficients data base; there will not be any comparison with experimental data, nor convolution with instrument profiles. For a full description of the program we refer to the TN4 part 2 from this study (ESA –AO/1-5467/07/NL/HE-TN4, part 2).

11 RB scattering uncertainty effects on ADM-Aeolus winds

11.1 Introduction

As described in this report the molecular scattering functions of light in air are not just Gaussian profiles, depending only on the Brownian motion probability density function (PDF) of the gas mixture. In fact, all collisional properties of the molecular gas contribute to the scattering profile. In particular acoustic phenomena, known to produce the characteristic Brillouin side-wings on the molecular backscatter profile have a strong effect. The ESA study, ILIAD [1], showed that Brillouin scattering has an important contribution to atmospheric backscatter from Lidars. ILIAD showed that the neglecting of Brillouin scattering might result in errors in the Doppler wind measurements by ESA's Lidar mission, ADM-Aeolus, of up to 10% in several cases.

As shown in section 9, the Brillouin effect is best described by the so-called Tenti S6 model. In previous sections, the Tenti S6 and S7 models were validated against new experimental measurements of spontaneous and coherent Rayleigh-Brillouin scattering (RBS) in air for a set of pressures and temperatures representative for the Earth's atmosphere. In light of this Tenti model validation, the implications of the Brillouin effect on the ESA ADM-Aeolus mission are investigated here.

ADM-Aeolus uses a priori information on the molecular motion PDF to determine shifts in this distribution by the mean atmospheric motion, or wind. This is done by placing two Fabry-Pérot (FP) interferometers, each centered at one side of the molecular motion PDF, and measuring the normalized difference in signal detected by the two FPs. As the molecular motion PDF is shifted by the local atmospheric motion (wind), one of the FPs detects an increasing signal, while the other FP detects a decreasing signal (Figure 11-1).

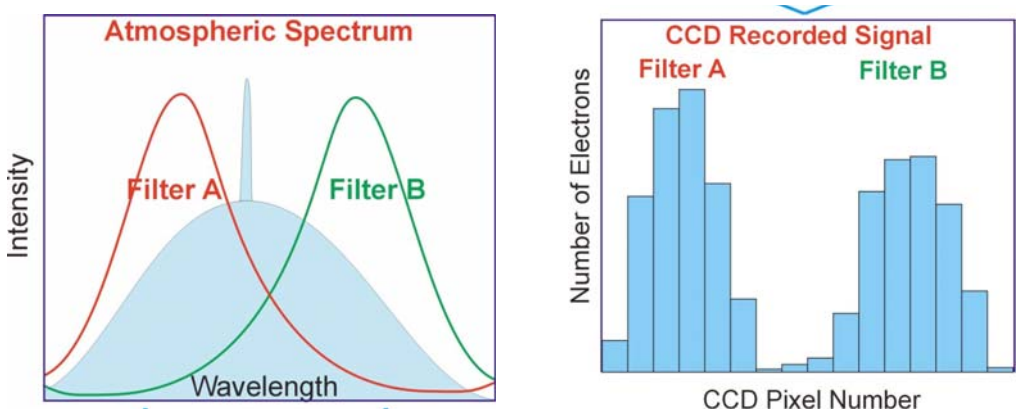

Figure 11-1: Detection of the Doppler shifted backscattered laser light (left panel) on the Aeolus Dual Fabry-Pérot detectors. CCD: Charge-Coupled Device. Note that the varying signal for the columns for filter A (or B) are not caused by a wavelength dependent transmission (as would be suggested by comparing with the spectrum in the left panel), but are a consequence of the circular shape of the spot in which the output signal of Filter A (or B) is projected onto the ACCD.

Following this effect, a response, which is the normalized difference in the FP signals, is defined. The response is (almost) proportional to the measured wind. The ADM-Aeolus detectors are time-gated, allowing the detection of a wind profile from 24 atmospheric layers throughout the atmosphere. In addition, the ADM-Aeolus instrument also contains a Fizeau spectrometer to resolve the Mie scattered light. A schematic view of the spectrometers is given in Figure 11-2.

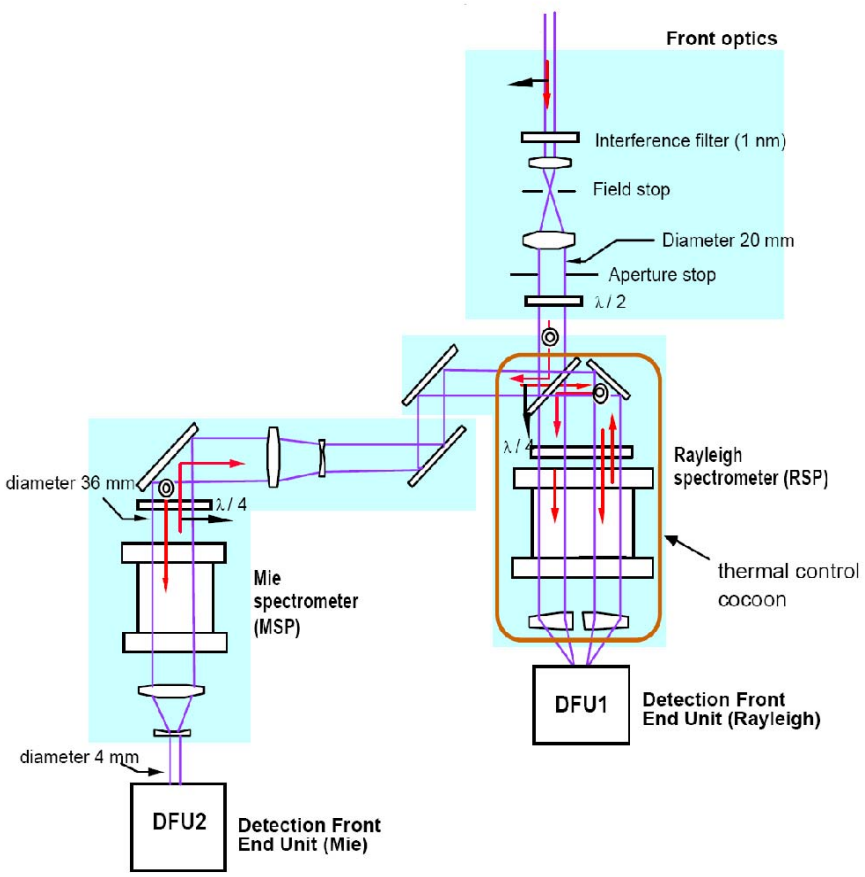

Figure 11-2: Schematic view of the Spectrometers used by ADM-Aeolus

It is important to note here that the light is first transferred to the Fizeau spectrometer (Mie signal detector). The light reflected from this Fizeau spectrometer is transferred to the first (direct) FP spectrometer. The remaining light, reflected from this first FP spectrometer, is finally transferred to the second (indirect) FP spectrometer. For more details on the Aeolus mission and measurement concept, see [61].

In the case that the exact shape of the Rayleigh-Brillouin (RB) molecular motion PDF is not precisely known, the interpretation of this normalized signal difference (response) as an integral shift of the RB spectral shape becomes uncertain. Here the effect of the uncertainty in the temperature and pressure dependent shapes of RBS on

the expected quality of the ADM-Aeolus wind profiles that will be retrieved by the L2b processing software is estimated. This is done by using the measured RB line shapes for a set of temperatures and pressures from the Spontaneous Rayleigh-Brillouin Scattering (SRBS) experiments at the VU University of Amsterdam and the updated version of the Tenti S6 code developed at the University of Nijmegen and Eindhoven (described in section 10).

The SRBS measurements, as performed with the novel UV-laser RB-spectrometer developed at VU, are described in section 11.3. The effect of the measured RBS line shapes on the Aeolus wind retrieval is presented in section 11.6. The measurements by the Coherent Rayleigh Brillouin Scattering (CRBS) experiment in Nijmegen were not used here because the SRBS measurements are more representative of the laser and the atmospheric conditions that will be encountered by Aeolus. However, it should be noted that the CRBS results are consistent with the SRBS results when compared to the Tenti S6 model, as concluded in the above.

At first a simple approach was followed, trying to convert the residuals between observation and theory from the VU to the ADM measurement geometry. In this approach the effect of convolution by the VU FP instrument function and the difference in wavelength was neglected, and the frequency axis was scaled by a factor sqrt(2) to account for the change in geometry. After discussions within the team it was felt this was not the right approach. The VU FP instrument function, the difference in wavelength and in geometry needed to be taken into account in a more systematic way. A relatively easy to implement solution was to use deconvolution of the data by the instrument function, and use the x parameter to scale the shape from one wavelength and geometry to the other. This new approach is the one described in the following sections.

This section is organized in the following manner:

- First the response functions of the Fabry-Pérot systems used at the VU experiment, and the system used in the ADM-Aeolus satellite are described (see section 11.2);
- Then a number of SRBS experiments for dry Air performed at the VU have been selected (see section 11.3);
- The measured spectra are then deconvolved to remove the effect of the Airy transmission function of the Fabry-Pérot spectrometer used in the experiment (see section 11.4);
- Using the measured temperature, pressure and geometry, the theoretical RB spectral shapes are calculated using the Tenti S6 and S7 models and, as a reference, also a Gaussian model. For these calculations, the new Tenti code presented in section 10 was used. Then the differences between modelled line shapes and the experiment (the residuals) are converted from the VU to the Aeolus geometry and wavelength (see section 11.5);
- These rescaled residuals are added to the Tenti model calculated RBS spectral shape for the ADM-Aeolus wavelength and geometry. The spectra are then Doppler-shifted to simulate a set of LOS wind velocities as measured by ADM-Aeolus.. Then the original (Tenti) and modified (Tenti + measurement residual) shapes are used to estimate the response as seen by the Aeolus Fabry-Pérot spectrometer for the above mentioned series of Line-of-Sight (LOS) wind velocities. The responses are then used to calculate the LOS wind deviations

(see section11.6);

- Finally, the results are summarized, some conclusions and recommendations are given and the application to the Aeolus L2B processing stage is discussed (see section 11.7).

11.2 Tenti Spectral Shapes

Both the experimental setup at the VU, and the ADM-Aeolus satellite, use Fabry-Pérot interferometers to detect the Rayleigh scattered light. However, apart from the different characteristics of the spectrometers themselves (as listed in Table 11.1), the ADM-Aeolus system also has a very different setup because the light is transferred from one spectrometer to the other (see Figure 11-2). This implies that the 3 spectrometers used in the ADM-Aeolus system all leave their signature in the detected spectrum once the light reaches the 3rd and last spectrometer.

	FSR	FWHM	peak transmission
VU FP	232 MHz	7440 MHz	1. (normalised)
ADM Direct FP	1666 MHz	10950 MHz	0.68
ADM Reflected FP	1666 MHz	10950 MHz	0.61
ADM Fizeau	2150 MHz	184 MHz	0.60
Some ADM specific settings:			
ADM FP spectral spacing		ADM Fizeau USR	
5475.1 MHz or 2.3 pm		1502 MHz	

Table 11.1: Some properties of the Fabry-Pérot and Fizeau spectrometers

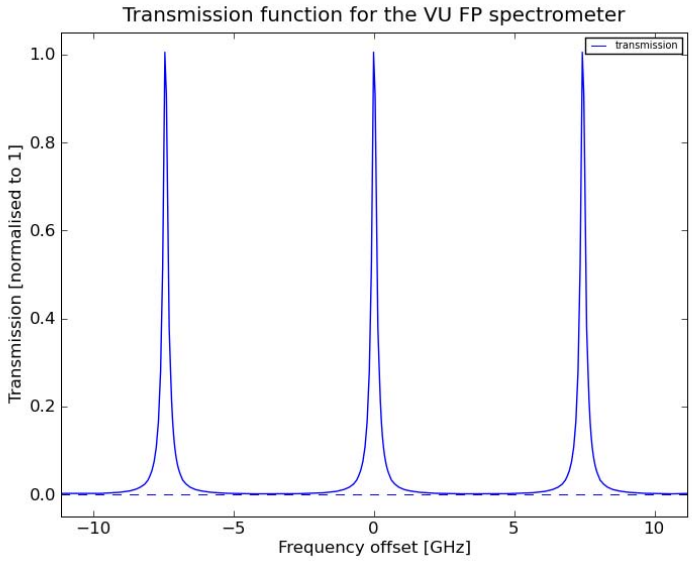

Figure 11-3: Airy function used to model the transmission of the VU FP spectrometer.

The response functions of the Fabry-Pérot systems used at the VU experiment are modelled using an Airy instrument function (see section 5.4.3) with FSR and FWHM as specified in Table 11.1. No additional Gaussian instrument error function has been applied (Figure 11-3). Note that this same response function is used in the deconvolution of all experiments described below. There has been some discussion on the validity of this approach. The perfect Airy function does not fit the height of the different measured FP instrument modes very well. This is solved by rescaling each mode again to a top value of one. However, this rescaling combined with measurement noise might introduce small deviations in the shape of the transmission peak if many modes are accumulated to obtain a better SNR. This might be investigated in more detail in a follow-up study, but in view of the available time of the current task it is not possible within this project. Therefore the following chapters assume a perfect Airy function describes the instrument function to sufficient detail.

The system used in the ADM-Aeolus satellite is far more complicated. The response of the FP spectrometer of ADM-Aeolus Doppler Wind Lidar receiver has been modelled by taking a copy of the implementation in the End-to-End Simulator (E2S) provided by ESA, and converting the Matlab code into Fortran (see [61] section 7.9 and 7.10).

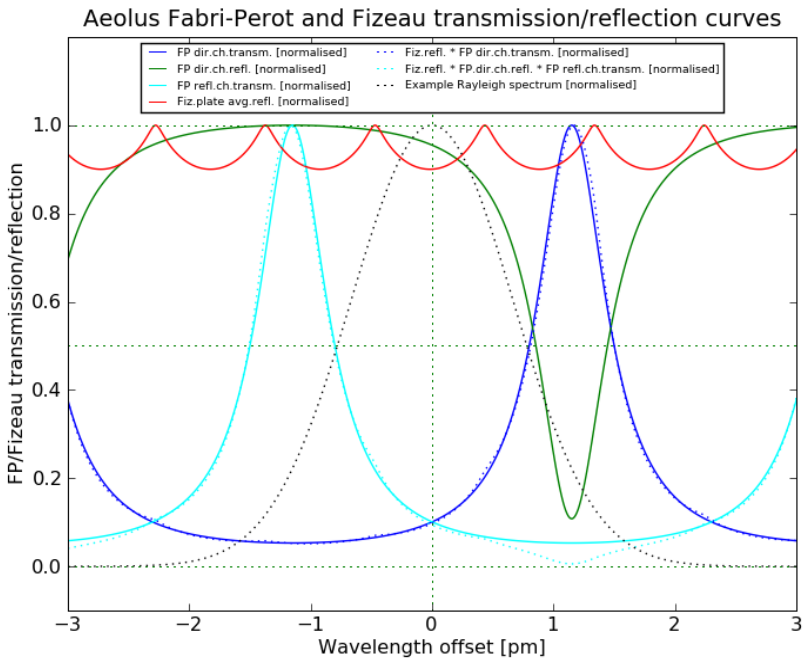

Figure 11-4: Simulated transmission and reflection on the active optical components used by the ADM-Aeolus detection system.

This includes the following steps:

- Calculate the reflection on the Fizeau plate, since this will be used as input for

the Fabry-Pérot spectrometer. This reflection depends on the location at the Fizeau plate on which the reflection occurs. At each location the transmission is assumed to have the shape of an Airy function, and the reflection is taken to be one minus the transmission.

- Since the FP transmission should not depend on the location of the light spot, the Fizeau reflection is now averaged over the whole Fizeau plate for each simulated frequency. This simplifies the calculations significantly, since otherwise some kind of ray-tracing procedure would be needed to proceed with the simulation. This reflection is illustrated in Figure 11-4 by the red wavy line just below the level of 1. The waves are caused by the periodicity of the Airy function, which causes a gradual shift in the number of periods that fit onto the Fizeau plate.
- The signal reflected on the Fizeau plate then enters the direct channel of the FP spectrometer, for which the transmission again is modelled as an Airy function (but with much broader Useful Spectral Range (USR) and FSR, see Table 11.1). Note that the USR is a specific Fizeau spectrometer property, since for that system the spectral range is determined by the size and geometry of the Fizeau plate, and not scanned as is done for the VU FP system. The transmission is given as the blue line in Figure 11-4, and the wiggly modulated dotted line around it depicts the combined Fizeau reflection and FP-direct channel transmission.
- The reflection from the first FP spectrometer is again taken to be one minus the transmission, and is shown as the green line in Figure 11-4.
- Finally the transmission for the reflected FP channel also is modelled using an Airy function (see the light blue line in Figure 11-4). The wiggly modulated line around it, going to zero close to 1.1 pm is the combined Fizeau reflection, direct-FP channel reflection and reflected-FP channel transmission.

Note here that all these lines have been scaled such that their maximum is at 1.

11.3 Selected experiments

A number of SRBS experiments for dry Air performed at the VU have been selected for this evaluation. Pressures range between 300 hPa and 1040 hPa, and have been chosen since these are realistic values that can occur in the real atmosphere as well.

There is not much temperature variation, since all these experiments where performed at room temperature. The gas mixture used to represent air was 79% pure N_2 and 21% pure O_2, representing dry air.

For convenience of referencing, the 9 selected experiments have been assigned the numbers 1 up to 9. An overview of the pressures and temperatures for the selected experiments is given in Table 11.2.

It has to be noted that experiment 4 was clearly contaminated by a Mie peak, and has been added on purpose, to study this effect and allow comparison with the other more clean cases.

Reference number	Pressure [hPa]	Tempera-ture [C]	Filename
1	300	24.8	Air_300mbar_scan20090625_06_7440MHz_res23.25MHz see section 7.3.1, case 1
2	503	25.7	Air_500mbar_scan20090617_02_7440MHz_res18.6MHz see section 7.3.2, case 1
3	504	24.8	Air_500mbar_scan20090625_07_7440MHz_res37.2MHz see section 7.3.2, case 2
4	500	23.5	Air_500mbar_mie_scan20091001_05_n_7440MHz_res25MHz see section 7.3.2, case 3
5	725	25.7	Air_725mbar_scan20090617_01_7440MHz_res37.2MHz see section 7.3.3, case 1
6	1040	23.5	Air_1000mbar_scan20090615_07_7440MHz_res18.6MHz see section 7.3.4, case 1
7	1040	22.9	Air_1000mbar_scan20090616_01_n_7440MHz_res46.5MHz see section 7.3.4, case 2
8	1040	25.0	Air_1000mbar_scan20090626_01_n_7440MHz_res37.2MHz see section 7.3.4, case 3
9	1008	24.0	Air_1000mbar_scan20090925_03_n_7440MHz_res25MHz see section 7.3.4, case 4

Table 11.2: Overview of the parameters for the selected experiments.

11.4 Deconvolution of the experimental data

The measured spectra are a convolution of the real spectral shape (modelled by the Tenti model) and a FP transmission function. To study the difference between Tenti model and experiments the measured spectra thus need to be deconvolved to remove the effect on the spectrum of the Airy transmission function of the Fabry-Pérot spectrometer used in the experiment. This deconvoluted spectrum is subsequently used to rescale to the different Aeolus geometry and wavelength (see next section). Such rescaling cannot be done on the actual measured signal because of the large difference in the properties of the spectrometers used for both cases (see Table 11.1) and because of the large effect of the FP properties on the measurements.

In theory deconvolution is a simple division in the Fourier domain, i.e. calculate the Fourier transformations of the spectrum and the instrument function, divide one by the other, and do an inverse Fourier transform.

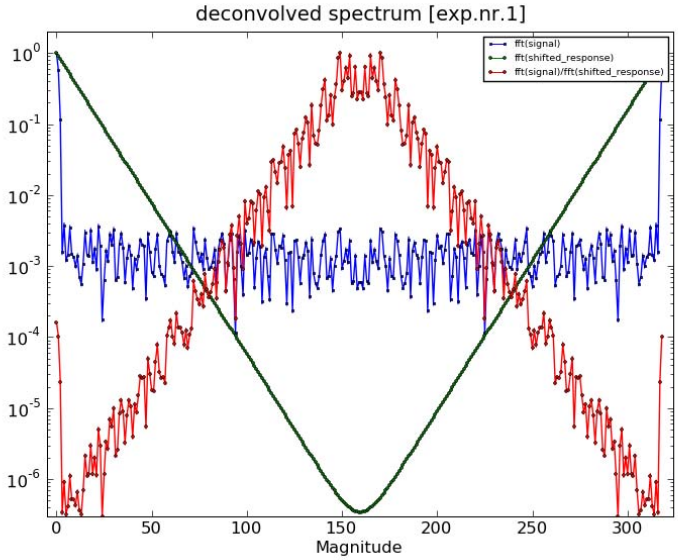

Figure 11-5: Illustration of deconvolution without filtering (see text).

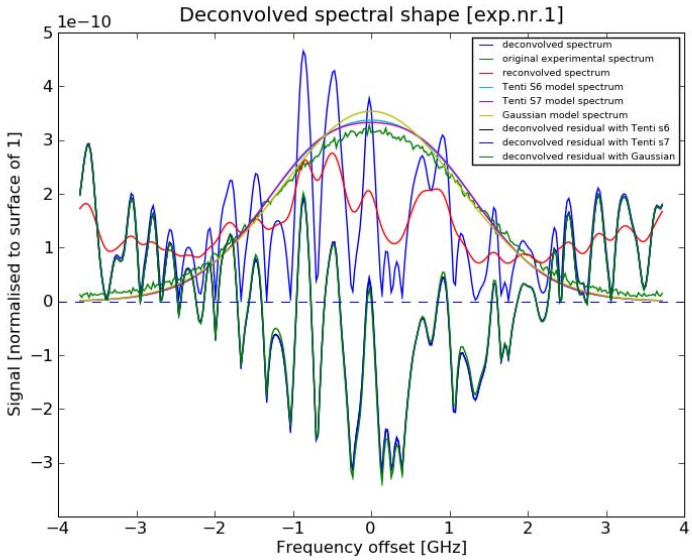

Figure 11-6: The resulting not well-behaved deconvoluted spectra (see text).

However this might work well for nicely defined theoretical functions, when applied to noisy data, this procedure is bound to fail. It usually strongly amplifies the Fourier terms that correspond to the higher frequencies, and in the end, the deconvolved signal seems to contain only noise. This is illustrated in Figure 11-5 and Figure 11-6. In Figure 11-5 the blue line indicates the Fourier transformed spectrum, the black line indicates the Fourier transformed transmission function, and the red line indicates the division between the two. Clearly the higher frequencies between 100 and 200 become dominant. The resulting deconvolved spectrum as shown in Figure 11-6 clearly cannot

be used for further analysis. The meaning of the different lines in this figure are explained in detail in the next section. This can be solved by applying filtering in the Fourier domain, which attenuates the higher frequencies and does not alter the lower frequencies too much.

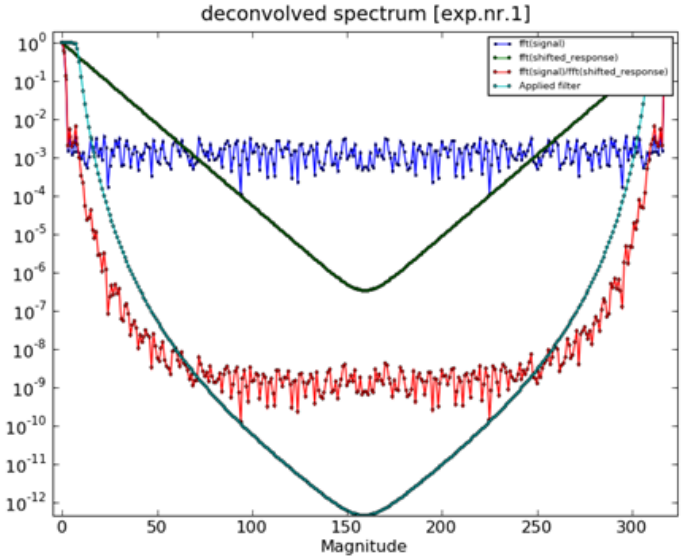

Figure 11-7: Illustration of the effect of filtering on the deconvolution.

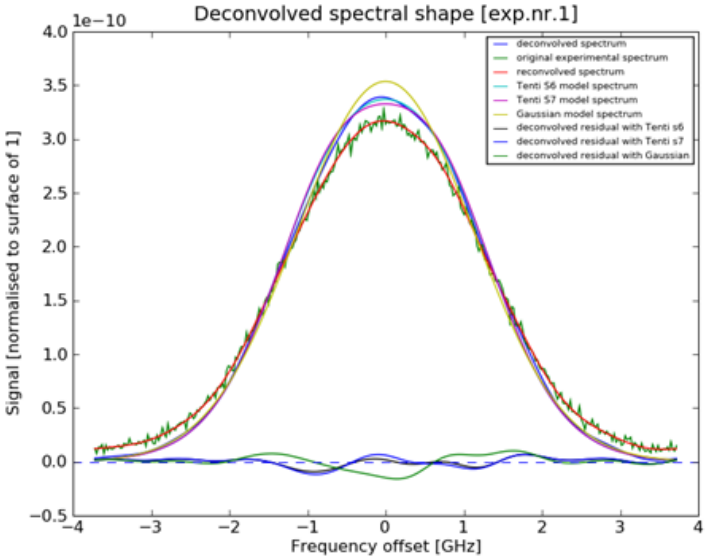

Figure 11-8: The resulting deconvoluted spectra.

For the current study a Butterworth filter has been applied on the Fourier terms, just before doing the inverse Fourier transform. The filter settings have been found by

trial and error, and eventually the settings used are a filter order of 9, and a -3dB location of 0.025 (this is after rescaling the Fourier domain to the range 0 - 1.0). When using these settings, no additional smoothing was needed to remove noise. The shape of the filter transmission is illustrated in Figure 11-7 as the light-blue line. The effect is clearly visible on the red curve, which now strongly suppresses all high frequency terms. The resulting deconvoluted spectra now look very clean and should be suitable for further analysis.

Finally, note that the offset correction that has been implemented in the rbs fitting program has not been applied here. This sometimes may lead to problems, which is further discussed in the conclusions (section 11.7).

11.5 Determination and rescaling of the residuals

The SRB measurements resulted in a residual, i.e., the difference between expected (Tenti modelled) and measured spectral shapes. This residual presents the remaining uncertainty after the measurements and here we attempt to compute its effect in the Aeolus geometry. An overview of the steps taken for each of the 9 experimental cases is given in the flow-diagram presented in Figure 11-9.

A stepwise description of the implemented method is:

1. Step a: Using the measured temperature, pressure and the geometry and wavelength of the VU experiment (365 nm, 90^o scattering), the expected spectral shapes are calculated using the Tenti S6 and S7 models and, as a reference, also a Gaussian model. This is done by running the rbs program (section 10).
2. Step b: the y-parameter (reduced wavelength) is retrieved from the outputs of the fit program as has been run in step a.
3. Step c: then the rbs program is run many times in a loop to allow finding a pair of T, p values for the ADM-Aeolus geometry that result in the same y-value as was retrieved in step b (typically it runs about 250 times). This is needed to ensure the spectrum has a comparable shape for both geometries, which may have an influence on the shape of the residual. For the first experiment at first the temperature was scanned manually, and a value of -50 °C was found to give a very close match of y-parameter. Then, the pressure was scanned in an automated way. This has less influence on the y-parameter than the temperature, but still it was possible to adjust the y-parameter to the slightly varying temperatures in the experimental VU setup, by only adjusting the pressure. The temperature and pressure values found are reported in Table 11.3.
4. Step d: the VU Fabry-Pérot instrument transmission function is calculated, assuming it can be modelled by an Airy function (see sections 11.2 and 11.7 for some discussion on this assumption).
5. step e: the x-parameter array (reduced frequency), the actual frequency array and the measured data from the VU experiment are retrieved from the output files of the rbs program as was run in step a.
6. Step f: the measured data is deconvolved using the instrument function calculated in step d, and using the method described in Section 11.4 above.
7. Step g: the deconvolved data is convolved again with the mentioned instrument function to verify the procedure does not introduce too severe loss of information content.

8. Step h: retrieve the theoretical Tenti spectra (Gaussian, S6 and S7) from the outputs of the rbs program, as was run in step a.
9. Step i: combine the theoretical spectra and the deconvolved data into the residual curves (i.e., the difference between deconvoluted experiment and theory), and calculate the asymmetry for these curves. The results of this procedure are displayed in Figure 11-10 to Figure 11-18. These figures show in the upper panel the measured spectrum (green line), the deconvolved spectrum (blue line), the reconvolved spectrum (red line), the model spectra (Tenti S6, light blue line, Tenti S7, purple line, Gaussian, yellow line), and the residuals in the lower panel (for Tenti S6, blue line, Tenti S7, green line, Gaussian, red line). Note that the y-axis scaling was determined by calculating the surface below the spectrum, and setting it to a value of 1. In this part this was done using a frequency in Hz, rather than in GHz, which explains the difference in y-axis scale of the plots presented e.g. in Section 7. To check the consistency of the deconvolution procedure, the deconvoluted spectrum has been convolved again with the instrument function (see step g) and overplotted in this figure. This clearly shows any problems in the deconvolution that might occur. A deconvolution that has some clear problems is for example the one for experiment 4, see Figure 11-13. For this case the deconvolved spectrum does not seem to go to zero for frequencies with larger offset. This may be related to the presence of Mie contamination in this experiment, or to the fact that we did not take the offset (deviation from the zero level) in the data into account.
10. Step j: run the rbs program using the temperature and pressure estimated for ADM-Aeolus in step c above, and the geometry and wavelength of ADM-Aeolus (355 nm, 180^{o} scattering angle), and calculate the expected spectral shapes using the Tenti S6 and S7 models, and as reference also for the Gaussian model.
11. Step k: retrieve the x-parameter array (reduced frequency), the frequency array, and the theoretical Tenti spectra (Gaussian, S6 and S7) from the outputs of the rbs program, as was run in step j.
12. Step l: resample the deconvoluted residuals (calculated in step i), from the x-array retrieved in step e, onto the x-array retrieved in step k. Undefined parts of the range are set to zero.
13. Step m: translate the x-array to frequency for the ADM-Aeolus geometry and add the resampled deconvolved residual (for Tenti S6 or Tenti S7) to the theoretical Tenti spectrum for the ADM-Aeolus geometry (for Tenti S6 or Tenti S7). For the Gaussian residual a slightly different approach was chosen, to enable comparison with the earlier results presented in the ILIAD report [1]. In this case the Tenti S6 spectral shape was taken as “truth” and then the Gaussian residual was added to that.
14. Step n: then the transmission function for the both Fabry-Pérot spectrometers of ADM-Aeolus is calculated (as described in Section 11.2).
15. Step o: finally a loop over a range of LOS wind values between -100 and 100 m/s in steps of 10 m/s was performed and for each wind velocity the LOS wind error was estimated by executing steps p to t. This loop is indicated by the box in the flow diagram in Figure 11-9.
16. Step p: the theoretical and the perturbed ADM-Aeolus spectra determined in step m are then shifted in frequency to reflect the Doppler shift for the current wind. Figure 11-19 shows an example of such shifted spectra.
17. Step q: for each Fabry-Pérot spectrometer of ADM-Aeolus the signal is calculated

by applying the transmission function determined in step n with the Doppler shifted perturbed spectrum determined in step p. From this the response R is calculated as is detailed in section 11.6 below. Figure 11-20 shows an example of the responses found for experiment 9.

18. Step r: the response (as function of LOS wind) derived from the theoretical spectrum is then numerically inverted to yield a function of LOS wind (as function of response)
19. Step s: now the response determined from the perturbed spectrum (calculated in step q) is inverted back to wind again, using the inverted response (calculated in step r).
20. Step t: finally the perturbed LOS wind found in step s is compared to the input LOS wind assumed in step o. The difference should give an idea how the ADM-Aeolus system responds to deviations in the spectral shape similar to the residuals that have been observed in the VU experiments.

	VU-geometry and wavelength			ADM_Aeolus-geometry and wavelength		
	scattering angle [degrees]		wavelength [nm]	scattering angle [degrees]		wavelength [nm]
	90.0		366	180.0		355
Reference number	Pressure [hPa]	Temperature [C]	y-parameter value	Pressure [hPa]	Temperature [C]	y-parameter value
1	300	24.8	0.1628	300.4	-50.0	0.16282
2	503	25.7	0.27198	501.8	-50.0	0.27197
3	504	24.8	0.27351	504.6	-50.0	0.27349
4	500	23.5	0.27285	503.4	-50.0	0.27284
5	725	25.7	0.39202	723.3	-50.0	0.39203
6	1040	23.5	0.56753	1047.1	-50.0	0.56752
7	1040	22.9	0.56899	1049.8	-50.0	0.56899
8	1040	25.0	0.5639	1040.4	-50.0	0.56389
9	1008	24.0	0.54889	1012.7	-50.0	0.54888

Table 11.3: Overview of the temperatures and pressures used for the ADM-Aeolus geometry and wavelength to ensure the y-parameter value matches with the VU case.

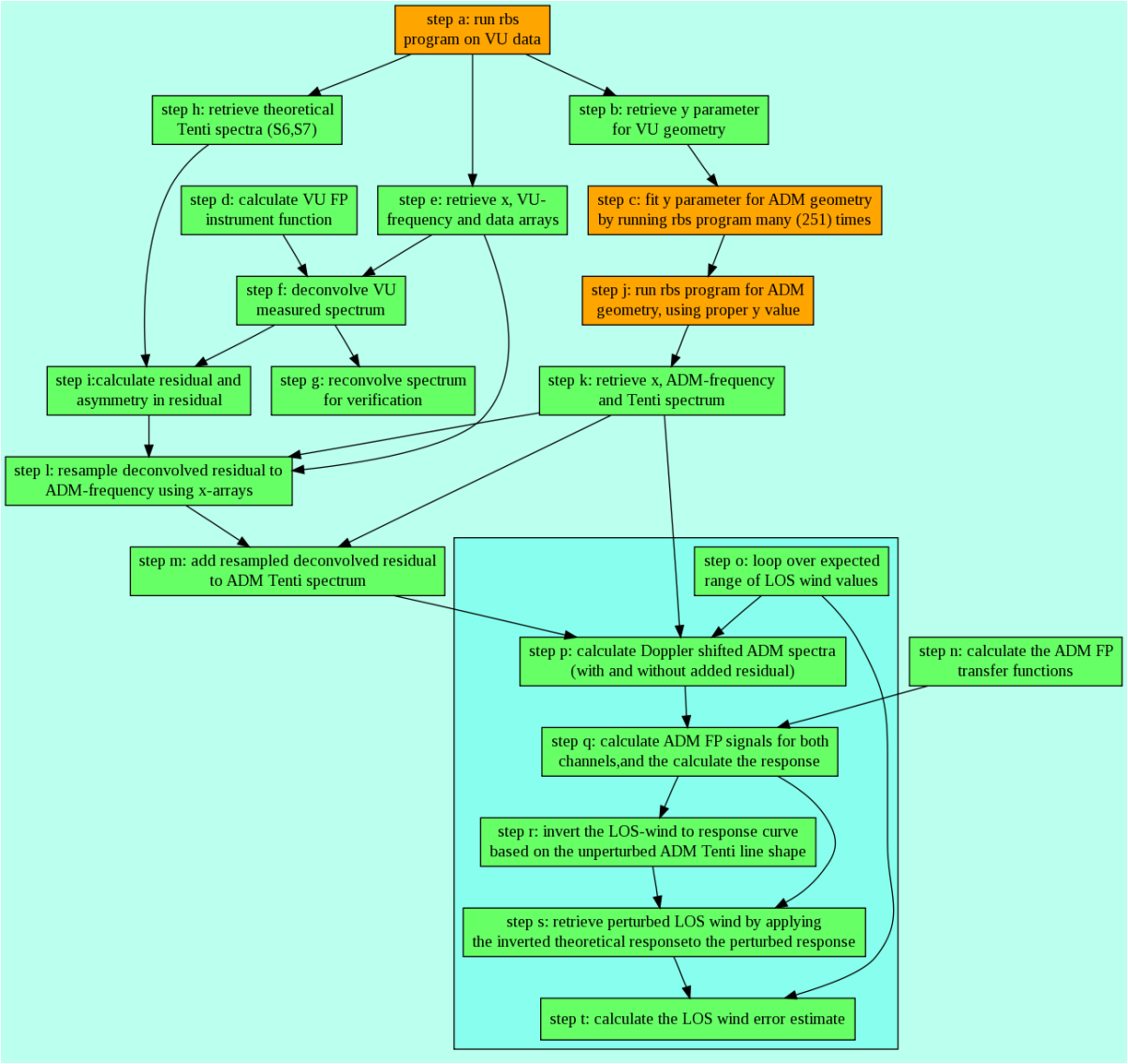

Figure 11-9: Flow-diagram of the steps needed to estimate the expected uncertainty in the LOS wind due to the uncertainty (residual) in the spectral shape.

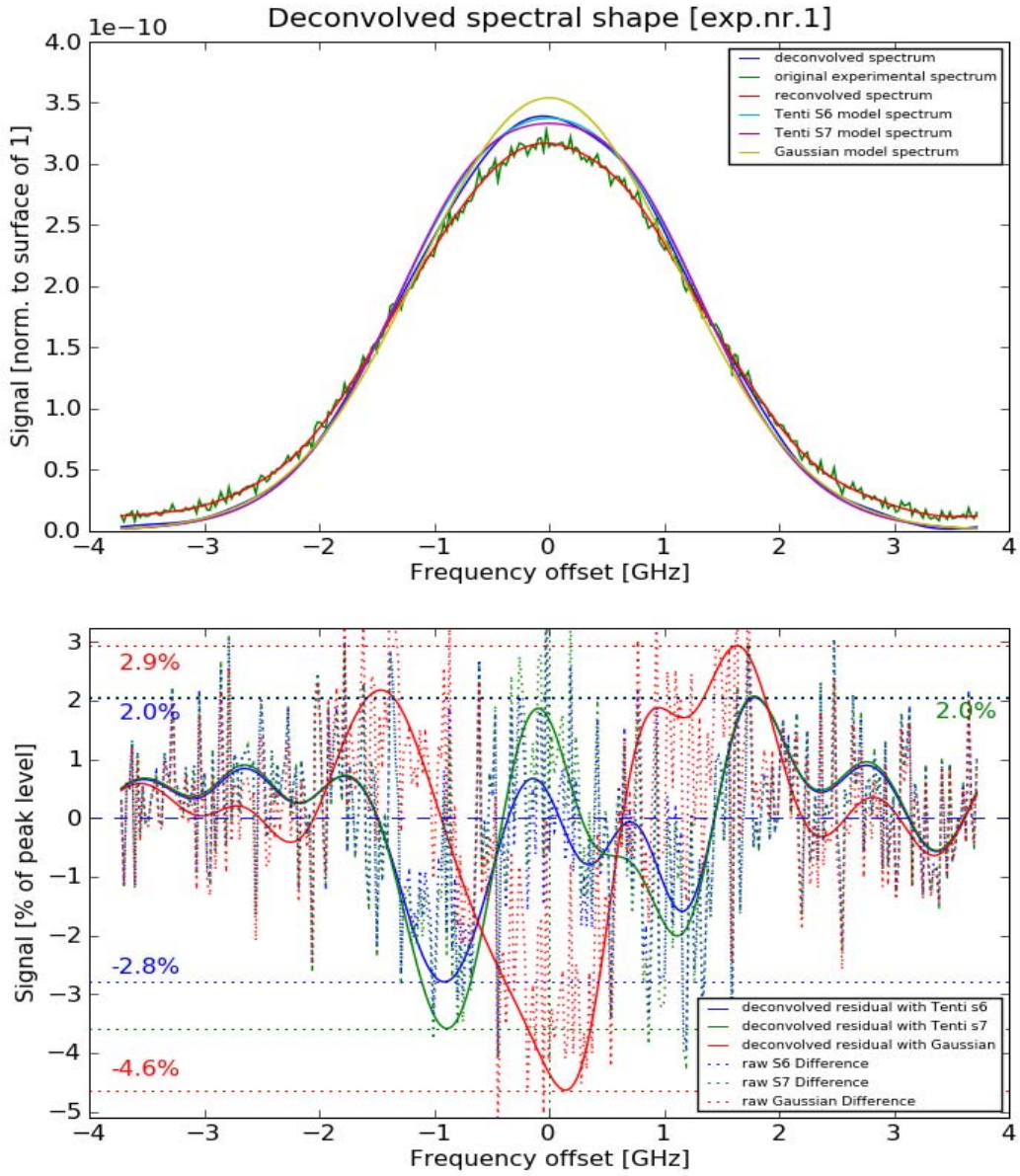

Figure 11-10: Deconvolution and residual calculation for experiment number 1 (pressure 300 hPa)

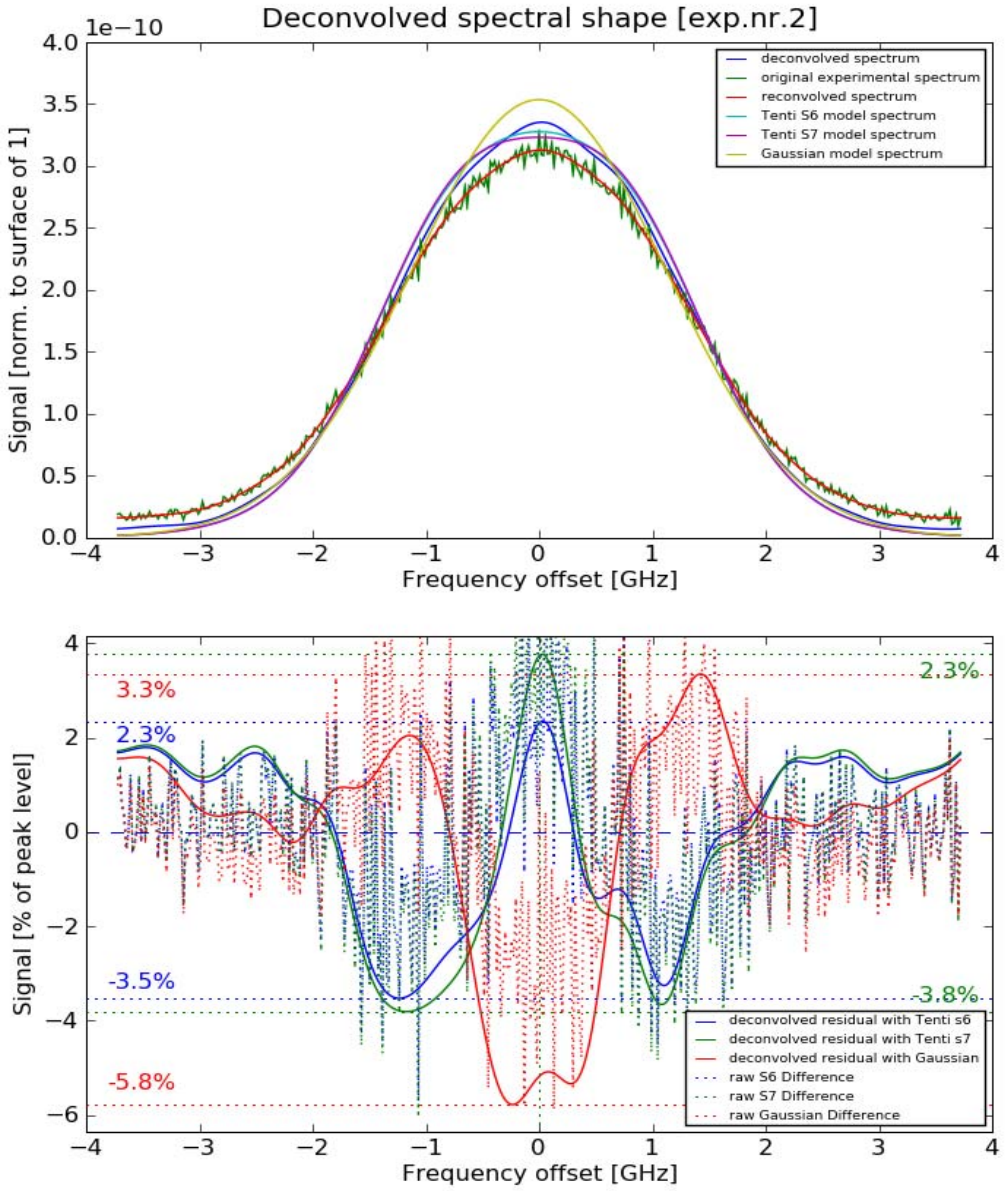

Figure 11-11: Deconvolution and residual calculation for experiment number 2 (pressure 503 hPa)

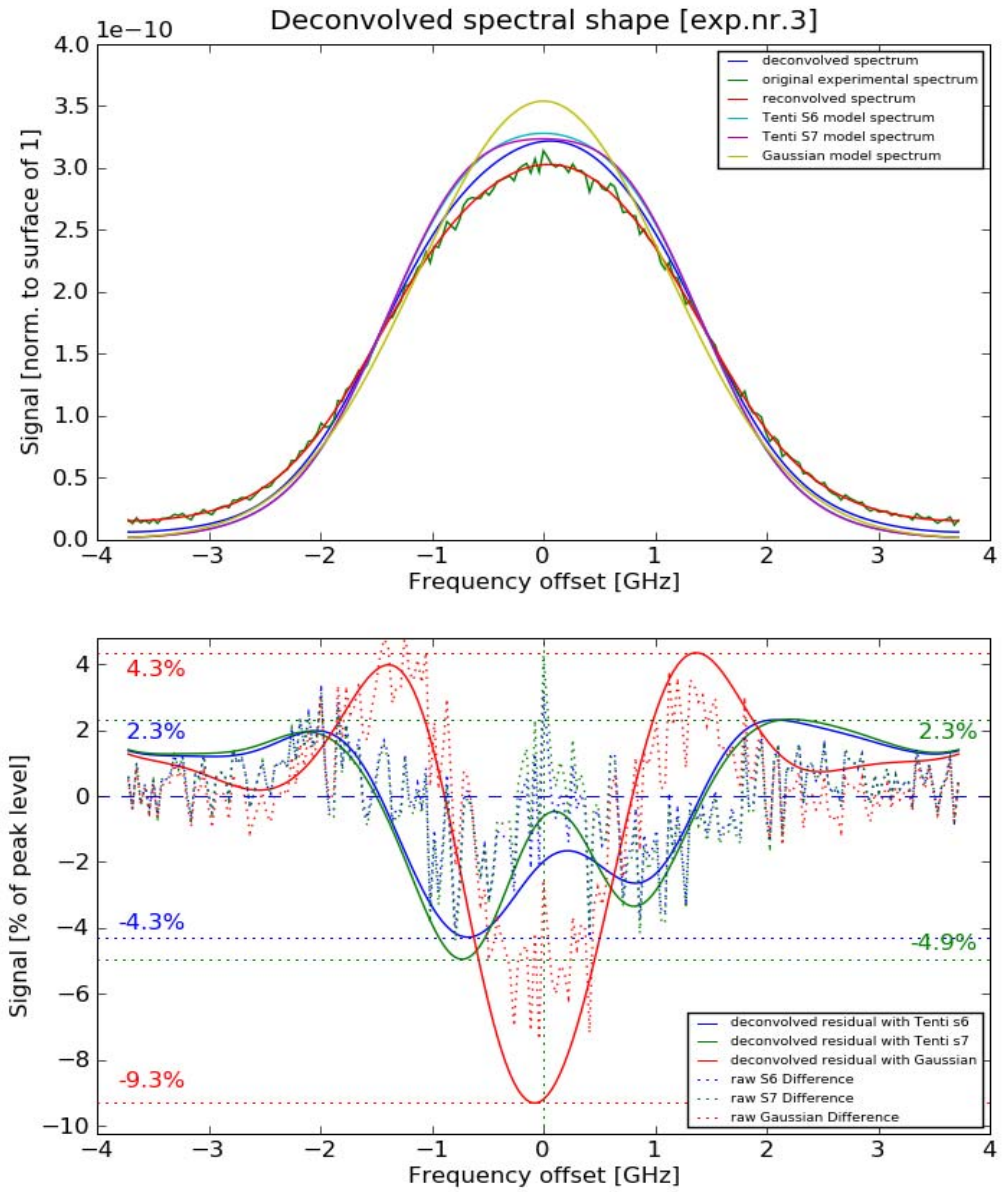

Figure 11-12: Deconvolution and residual calculation for experiment number 3 (pressure 504 hPa)

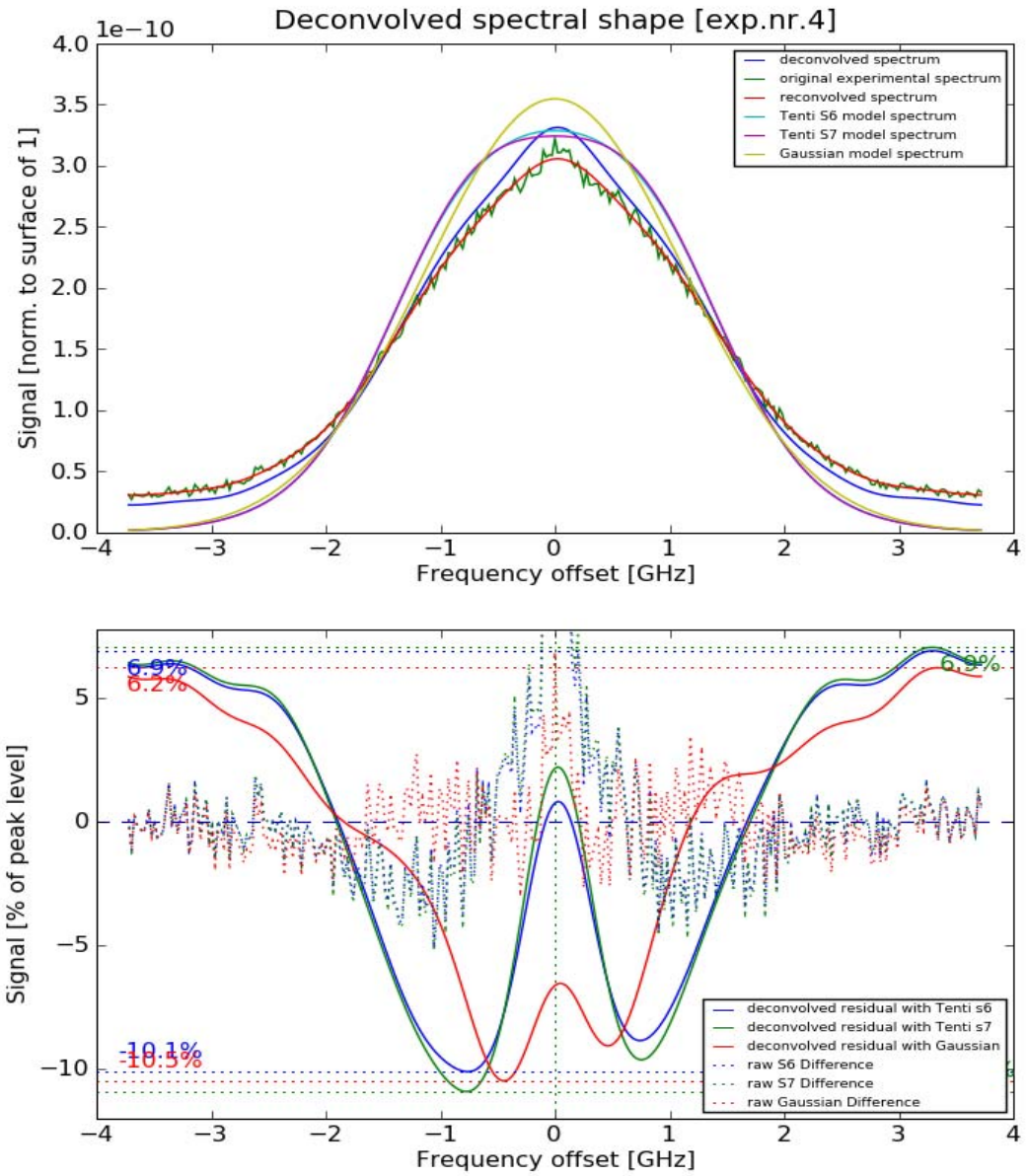

Figure 11-13: Deconvolution and residual calculation for experiment number 4 (pressure 500 hPa). Note that this experiment clearly suffered from some Mie contamination.

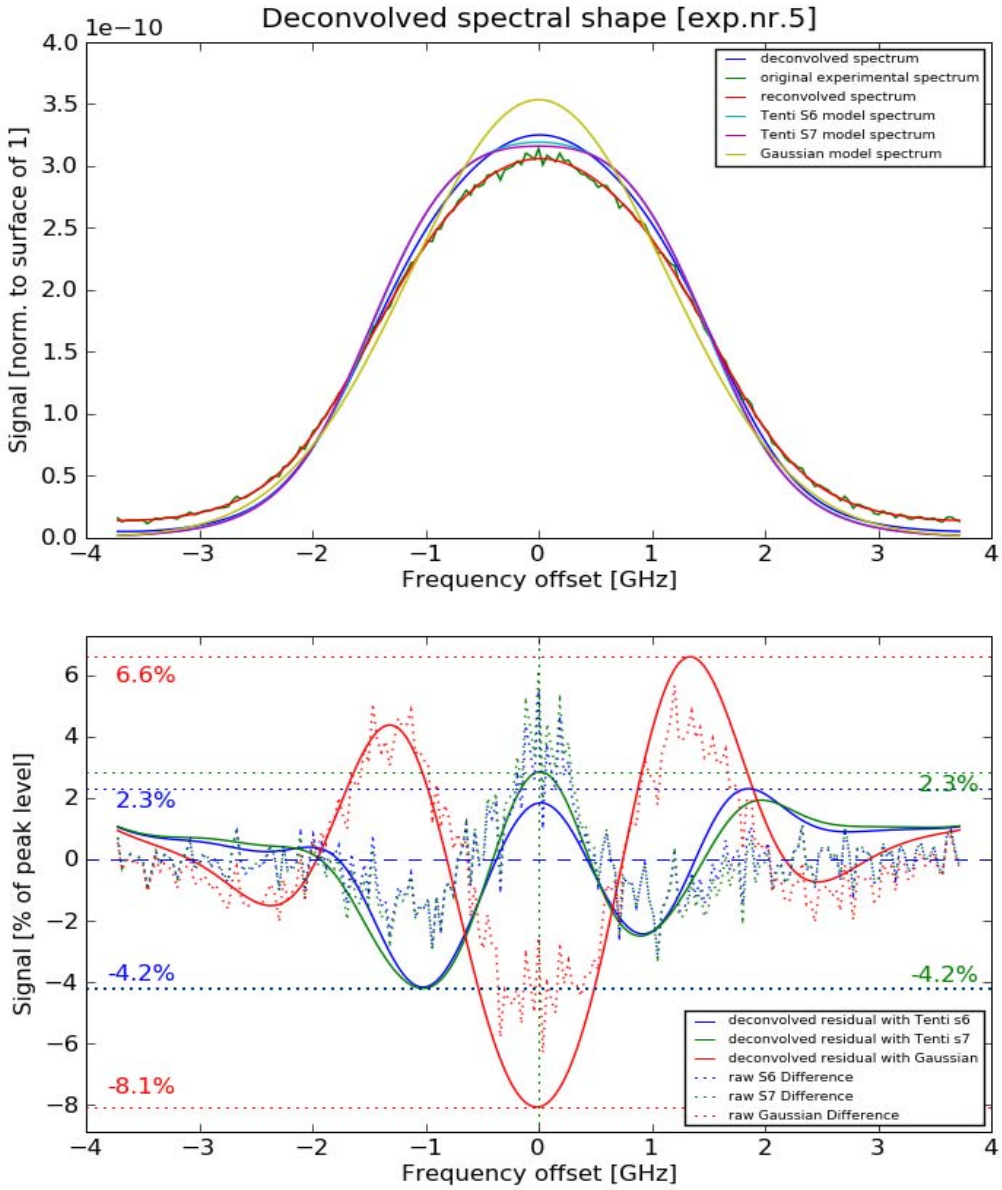

Figure 11-14: Deconvolution and residual calculation for experiment number 5 (pressure 725 hPa)

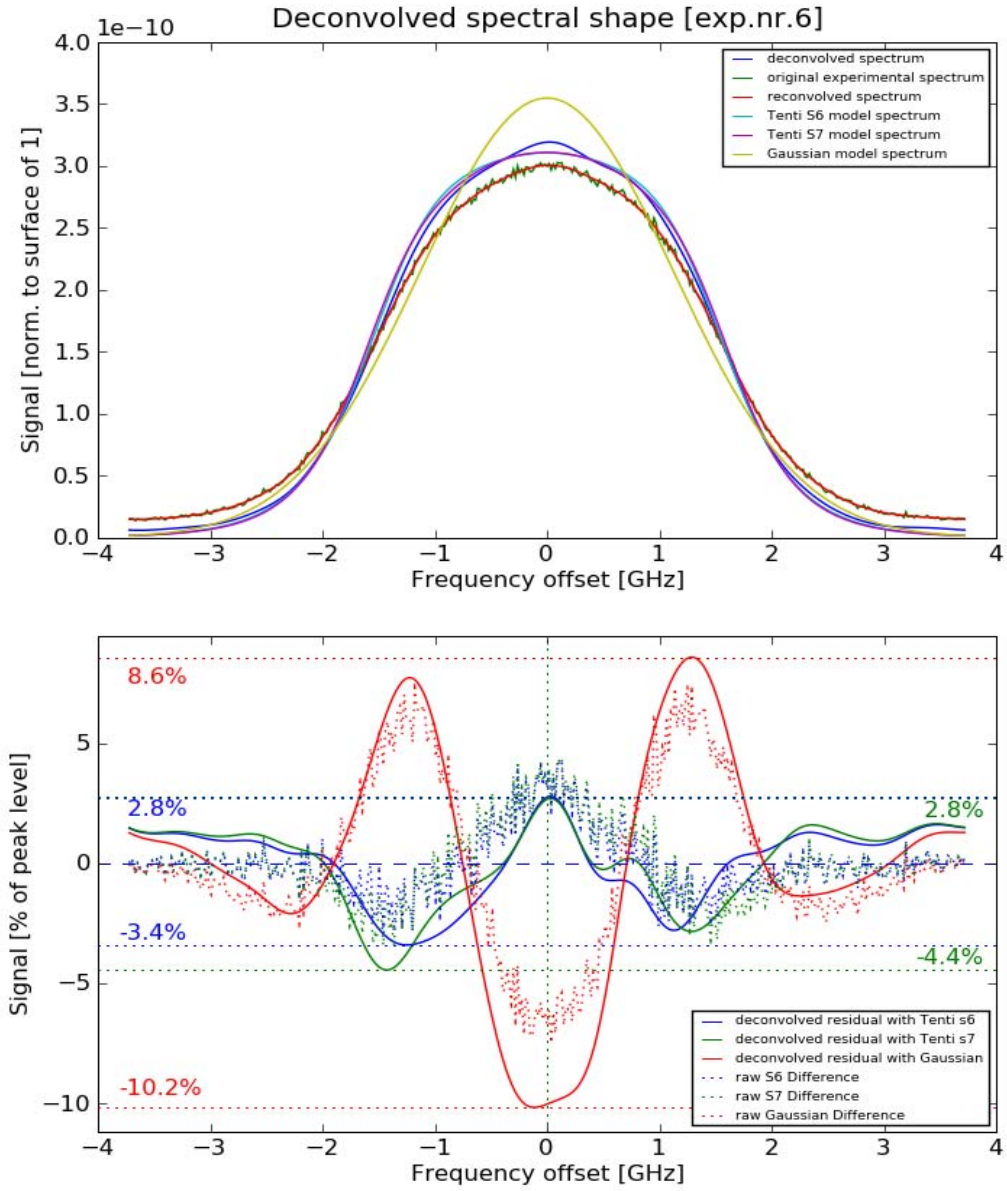

Figure 11-15: Deconvolution and residual calculation for experiment number 6 (pressure 1040 hPa)

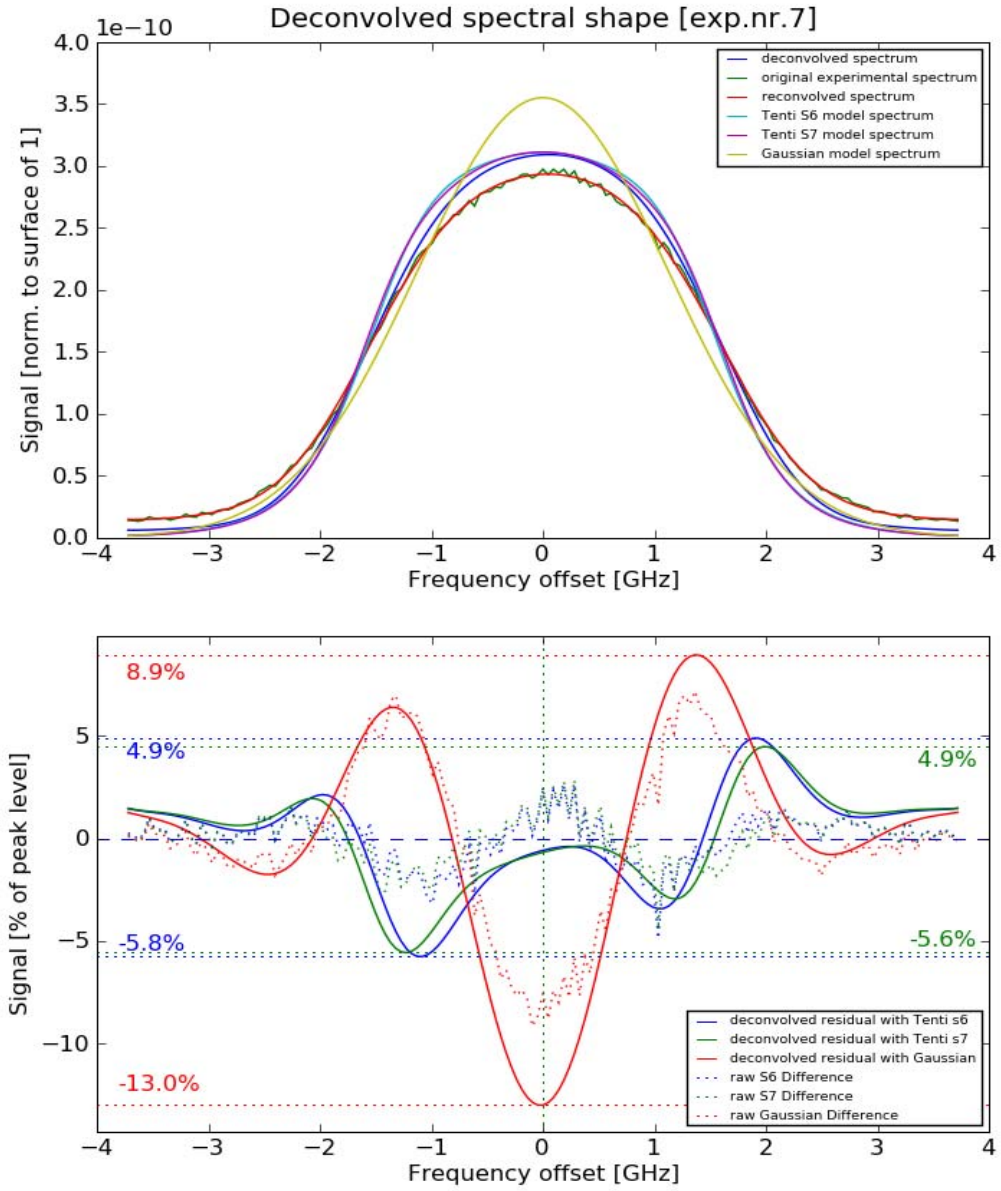

Figure 11-16: Deconvolution and residual calculation for experiment number 7 (pressure 1040 hPa)

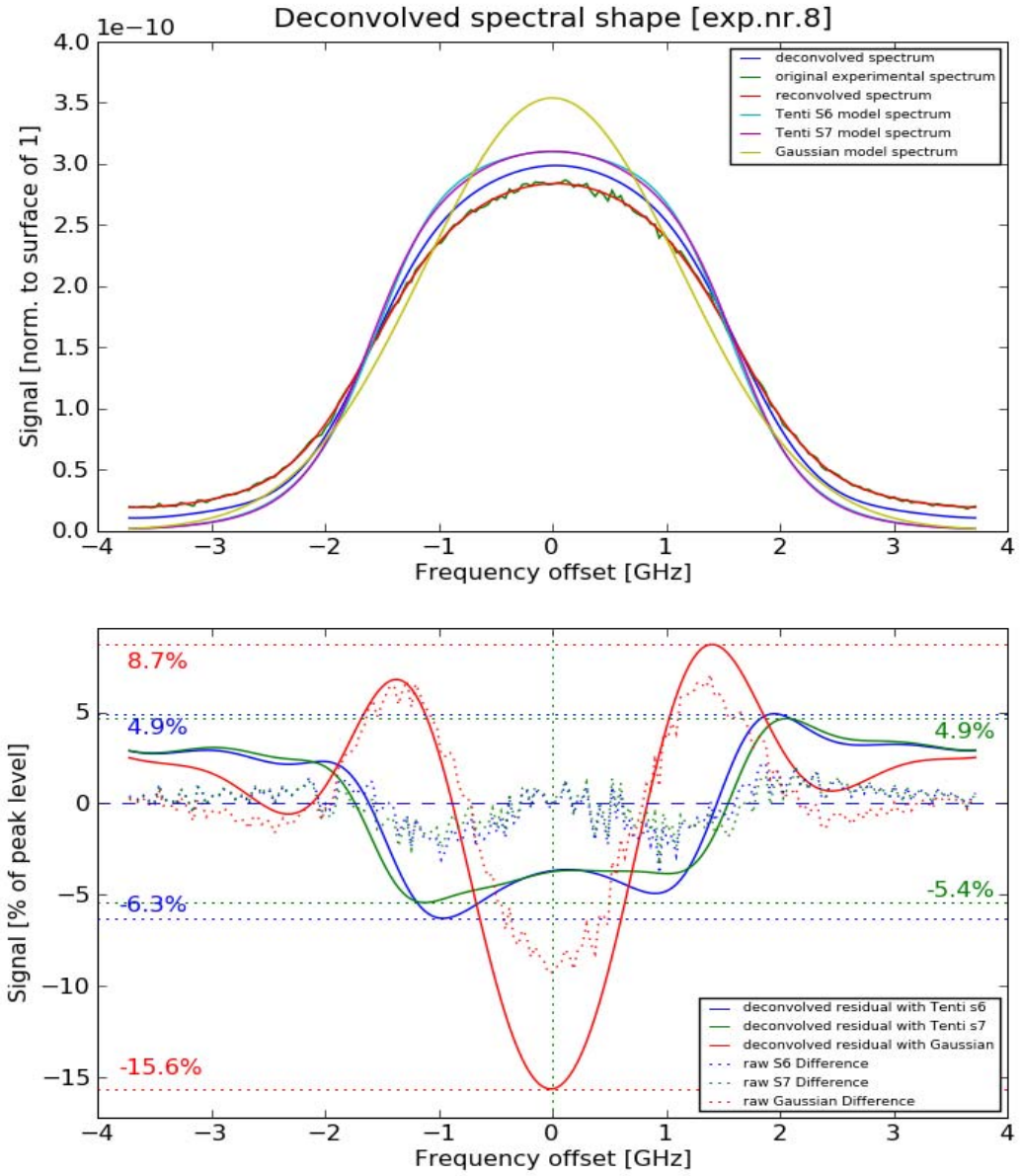

Figure 11-17: Deconvolution and residual calculation for experiment number 8 (pressure 1040 hPa)

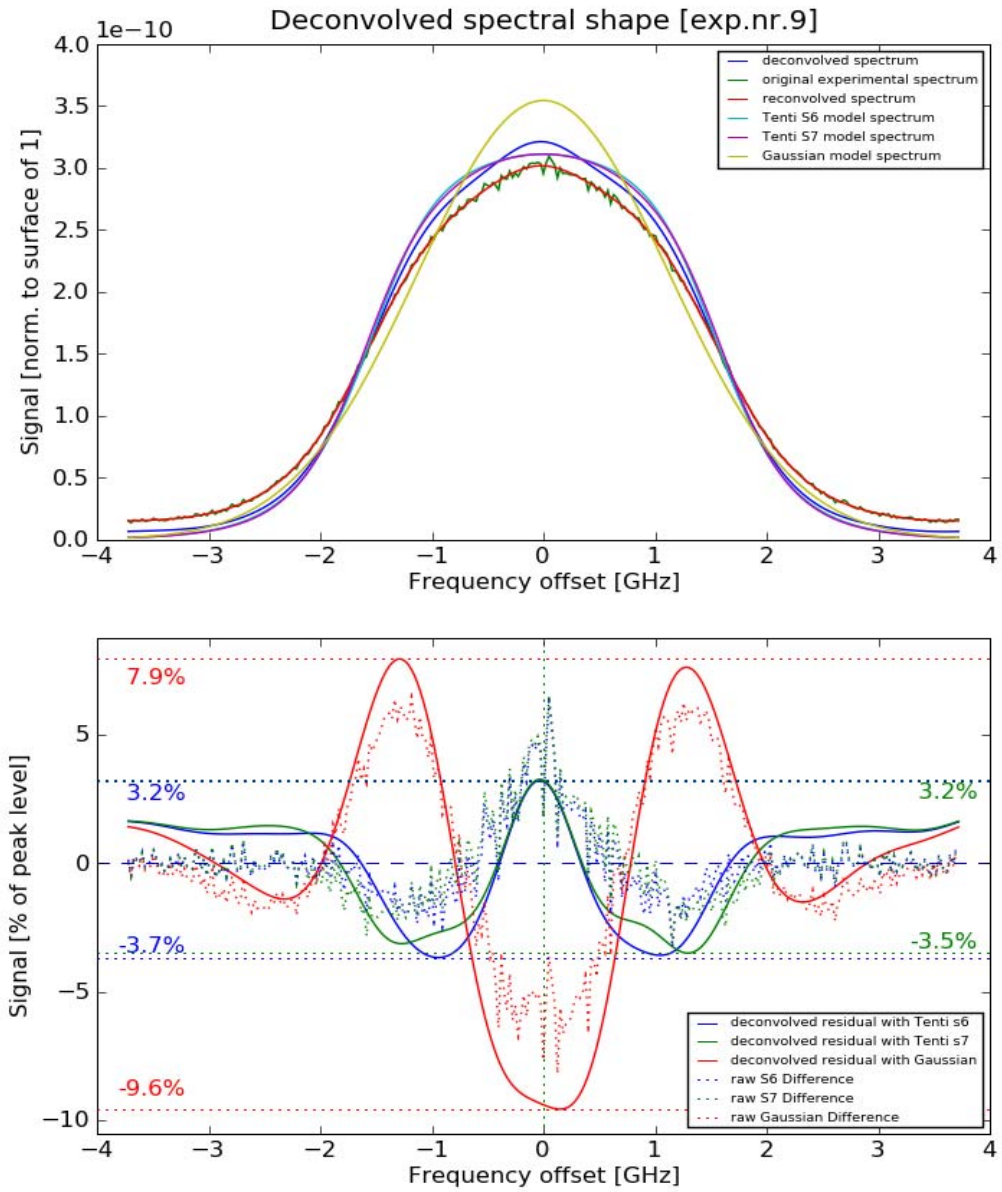

Figure 11-18: Deconvolution and residual calculation for experiment number 9 (pressure 1008 hPa)

11.6 Relating residual errors in the spectrum to wind deviations

Next, the LOS wind is taken into account by shifting the ADM-Aeolus spectral response by the Doppler shift, using:

$$\delta\lambda = \frac{2v_{LOS}\lambda}{c}$$

in which $\delta\lambda$ is the wavelength shift, and v_{LOS} the LOS wind speed. The factor of 2 is caused by the backscattering geometry. This is done for both the unperturbed theoretical spectra, and for the spectra perturbed by the above calculated residuals. An example of these shifted spectra is shown in Figure 11-19.

Note that due to the rescaling and shifting it can occur that a part of the spectrum needed in the following transmission calculation is missing. In those cases the signal is just taken to be zero for these missing parts (which are usually at some distance of the centre of the spectral peak).

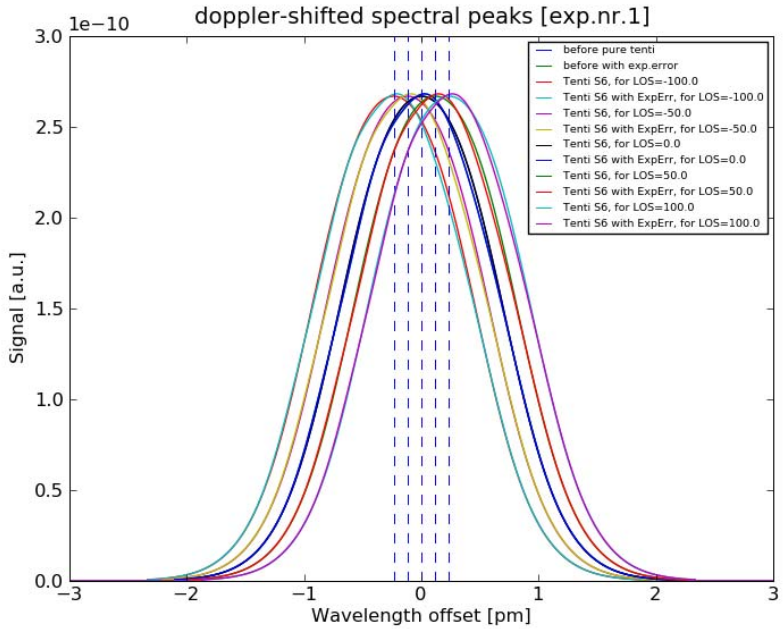

Figure 11-19: Spectra shifted by the Doppler effect, and used as input to the LOS error calculation.

The transmission found for both FP channels is then applied to the spectral shape derived in section 11.4 above, and this results in 2 signals, A and B. From this the response R is calculated using:

$$R = \frac{A - B}{A + B}$$

The responses have been calculated for each of the discussed 9 experiments, for the 3 theoretical models, and for a range of LOS wind velocities between -100 and 100 m/s.

The result is illustrated by Figure 11-20. The upper panel gives the calculated response against the assumed LOS wind. Because the curves are so close to each other, also the differences between the perturbed and unperturbed responses, and the derivative to the LOS wind has been plotted in the middle and lower panel.

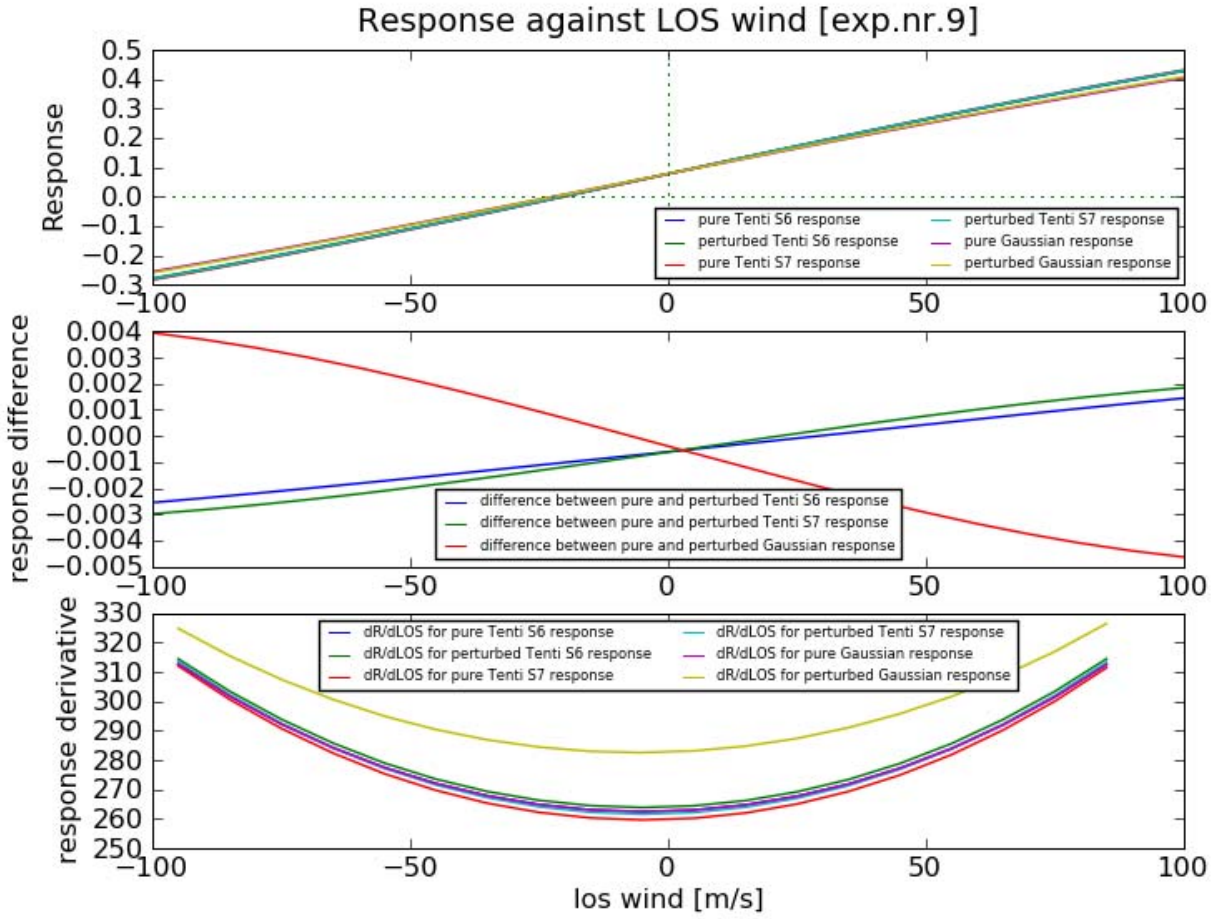

Figure 11-20: Response curves found for different LOS wind speeds, after perturbing the spectra with the residuals found from experiment 9.

Finally, a simplified wind retrieval needs to be done. For this, the perturbed spectral shape (model + rescaled residual) was taken as truth. This perturbed response is then "inverted" to LOS wind again, using the response calculated by the unperturbed theoretical spectrum. The resulting error compared to the true LOS wind then gives an idea how the deformation of the spectrum, as observed by the VU experiments, will translate to an error in LOS wind. The results of this final step are given in Figure 11-21 to Figure 11-29.

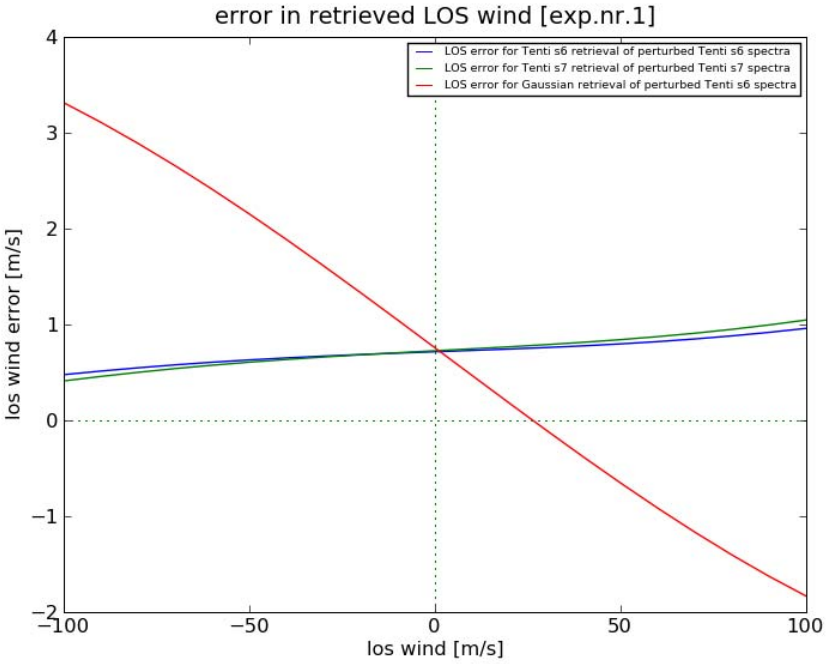

Figure 11-21: LOS wind error calculated from the residuals from experiment 1 (pressure 300 hPa).

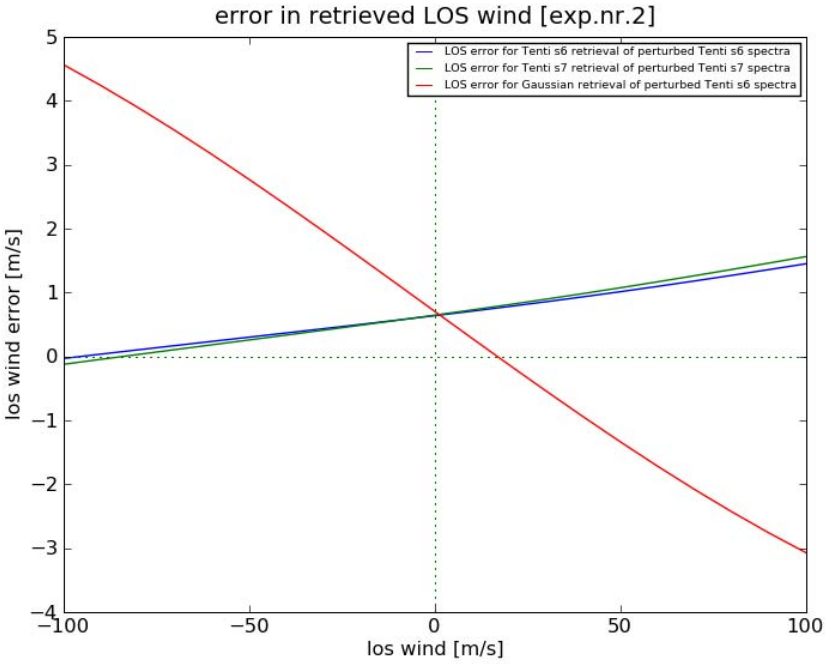

Figure 11-22: LOS wind error calculated from the residuals from experiment 2 (pressure 503 hPa).

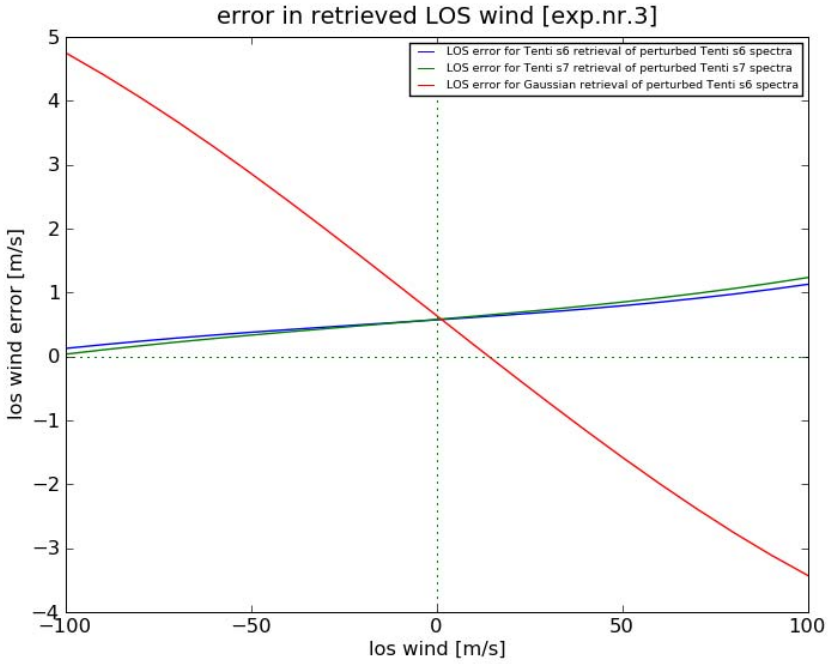

Figure 11-23: LOS wind error calculated from the residuals from experiment 3 (pressure 504 hPa).

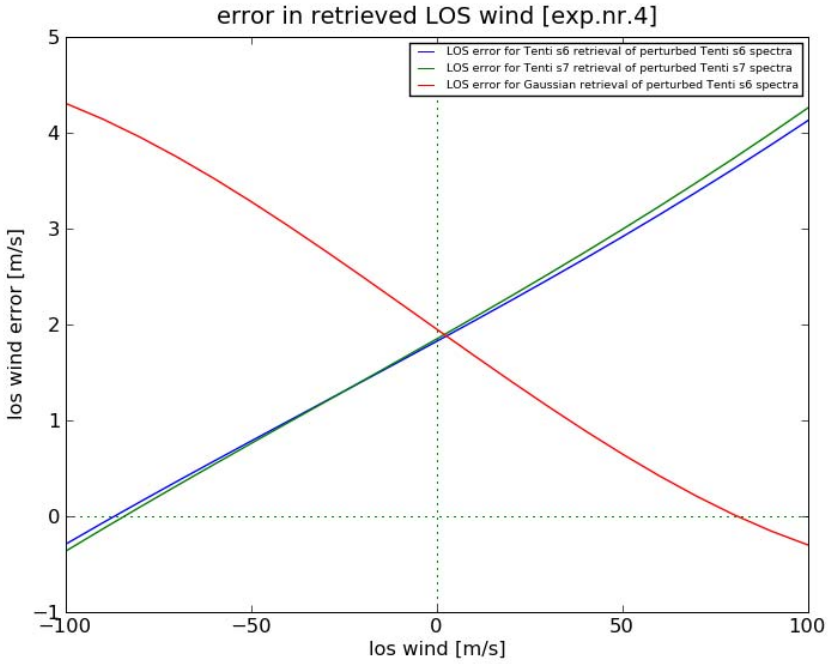

Figure 11-24: LOS wind error calculated from the residuals from experiment 4 (pressure 500 hPa). Note that this experiment clearly suffered from some Mie contamination.

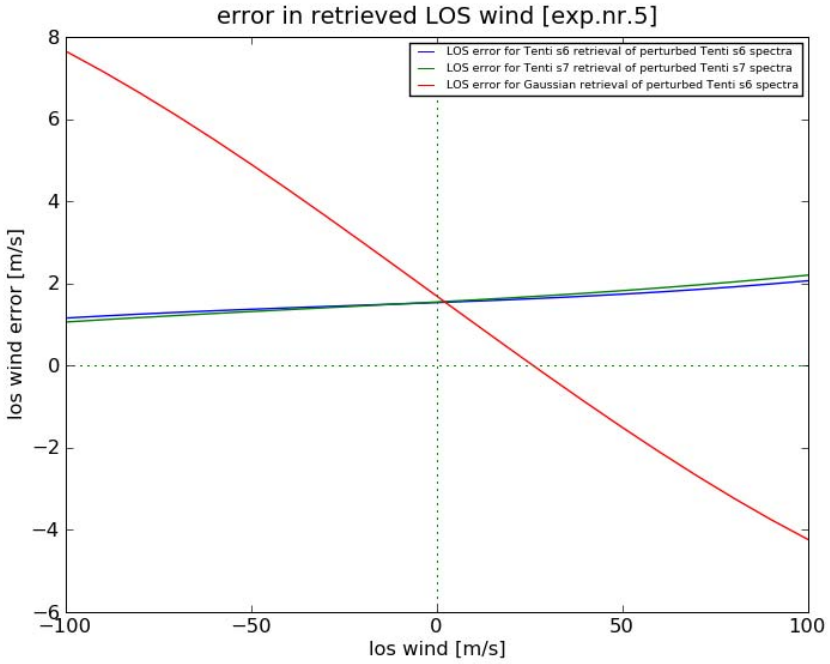

Figure 11-25: LOS wind error calculated from the residuals from experiment 5 (pressure 725 hPa).

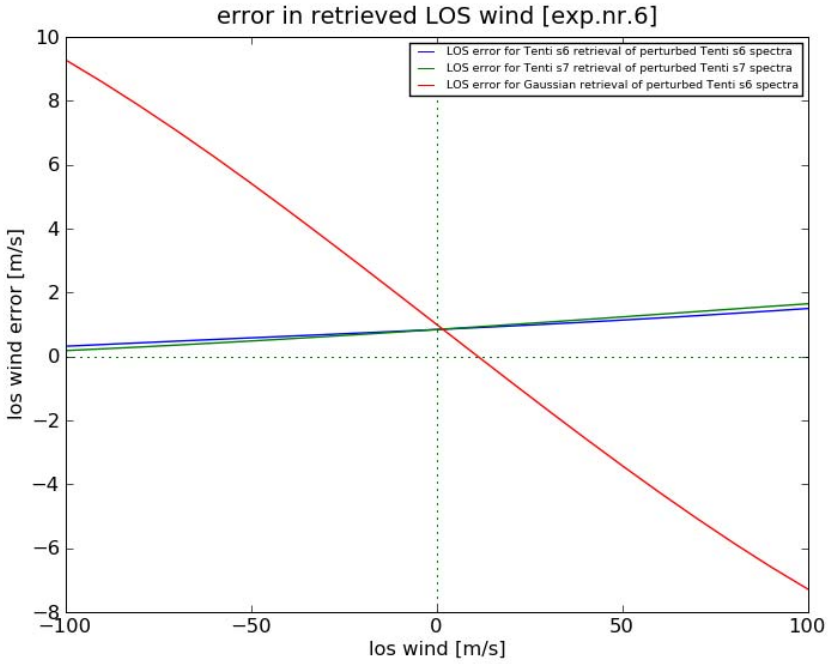

Figure 11-26: LOS wind error calculated from the residuals from experiment 6 (pressure 1040 hPa).

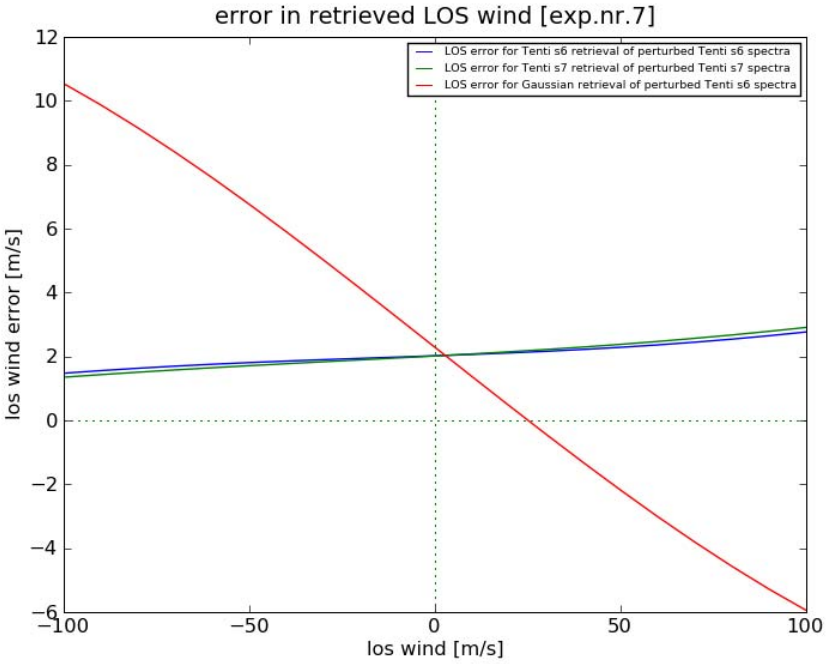

Figure 11-27: LOS wind error calculated from the residuals from experiment 7 (pressure 1040 hPa).

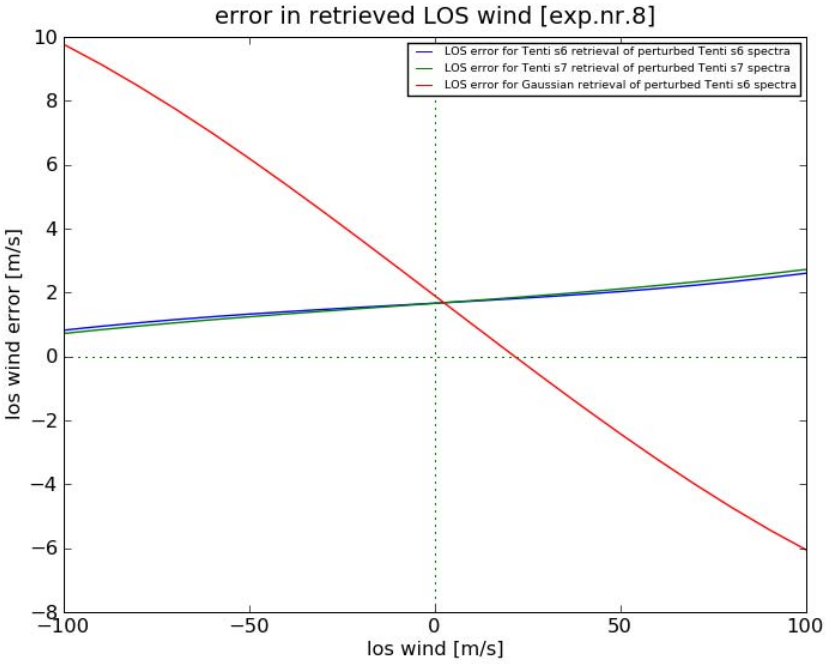

Figure 11-28: LOS wind error calculated from the residuals from experiment 8 (pressure 1040 hPa).

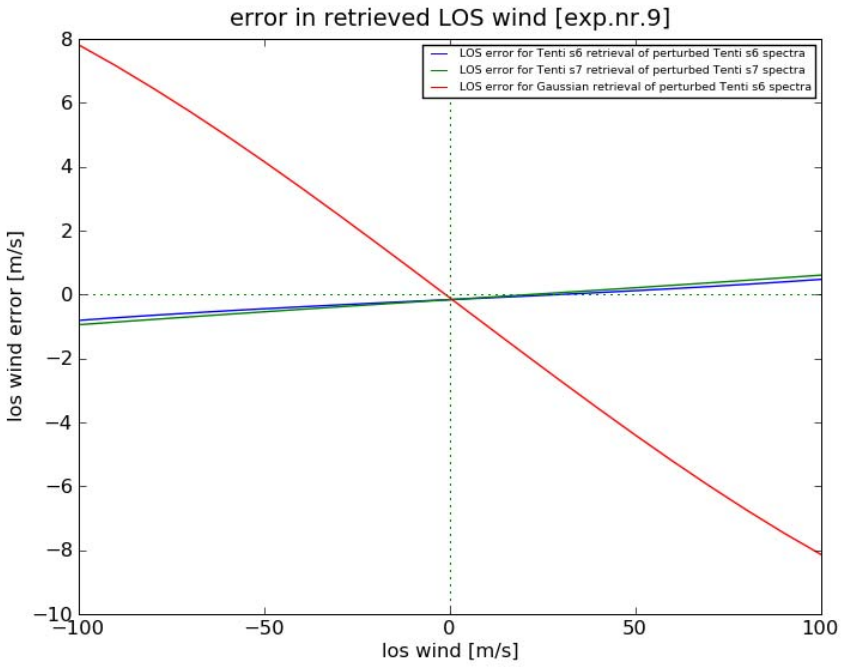

Figure 11-29: LOS wind error calculated from the residuals from experiment 9 (pressure 1008 hPa).

Clearly the error in LOS wind is much more sensitive to changes in the spectral shape than the responses are. The Gaussian results are fairly close to the ones reported in the ILIAD study [1], although ILIAD only report 2 LOS wind results. ILIAD reports LOS wind deviations in the order of 8 m/s for large input wind (LOS wind = 110 m/s) at the highest pressures (1000 hPa), and 1 m/s for moderate input winds (LOS wind – 13 m.s) ([1], chapter 7, Figures 7.10 and 7.11).

From results in Figure 11-21-Figure 11-29, it can be seen that the LOS wind error in most cases seems to have a significant constant offset and (on top) a small dependency on the input LOS wind. The only exception seems to be experiment 4, from which the LOS wind error shows a very strong dependency on input LOS wind. This is probably related to the deconvolution problem for that case, presumably due to Mie contamination. It is also noticeable that for experiment 9 (Figure 11-29), there seems to be almost no offset in the error curve. This could be related to the very symmetric shape of the residual for this case.

The asymmetry for each experiment has been defined as follows:

$$asymmetry = \frac{1}{N}\sum_{i=1}^{N} abs\left[residual(i) - residual(N-i+1)\right]$$

where *N* is the number of measurement points along the curve.

The calculated LOS wind errors in the Aeolus wind retrieval, when using the Tenti or Gaussian model line shapes in stead of the measured line shapes (Tenti model + measurement residual) are summarized in Table 11.4.

Exp.	Tenti S6			Tenti S7			Gaussian		
	Asymm. in residual	LOS wind error offset [m/s]	LOS wind error slope	Asymm. in residual	LOS wind error offset [m/s]	LOS wind error slope	Asymm. in residual	LOS wind error offset [m/s]	LOS wind error slope
1	0.754	0.715	0.0024	0.764	0.726	0.0032	0.719	0.749	-0.0257
2	0.530	0.666	0.0074	0.537	0.675	0.0084	0.491	0.719	-0.0382
3	0.648	0.593	0.0050	0.657	0.599	0.0060	0.601	0.643	-0.0409
4	1.325	1.861	0.0221	1.343	1.888	0.0231	1.228	1.970	-0.0230
5	1.069	1.563	0.0045	1.080	1.579	0.0057	0.965	1.696	-0.0594
6	0.621	0.868	0.0059	0.620	0.870	0.0073	0.543	0.994	-0.0828
7	1.451	2.058	0.0065	1.450	2.058	0.0078	1.270	2.290	-0.0824
8	1.195	1.684	0.0089	1.195	1.685	0.0100	1.047	1.880	-0.0791
9	0.211	-0.162	0.0064	0.211	-0.164	0.0078	0.185	-0.129	-0.0798

Table 11.4: Overview of the LOS wind error properties found for the 9 experiments.

11.7 Conclusions

As is shown above, small uncertainties in the knowledge of the spectral shape of the Rayleigh-Brillouin backscattered signal are of importance to ESA's Lidar missions. For the ADM-Aeolus Lidar mission in particular, such uncertainties may lead to errors in the Aeolus retrieved line-of-sight winds of a few m/s.

The Aeolus system requirements for the horizontally projected line-of-sight winds are 2 m/s in the free troposphere (between 2 and 16 km altitude). Errors in the line-of-sight wind retrieval on the order of m/s, caused by an imperfect knowledge of the RB-lineshape is therefore not acceptable (see [62], Table 4.1). Moreover, the type of errors reported here will be of a systematic nature (on each pressure level) and the requirement for the bias and so-called slope errors is even more stringent.

This error is related to (and partly proportional with) the actual wind velocity, so a part of the effect could be removed by calibrating the ADM-Aeolus instrument to the actual atmosphere. The difficulty will of course be the lack of in-situ measurements, so this calibration would need to be performed against a priori winds, pressures and temperatures produced by a Numerical Weather Prediction model. Mean global bias errors in NWP winds, pressures and temperatures are thought to be sufficiently low with respect to the systematic errors reported here to allow such calibration.

The question remains whether the Tenti model may be adapted/tuned to reduce the residuals with respect to the experiments, which present a more ideal solution.

The residuals between the modelled (Tenti) and “measured” (Tenti + measurement residuals) line shapes that were projected to the Aeolus configuration, showed that the uncertainties in the Tenti S6 RB model are generally much smaller than errors made when assuming a purely Gaussian molecular motion PDF. When assuming that the “measured” (Tenti + residual) line shape is correct, most simulations show a bias of around 1 m/s and a response slope error of 0.2-0.9% in the Aeolus retrievals when using the Tenti S6 RBS line shapes (Table 11.4). Some of the uncertainty in the measurements may be related to Mie contamination and in case 4 we were not able to fit the residual well in the deconvolution approach adopted due to this. We thus excluded case 4 as unrepresentative.

From the presented results it is clear that there still is some room for improvement, in the applied procedure of translating the measured line shapes to the Aeolus configuration. In a number of cases the deconvoluted signal, using the measurement FP-instrument function, clearly amplifies the asymmetry in the residual as present in the VU experiments. This appears to result in the wind bias as seen from the different cases processed (Table 11.4). A better noise filtering may perhaps provide improved fits of the asymmetry in the residuals, and thus somewhat reduced biases. The slope error does not appear much affected by the amplified asymmetry.

Also the deconvolved residual seems to have an offset FSR (while it was expected to go to almost zero in the wings of the backscattered signal). This may be due to the fact that the data was not compensated for any arbitrary offsets (contrary to what was implemented in the rbs fitting program).

There has been some discussion on the validity of using a perfect Airy function to deconvolve the measured spectrum. The perfect Airy function does not fit the height of the different measured FP instrument modes very well. This is solved by rescaling each mode again to a top value of one. However, this rescaling combined with measurement noise might introduce small deviations in the shape of the transmission peak if many modes are accumulated to obtain a better SNR. An alternative approach would be to use the actual measured instrument function for this deconvolution, although this would introduce an additional noise term, which may deteriorate the results. This subject might be investigated in more detail in a follow-up study, but in view of the available time of the current task it is not possible within this project.

The Filtering Fourier Transform (FFT) deconvolution approach used here was chosen because it is easy to implement with available standard tools. The approach provides a reasonable fit of the noisy and fitted residuals and a new approach may not yield very different results. Doing a Fourier transform and then applying a strong filter, basically seems equivalent to fitting to a sum of a few low-order polynomials (or any other set of basis functions). In both cases you need to truncate at some point, and this point will be rather arbitrary. This is true both for the FFT method and for a fitting method using any other basis. Wiener proposes an objective method where detection noise on top of the convoluted signal and instrument function is taken into account more rigorously [63]. The

method is based on an FFT basis and is well exploited in image processing [64]. Although, the method closely resembles the approach taken here, it may well be able to correct some of the remaining artefacts noted above.

Note that the temperature and pressure dependency of the LOS wind errors have been studied before in the ILIAD study [1]. The results from this study are consistent with the current results since the same LOS wind deviations, up to about 8 m/s where found at surface pressures and high input winds, when the wind retrieval was done using the Gaussian spectral shape.

Finally, since the L2B processing stage uses a look-up-table to invert the response of the FP spectrometer to wind, the table can be simply exchanged for a new one without much effort, as soon as a new and better model of the molecular motion spectrum would become available. Therefore efforts to improve the model can be continued until and even after the launch of ADM-Aeolus (validation from space).

12 Conclusions and recommendations

The objectives of the present study, as defined in the contract, were:

- Quantify the contribution of RB scattering to LIDAR molecular backscatter in a well-defined laboratory experiment.
- Validate the performance of the test equipment by reproducing the measurements of spontaneous RB scattering in N_2 as given by literature.
- Validate the TENTI (S6 and S7) model for atmospheric gas mixtures representing the Earth's atmosphere and assess the necessity of applying refinements to it.
- Make the necessary improvements of the TENTI (S6 and S7) model.
- Make recommendations for the use of the model in the Earth Explorer Core Mission and post-EPS Doppler Wind LIDAR retrieval algorithms.

For the present project two experimental setups have been constructed to investigate the Rayleigh-Brillouin (RB) scattering line profile. At VU University Amsterdam an RB-spectrometer was built to detect and analyze spontaneous RB-scattering in the ultraviolet domain, while at Radboud University Nijmegen coherent RB was investigated. The combination of these experiments allows for an independent test of the Tenti-models describing RB-scattering and they provide the possibility to probe the parameter space of the Tenti models in a wide range.

Both experiments were successful in that they produced the highest quality (highest signal-to-noise) RB-profiles of gaseous species measured so far, both for the spontaneous as for the coherent case. These results allow for sensitive quantitative tests of model descriptions of the RB-profile.

In the ESA-defined targets for the study it was requested to "validate the performance of the equipment by reproducing measurement of spontaneous RB-scattering in N_2 as given by literature". This turned out to be not possible for the spontaneous RB setup, for the simple reason that no measurements had been performed previously in the ultraviolet domain, while changing wavelengths cannot be done without affecting the throughput and bandwidth characteristics of the Fabry-Perot (FP) analyzer. Verifications of the experimental set-ups were therefore done by (i) measurements of Kr, where the RBS side peaks are very much pronounced, and (ii) by comparing the RB scattering from an open volume (air) with measurements with a scattering cell containing air at room temperature [65]. The latter was done for the spontaneous RB scattering experiment, and no differences in the backscattered line shapes were detected. This indicates that there should be no significant contribution of scattering from the cell walls and optics. Later, this turned out to be very dependent on alignment. For some measurements, scattering off the cell walls was occasionally detected resulting in an increase of the peak in the center of the RB scattered spectrum.

In addition, from an experimental perspective it was soon realized that RB-scattering cannot be measured in an exact back-scatter geometry under laboratory conditions (when employing a cell), for the reason that scattering from the windows in the line-of-sight tends to dominate the weak RB-scattering intensity. This does not hold for satellite remote sensing applications where signals are obtained from the open atmosphere. In the coherent RB-experiments the choice was made for a close to back-scatter geometry of 178^o; this helps increasing the volume defined by the nearly counter-

propagating and overlapping laser beams, and therewith the signal intensity. In the spontaneous RB-experiment a 90° scattering geometry was chosen because;

- This allows for suppressing the background signals to the lowest levels.
- This allows for testing the Tenti parameters to better accuracy, since the Brillouin acoustic side-modes become more *pronounced* at smaller scattering angles than at 180° backscatter.
- The scattering geometry strongly affects the full width of the scattering profile; the free-spectral-range and the finesse of the FP-analyzer must be adapted to this value; the perpendicular geometry matched the FSR conditions obtained from the available optics in the ultraviolet.

Measurements were performed in the pressure ranges between 300 mbar and 3 bar for the spontaneous RB setup and between 1 and 3 bar for the coherent RB setup. Both setups measured scattering in dry air, pure N_2 and pure O_2 gases, as well as Kr. With the coherent setup also measurements were performed in CO_2 and Ar. It was decided to extend the pressure range above the atmospherically relevant value of 1 bar, because these higher pressures are closer to the hydrodynamic regime, where the Brillouin side peaks are more pronounced. Hence, in this part of the parameter space the deviations on the profile from a pure Gaussian can be better modeled, and the Tenti model better tested.

The possible effect of water vapor was addressed in a spontaneous RB-measurement, while making a comparison between line shapes for dry air and humid air (i.e. air fully saturated with water vapor) at 1 bar. This resulted in a non-observable difference, which may be quantified as an effect by the water vapor content contributing less than 0.5% to the scattering intensity.

A new FORTRAN code was written for both the Tenti-6 and Tenti-7 models, which is now applicable for all gases, for all scattering geometries and for both the spontaneous and the coherent RB scattering cases. This code contains the transport coefficients (best known so far) of several gases (N2, O2, CO2, Ar, Kr, He, Xe, HD, air, SF6, H2O vapor), while for air also the possibility of temperature dependence of the transport coefficients is implemented. The Tenti model is from its principles adaptable for single species gases, but it was made applicable to air, by treating air as consisting of a single-species molecule with some macroscopic transport coefficients as know from literature. The code is easily implemented to produce model profiles for any RB-condition, where it can be compared with a measured profile. We must stress that the program is very user-friendly, while allowing for the treatment all gases (just the database of constants must be filled), and maintaining a high processing speed that would allow for its use online with the satellite measurements.

Comparisons between the high quality experimental data with the Tenti-codes led to the following conclusions, which are of key relevance for the current project:

(i) The Tenti-S6 model provides a better fit to the spectra of N_2, O_2 and air than the Tenti-S7 model.

(ii) The precise value of the needed transport coefficients is a challenge. This is especially the case for the bulk viscosity. For N_2 and air and large pressures ($p > 1$ bar) it had to be chosen significantly larger than the literature value. The performance of models and the value of transport coefficients can be studied best at pressures larger than atmospheric, where line shapes display a bigger influence of thermal sound (and therefore, on transport coefficients). The bulk viscosity is a relaxation parameter and is essentially dependent on frequency. It is not ruled out that we may still not know its

value at these (optical) frequencies. At low pressures the statistical and systematic accuracy of our experiments is not good enough to decide on a value of η_b that differs from the literature value.

(iii) It is reassuring that the findings of the spontaneous Rayleigh-Brillouin scattering experiments are supported by the coherent Rayleigh-Brillouin scattering experiments, although both experiments have completely different line shapes, and probably weigh the influence of the bulk viscosity differently.

(iv) Overall, favorable fits between experiment and models depend on an important transport coefficient, namely the bulk viscosity. However, this physical quantity is then considered as a fit parameter. This degrading of η_b to a fit parameter is in a sense unphysical. On the other hand the value of η_b is currently not (or insufficiently) know from experiment; it is simply not measured at optical frequencies. Furthermore, its value should not depend on pressure, but at large pressures, we find the best value to be pressure-dependent. Since line shapes at low pressure do not sensitively depend on η_b, a best guess based on a high-pressure measurement may be prudent here. This project may have taught us how to fit, but the full scope of the effects of the elusive bulk parameter is not understood.

Phrased in quantitative terms the key conclusion of the present study is that the Tenti-6 model describes the observations for air, N_2 and O_2, over a wide parameter space to within 2%, at least for the atmospherically relevant conditions of pressure. In the ESA-defined targets it was requested to “validate the TENTI (S6 and S7) model for atmospheric gas mixtures representing the Earth’s atmosphere and assess the necessity of applying refinements to it”. In these terms the quantitative validation may be expressed in terms of the deviation falling within 2%. Two refinements have been performed in the treatment of the model: to allow the use of the air transport coefficients (treating air as a “single species”) and the “fit” of the bulk viscosity value. Overall, the model (Tenti S6) matches the air measurements better with a bulk viscosity value that it is roughly double of the literature value.

Extra refinement of the Tenti model is at this stage not a workable option. The model is the current “best description” of the RB-scattering process, and it has a solid basis in physics. It is indeed based on some assumptions on collision phenomena at the microscopic level (e.g. the use of the Maxwell force scaling as $1/r^5$), but these are assumptions generally made in statistical thermodynamics of gases to make problems tractable, and can therefore hardly been altered. Numerical adaptation of the Tenti model is not an option either (perhaps it can for a determination of the bulk viscosity parameter as discussed above). It is very difficult to optimize the model in a numerical fashion; such procedure should then describe the results in the very wide parameter space of all possible RB-configurations and for all gases. The major difficulty with such approach would be that the macroscopic transport coefficients of the gases would acquire different values; the Tenti-models are based on reproducing that information. We stress also that more precise experimental data on some of the transport coefficients would be needed, in particular as a function of temperature. A direct measurement of the bulk viscosity at optical frequencies would also be very useful to unravel the riddle of the RB-scattering profile.

For the moment it must be concluded that the Tenti-6 model yields the best description and is at the same time rooted in physical insight in the processes underlying the scattering profile. Deviations at the 2% level are found when subjecting this model to experimental tests under various conditions, and these deviations are beyond the possibility of modeling. So the current situation is that there exists an optimum line

shape (Tenti-6) and there is quantitative knowledge on the deviation of the experimental data from this line shape.

As is shown in this study, small uncertainties in the knowledge of the spectral shape of the Rayleigh-Brillouin backscattered are of importance to ESA's Lidar missions. For the ADM-Aeolus Lidar mission in particular, such uncertainties may lead to errors in the Aeolus-retrieved-line-of-sight-winds of a few m/s.

The Aeolus system requirements for the uncertainty of the horizontally projected line-of-sight winds are 2 m/s in the free troposphere (between 2 and 16 km altitude). Errors in the line-of-sight wind retrieval on the order of m/s, caused by an imperfect knowledge of the RB-lineshape is therefore not acceptable. Moreover, the type of errors reported here will be of a systematic nature (on each pressure level) and the requirement for the bias and so-called slope errors is even more stringent.

This error is shown to be related to (and partly proportional with) the actual wind velocity, so a part of the effect could be removed by calibrating the ADM-Aeolus instrument to the actual atmosphere. The difficulty will of course be the lack of in-situ measurements, so this calibration would need to be performed against a priori winds, pressures and temperatures produced by a Numerical Weather Prediction model. Mean global bias errors in NWP winds, pressures and temperatures are thought to be sufficiently low with respect to the systematic errors reported here to allow such calibration.

As discussed, the Tenti model cannot be simply adapted/tuned to reduce the residuals with respect to the experiments. There are no free parameters to adapt, with the possible exception of the bulk viscosity; but even there it is preferable to perform dedicated measurements at optical frequencies (possibly at a function of pressure and temperature) to determine its value.

The residuals between the modelled (Tenti) and "measured" (Tenti + measurement residuals) line shapes that were projected to the Aeolus configuration, show that the uncertainties in the Tenti S6 RB model are generally much smaller than errors made when assuming a purely Gaussian molecular motion PDF. When assuming that the "measured" (Tenti + residual) line shape is correct, most simulations show a bias of around 1 m/s and a response slope error of 0.2-0.9% in the Aeolus retrievals than when using the Tenti S6 RBS line shapes.

From the presented results it is clear that there still is some room for improvement in the applied procedure of translating the measured line shapes to the Aeolus configuration. In a number of cases the deconvoluted signal, using the measurement FP-instrument function, clearly amplifies the asymmetry in the residual as present in the VU experiments. This appears to result in a wind bias as seen from the different cases processed. A better noise filtering may perhaps provide improved fits of the asymmetry in the residuals, and thus somewhat reduced biases.

There has been some discussion on the validity of using a perfect Airy function to deconvolve the measured spectrum. The perfect Airy function does not fit the height of the different measured FP instrument modes very well. Also, the deconvolution method applied in section 11.4 on this report may be further refined and improved. Therefore, the results on the impact of the difference between the Tenti model and the measured RBS spectra are qualitative. As an example, the asymmetry found in the deconvoluted measurement spectra are not believed to be representative. Thiese subjects might be investigated in more detail in a follow-up study, but in view of the available time of the current task it is not possible within this project.

The temperature and pressure dependency of the line-of-sight wind errors have been studied before in the ILIAD study. The results from this study are consistent with the current results since the same line-of-sight wind deviations, up to about 8 m/s where found at surface pressures and high input winds, when the wind retrieval was done using the Gaussian spectral shape.

Finally, since the Level-2B processing stage uses a look-up-table to invert the response of the FP spectrometer to wind, the table can be simply exchanged for a new one without much effort, as soon as a new and better model of the molecular motion spectrum would become available. Therefore efforts to improve the model can be continued until and even after the launch of ADM-Aeolus (validation from space).

The present study has delivered a wide variety of scattering profiles from both RB-spectrometers that were specifically developed for this ESA study. The 18-month duration was too short to cover the entire parameter space. Some important issues dealing with the understanding of the RB-profiles are therefore still open, and could be measured without major difficulty now that the time-consuming process of constructing the spectrometers has been overcome. Interesting open issues are:

- *Wavelength* effects. Although both experiments on SRBS and CRBS have been performed at totally different wavelength, their theoretical treatment in the Tenti model is quite different. Therefore, it could be a possibility to test the Tenti model in the wavelength dependence (towards longer wavelength) with small adaptations of the setup.
- *Angle* effects. The angular dependence of the SRBS shape has been tested only once and a further test on this parameter could be desirable. The SRBS experiment can be adapted to the measurement at a different angle without too much effort.
- *Temperature* effects were not dealt with except for a few measurements in spontaneous RB-scattering on a single elevated temperature at pressures of 1 bar and 3 bar in air. In principle the existing cell could be redesigned for intra-cavity operation at elevated and lower temperatures, in the range relevant. The goal would not only be to measure profiles of relevance for atmospheric conditions, but to extend the parameter space for testing Tenti-6 as a function of temperature. Possibly this would provide further insight in the effect of the bulk viscosity parameter. This important parameter η_b playing a crucial role in the Tenti models has been experimentally determined for much lower acoustic frequencies, and not for the relevant optical frequencies. Moreover, most transport coefficients have been measured at ambient temperatures and their temperature dependence is not sufficiently known. Further measurements in temperature parameter space are therefore adviced.
- *Polarization*. In the present investigation the full intensity of the scattered light was analyzed irrespective of the polarization properties of the scattered light. As may be deduced from the experimentally deduced King factors depolarization plays an important role for molecular gases, with ratios range from 3% for N_2 to 6% for O_2. It remains an intriguing question how the depolarization ratio would change over the scattering profile. This issue is of direct relevance for the ADM-Aeolus mission because the detection system contains polarization-sensitive optics. Careful placing of polarizing optics in the experimental setting would allow for polarization measurements.

In addition we mention two further possibilities to use the novel constructed spectrometers and to extend the knowledge of RB scattering profiles in a scientifically important domain. Scattering profiles of carbon dioxide are of major relevance for the atmosphere of Venus, which is subject to existing studies, and possibly also of future ESA missions. It is known that CO_2 has the largest of all depolarization ratio of all gases existing at high pressures; this makes CO_2 interesting for reasons of testing the Tenti-framework as such. Also, the Tenti model has not been tested for molecules with specific attractive forces, as for example occurring in polar gases. This could be tested by probing scattering profiles in high density gases such as CO, ammonia, or NO.

13 Acknowledgements

The authors wish to thank the following persons for their collaboration and support:

Mr. Jacques Bouma (VU Amserdam) for the technical support in setting up the spontaneous Rayleigh-Brillouin scattering experiment.

Dr. Astrid de Wijn (Radboud University Nijmegen) for many fruitful discussions on the background of the TENTI models.

Mr. Benjamin Witschas and Dr. Oliver Reitebuch (DLR, Oberpfaffenhofen) for the collaboration in the spontaneous RB measurement on dry and humid air.

Dr. W. Marquez (Universita do Parana, Curitiba, Brazil) for fruitful discussions on the effects of binary mixtures on the scattering profile.

Dr. Anne Straume and Dr. Oliver LeRille from ESA for supervising and reviewing this project and for the pleasant and constructive collaboration.

14 References

1 *ILIAD - Impact of Line Shape on Wind Measurements and Correction methods*
C. Loth, P. H. Flamant, A. Dabas, M.-L. Denneulin, A. Dolfi-Bouteyre, A. Garnier and D. Rees, *ESA Contract No 18334*, (2005) 124p.

2 *On the transmission of light through an atmosphere containing small particles in suspension and on the origin of the blue of the sky*
J. W. Strutt (Lord Rayleigh) Philos. Mag. **47** (1899) 375-384. Reprinted in: Lord Rayleigh, Scientific papers, Dover Publications, New York (1964), part IV, page 397.

3 *Nonlinear Optics*
Robert W. Boyd, Academic Press, 1992.

4 *Doppler shifts in light scattering from pure liquids and polymer solutions*
R. Pecora, J. Chem. Phys. **40**, 1604 (1964).

5 *On the Rayleigh-Brillouin scattering in air*
Q. Zheng, PhD thesis, 2004

6 *Rayleigh-Brillouin spectra in molecular nitrogen*
R. P. Sandoval and R. L. Armstrong, Phys. Rev. A **13**, (1976) 752

7 *Molecular backscatter heterodyne lidar: a computational evaluation*
B.J. Rye, Appl. Opt **37** (1998) 6321.

8 *Spectrum of light scattered from thermal fluctuations in gases*
T.J. Greytak and G. B. Benedek, Phys. Rev. Lett. **17** (1966) 179.

9 *Kinetic models and Brillouin scattering in a Molecular gas*
C.D. Boley, R.C. Desai and G. Tenti, Can. J. Phys. **50**, (1972) 2158.

10 *Rayleigh scattering by air*
D.R. Bates, Planet. Space. Science **32** (1984) 785.

11 *The polarization of laser light scattered by gases*,
N.J. Bridge and A.D. Buckingham, Proc. R. Soc A. **295**, (1966) 334-349.12 *Measurement of the dispersion in polarizability anisotropies*
G. R. Alms, A.K Burnham and W. H. Flygare, J. Chem. Phys. **63**, (1975) 3321-3326.13 *Dynamic polarizabilities and Raman intensities of CO, N_2, HCl and Cl_2*
J. Oddershede and E. N. Svendsen, Chem. Phys. **64** (1992) 359.

14 *The atmosphere in the laboratory: cavity ring-down measurements on scattering and absorption*
M. Sneep, PhD thesis 2004.

15 *Rayleigh-Brillouin spectrum of compressed He, Ne and Ar. I. Scaling*
V. Ghaem-Maghami and A. D. May, Phys. Rev A **22** (1980) 692

16 *Molecular filtered Rayleigh scattering applied to combustion*,
G. S. Elliott, N. Glumac, and C. D. Carter, Meas. Sci. Technol. **12** (2001) 452-466

17 *Rayleigh-Brillouin scattering to determine one-dimensional temperature and number density profiles of a gas flow field*
J. A. Lock, R. G. Seasholt and W. T. John, Appl. Opt. **31** (1992) 2839

18 *Property and velocity measurements in a supersonic flow*
M. Boguszko, R. Huffman and G. Elliott, University of Illinois, Urbana-Champaign, IL
AIAA-2006-1390 , 44th AIAA Aerospace Sciences Meeting and Exhibit, Reno, Nevada, Jan. 9-12, 2006

19 *Stimulated Rayleigh-Brillouin Gain Spectroscopy in Pure Gases*
C. Y. She, G. C. Herring, H. Moosmüller, and S. A. Lee, Phys. Rev. Lett. **51** (1983) 1648 - 1651

20 *Stimulated Rayleigh-Brillouin gain spectroscopy*
C. Y. She, G. C. Herring, H. Moosmüller, and S. A. Lee, Phys. Rev. A **31** (1985) 3733 - 3740

21 *Coherent Rayleigh scattering*
J. H. Grinstead and P. F. Barker, Phys. Rev. Lett. **85** (2000) 1222 - 1225

22 *Coherent Rayleigh-Brillouin scattering in molecular gases*
X. Pan, M. N. Shneider, and R. B. Miles, Phys. Rev. A **69** (2004) 033814

23 *Coherent Rayleigh-Brillouin scattering*
X. Pan, M. N. Shneider, and R. B. Miles, Phys. Rev. Lett. **89** (2002) 183001

24 *Temperature measurements by coherent Rayleigh scattering*
X. Pan, P. F. Barker, A. Meschanov, J. H. Grinstead, M. N. Shneider and R. B. Miles, Opt. Lett. **27** (2002) 161

25 *Narrow-band coherent Rayleigh scattering in a flame*
H. T. Bookey, A. I. Bishop and P. F. Barker, Opt. Expr. **14** (2006) 3461

26 *Decelerating and bunching molecules with pulsed traveling optical lattices*
G. Dong, W. Lu, and P. F. Barker, Phys. Rev. A **69** (2004) 013409

27 *Optical microlinear accelerator for molecules and atoms*
P. F. Barker and M. N. Shneider, PRA **64** (2001) 33408

28 *Coherent Rayleigh scattering in the high intensity regime*
M. N. Shneider, P. F. Barker, X. Pan, and R. B. Miles, Opt. Commun. **239** (2004) 205

29 *Spectral Narrowing in Coherent Rayleigh Scattering*
H. T. Bookey, M. N. Shneider and P. F. Barker, PRL **99** (2007) 133001

30 *Polarization-decoupled Brillouin-enhanced four-wave mixing*
W. A. Schroeder, M. J. Damzen, and M. H. R. Hutchinson, IEEE J. Quantum Electron. **25** (1989) 460

31 *Optics*
E. Hecht, 4th ed. Addison Wesley International (2002).

32 *Single-shot spectral measurements and mode correlations in a multimode pulsed dye laser*
L.A. Westling, M.G. Raymer and J.J. Snyder, J. Opt. Soc. Am. B 1, 150 (1984)

33 *Power spectrum of coherent Rayleigh-Brillouin scattering in carbon dioxide*
X. Pan, M.N. Shneider, R.B. Miles, Phys. Rev. A 71, 045801 (2005).

34 *Interference pattern of the Fizeau interferometer*
T. T. Kajava, H. M. Lauranto, A. T. Friberg, J. Opt. Soc. Am. A 11, 2045 (1994)

35 *Fringe shifts in multiple-beam Fizeau interferometry*,
J. R. Rogers, J. Opt. Soc. Am 72, 638 (1982)

36 *Molecular transport in pulsed optical lattices*
M.N. Shneider, P.F. Barker, S.F. Gimelshein, Appl. Phys. A 89: 337-350 (2007).

37 *Light scattering studies of moderately dense gas mixtures: Hydrodynamic regime*
L. Letamendia, J. P. Chabrat, G. Nouchi, J. Rouch and C. Vaucamps, Phys. Rev. A **24** (1981) 1574

38 *Brillouin scattering in liquids excited by He-Ne maser*
R. Y. Chiao and B. P. Stoicheff, J. Opt. Soc. Am. **54** (1964) 1286

39 *Brillouin scattering in liquids + solids using low power lasers*
G. B. Benedek, T.J. Greytak and K. Fritisch, J. Opt. Soc. Am. **54** (1964) 1284

40 *Optical heterodyne studies of Brillouin scattering in Xenon near the critical point*
D. Eden and H. L. Swinney , Opt. Comm. **10** (1974) 191

41 *Brillouin-scattering in photon-correlation spectroscopy of liquids*
G. Simonsohn, Opt. Acta **30** (1983) 875

42 *High resolution Rayleigh-Brillouin correlation spectroscopy*
G. Simonsohn and F. Wagner, Opt. Lett. **14** (1989) 110

43 *Resolved forward Brillouin scattering in optical fibers*
R. M. Shelby, M. D. Levenson and P. W. Bayer, Phys. Rev. Lett. **54** (1985) 939

44 *Light beating spectroscopy of polarized and depolarized scattering in p-n-hexyl p'-cyanobiphenyl*
T. Matsuoka, K. Sakai and K. Takagi, Phys. Rev. Lett. **71** (1993) 1510

45 *Superheterodyne light beating spectroscopy for Rayleigh-Brillouin scattering using frequency-tunable lasers*
H. Tanaka and T. Sonehara, Rev. Scient. Instr. **73** (2002) 1998

46 *Rayleigh-Brillouin scattering in compressed H_2, D_2 and HD*
E. H. Hara, A. D. May and H. P. F. Knaap, Can. J. Phys. **49** (1971) 420

47 *Rayleigh-Brillouin scattering of gases with internal relaxation*
Q. H. Lao, P. E. Schoen and B. Chu, J. Chem. Phys. **64** (1976) 3547

48 *Zero-crossing signal averaging system for Fabry-Perot interferometry*
Q. H. Lao, P. E. Schoen and B. Chu , Rev. Sci. Instr. **47** (1976) 418

49 *Rayleigh-Brillouin spectrum of compressed He, Ne and Ar. II. The hydrodynamic regime*
V. Ghaem-Maghami and A. D. May, Phys. Rev. A **22** (1980) 698

50 *Contamination monitoring for the Laserlab at VU Amsterdam*, material report number 5562. Materials Space Evaluation & Radiation Effects Section, Materials & Space Components Space Evaluation Division, ESA.

51 http://en.wikipedia.org/wiki/Gaussian_beam

52 *Nonlinear absorption phenomena in optical materials for the UV spectral range*
E. Eva, K. Mann, Appl. Surf. Sci. 109/110 (1997) 52-57.

53 *The airborne demonstrator for the direct-detection Doppler wind Lidar ALADIN on ADM-Aeolus: I. Instrument design and comparison to satellite instrument*
O. Reitebuch, C. Lemmerz, E. Nagel, U. Paffrath, Y. Durand, M. Endermann, F. Fabre, M. Chaloupy (unpublished).

54 *Model for polarized and depolarized Rayleigh-Brillouin scattering spectra in molecular gases*
Q. Zheng, Optics Express, **21** (2007) 14257

55 On the kinetic model description of Rayleigh-Brillouin scattering from molecular gases
G. Tenti, C. Boley and R. Desai, Can J. Phys. **52**, 285 (1974)

56 *Light scattering studies of moderately dense gases. (ii) nonhydrodynamic regime*
L. Letamendia, P. Joubert, J. Chabrat, J. Rouch, C. Vaucamps, C. Boley, S. Yip, S. Chen, Phys. Rev. A 25: 481 (1982).

57 Coherent Rayleigh-Brillouin scattering in binary mixtures
W. Marquez Jr., J. Stat. Mech. **P03013**, (2007)

58 *Kinetic model nalaysis of light scattering in binary mixtures of monatomic ideal gases*
J.R. Bonatto, W. Marquez, J. Stat. Mech. **P09014** (2005).

59 *Absorption and dispersion of ultrasonic waves, Vol 7*
K.E. Herzfeld, T. Litoviz, Academic Press, New York (1959).

60 *Bulk viscosity as a relaxation parameter: Fact or fiction ?*
W.E. Meador, G.A. Milner, L.W. Townsend, Phys. Fluids, 8, 258 (1996).

61 *ADM-Aeolus Science Report, ESA-SP 1311, April 2008.*
(see: http://esamultimedia.esa.int/docs/SP-1311_ADM-Aeolus_FINAL_low-res.pdf)

62 *Aeolus Level 1b Processor and End-to-End Simulator, End-to-End Simulator Detailed Processing Model (E2S DPM), ADM-MA-52-1801_E2S-DPM*, v2.5, 27-Aug-2008

63 *The Extrapolation, Interpolation, and Smoothing of Stationary Time Series with Engineering Applications*
N. Wiener, Wiley, New York, 1949.

64 *Digital Image Processing Using Matlab*
R. Gonzalez, R. Woods, and S. Eddins. Prentice Hall, 2003.

65 Technical Note 2 part 1: Validation measurements for SRBS experiment.